

THE TURBULENT BOUNDARY LAYER ON A POROUS PLATE:
AN EXPERIMENTAL STUDY OF THE FLUID MECHANICS
FOR ADVERSE FREE-STREAM PRESSURE GRADIENTS

By

P. S. Andersen, W. M. Kays and R. J. Moffat

Report No. HMT-15

Prepared Under Grant NASA NGR-05-020-134

for

The National Aeronautics and Space Administration

Thermosciences Division
Department of Mechanical Engineering
Stanford University
Stanford, California

May 1972



ACKNOWLEDGMENTS

This research was made possible through a grant from the National Aeronautics and Space Administration, NGL 05-020-134. The authors wish to express appreciation for the interest of Dr. Robert W. Graham of the NASA Lewis Laboratories.

The authors also wish to thank Mr. Robin Birch for his contribution to the design of the hot-wire probes and for his admirable execution of both probes and test section, Mr. James F. Marshall for his valuable assistance in the data taking, and last but not least Ms. Jan Elliott for her speedy typing of the manuscript and competent coordination of the publication process.

ABSTRACT

An experimental investigation of transpired turbulent boundary layers in zero and adverse pressure gradients has been carried out. Profiles of: a) the mean velocity, b) the three intensities of the turbulent fluctuations, and c) the Reynolds stress were obtained by hot-wire anemometry. The friction coefficients were measured by using an integrated form of the boundary layer equation to "extrapolate" the measured shear stress profiles to the wall.

The two adverse pressure gradients correspond to free-stream velocity distributions of the type, $u_\infty \propto x^m$, where $m < 0$. Equilibrium boundary layers (i.e. flows with defect profile similarity) were obtained when the transpiration velocity, v_o , was varied such that the blowing parameter, $B = \rho v_o u_\infty / \tau_o$, and the Clauser pressure gradient parameter, $\beta = \frac{\delta_1}{\tau_o} \frac{dp}{dx}$, were held constant.

In the analysis of the data it was found that the Prandtl mixing-length, ℓ , can be expressed as $\ell = \kappa y$ ($\kappa = 0.41$ is the von Kármán constant) in the "logarithmic" region of all the mean velocity profiles.

The following new law of the wall,

$$\frac{u}{\sqrt{\tau_c/\rho}} = \frac{1}{0.41} \ln\left(\frac{y \sqrt{\tau_c/\rho}}{\nu}\right) + 5.0 + 14.0 \left(\sqrt{\frac{\tau_o}{\tau_c}} - 1\right)$$

has been proposed and verified for the present data. The shear stress, $\tau_c = \tau(y_c)$ is characteristic for the logarithmic region. The parameter y_c , which is a measure of the thickness of the viscous sublayer, is related to τ_c through the equation:

$$\frac{y_c \sqrt{\tau_c/\rho}}{\nu} = 72 .$$

The Reynolds number of turbulence, $Re_T = \ell \sqrt{-\overline{u'v'}}/\nu$ was found to have the constant value of $Re_{T,c} = 29$ at $y = y_c$.

Predictions of some of the experimental boundary layers were performed by solving the boundary layer equations numerically. The "mean field closure" in the inner region was provided by van Driests mixing-length model, $\ell = 1 - \exp(-3y/y_c)$. The length scale, y_c , was obtained from $y_c = 72\nu/\sqrt{\tau(y_c)\rho}$ by invoking the computed local shear stress profile.

TABLE OF CONTENTS

	Page
Acknowledgments	iii
Abstract	iv
Table of Contents	vi
List of Figures	ix
List of Tables	xiii
Nomenclature	xiv
CHAPTER 1. PRELIMINARY REMARKS	1
CHAPTER 2. EXPERIMENTAL BOUNDARY CONDITIONS	3
2.1 The Velocity Defect Law	4
2.2 Analysis of Boundary Conditions for Equilib- rium Boundary Layers	6
2.3 Nominal Boundary Conditions	9
CHAPTER 3. EXPERIMENTAL APPARATUS, INSTRUMENTATION AND PROCEDURE	12
3.1 Main Air Systems	12
3.2 Test Section	14
3.3 Transpiration Air System	17
3.4 Procedure for Setting-up a New Run	17
3.5 Pressure Measurements	18
3.6 Velocity Measurements	18
3.6.1 Hot-Wire Instrumentation	19
3.7 Traversing Mechanism	24
3.8 Calibration of Hot-Wire	24
3.9 Qualifications of the Apparatus	26
CHAPTER 4. MEASUREMENT OF WALL SHEAR STRESS	31
4.1 The Shear Stress Equation	31
4.1.1 The Momentum Integral Equation	32
4.1.2 The Shear Stress Method	33
CHAPTER 5. DATA REDUCTION	35
5.1 Mean Velocity Profiles and $\overline{u'^2}$	35

	Page
5.2 Viscous Shear Stress	35
5.3 $-\overline{u'v'}$, $\overline{v'^2}$ and $\overline{w'^2}$	36
5.4 The Free-Stream Velocity	37
5.5 Virtual Origin and $d\delta_2/dx$	37
5.6 Correlation of Friction Coefficients	38
5.7 Shear Stress Profiles	38
CHAPTER 6. ANALYSIS AND DISCUSSION OF EXPERIMENTAL RESULTS	41
6.1 Friction Coefficients	42
6.2 The Outer Region	48
6.2.1 Velocity Defect Profile Similarity.	48
6.2.2 Shear Stress, Eddy Viscosity and Mixing-Length	49
6.3 The Inner Region	56
6.3.1 Mean Velocity Profiles in Wall Coordinates	56
6.3.2 Mixing-Length and Eddy Viscosity	58
6.4 Profiles of Turbulence Intensities	62
6.5 Shear Stress Profiles	62
CHAPTER 7. THEORETICAL RESULTS	78
7.1 Theories for A^+	78
7.2 Sublayer Thickness and Characteristic Shear Stress	80
7.3 Generalized Law of the Wall	84
7.4 Predictions of Experimental Boundary Layers.	92
CHAPTER 8. SUMMARY AND CONCLUSIONS	99
CHAPTER 9. TABULATED EXPERIMENTAL DATA	103
9.1 Constant Pressure, $m = 0$	106
9.2 Weak Adverse Pressure Gradient, $m = -.15$	107
9.3 Strong Adverse Pressure Gradient, $m = -.20$	110
REFERENCES	157

	Page
APPENDIX A. MEASUREMENT OF TURBULENCE INTENSITIES AND REYNOLDS STRESS	160
1. Directional Sensitivity of the Hot-Wire	160
2. Probe Position and Velocity Decomposition	161
3. The Hot-Wire Response to Turbulence	163
4. Measurement of Turbulent Velocity Correlations	164
5. Error Due to Misalignment of Probe	166
6. Error on $\overline{u'v'}$ Due to the Neglect of the Triple Correlations	169
APPENDIX B. DESCRIPTION OF THE COMPUTER PROGRAM "SLOT".	172
1. Principles of the Program	172
2. Fit of the Measured Velocity	175
3. Correction of Slot-Widths	175
4. Potential Flow Field in Test Section	176

LIST OF FIGURES

Figure		Page
3-1	Longitudinal cross section of the tunnel test section	16
3-2	Photograph of test section with traversing mechanism in position	16
3-3	Comparison of probes. Velocity profile in an adverse pressure gradient	20
3-4	Horizontal hot-wire probe	21
3-5	Rotatable hot-wire probe	23
3-6	Photograph of rotatable hot-wire probe in operating position	25
3-7	Photograph of rotatable hot-wire traversing mechanism in operating position	25
3-8	Typical hot-wire calibration: linearizer output versus air velocity	28
3-9	Friction coefficients for constant pressure and no transpiration	28
3-10	Comparison of measured velocity profiles at five different transverse locations but at the same streamwise position	29
3-11	Lateral variation of the momentum thickness	29
3-12	Measured strength of the wake compared to Coles [16] "normal" strength ($\kappa = 0.41$)	30a
6-1	$c_f/2$ versus Re_{δ_2} ; $m = 0$, constant blowing fractions	43
6-2	$c_f/2$ versus Re_{δ_2} ; $m = -0.15$, constant blowing fractions	43
6-3	$c_f/2$ versus Re_{δ_2} ; $m = -0.15$, equilibrium boundary layers	44
6-4	$c_f/2$ versus Re_{δ_2} ; $m = -.20$, equilibrium boundary layers	44

Figure		Page
6-5	Ratio of friction coefficient to the friction coefficient for the non-transpired boundary layer at the same momentum thickness Reynolds number versus a modified blowing parameter, $m = 0$	46
6-6	Ratio of friction coefficient to the friction coefficient for the non-transpired boundary layer at the same momentum thickness Reynolds number versus a modified blowing parameter, $m = -.15$. . .	47
6-7	Defect profiles for a blown equilibrium boundary layer	50
6-8	Clauser shape factor. All runs except 102171-1 and 092271-5 are represented	50
6-9	Profiles of non-dimensional eddy viscosity in outer region. Weak adverse pressure gradient, no transpiration	52
6-10	Non-dimensional shear stress profiles for three equilibrium boundary layers. Weak adverse pressure gradient	52
6-11	Profiles of non-dimensional mixing-length in outer region. Weak adverse pressure gradient, no transpiration	54
6-12	Profiles of non-dimensional mixing-length in outer region. Comparison for selected boundary conditions	54
6-13	Profiles of non-dimensional eddy viscosity in outer region. Comparison for selected boundary conditions	55
6-14	Velocity profiles in wall coordinates for the three boundary layers without transpiration . . .	57
6-15	Velocity profiles in wall coordinates for equilibrium boundary layers. Weak adverse pressure gradient	57
6-16	Comparison of two profiles of the normalized mixing-length in the inner region	60
6-17	Profiles of the normalized mixing-length versus the distance from the wall divided by van Driest's length scale	60

Figure		Page
6-18	Profiles of the non-dimensional eddy viscosity, $\epsilon^+ = \epsilon/\nu$	61
6-19	Empirical correlation for A^+ from Eq. (6-20) . .	61

TURBULENCE INTENSITIES

6-20	Run 120771-1	64
6-21	Run 122271-2	64
6-22	Run 122771-3	65
6-23	Run 121671-3	65
6-24	Run 122971-1	66
6-25	Run 121171-3	66
6-26	Run 010372-1	67
6-27	Run 071571-5	67
6-28	Run 111571-1	68
6-29	Run 111771-3	68
6-30	Run 101371-2	69
6-31	Run 112871-1	69
6-32	Run 102171-1	70
6-33	Run 021572-5	70
6-34	Run 110971-1	71

SHEAR STRESS PROFILE

6-35	Run 122271-2	71
6-36	Run 122771-3	72
6-37	Run 121671-3	72
6-38	Run 122971-1	73
6-39	Run 121171-3	73
6-40	Run 010371-1	74
6-41	Run 071571-5	74
6-42	Run 111571-1	75
6-43	Run 111771-3	75
6-44	Run 101371-2	76
6-45	Run 021572-5	76

Figure		Page
6-46	Run 110971-1	77
7-1	$\frac{A^+}{A_0^+} \sqrt{\tau^+}$ versus $y^+ \frac{A_0^+}{A^+}$ for selected boundary conditions	82
7-2	u^+ versus $yu_c/\nu = y^+ A_0^+ / A^+$ for selected runs . .	89
7-3	Verification of the generalized law of the wall, Eq. (8-19)	90
7-4	Comparison of prediction of the Re_{δ_2} with experimental data	95
7-5	Comparison of prediction of $c_f/2$ with experimental data	95
7-6	Comparison of prediction of A^+/A_0^+ with experimental data	96
7-7	Comparison of predicted and experimental velocity profiles	97
7-8	Comparison of predicted and measured velocity profile	98
A-1	Geometry and position of hot-wire probe (schematic). Probe shown for $\theta = 0$	161
A-2	Misalignment of probe axis - (x_1, y_1, z_1) is the 'mean flow' coordinate system	167

LIST OF TABLES

Table		Page
2-1	Experimental velocity distributions (nominal) . .	9
2-2	Experimental transpiration boundary conditions (nominal)	10
9-1	Run numbers and nominal boundary conditions . . .	103
9-2	Measured free-stream velocity distributions; u_{∞} [ft/s]	105
9-3	Measured blowing fraction, F	105

NOMENCLATURE

a	coefficient in Eq. (5-9)
A	length scale in van Driest's mixing-length model, $l = ky[1 - \exp(-y/A)]$
A^+	$= Au_\tau/\nu$
A_0^+	value of A^+ for $v_0^+ = p^+ = 0$
b	exponent in Eq. (5-9)
B	$= F/(c_f/2)$, blowing parameter
B_0	$= F/(c_f/2)_0$, modified blowing parameter
$c_f/2$	$= \tau_0/\rho u_\infty^2$, friction coefficient
$(c_f/2)_0$	friction coefficient for $v_0 = 0$
E, e, e'	instantaneous value, mean value and fluctuation of linearizer output
F	$= v_0/u_\infty$, blowing fraction
F_1	reference blowing fraction in Eq. (2-13)
G	$= \frac{1}{\Delta} \int_0^\infty \frac{u_\infty - u}{u_\tau} dy$, Clauser shape factor
H	$= \delta_1/\delta_2$, shape factor
k	$= \epsilon/\delta_1 u_\infty$
K	$= \frac{\nu}{u_\infty^2} \frac{du_\infty}{dx}$
l	$= \sqrt{-u'v'}/\frac{du}{dy}$, mixing-length
m	exponent in Eq. (2-12)

m_F	exponent in Eq. (2-13)
p	static pressure
p_d	dynamic pressure
p_{d_1}	$= \rho u_1^2$, reference dynamic pressure
p^+	$= \frac{v}{\rho u_\tau^3} \frac{dp}{dx}$
Re_{δ_2}	$= \delta_2 u_\infty / \nu$, momentum thickness Reynolds number
Re_T	$= \ell \sqrt{-u'v'} / \nu$, Reynolds number of turbulence
u, v, w	components of mean velocity
u', v', w'	components of instantaneous turbulent fluctuations
U	$= u + u'$, instantaneous velocity in the x-direction
u_1	reference velocity in Eq. (2-12)
u_i	"indicated" velocity defined by Eq. (A-1)
u_τ	$= \sqrt{\tau_o / \rho}$, friction velocity
u_c	$= \sqrt{\tau_c / \rho}$, "characteristic" velocity scale
u^+	$= u / u_\tau$
u_c^+	$= u^+$ at $y^+ = y_c^+$
v_o	blowing velocity
v_o^+	$= v_o / u_\tau$
x	streamwise coordinate
x_o	virtual origin of turbulent boundary layer

x_1	reference location in Eqs. (2-12) and (2-13)
y	coordinate normal to wall
y_c	$= 3A$, characteristic distance from the wall
y^+	$= yu_\tau/\nu$
z	transverse coordinate
β	$= \frac{\delta_1}{\tau_o} \frac{dp}{dx}$, Clauser pressure gradient parameter
δ	boundary layer thickness
δ_1	$= \int_0^\infty (1 - \frac{u}{u_\infty}) dy$, displacement thickness
δ_2	$= \int_0^\infty \frac{u}{u_\infty} (1 - \frac{u}{u_\infty}) dy$, momentum thickness
δ_{99}	boundary layer thickness defined such that $u(\delta_{99}) = .99u_\infty$
Δ	$= \int_0^\infty \frac{u_\infty - u}{u_\tau} dy$, Clauser boundary layer thickness
ϵ	$= \sqrt{-u'v'}/\frac{du}{dy}$, eddy viscosity
ϵ^+	$= \epsilon/\nu$
κ	von Kármán constant ($l = \kappa y$)
λ	computational value of l/δ_{99} in outer region
μ	dynamic viscosity

ν	kinematic viscosity
ρ	density
τ	shear stress
τ_c	$= \tau(y_c)$, characteristic shear stress
τ_v	$= \mu \frac{du}{dy}$
τ_o	shear stress at wall
τ^+	$= \tau/\tau_o$
ϕ	slant of hot-wire
θ	angle of rotation of hot-wire spindle

CHAPTER 1

PRELIMINARY REMARKS

The present work is primarily concerned with "transpired" turbulent boundary layers, i.e. flows for which the normal velocity at the wall is different from zero. The terms "blowing" and "suction" will be used to describe the direction of the flow normal to the wall.

In the last twenty years interest in transpired turbulent boundary layers has been rapidly increasing and a great number of both experimental and theoretical contributions to the field have been published. For example, the Heat and Mass Transfer group at Stanford University has since 1967 been engaged in a continued effort directed towards the understanding of transpired turbulent boundary layers. Constant pressure boundary layers (Simpson [2]) and boundary layers in favorable pressure gradients (Julien [3], Loyd [4]) have been studied experimentally. Kays [5] summarizes the findings for these flows.

Only one experimental study of turbulent boundary layers in adverse pressure gradients with transpiration has been reported in the literature. McLean [7] studied blown turbulent boundary layers in very strong adverse pressure gradients. The main objective of this work was to study the onset of separation. McLean did not, however, measure the skin friction, but instead relied on Stevenson's [8] law of the wall. This reflects the great difficulty of measurement of the wall shear stress. The severity of this difficulty may be gauged by the very large discrepancies between the skin friction coefficients generated by different experimenters even for the constant pressure blown boundary layers. Squire [6] gives a comparative analysis of McQuaid's [27] and Simpson's [2] data, which disagree considerably.

Coles [24] surveys all existing data for basic transpired turbulent boundary layers.

In the present work it was proposed to determine the wall shear stress by measuring the shear stress away from the wall (as the sum of the Reynolds stress and the viscous stress) and extrapolating to the wall by the integrated boundary layer equations. This novel technique should give a degree of "independence" to the present data.

In addition to investigating the adverse pressure gradient boundary layers, which are the main focus of the present work, it seemed natural to repeat some of Simpson's constant pressure flows. A secondary motivation for doing this was the finding, during exploratory tests, that the mean velocity profiles obtained by hot-wire anemometry differed appreciably (especially very close to the wall) from the earlier flattened pitot tube results of Simpson.

Many ideas have been advanced, over the years, to provide a mean field closure (i.e. an empirical relationship between the shear stress profile and the mean velocity profile). Some of these will be treated as an introduction to the present treatment of the problem of closure. The idea of a law of the wall for transpired boundary layers will likewise be discussed and the empirical bases for some of the laws which have been proposed in the literature will be treated as an introduction to the present attack on the problem.

CHAPTER 2

EXPERIMENTAL BOUNDARY CONDITIONS

The principal objective of the experimental part of the present study has been to provide measurements for transpired boundary layers in adverse pressure gradients.

The experimental program was carried out on the Stanford Heat and Mass Transfer Apparatus [1] which has been modified to permit the establishment and accurate control of adverse pressure gradients.

It has been attempted to remove all complicating circumstances from the basic problem. This investigation is therefore limited to low speed, constant property flows with the transpiration fluid being the same as the free-stream fluid (air). Boundary conditions leading to strong deviations from "equilibrium" (e.g. steps in the pressure gradient or in the transpiration rate) have been avoided. Adverse pressure gradients strong enough to cause separation are also outside the scope of this investigation.

It is well known that the "outer region" (say the outer 90%) of the boundary layer reacts much slower than the inner wall region to changes in the boundary conditions. In fact, for most continuously varying boundary conditions the wall region may be considered to be in "equilibrium" in the sense that only local values of the pressure gradient and transpiration rate are important. The outer region of the boundary layer, on the contrary, shows a pronounced "history effect". The experimental boundary conditions will be chosen such that the outer region of the boundary layer is close to equilibrium.

Clauser 1954 [9] considered the problem of similarity in turbulent boundary layers. It had been known for a long time that the constant pressure boundary layer has both inner region similarity ("the law of the wall") and outer

region similarity ("velocity defect law"). It was Clauser's idea to extend the concept of outer similarity to also include turbulent boundary layers in adverse pressure gradients. He succeeded in experimentally creating adverse pressure gradient boundary layers with a defect similarity just as in the case of the zero pressure gradient boundary layer. Clauser called all boundary layers with outer similarity, "equilibrium boundary layers".

In this chapter it will be shown that one reasonably may hope to extend the equilibrium boundary layer concept to also include adverse pressure gradient boundary layers with transpiration. The boundary conditions necessary for such flows will be discussed in Section 2.2.

2.1 The Velocity Defect Law

The velocity defect i.e. $(u_\infty - u)$ normalized on the "friction velocity", u_τ , is seen to be a similarity variable for the outer region of the constant pressure boundary layer if plotted against y/δ : The outer $\approx 90\%$ of the boundary layer has a unique shape (independent of the Reynolds number) when plotted this way. Thus:

$$\frac{u_\infty - u}{u_\tau} = F\left(\frac{y}{\delta}\right) \quad , \quad (2-1)$$

is the defect law for the zero pressure gradient boundary layer (δ is the boundary layer thickness).

Clauser defined a new boundary layer thickness, Δ , such that

$$\Delta = \delta \int_0^1 \frac{u_\infty - u}{u_\tau} d\left(\frac{y}{\delta}\right) \quad (2-2)$$

Note that the Clauser thickness, Δ , is a constant factor times δ when Eq. (2-1) is satisfied, i.e. when the boundary layer has outer region similarity. The defect law Eq. (2-1)

may therefore equivalently be written,

$$\frac{u_\infty - u}{u_\tau} = F\left(\frac{y}{\Delta}\right) \quad (2-1a)$$

The advantage of using the Clauser thickness, Δ , rather than δ is that it is more precisely defined and may be determined with greater accuracy from experimental data.

Clauser now showed experimentally that a relationship of the type (2-1a) exists also for certain adverse pressure gradients. The family of these pressure gradients will, following Clauser, be called "equilibrium pressure gradients"; the corresponding boundary layers are equilibrium boundary layers.

Clauser described the shape of the equilibrium velocity profiles by the shape factor,

$$G = \frac{1}{\Delta} \int_0^1 \left(\frac{u_\infty - u}{u_\tau} \right)^2 d\left(\frac{y}{\delta}\right) \quad (2-3)$$

Thus each equilibrium flow corresponds to a certain value of the "Clauser shape factor", G . For example, the zero pressure gradient boundary layer corresponds to $G \approx 7$. Adverse pressure gradient boundary layers have higher values of G .

Clauser reasoned that an equilibrium boundary layer would be obtained if the ratio of the wall shear force and the pressure force acting on the boundary layer is constant. More precisely this condition implies that $\beta = \frac{\delta_1}{\tau_0} \frac{dp}{dx} = \text{const.}$ Bradshaw [10] writes the von Kármán momentum integral equation in the form,

$$\frac{d}{dx}(\delta_2 u_\infty^2) = \frac{\tau_0}{\rho}(1 + \beta) \quad (2-4)$$

From Eq. (2-4) β can be interpreted as the ratio between the contributions of the pressure and the shear stress to the production of the momentum defect in the boundary layer. Bradshaw found that an adverse equilibrium pressure gradient corresponds to an experimentally decreasing free-stream velocity, $u_\infty \propto x^m$; $m < 0$. The basis for this finding is both Clauser's work and Bradshaw's own measurements.

In the present work the idea of an equilibrium boundary layer in an adverse pressure gradient will be extended to include flows with transpiration. If the transpiration velocity, v_o , is not zero then the momentum integral equation (2-4) takes the form:

$$\frac{d}{dx}(\delta_2 u_\infty^2) = \frac{\tau_o}{\rho} (1 + \beta + B), \quad (2-5)$$

where $B = \rho v_o u_\infty / \tau_o$ will be called "the blowing parameter"; it is the ratio between the rate of change of x-momentum of the transpiration fluid and the wall shear force. B may also be interpreted as the ratio between the contributions of the transpiration fluid and the wall shear stress to the production of momentum defect in the boundary layer.

For flows with zero pressure gradient ($\beta = 0$) the results of Simpson [2] indicate that constant B flows also have $G = \text{constant}$, i.e. are equilibrium boundary layers. It is therefore reasonable to hope that keeping β and B constant will result in transpired adverse pressure gradient equilibrium boundary layers. The appropriate boundary conditions for such flows will be considered in the following section.

2.2 Analysis of Boundary Conditions for Equilibrium Boundary Layers

The boundary conditions which control the behavior of the boundary layer will be stated as $u_\infty = u_\infty(x)$ and

$F = F(x)$, where $F = v_o/u_\infty$ is the "blowing fraction". A priori it cannot be known which boundary conditions will produce a constant β and B simultaneously. It turns out, however, that a few reasonable assumptions permit the prediction of the correct boundary conditions. Furthermore, the hope that a constant β and B corresponds to an equilibrium boundary layer (constant G) will be verified experimentally (see Chapter 7).

In the following analysis the basic assumption is that β and B are constant. The following additional assumptions will be made:

$$(a) \quad u_\infty = u_1 x^m ,$$

where u_1 is a constant. In other words, it is assumed that the free-stream velocity variation that leads to an equilibrium boundary layer for $B = 0$ also produces a constant G boundary layer for $B \neq 0$ (assuming of course that the correct transpiration rate boundary condition is used).

$$(b) \quad (c_f/2)_o = a Re_{\delta_2}^{-b} ,$$

where $(c_f/2)_o$ is the friction coefficient for a non-transpired boundary layer. This assumption is of course always valid in practice for a small enough range of Reynolds numbers, Re_{δ_2} . For the present experiments it was found to remain valid² for the whole range of experimental Reynolds numbers.

$$(c) \quad \left(\frac{c_f}{c_{fo}} \right)_{m, Re_{\delta_2}} = f(B) .$$

This equation expresses the assumption that the ratio of the friction coefficient for the transpired boundary layer to the friction coefficient for the corresponding (same m) non-transpired boundary layer at the same Reynolds number, is a unique function of the blowing parameter, B . This assumption was verified by Simpson [2] for the case of $m = 0$. It turns out to be equally valid for $m < 0$ although the function, f , may depend parametrically upon m .

From the definition of B one has $F = Bc_f/2$, or, on account of assumptions (b) and (c):

$$F = Bf(B)aRe_{\delta_2}^{-b} . \quad (2-6)$$

An explicit expression for the dependence of the Reynolds number upon x will now be sought by writing the momentum integral Eq. (2-5) in the form,

$$\frac{v}{u_\infty} \frac{d}{dx} (u_\infty Re_{\delta_2}) = (1 + \beta + B)c_f/2 . \quad (2-7)$$

By introducing assumptions (a), (b), and (c) into this equation one may obtain:

$$\frac{d}{dx} Re_{\delta_2} + mx^{-1} Re_{\delta_2} - x^m \frac{u_1}{v} af(B)(1 + \beta + B)Re_{\delta_2}^{-b} = 0 . \quad (2-8)$$

For $(\beta + B) = \text{constant}$ the solution is:

$$Re_{\delta_2} = \left(\frac{u_1 a (1+b) (1+\beta+B) f(B)}{v (2m + mb + 1)} \right)^{\frac{1}{1+b}} x^{\frac{1+m}{1+b}} \quad (2-9)$$

Introducing this result into Eq. (2-6) one obtains the desired boundary condition for the blowing fraction:

$$F(x) \propto x^{m_F} , \quad \text{where } m_F = - (1 + m) \frac{b}{1 + b} . \quad (2-10)$$

In conclusion it is expected that the boundary conditions:

$$u_{\infty} \propto x^m \tag{2-11}$$

$$F \propto x^{m_F} ; m_F = - (1 + m) \frac{b}{1 + b}$$

will lead to boundary layers with constant β and B . These flows are then hoped to be equilibrium (constant G) boundary layers.

2.3 Nominal Boundary Conditions

Three different velocity distributions have been established experimentally in the present work. They may all be represented by:

$$u_{\infty} = u_1 \left(\frac{x - x_0}{x_1 - x_0} \right)^m , \quad \text{where } u_1 = \sqrt{\frac{2p_{d1}}{\rho}} . \tag{2-12}$$

In this equation, p_{d1} , is a reference dynamic pressure, whereas ρ is the actual air density during a given experiment (run). x_0 is the (virtual) origin of the turbulent boundary layer. The three experimental velocity distributions (nominal) are determined by the parameters given in the table below.

m	u_1 [ft/s]	x_0 [in]	x_1 [in]
0	31.1	-	-
-0.15	29.2	-3	4
-0.20	29.2	-2	4

Table 2-1 Experimental velocity distributions (nominal)

The parameters in Table 2-1 are defined by Eq. (2-12). The values of u_1 are only approximate since ρ may vary slightly from run to run. The values of x_0 obtained by upstream extrapolation of δ_2 (see Section 6.5) may vary ± 1 inch from run to run; nevertheless the values indicated in Table 2-1 were always used in Eq. (2-12).

The transpiration boundary condition is expressed as

$$F = F_1 \left(\frac{x - x_0}{x_1 - x_0} \right)^{m_F}, \quad (2-13)$$

where F_1 is a reference value obtained at $x = x_1$. The boundary conditions which have been established in the present work are summarized in Table 2-2 below.

m	F_1	m_F
0	$\left\{ \begin{array}{l} 0 \\ 0.001 \\ 0.002 \\ 0.00375 \\ 0.008 \end{array} \right\}$	$\begin{array}{l} - \\ 0 \end{array}$
-0.15	$\left\{ \begin{array}{l} 0 \\ +0.001 \\ \mp 0.002 \\ \mp 0.004 \end{array} \right\}$	$\begin{array}{l} - \\ 0 \text{ and } -0.17 \end{array}$
-0.20	$\left\{ \begin{array}{l} 0 \\ -0.002 \end{array} \right\}$	$\begin{array}{l} - \\ -0.16 \end{array}$

Table 2-2 Experimental transpiration boundary conditions (nominal)

The non-zero values of m_F satisfy the condition $m_F = -(1 + m)b/(1 + b)$ and thus correspond to constant B boundary layers.

As explained in Appendix B, the nominal boundary conditions (2-12) and (2-13) cannot be satisfied exactly. In the case of the velocity distribution Eq. (2-12) is not satisfied for $x < 10$ inches (except when $m = 0$) because of design limitations of the apparatus. The transpiration boundary condition (2-13) is only satisfied exactly at the center of each of the 24 porous plates. The continuous distribution of the blowing fraction of F expressed by Eq. (2-13) is approximated by 24 constant values of the blowing velocity, v_o .

CHAPTER 3

EXPERIMENTAL APPARATUS, INSTRUMENTATION AND PROCEDURE

The basic wind tunnel, the "Stanford Heat and Mass Transfer Apparatus" has been very adequately described by previous experimenters, see in particular Ref. [1]. The present chapter will therefore only give a very short description of the basic experimental apparatus. The heat transfer characteristics of the apparatus will not be treated at all.

The only major modification of the apparatus was a re-designing of the test section; it was carried out to permit the present work on adverse pressure gradients. The new test section has a constant cross section and features 23 adjustable slots in the top wall. The slots permit control of the pressure gradient and also prevent boundary layer separation on the top wall.

Two different hot-wire probes were designed and built: a horizontal hot-wire probe, and a rotatable probe with a single slant wire. Detailed descriptions of these instruments will be given below.

3.1 Main Air Systems

The apparatus is essentially an open-end wind tunnel. It features two independent air systems which come together in the test section: The Main Air System and the Transpiration Air System.

The flow path of the main air is as follows: (a) Inlet Air Filter: The filter is made of 0.7 micron retention felt-type filter material, (b) Main Air Blower: The centrifugal blower has a 2000 scfm capacity at 30 inches of water; it is powered by a 7.5 HP electrical motor, (c) Heat Exchanger: The heat exchanger is water cooled and it is effective enough that the air leaves it essentially at the temperature of the

cooling water. The cooling water is taken from the building water supply. However, in order to remove unacceptable fluctuations in the temperature of the water which occur at certain hours of the day the water passes through two large tanks in series before entering the heat exchanger. Just upstream and downstream of the heat exchanger the air passes through 1-1/2 inch thick honeycomb with 3/16 inch cell size. (d) In the constant 23 x 23 inch cross section after the heat exchanger the air passes through six 32 x 32 mesh stainless steel screens. (e) The nozzle, which is 36 inches long, provides an almost two-dimensional contraction to a 6 x 20 inch cross section. The nozzle is symmetric with a sine function as basic shape. However, it was found that a small separation occurred in the upstream end of the nozzle. This disturbance was effectively removed by modifying the basic shape of the nozzle to incorporate an initial contracting angle of 5° just downstream of the last screen. Very close to the exit the nozzle features a 3/16 inch wide slot in the bottom wall and the side walls. Because the tunnel is operated with a static pressure slightly above ambient this slot effectively removes the bottom and side wall boundary layers. This boundary layer suction slot was initially incorporated in an effort to eliminate a non-uniformity in the lateral distribution of the boundary layer thickness. It was later found, however, that the non-uniformity was due to a small crease in the last screen and was unrelated to the nozzle boundary layers. The boundary layer suction was never-the-less retained for reasons related to the heat transfer research which was carried out in parallel with the present hydrodynamic investigation. (f) A 6 inch long transition section between the nozzle and the test section contains a 1/32 inch high, 1/4 inch wide boundary layer trip on the bottom wall, 6 inches upstream of the test section. There are no trips on the side walls or on the top wall.

3.2 Test Section

The test section is an 8 ft. long straight duct with a rectangular cross section (20 inches wide and 6 inches high). The test plate (the floor of the test section) is composed of 24 porous plates each 18 inches wide and 4 inches in the direction of the main flow. Each porous plate is connected to the transpiration air system which permits control and measurement of the flow rate. The porous plates are 0.25 inches thick and made of sintered bronze material composed of particles with diameters between 0.0023 and 0.0007 inches. The porosity is approximately 40% and the flow rate uniformity is within $\pm 6\%$ in the center 6 inch span. The flow resistance offered by the plates is large enough that the uniformity of the transpiration velocity is not significantly affected by the pressure gradients in the main flow.

The side walls of the test section are made of 1/2 inch plexiglass. One of the side walls has 0.040 inch diameter square edged static pressure tap holes drilled with a 2 inch pitch 1 inch above the test plate. These static pressure taps were used in connection with a Kiel probe in the free-stream, for the measurement of the free-stream dynamic pressure distribution. Every 12 inches in the flow direction four additional pressure taps are provided 2, 3, 4 and 5 inches above the test plate in both side walls. These pressure taps were used for comparing the static pressures at the two side walls and for check of the vertical pressure gradient in the boundary layer. It was found that the difference in static pressures between the two sides of the tunnel was always smaller than 0.002 inches H_2O . No significant pressure differences between static pressures at various heights above the test plate could be detected at any streamwise position for any of the flows.

The upper wall of the test section consists of 24, 5/16 inch thick, 3.5 inches wide plates (material: tooling

aluminum). Each of the 23, 0.5 inches wide spaces between the plate is partially covered with a movable 1.25 x 0.25 inch aluminum bar fastened on top of the upstream plate and a 0.75 x 0.25 bar fixed on top of the downstream plate. See Fig. 3-1 for a longitudinal cross section of the test section. Figure 3-2 is a photograph of the test section; it shows in particular the arrangement of the top plates. The arrangement just described provides 23 slots extending across the tunnel with widths adjustable to between 0 and 0.4 inches. The slot widths can be set to an accuracy of 0.001 inches by means of a simple feeler gauge. Since the tunnel is operated with a static pressure in the test section slightly above ambient (0.4 - 1.1 inches H₂O), the adjustable slots provide a means of controlling the velocity distribution (i.e. pressure gradient) at the test plate. (See Appendix B for details)

The length of the slots (in the lateral direction of the tunnel) may be restricted by movable "fingers". These permit the length of the slots to be equal to or less than the width of the tunnel (20 inches). This feature was incorporated because Clauser [9] reported a lateral divergence in the bottom wall boundary layer of a wind tunnel where an adverse pressure gradient was generated by removal of air through slots in the top wall. Clauser found that this undesired three-dimensionality could be eliminated by restricting the length of the suction slots.

Tests were carried out in the present tunnel both with the fingers flush with the sidewalls and restricting the slot lengths up to 0.5 inches on each side. No significant effect on the rate of growth, $d\delta_2/dx$, of the test plate boundary layer was found. The effect reported by Clauser could therefore not be detected. This is possibly because the present tunnel has a greater width to height ratio (20/6) than Clauser's tunnel (3/4). For all the runs reported the fingers were set to restrict the length of the slots by approximately

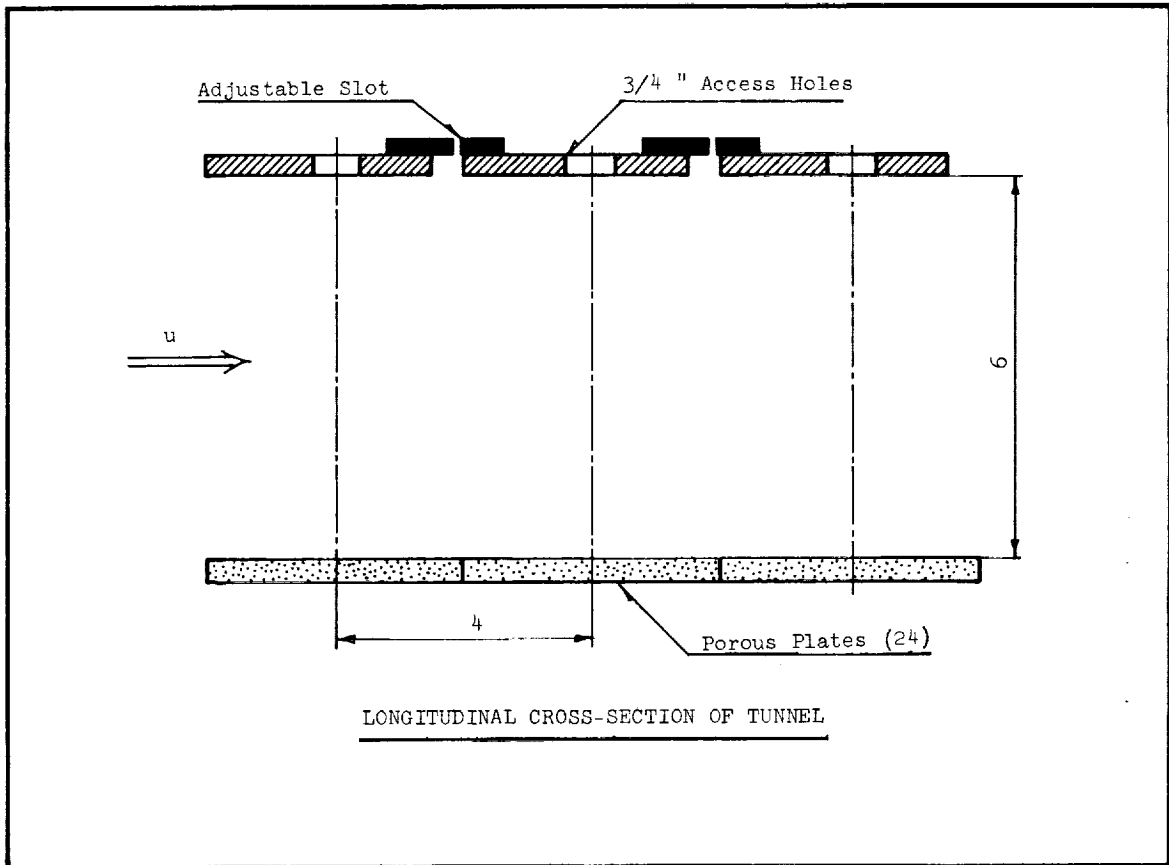


Fig. 3-1 Longitudinal cross section of the tunnel test section

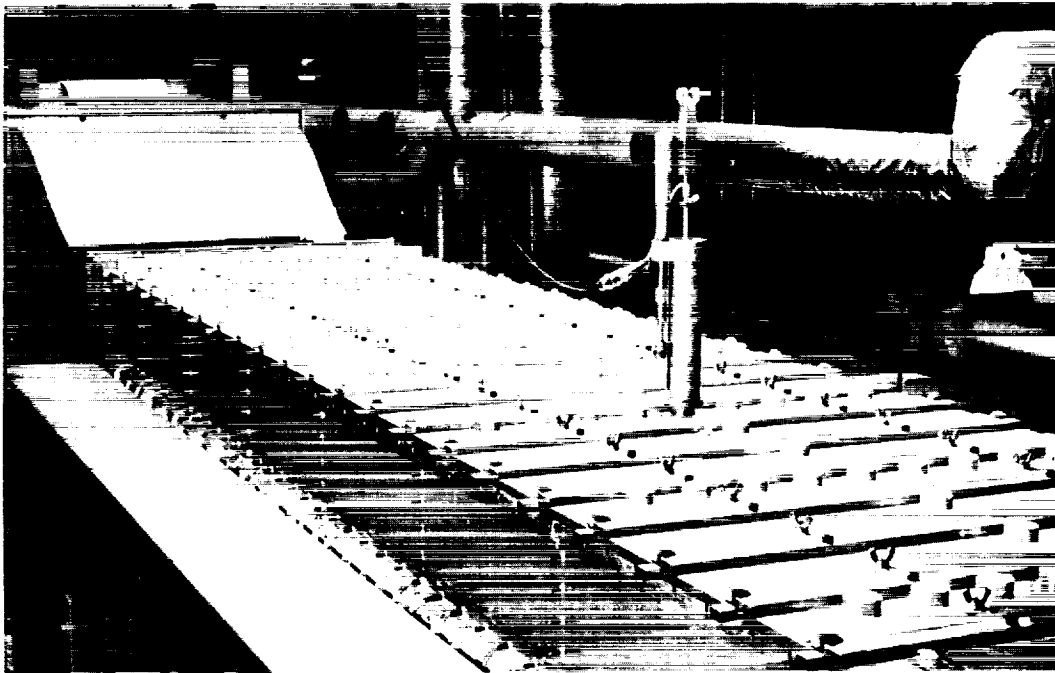


Fig. 3-2 Photograph of test section with traversing mechanism in position

the displacement thickness of the side wall boundary layers in zero pressure gradient.

Each of the 24 plates that form the top wall has a 3/4 inch access hole at the centerline of the test section. Every third plate has 8 additional 3/4 inch access holes at 2 inch intervals in the transverse direction. When not in use the access holes are closed with plugs which are flush with the inside of the top plates.

The test section is at the downstream provided with a 14 inch long extension with constant cross section. The extension is terminated with vertically movable gate. This gate valve permits adjustment of the pressure in the test section. The main function of the extension is to assure that the disturbing effect of the exit gate valve is sufficiently far removed from the test section.

3.3 Transpiration Air System

The flow rate of transpiration air is controlled and metered individually for each of the 24 porous plates. There are two rotameters for each plate providing a metering capability from 0.5 to 18 scfm. The transpiration air is supplied by a transpiration air blower. In the blowing mode the transpiration air is filtered in a 0.7 micron retention felt-type filter.

3.4 Procedure for Setting-up a New Run

The setting-up of a new run to a specified free-stream velocity and transpiration boundary condition is an iterative procedure: For a desired velocity distribution, the computer program, SLOT (see Appendix B) supplies the desired dynamic pressure at $x = 2$ inches. The total and static pressure at this position (pressure tap #1) are then held constant during the course of the iterations. (This can be done by means of the control provided by the main flow valve and

the exit gate valve). The rotameter readings (in case transpiration is used) and the slot widths are reset at each iterative cycle. The computer program mentioned above is designed to aid in the iterative procedure. On the basis of the measured distribution of dynamic pressures, the total pressure and the rotameter settings it computes a correction to the slot widths and the rotameter settings which should result in attainment of the desired boundary conditions. In very few cases have more than two resettings been necessary. As a practical matter the iterations were discontinued when the SLOT predicted changes in slot widths of 0.001 inches or less. This corresponds in practice to an error in the velocity gradient of less than $\approx 3\%$.

3.5 Pressure Measurements

All pressures were measured with a STATHAM strain gauge transducer, type PM97 with a maximum reading of 1.4 inches H_2O . The Wheatstone bridge for the transducers was powered by stable power supply that assured negligible drift. The transducer was calibrated at regular intervals against a MERIAM micro manometer model 34FB2; the calibration curve was found to be linear and stable to ± 0.001 inches H_2O . The electrical signal was read by a VIDAR 5206 D-DAS Data Acquisition System employing a DIGITAL PDP 8/L computer. The average of 50 measurements taken during 6 seconds was used.

3.6 Velocity Measurements

The free-stream velocity distribution was computed from the dynamic pressure distribution using Bernoulli's equation. However, all velocity profiles and turbulence profiles were obtained by linearized constant temperature hot-wire anemometry. The reason that pitot tubes (which are more convenient to use) were discarded is that serious discrepancies were found in turbulent shear flow between tubes with rounded

and flattened mouths. As an example Fig. 3-3 shows experimental mean velocity profiles obtained by a round mouth (0.020 inches O.D.) and a flattened mouth pitot tube (external height = 0.015, width = 0.032 inches) in an adverse pressure gradient, non-transpired boundary layer. The Young and Maas [11] shear correction was applied for both pitot probes. The correction amounts to a displacement away from the wall (for all the profile points) of $\Delta y = 0.15D + 0.08d$, where D is outer diameter and d the inner diameter of the mouth of the pitot tube. For the flattened probe D and d are taken to be external and internal probe heights respectively. It is obvious from Fig. 3-3 that the two pitot probes disagree greatly in the inner regions of the boundary layer. The disagreement would have been even greater without the shear correction; however, no correction amounting to a simple constant displacement, Δy , of the effective probe center would be able to bring the results from the two probes into agreement. The effect displayed on Fig. 3-3 was found very consistently both for the zero and adverse pressure gradient boundary layers for which the probes were compared. Also shown in the figure is the same velocity profile as measured with a hot-wire.

3.6.1 Hot-Wire Instrumentation

The hot-wire instrumentation consisted of a DISA 55D05 Constant Temperature Anemometer in connection with a DISA 55D15 Linearizer. For mean velocity measurements the linearizer output was read by the VIDAR Data Acquisition System effectively using a 6 second average. The mean square of the linearizer output was obtained from a THERMO-SYSTEMS RMS Voltmeter Model 1060 with the time constant set at 10 sec. (It was found that a 3 second time constant gave slightly low readings for the very thick boundary layers). The mean square output from the RMS meter was integrated

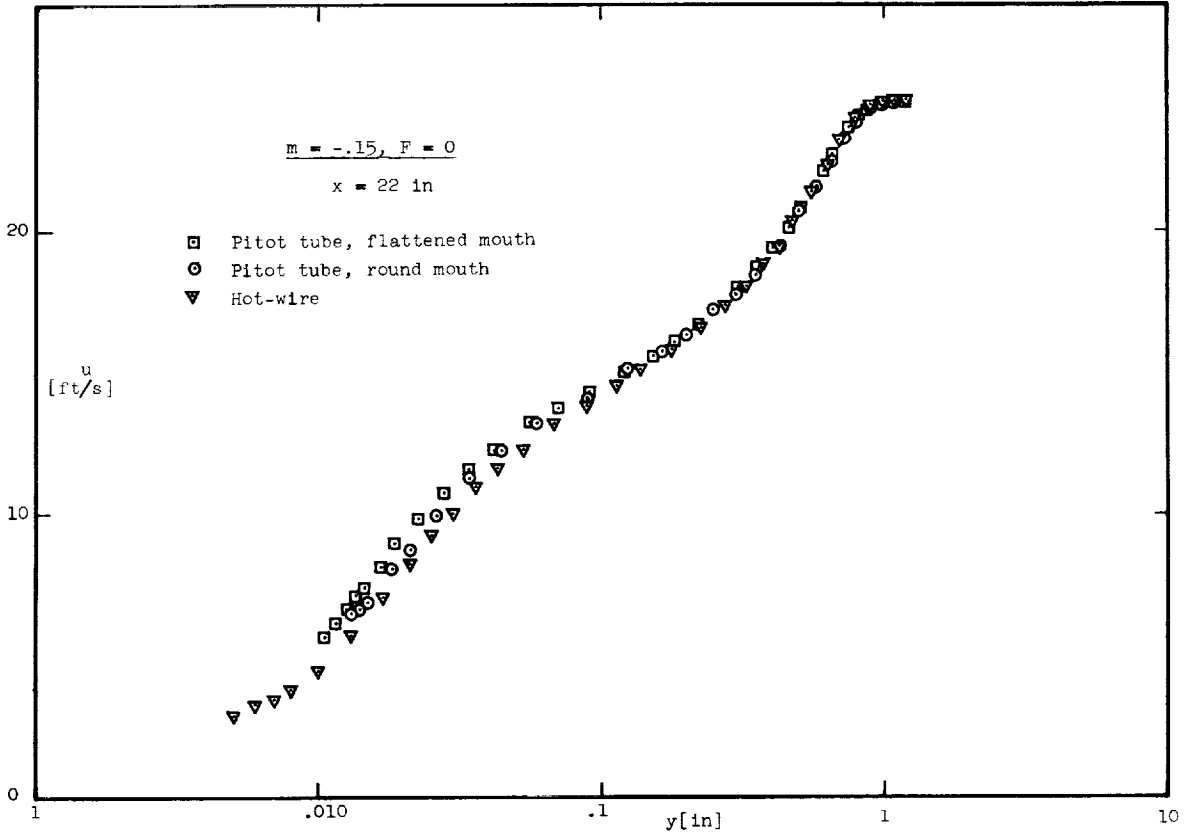


Fig. 3-3 Comparison of probes. Velocity profile in an adverse pressure gradient

over 200 secs. by a Hewlett-Packard Integrating Digital Voltmeter, Model 2401C, in connection with an external quartz crystal oscillator. The very long integration time was necessary to reduce the random scatter of the mean square values to below 1%.

Two different hot-wire probes were used:

(a) A horizontal hot-wire was used for the measurement of mean velocities and of $\overline{u'^2}$. The probe features a 0.0002 inches diameter, 0.080 inches long platinum wire soft soldered to the prongs of a DISA 55F01 probe element. The cold resistance of the wire is about 8Ω ; the operating resistance was 13Ω , corresponding to an overheat ratio of ≈ 1.6 . The hot-wire probe is shown in Fig. 3-4.

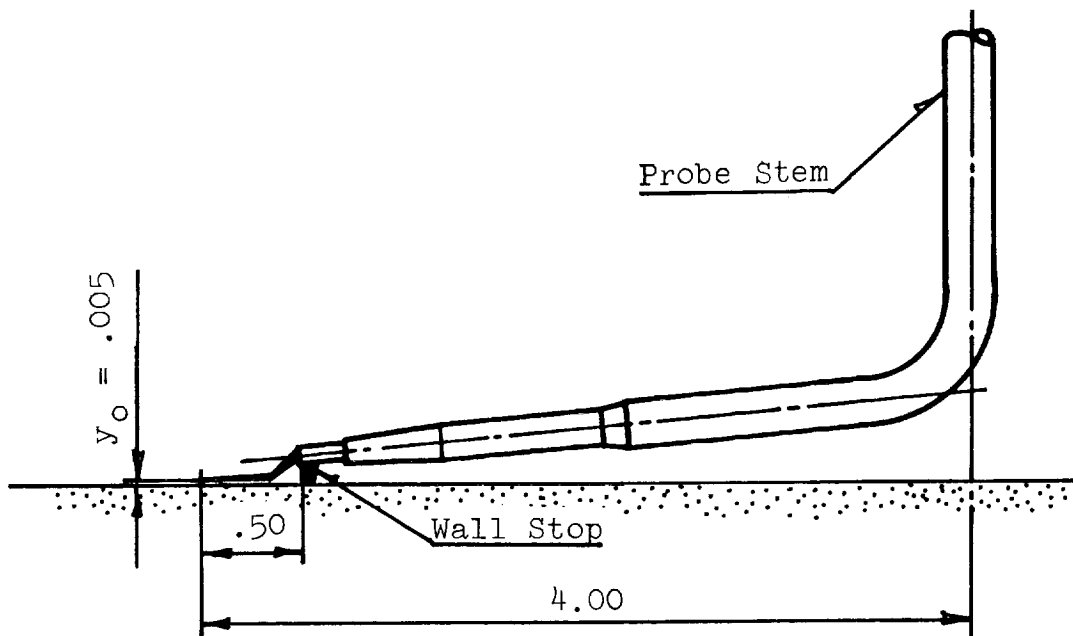


Fig. 3-4 Horizontal Hot-Wire Probe

Because of the flexibility of the probe stem the "wall stop" effectively prevents the wire from accidentally being damaged by the wall. The wire distance from the wall when the wall stop just touches is nominally 0.005 inches (as

measured by an optical comparator). In practice the probe stem may deviate up to $\approx 0.1\%$ from verticality with a corresponding influence on the wire distance from the wall of ≈ 0.001 inches. It appears, however, that for a given x-position (i.e. a given access hole) the wall distance of the wire is reproducible to a greater accuracy; this conclusion is based on repeated evaluations of the wall shear stress using the first data point for the computation of the wall gradient, $\left(\frac{du}{dy}\right)_{y=0}$.

Individual wall distances for the nine x-positions used in the present tests have been computed by the sublayer method using the accepted zero pressure gradient friction coefficient correlation. The wall distances used for the data reduction are: $y_o(2) = 0.0043$, $y_o(34) = 0.0056$ and $y_o(90) = 0.0068$ inches; for all other positions, $y_o = 0.0050$ inches. These numbers may give the illusion of greater accuracy than is actually obtained; ± 0.001 inches is a reasonable estimate of the uncertainty of the wire distance from the wall.

(b) A rotatable 45° slant hot-wire was used for the measurement of the Reynolds stress, $-\overline{u'v'}$ and (in connection with the horizontal wire) of $\overline{v'^2}$ and $\overline{w'^2}$. The rotatable probe features a DISA 55F02 hot-wire element. The wire has a total length of 3 mm with a 1.25 mm active center portion. The ends of the wire are gold plated to reduce prong interference at the central sensing part of the wire. The wire is made of tungsten and has a diameter of $5 \mu\text{m}$. The cold resistance is $\approx 4.8\Omega$ and it was operated at 7.5Ω giving an overheat ratio of ≈ 1.6 .

The choice of a single, rotatable, slant wire over x-wires was made for three reasons: (1) Any uncertainty about possible interaction between two wires and 4 prongs is eliminated. The directional sensitivity of the single hot-

wire of the type used is well documented, see for example [12]. (2) The need for two anemometers and two linearizers together with a critical matching of the two hot-wire calibrations is avoided. (3) There is only one wire to break! The rotatable hot-wire probe is shown in Fig. 3-5. A cable drive permits the probe to be rotated while in position in

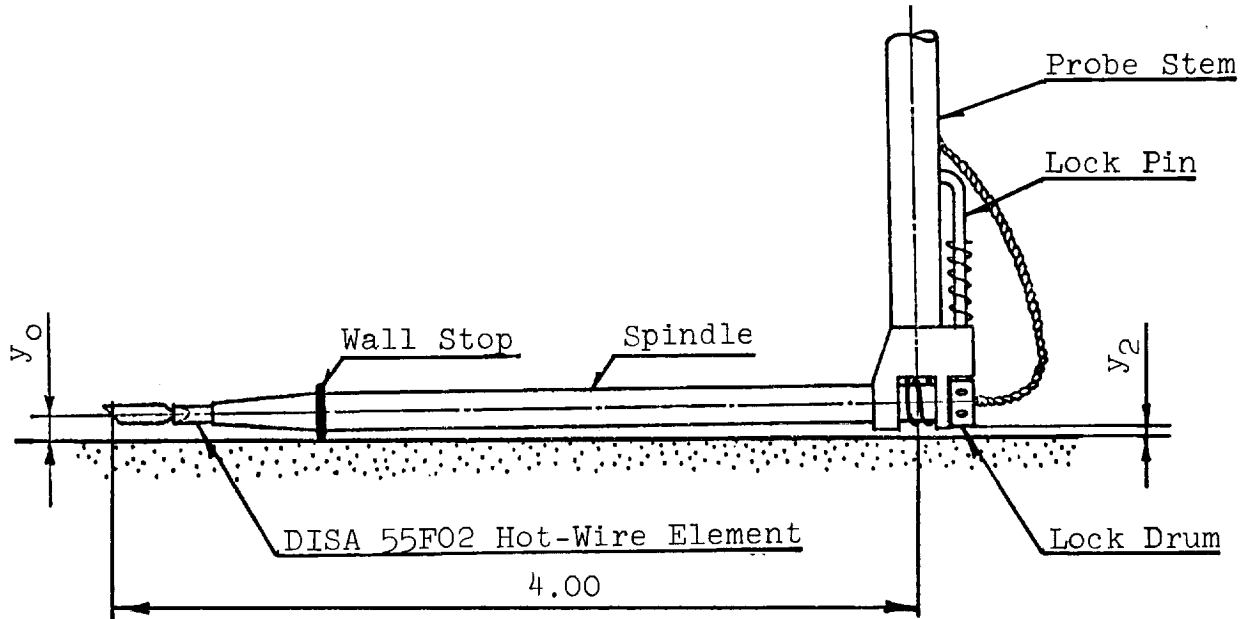


Fig. 3-5 Rotatable Hot-Wire Probe

the tunnel. The probe spindle incorporates a "lock-drum" which features six radially drilled holes spaced at 60° . The spring loaded "lock pin" which fits into the holes in the lock drum may be lifted by means of a lever located on top of the traversing mechanism. The arrangement permits turning of the probe to any of the six angular positions, $\phi_n = (n - 1)\frac{\pi}{6}$; $n = 1, 2 \dots 6$, while operating in the tunnel.

The "wall stop" is an interchangeable wire of known diameter, D , wrapped around the spindle. The distance, y_2 , (see Fig. 3-5) may be measured by the micrometer drive

incorporated in the traversing mechanism. The knowledge of D and y_2 permits calculation of the position of the center of the hot-wire, y_0 , when the wall stop just touches the wall.

Ideally the hot-wire spindle should be aligned with the "mean flow vector" (see Appendix A on hot-wire anemometry). This alignment has been accomplished to within $\pm 0.25^\circ$ by bending the probe stem according to transpiration rate and pressure gradient. The direction of the mean flow vector was inferred from the mean velocity profiles. Figure 3-6 is a photograph of the rotatable probe in operating position in the test section.

3.7 Traversing Mechanisms

Figure 3-7 is a photograph of the traversing mechanism for the rotatable probe. The traversing mechanism for the horizontal probe is identical except that it does not have the cable drive and the spindle lock lever.

The traversing mechanisms fit into the access holes in the top plates and are locked in place. The accuracy of the lateral probe alignment is $\approx 0.5^\circ$.

The probe is traversed manually by starting from the position where the probe wall stop just touches the wall. The smallest division on the micrometers is 0.001 inches.

3.8 Calibration of Hot-Wires

The hot-wires were calibrated in the test section outside of the boundary layer. The dynamic pressure at the position of the wire was measured as the difference between the total pressure measured by a 1/4 inch pitot tube and the static pressure at a wall tap. The minimum calibration velocity was ≈ 2.4 ft/s. The corresponding Reynolds number based on the pitot tube O.D. is ≈ 340 ; according to

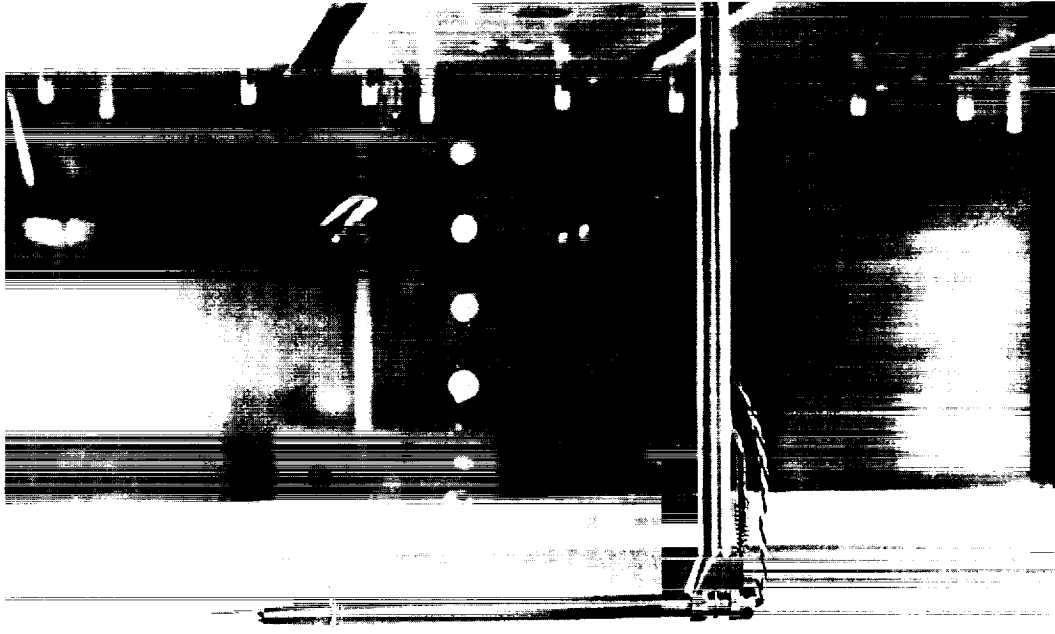


Fig. 3-6 Photograph of rotatable hot-wire probe in operating condition

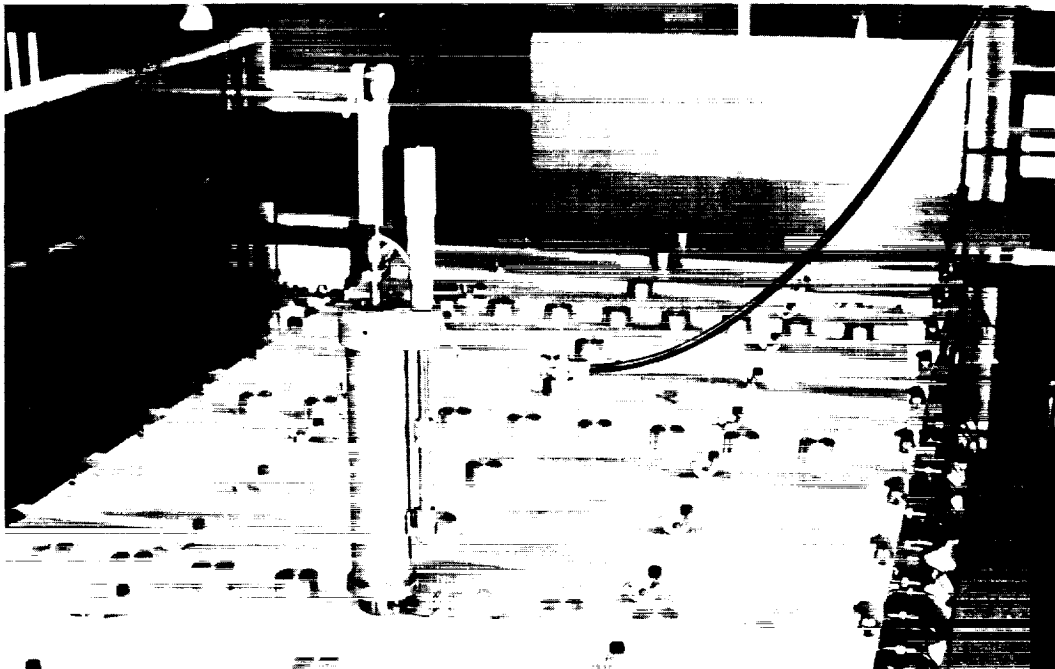


Fig. 3-7 Photograph of rotatable hot-wire traversing mechanism in operating position

McMillan [13], no correction is necessary at this Reynolds number. The maximum temperature variation during a calibration was $\pm 0.25^{\circ}\text{F}$.

The calibration curves were obtained by least square fitting measured values of velocity, U , and linearizer output, E . For the horizontal wire a 3rd order polynomial was used.

For the slant wire a straight line was used i.e.

$$U = c_1 + c_2 E \quad . \quad (3-1)$$

The calibration would be repeated with a slightly different value of V'_0 (see the DISA manual for the 55D15 linearizer) until the intercept c_1 in Eq. 3-1 assumed a value below 0.05 ft/s. The reason that special care was taken in obtaining a "straight line through zero" as a calibration curve for the slant wire is that proportionality between U and E is assumed in the data reduction for measurements with this wire (see Section 6.3).

The RMS deviation of the experimental velocities from the calibration curves was always less than 0.02 ft/s. A typical calibration curve together with experimental points is shown in Fig. 3-8.

The calibration of both wires was repeated several times during the course of the experiments. No significant drift was found. All the slant wire results were obtained using the same wire. Two different horizontal wires were used.

3.9 Qualifications of the Apparatus

Surveys in the potential core in the test section have shown that the lateral variation of the free-stream velocity was less than 0.5% at all streamwise locations for all three pressure gradients. The experimental free-stream velocities never deviated more than 0.5% from the desired "practical"

velocity distribution (see Appendix B for details). For the two adverse pressure gradients the nominal velocity distribution (Eq. 2-12) and the desired "practical" distribution are very nearly identical for $x > 10$ inches. The temperature drift in the tunnel was less than 1°F during any run.

The zero pressure gradient boundary layer provides a good test case for the apparatus and the hot-wire equipment. Figure 3-9 shows the friction coefficients as measured by the "shear stress" method, a method that requires measurement of the Reynolds stress $-\overline{u'v'}$ (see Section 4.1.2); also shown is the "best fit", $c_f/2 = 0.120 \text{ Re}_{\delta_2}^{-0.25}$, of the measured friction coefficients. The friction coefficients obtained by the two-dimensional momentum integral equation (Eq. 4-5 with $3D = 0$) can be seen to lie slightly below the "best fit"; the difference is probably due to a slight lateral divergence of the stream lines in the boundary layer. Discrepancies of this order of magnitude (i.e. $\Delta c_f \approx 0.0001$) were found for most of the experimental flows, the two-dimensional momentum integral equation usually giving the lowest friction coefficients. In Fig. 3-9 the skin friction coefficient recommended by Coles [16] is displayed for comparison. The measured skin friction coefficients are slightly lower than the values of Coles.

The uniformity of the boundary layer in the lateral direction was checked by measuring mean velocity profiles at the nine transverse positions, $z = -8, -6, \dots, 8$ inches both for zero and adverse pressure gradients. Figure 3-10 shows as an example five mean velocity profiles measured at $x = 82$ inches in an adverse pressure gradient ($m = -0.15$). The profiles for $z \leq 4$ inches appear to be identical; for $z \geq 6$ inches the effect of the side wall boundary layer becomes noticeable. The same conclusion may be drawn from Fig. 3-11 in which the momentum thickness, δ_2 , is plotted versus the transverse coordinate, z . It may be seen that

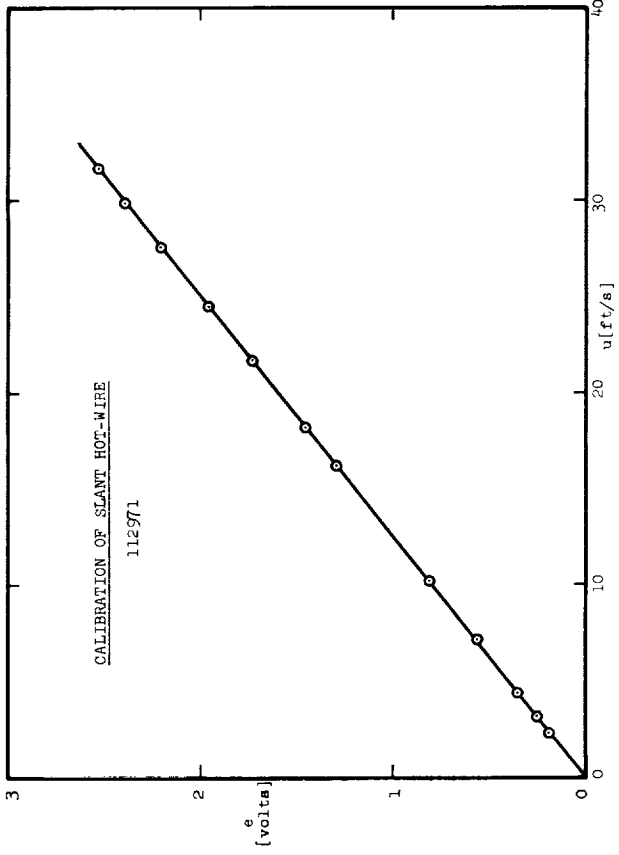
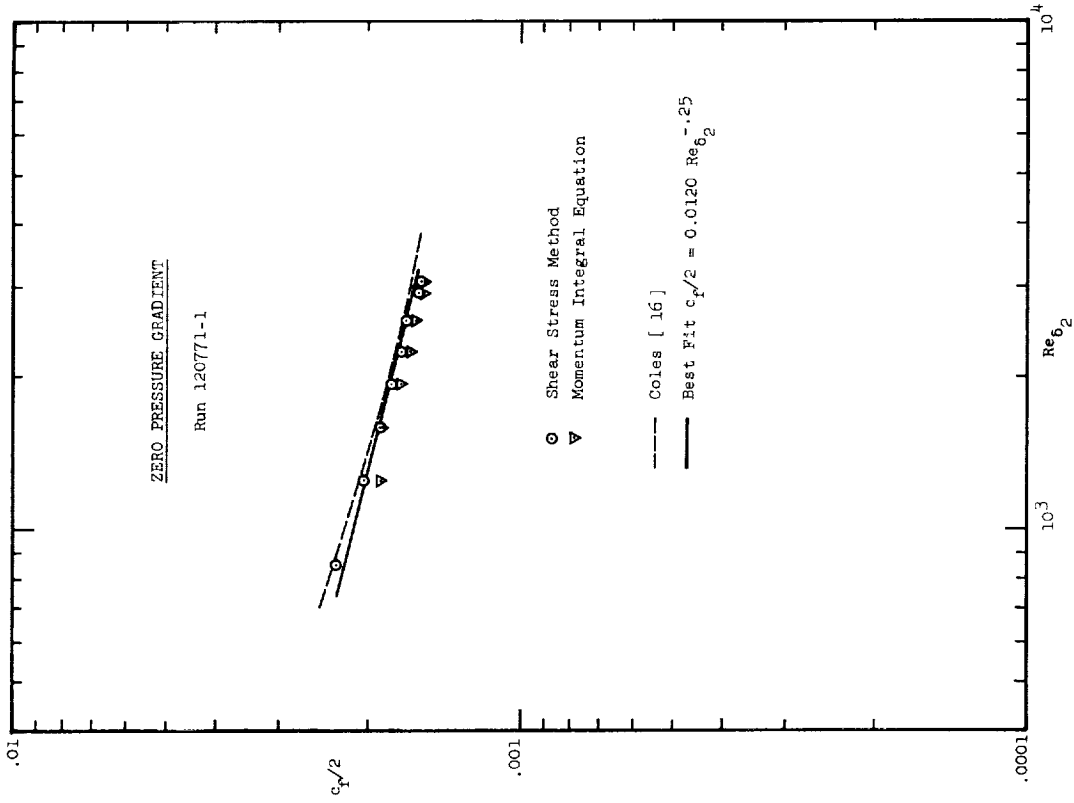


Fig. 3-8 Typical hot-wire calibration: linearizer output versus air velocity

Fig. 3-9 Friction coefficients for constant pressure and no transpiration

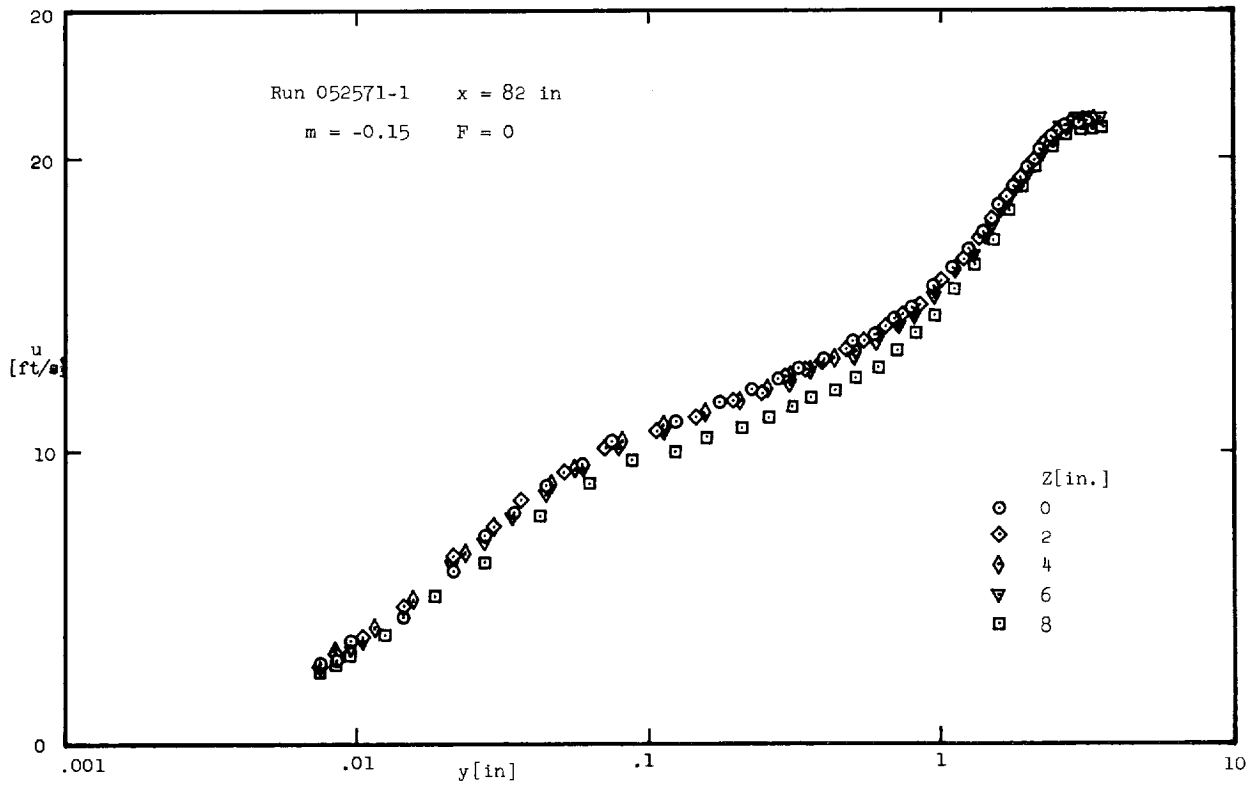


Fig. 3-10 Comparison of measured velocity profiles at five different transverse locations but at the same streamwise position

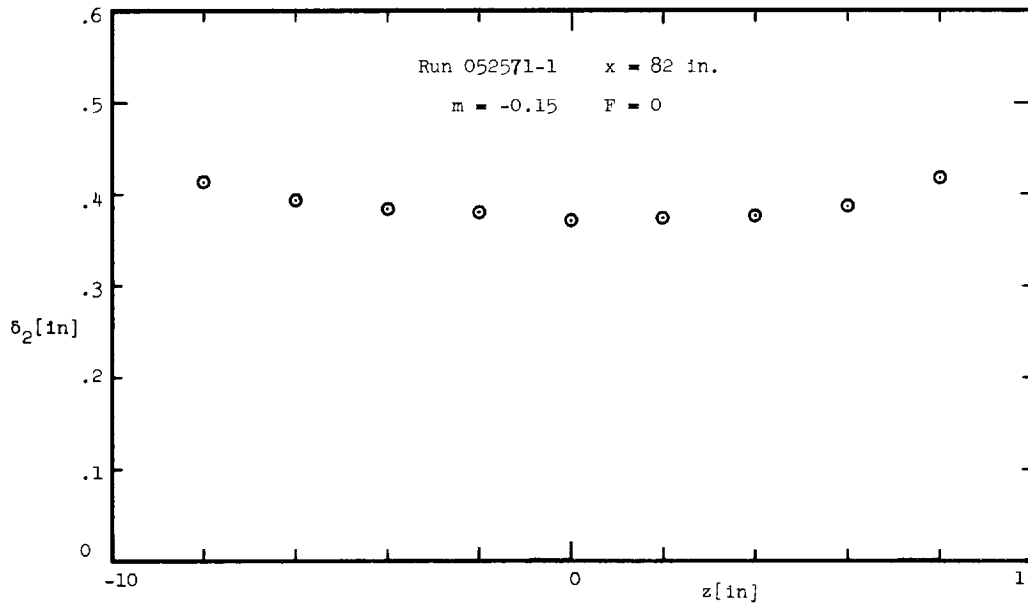


Fig. 3-11 Lateral variation of the momentum thickness

δ_2 varies less than 3% over the central 8 inches of the span. Further upstream and for zero pressure gradient flows the width of the uniform central span is even greater. This degree of uniformity was only achieved after a rather extensive "debugging" of the components upstream of the test section. The main reason for the initial non-uniformity was a small crease in the last screen. It was found that the quality of the screens is of the greatest importance (this has also been reported by Bradshaw [15] who did a careful study of wind tunnel screens). The crease responsible for the non-uniformity was barely noticeable!

The mean velocity profiles fit the law-of-the-wall, $u^+ = \frac{1}{0.41} \ln y^+ + 5.0$, with constants from Coles [14] (see for example Fig. 7-12). The above law-of-the-wall is applicable for boundary layers on smooth surfaces; the fact that it fits the present velocity profiles is a sensitive test of the aerodynamic smoothness of the porous test plate (at least for zero pressure gradient).

The "strength of the wake" (Coles [16]) i.e. the maximum deviation of u^+ from the law-of-the-wall, Eq. 3-2, in the outer region is shown in Fig. 3-12 as a function of the Reynolds number, Re_{δ_2} . Also shown in the figure is Coles "normal" strength of the wake. The profiles appear to be close to normal in the sense of Coles.

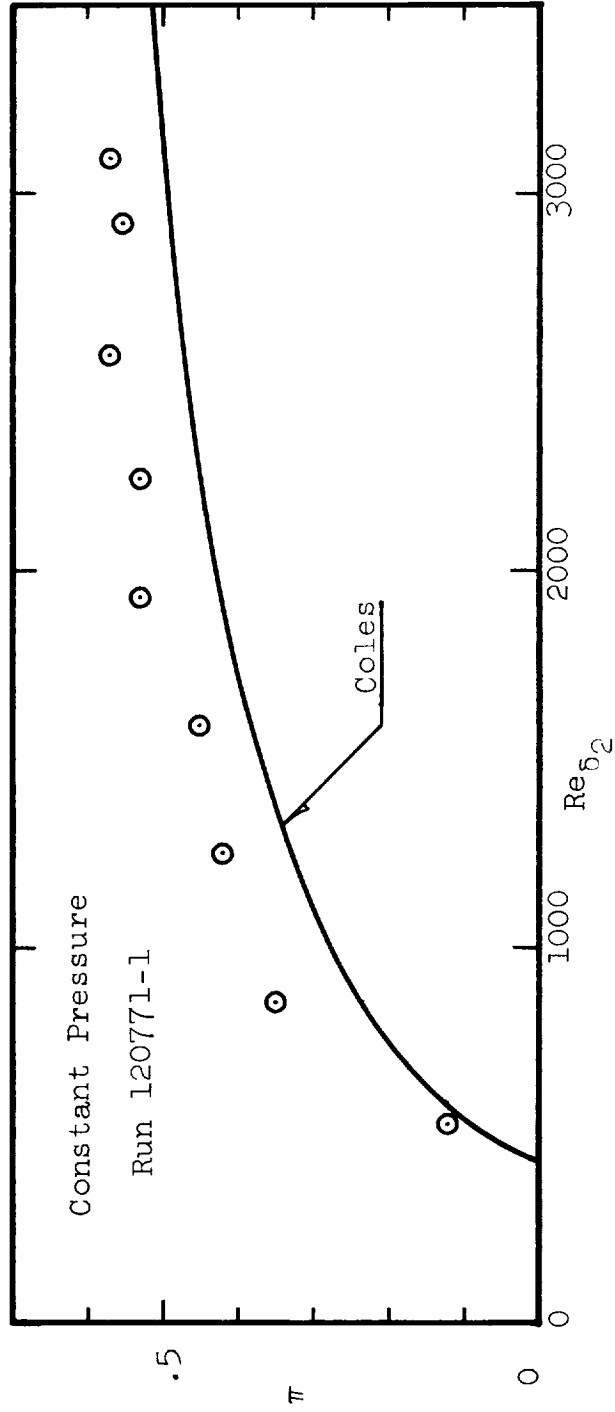


Fig. 3-12 Measured strength of the wake compared to Coles [16] "normal" strength ($\kappa = 0.41$)

CHAPTER 4

MEASUREMENT OF WALL SHEAR STRESS

For a given Reynolds number, Re_{δ_2} , boundary layers in adverse pressure gradients have lower friction coefficients than constant pressure or favorable pressure gradient boundary layers. Blowing similarly lowers the friction coefficient. In the present work very low values of friction coefficients must therefore be measured.

The method used to measure the wall shear stress must be fundamental because the flow regimes to be explored are unknown a priori. Methods which depend upon similarity in the inner region of the boundary layer cannot be used for the flows investigated in this work.

A direct measurement of the wall shear force is, in practice, impossible to carry out for flows on a porous wall. (It is a very difficult measurement even on an impermeable wall with no pressure gradient). The wall shear stress must therefore be inferred from measurements carried out in the flow and by invoking fundamental principles.

4.1 The Shear Stress Equation

For the incompressible boundary layer the time averaged x-momentum and continuity equations may be written:

$$\frac{\partial u^2}{\partial x} + \frac{\partial (uv)}{\partial y} + \frac{\partial (uw)}{\partial z} = u_{\infty} \frac{du_{\infty}}{dx} + \frac{1}{\rho} \frac{\partial \tau}{\partial y}, \quad (4-1)$$
$$\frac{\partial u}{\partial x} + \frac{\partial v}{\partial y} + \frac{\partial w}{\partial z} = 0.$$

Note that the shear stress, τ , is understood to be equal to the sum of a viscous contribution, $\mu \frac{\partial u}{\partial y}$, and a Reynolds stress, $-\overline{\rho u'v'}$, thus:

$$\tau(y) = \mu \frac{\partial u}{\partial y} - \rho \overline{u'v'} \quad (4-2)$$

The normal Reynolds stress term, $-\frac{\partial}{\partial x}(\overline{u'^2})$, which belongs on the right hand side of Eq. (4-1) has been neglected.

Integrating Eqs. (4-1) from $y = 0$ to $y = y$ leads to an equation for the shear stress, τ :

$$c_f/2 = \frac{\tau(y)}{\rho u_\infty^2} + \frac{y}{u_\infty} \frac{du_\infty}{dx} - F + \frac{1}{u_\infty^2} \left(u \int_0^y \frac{\partial u}{\partial x} dy - 2 \int_0^y u \frac{\partial u}{\partial x} dy \right) + 3D(y) \quad (4-3)$$

where

$$3D(y) = \frac{1}{u_\infty^2} \left(\int_0^y u \frac{\partial w}{\partial z} dy - u \int_0^y \frac{\partial w}{\partial z} dy \right) \quad (\text{for } w = 0) \quad (4-4)$$

In this equation $c_f/2 = \tau/\rho u_\infty^2$ is the friction coefficient. The term, $3D(y)$, is non-zero if the boundary layer flow deviates from the ideal of two-dimensionality. It can reasonably be assumed that $3D(y)$ is an increasing function of y and that it is very small compared to the two integrals involving only u .

4.1.1 The Momentum Integral Equation

If y in the shear stress equation (4-3) is taken to be equal to the boundary layer thickness then $\tau = 0$, and the equation may be written

$$c_f/2 = \frac{d\delta_2}{dx} + \delta_2(2 + H) \frac{1}{u_\infty} \frac{du_\infty}{dx} - F + 3D(\delta) \quad (4-5)$$

This is the von Kármán momentum integral equation with a correction, $3D(\delta)$, for a deviation from the ideal of two-dimensionality.

There are two reasons why it is difficult to obtain reliable results from Eq. (4-5) for small values of the friction coefficient:

- (a) In adverse pressure gradients, for boundary layers with blowing, du_{∞}/dx and/or F are negative and $c_f/2$ must be computed as the small difference between large numbers.
- (b) The computation of $3D(\delta)$ from Eq. (4-4) would require the knowledge of $\partial w(y)/\partial z$, but the direct measurement of this quantity was found to be impractical. The term, $3D(\delta)$ in Eq. (4-3) is a priori unknown.

Because of the above reasons the momentum integral Eq. (4-5) was not in any case relied upon for the determination of the friction coefficient correlations (Section 6.1).

However, friction coefficients were computed from Eq. (4-5) with $3D(\delta)$ set equal to zero for all profiles for $34 \text{ inches} \leq x \leq 82 \text{ inches}$ and compared to the adopted correlations. It was found that the discrepancy was usually of the order of magnitude $\Delta c_f/2 = 0.0001$. The momentum equation results were in most cases the lowest, but not always. Therefore in most cases it may be assumed that $3D(\delta) > 0$ indicating positive average values of $\frac{\partial w}{\partial z}$ i.e. a slight divergence of the streamlines.

4.1.2 The Shear Stress Method

The friction coefficient, $c_f/2$, can be determined from Eq. (4-3) using a measured shear stress $\tau(y)$ evaluated according to Eq. (4-2). The viscous contribution was obtained by differentiation of the mean velocity profile (see Section 5.2 for details). The Reynolds stress was measured using a slant hot-wire (see Section 5.3).

The shear stress $\tau(y)$ was measured in the fully turbulent region of the boundary layer, but as close to the wall as the Reynolds stress measuring hot-wire probe would permit. By performing the measurement of $\tau(y)$ at a small y the accuracy of the terms on the right hand side of Eq. (4-3) becomes of lesser importance. In particular the two integrals containing $\partial u/\partial x$ become very small (in some cases negligible). The same holds to an even greater extent for the 3D-term which can be considered truly vanishing for small y . Figures 6-35 through 6-46 show examples of the relative magnitudes of the various terms in Eq. (4-3). The Reynolds stress measured closest to the wall (at $y \approx .1$ inches) has been used for the determination of the friction coefficient.

All measured wall shear stresses in the present work (with the only exception being those for Runs 112871-1, 102171-1 and 092271-5) were determined by the method described in this section. The reason that a different method had to be used for the above mentioned three runs is a difficulty in measuring the Reynolds stress accurately enough for runs with very low friction coefficients (see Appendix A, Section 5).

CHAPTER 5

DATA REDUCTION

5.1 Mean Velocity Profiles and $\overline{u'^2}$

The distance from the wall, y , was obtained directly from the micrometer readings, the wall having been "found" as explained in Section 3.6.1.

The mean velocity, u , was computed as

$$u = c_1 + c_2 e + c_3 e^2, \quad (5-1)$$

where e is the time averaged output from the linearizer and the coefficients are known from the hot-wire calibration (see Section 3.8 for details).

The turbulence intensity $\overline{u'^2}/u_\infty^2$ was computed by

$$\frac{\overline{u'^2}}{u_\infty^2} = \frac{c_2 + 2c_3 \overline{e'^2}}{c_1 + c_2 e_\infty^2 + c_3 e_\infty^3}. \quad (5-2)$$

5.2 Viscous Shear Stress

The normalized viscous shear stress is

$$\frac{\tau_v}{\rho u_\infty^2} = \frac{\nu}{u_\infty^2} \frac{du}{dy}. \quad (5-3)$$

The derivative, $\frac{du}{dy}$; was evaluated by least-square fitting seven profile points by a polynomial in $\ln y$,

$$u = a_1 + a_2 \ln y + a_3 (\ln y)^2,$$

and then computing $\frac{du}{dy}$ at the center point. For the first and last three profile points the fit of the seven first and last points respectively were used.

5.3 $-\overline{u'v'}$, $\overline{v'^2}$ and $\overline{w'^2}$

The calibration curve for the rotatable hot-wire probe is (see Section 3.8):

$$U = c_2 E \quad (5-5)$$

The indicated velocity, U_i , defined by Eq. (A-1), is related to U according to Eq. (A-5). In terms of the indicated velocity the calibration curve thus becomes, $U_i = A c_2 E$, where $A = 0.502$ for a hot-wire with $\phi = 45^\circ$ and $k_1 = 0.2$. The mean square of the fluctuating part of the indicated velocity, $\overline{u_i'^2}$, is therefore related to the mean square of the linearizer output, $\overline{e'^2}$, as

$$\overline{u_i'^2} = A c_2 \overline{e'^2} \quad (5-6)$$

The normalized Reynolds stress, $-\overline{u'v'}/u_\infty^2$ was evaluated from either one of Eqs. (A-10) or (A-12). In Eq. (A-10) the Reynolds stress is computed from measurements performed at two angular positions of the hot-wire ($\theta_1 = 0$ and $\theta_2 = \pi$). All the friction coefficients obtained from the "shear stress method" (see Section 4.12) are obtained from Reynolds stresses computed from this equation.

The Reynolds stress profiles (one for each run, taken at $x = 70$ inches) were all computed from Eq. (A-12) which require measurements at six angular positions of the hot-wire ($\theta_n = (n - 1)\frac{\pi}{6}$; $n = 1, 2, \dots, 6$). As discussed in Section (A-6) the results from Eqs. (A-10) and (A-12) are equivalent to the order of the triple correlations of the turbulent fluctuations. In practice the two equations give identical values of the Reynolds stress except for Runs 112871-1, 102171-1 and 092271-5. For these three runs, which all have very low values of the friction coefficient, the measured Reynolds stresses were not used for the evaluation of friction coefficients.

The normalized turbulent fluctuations, $\overline{v'^2}/u_\infty^2$ and $\overline{w'^2}/u_\infty^2$ were evaluated using Eq. (A-13) combined with Eq. (5-6).

5.4 The Free-Stream Velocity

The free-stream velocity, u_∞ , was deduced from dynamic pressures, P_d , measured at the position of the 46 static pressure taps in the side wall. Thus the free-stream velocity is computed as

$$u_\infty = \sqrt{\frac{2P_d}{\rho}},$$

where ρ is the air density obtained from the measured values of pressure, temperature and humidity in conjunction with saturation data from Ref. [17].

The measured velocities were curve-fit and du_∞/dx was obtained by differentiation of the analytical fit (see Appendix B for details). The RMS - difference between measured values of the free-stream velocity and the fit was about 0.03 ft/s for most runs.

5.5 Virtual Origin and $d\delta_2/dx$

The experimental values of δ_2 for 10 inches $\leq x \leq$ 90 inches were fitted by an equation of the form:

$$\delta_{2,fit} = \alpha(x - x_0)^\beta. \quad (5-8)$$

The constants α , β , and x_0 were determined by the method of least squares. The "virtual origin" of the boundary layer was taken to be at $x = x_0$.

The derivative, $d\delta_2/dx$, was taken to be equal to the derivative of $\delta_{2,fit}$ from Eq. (5-8).

5.6 Correlation of Friction Coefficients

The friction coefficients, $(c_f/2)_o$, for the three boundary layers without transpiration (corresponding to $m = 0$, -0.15 and -0.20) have been fitted by equations of the form:

$$(c_f/2)_o = a \text{Re}_{\delta_2}^{-b} . \quad (5-9)$$

All the friction coefficients for boundary layers with transpiration belonging to each of the three pressure gradients were correlated with an equation of the type:

$$c_f/2 = (c_f/2)_o [1 + a_1 B_o + a_2 B_o^2 + a_3 B_o^3] , \quad (5-10)$$

where

$$B_o = F/(c_f/2)_o$$

and $(c_f/2)_o$ is determined from Eq. (5-9). The fitted values of the friction coefficient, as determined by the three equations of type (5-10) were then used for the data reduction (i.e. for the computation of y^+ , u^+ , v_o^+ etc.).

It should again be stressed that the friction coefficients used to evaluate the coefficients for Eqs. (5-9) and (5-10) were all obtained from the "shear stress method" except in the case of Runs 112871-1, 102171-1 and 092271-5 for which $c_f/2$ was evaluated from the "generalized law of the wall", Eq. (7-25).

5.7 Shear Stress Profiles

The shear stress profiles may be computed from Eq. (4-3). However, because of the uncertainty in $\partial u/\partial x$, and because of the unknown magnitude of the left out 3D term, the equation usually predicts a non-zero shear stress at the outer edge of the boundary layer.

The derivative $\partial u / \partial x$ in Eq. (4-3) was evaluated at the measured profile points of a given profile by using interpolated values for u (at the same y) at the first upstream and downstream profiles assuming a linear variation of u with x . The integrations were performed by using the trapezoidal rule.

It was assumed that the major reason for the failure of Eq. (4-3) to satisfy the outer boundary condition, $\tau(\delta) = 0$, was experimental uncertainty of $\partial u / \partial x$. By further assuming that the percentage error in $\partial u / \partial x$ is independent of y , the shear stress profiles may be corrected by multiplying the bracketed term in Eq. (4-3) containing the two integrals, by a factor, α , which is adjusted such that $\tau(\delta) = 0$. The computing equation for the shear stress then becomes:

$$\frac{\tau(y)}{\rho u_\infty^2} = c_f/2 - \frac{y}{u_\infty} \frac{du_\infty}{dx} - \frac{\alpha}{u_\infty^2} \left(u \int_0^y \frac{\partial u}{\partial x} dy - 2 \int_0^y u \frac{\partial u}{\partial x} dy \right), \quad (5-11)$$

where

$$\alpha = \frac{c_f/2 - \frac{y}{u_\infty} \frac{du_\infty}{dx}}{\left(u \int_0^\delta \frac{\partial u}{\partial x} dy - 2 \int_0^\delta u \frac{\partial u}{\partial x} dy \right) / u_\infty^2}$$

If profiles at $x = 10$ inches are excluded $\partial u / \partial x$ has in general been corrected by less than $\pm 6\%$. Furthermore, the correction never has the same sign for all profiles belonging to a given run; this seems to indicate that experimental uncertainty on $\partial u / \partial x$ (rather than effects of three-dimensionality) is indeed largely responsible for the necessity to correct the shear stress profiles.

It should be noted that the influence of the corrective factor, α , on the shear stress profiles computed from Eq. (5-11) is extremely small close to the wall. For example only in a few cases does the correction influence the evaluation of friction coefficients by the "shear stress" method.

CHAPTER 6

ANALYSIS AND DISCUSSION OF EXPERIMENTAL RESULTS

In the present chapter certain aspects of these results will be discussed in detail. In particular correlations for the friction coefficients and for the Clauser shape factor, G , (defined in Section 2.2), will be given. It will be shown that equilibrium boundary layers are in

fact obtained when the acceleration parameter, $\beta = \frac{\delta_1}{\tau_0} \frac{dp}{dx}$, and the blowing parameter, $B = \rho v_0 u_\infty / \tau_0$, are held constant.

Attention will be given to the behavior of the "eddy viscosity", ϵ , defined by

$$\tau = \rho(\nu + \epsilon) \frac{du}{dy} \quad (6-1)$$

and the "mixing length", ℓ , which is related to the eddy viscosity through the definition:

$$\epsilon = \ell^2 \frac{du}{dy} \quad (6-2)$$

It will be shown that for all the experimental boundary layers reported herein, there exists a range of y close to the wall where the mixing length is approximately proportional to the distance from the wall, i.e. where

$$\ell = \kappa y \quad (6-3)$$

Moreover, the factor of proportionality, the von Kármán constant, κ , is the same for all the flows: i.e., κ is independent of the pressure gradient, the transpiration rate, and the Reynolds number.

The range of distances from the wall where approximate proportionality between ℓ and y exists (i.e. where Eq.

(6-3) remains valid) will be called the "overlap region". It separates the inner "wall region" from the "outer region". In both the inner and outer regions, $l \leq ky$, may then be considered the "common asymptote" for the wall region and the outer region.

6.1 Friction Coefficients

All the measured friction coefficients are plotted versus the momentum thickness Reynolds number in the following figures: Fig. 6-1 for $m = 0$ (constant pressure flows), Fig. 6-2 and Fig. 6-3 for $m = -0.15$ and Fig. 6-4 for $m = -0.20$. The "open" symbols represent friction coefficients evaluated by the shear stress method (Section 4.1.2); the "solid" symbols correspond to friction coefficients obtained from the "generalized law of the wall" (see Section 7.3). Also shown in the figures are lines representing analytical "fits" of the friction coefficient data.

The friction coefficients, $(c_f/2)_o$, for the three non-transpired flows (corresponding to $m = 0$, -0.15 and -0.20) have been fitted by the following equations:

$$(c_f/2)_o = a \text{Re}_{\delta_2}^{-0.25}, \quad (6-4)$$

where

$$m = 0, \quad a = 0.0120 \quad (850 < \text{Re}_{\delta_2} < 3000)$$

$$m = -0.15, \quad a = 0.0102 \quad (1500 < \text{Re}_{\delta_2} < 3500)$$

$$m = -0.20, \quad a = 0.0083 \quad (1700 < \text{Re}_{\delta_2} < 4200)$$

These fits seem to be quite adequate for the present range of Reynolds numbers.

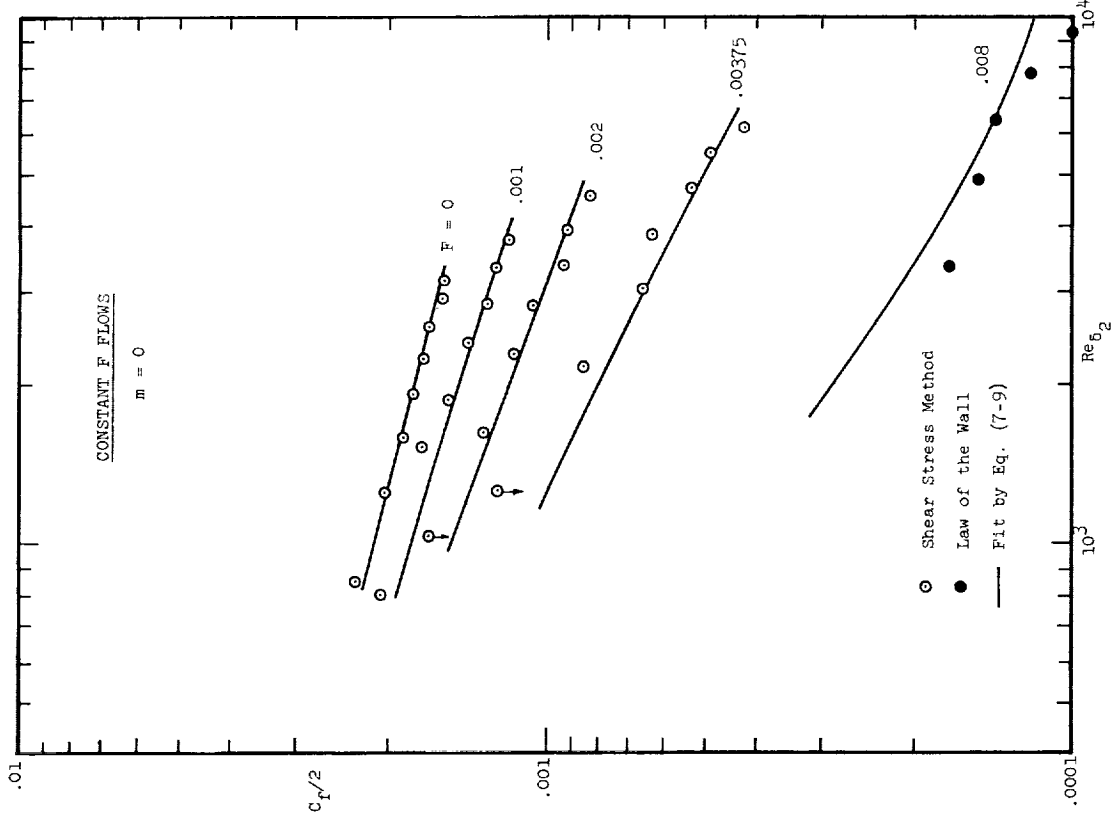


Fig. 6-1 $c_f/2$ versus Re_{δ_2} ; $m = 0$, constant blowing fractions

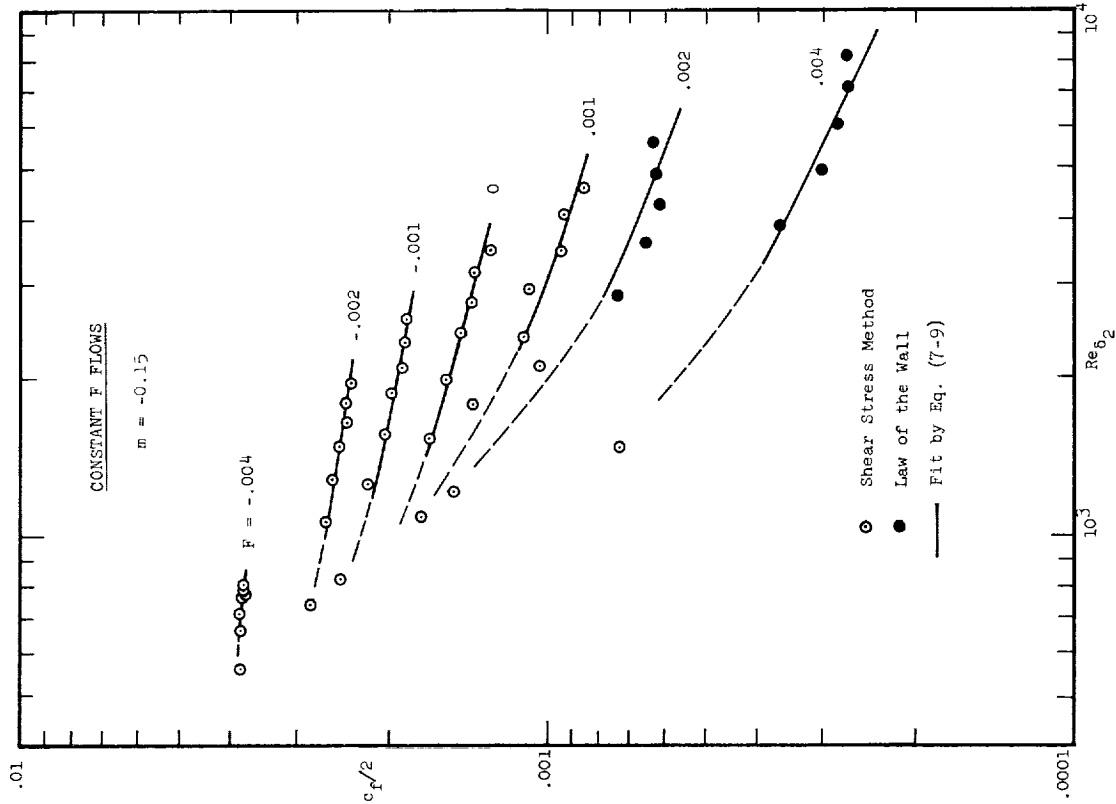


Fig. 6-2 $c_f/2$ versus Re_{δ_2} ; $m = -0.15$, constant blowing fractions

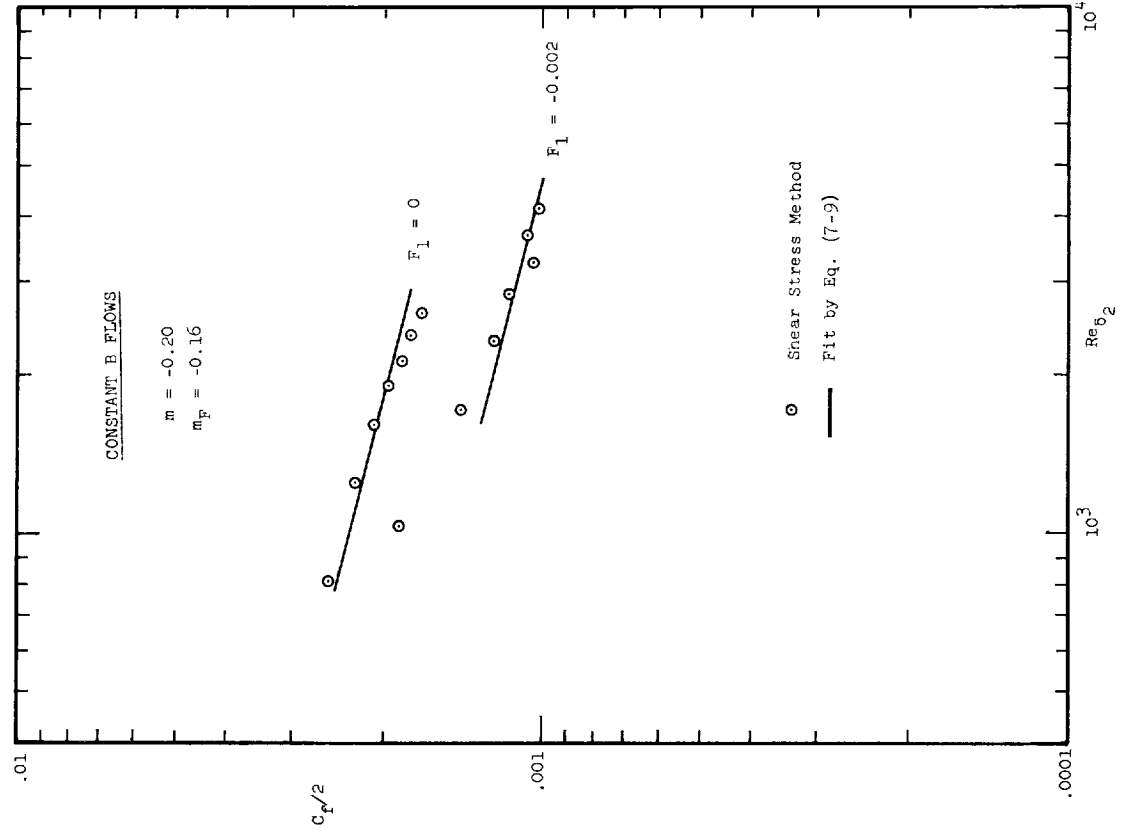


Fig. 6-4 $c_f/2$ versus Re_{δ_2} ; $m = -0.20$, equilibrium boundary layers

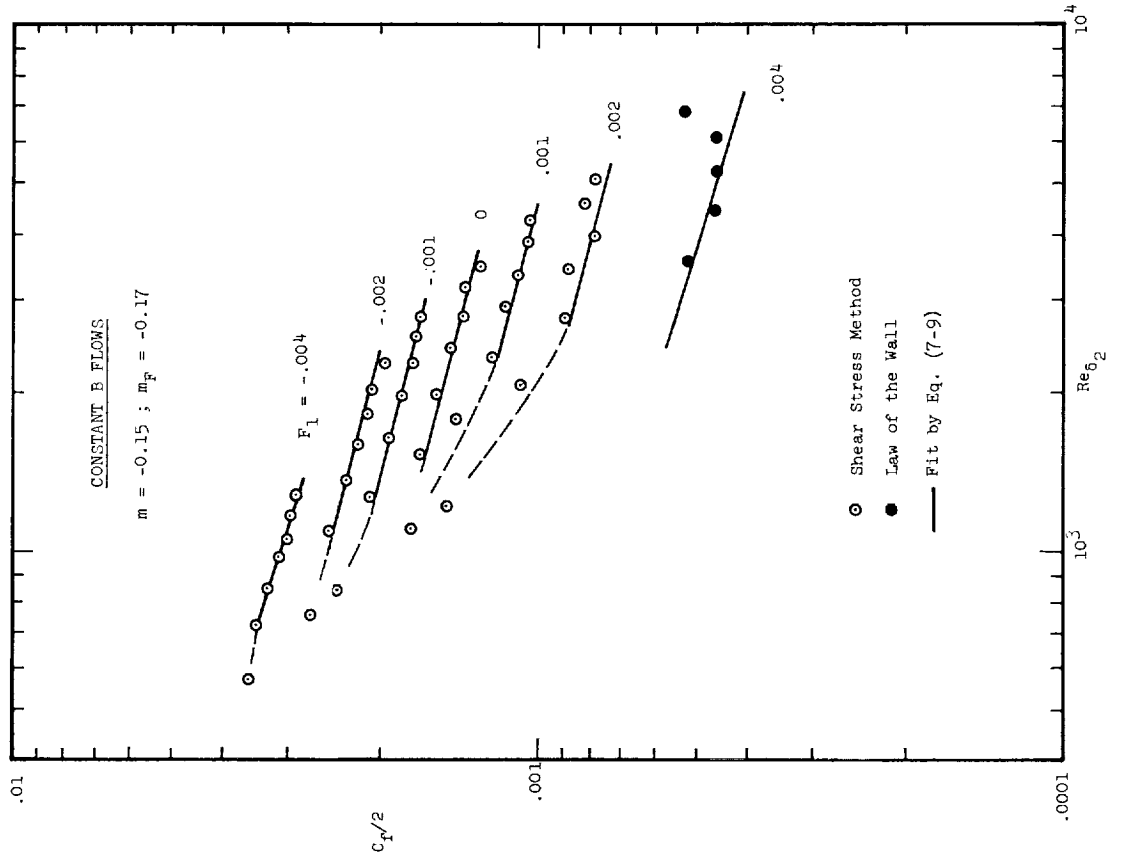


Fig. 6-3 $c_f/2$ versus Re_{δ_2} ; $m = -0.15$, equilibrium boundary layers

In an attempt to correlate all transpired and non-transpired friction coefficients for flows with the same pressure gradient (same m) one might try to determine a function $f = f(B)$ such that

$$\left(\frac{c_f}{c_{f,0}} \right)_{m, \text{Re}_{\delta_2}} = f(B) \text{ , where } B = \frac{F}{(c_f/2)} \text{ .} \quad (6-6)$$

A correlation of the above type was shown by Simpson [2] to exist for constant pressure ($m = 0$) boundary layers. However, for convenience the following relationship will be preferred:

$$\left(\frac{c_f}{c_{f,0}} \right)_{m, \text{Re}_{\delta_2}} = f_0(B_0) \text{ where } B_0 = \frac{F}{(c_f/2)_0} \text{ .} \quad (6-7)$$

From the above definitions it is obvious that $B_0 = Bf(B)$, $B = B_0/f_0(B_0)$ and $f(B) = f_0(B_0)$ so that if Eq. (6-6) holds true then Eq. (6-7) follows, and vice versa. Therefore correlations (6-6) and (6-7) are equivalent formulations.

Figure 6-5 shows $\left(\frac{c_f}{c_{f_0}} \right)_{\text{Re}_{\delta_2}}$ for constant pressure

($m = 0$) boundary layers plotted versus B_0 (only data for $x \geq 22$ inches is shown). The existence of a relationship of the form (6-7) for these zero pressure gradient boundary layers merely confirms Simpson's earlier experimental finding. Simpson's best fit of his experimental results is represented by the dashed line in the figure.

Figure 6-6 displays experimental results (for $x \geq 34$ inches) for the $m = -0.15$ boundary layers. Note that the data, as anticipated, can be adequately correlated by an equation of the type (6-7). The best fits (least square)

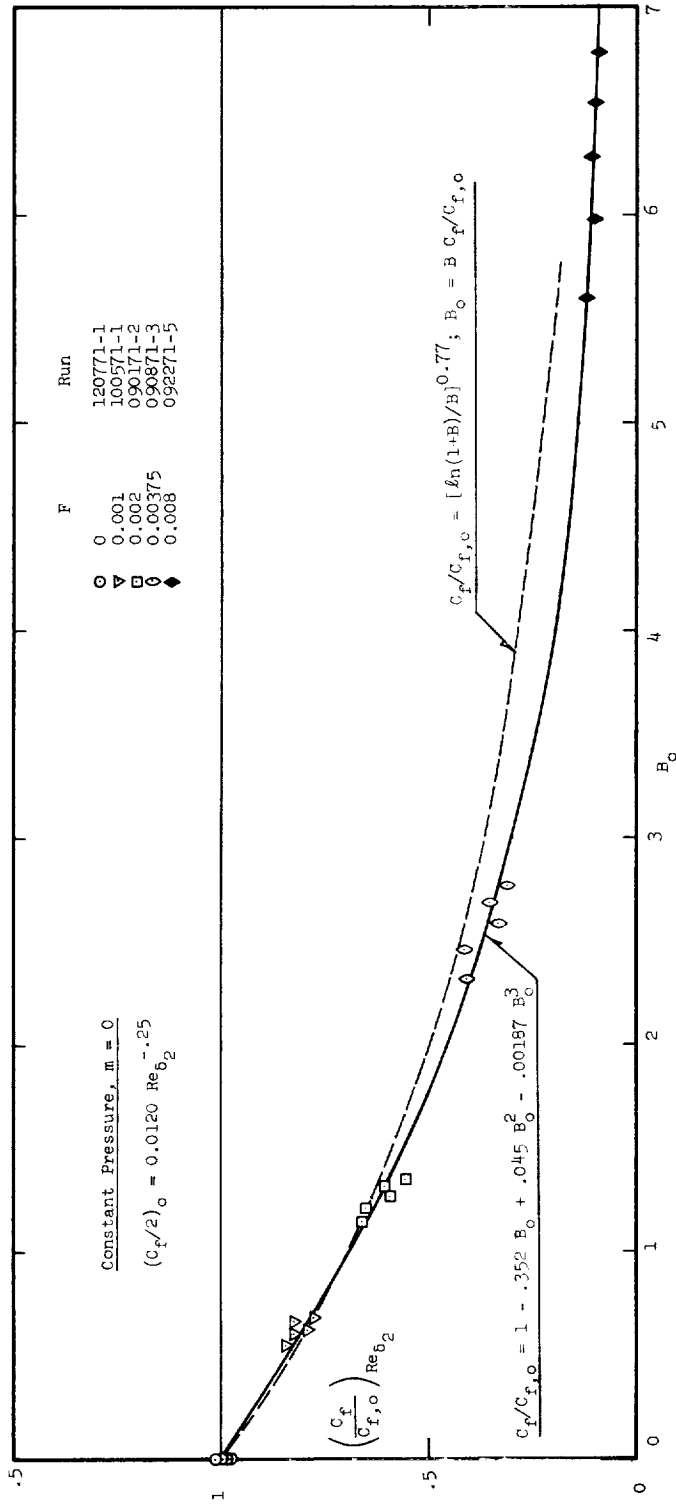


Fig. 6-5 Ratio of friction coefficient to the friction coefficient for the non-transpired boundary layer at the same momentum thickness Reynolds number versus a modified blowing parameter, $m = 0$.

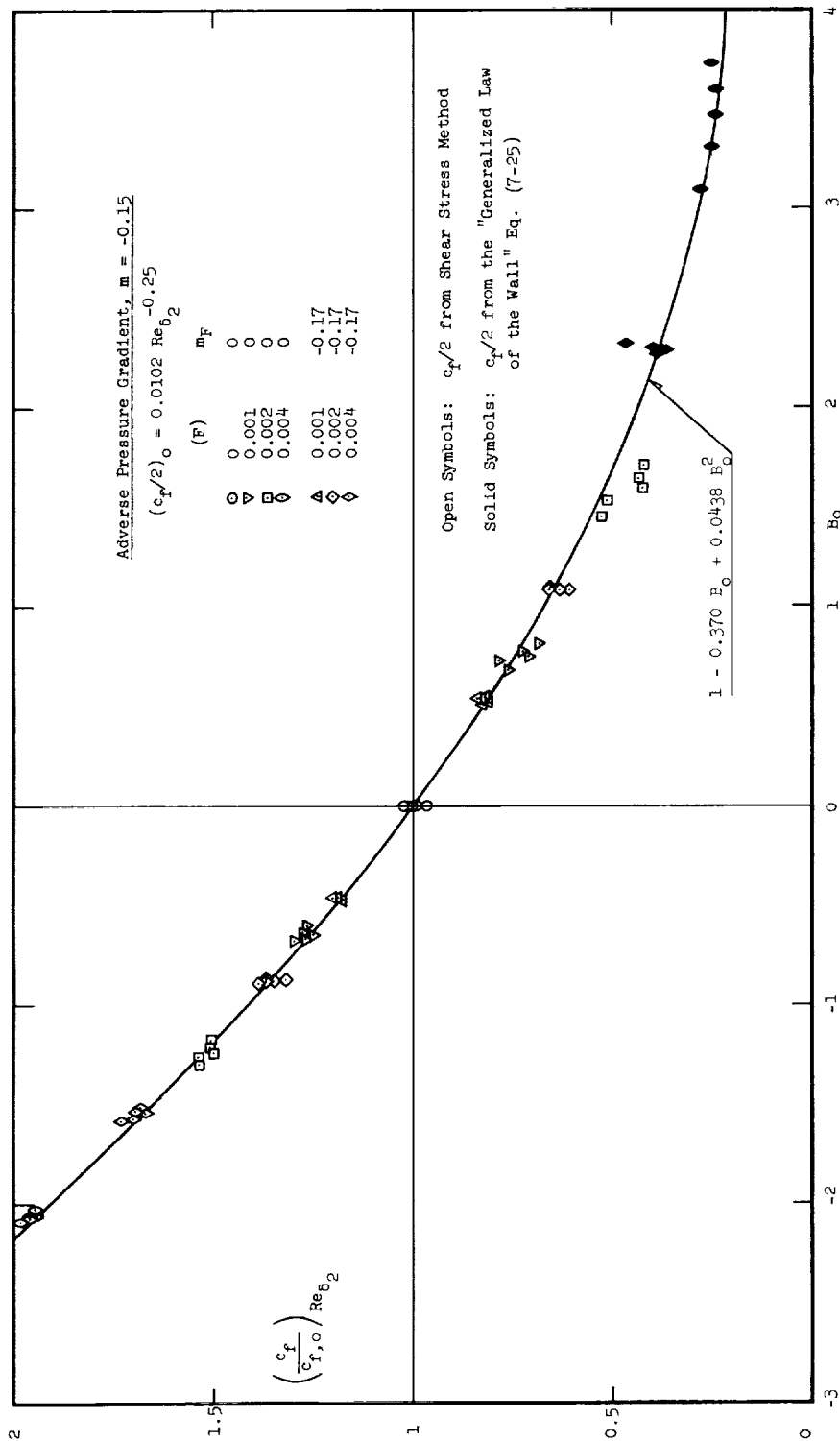


Fig. 6-6 Ratio of friction coefficient to the friction coefficient for the non-transpired boundary layer at the same momentum thickness Reynolds number versus a modified blowing parameter, $m = -0.15$.

for the three pressure gradients are summarized below:

$$m = 0 \quad : \quad f_o = 1 - .351B_o + .045B_o^2 - .00187B_o^3 ; 0 \leq B_o < 7$$

$$m = -0.15 \quad : \quad f_o = 1 - .370B_o + .0438B_o^2 ; -2.2 < B_o < 4$$

$$m = -0.20 \quad : \quad f_o = 1 - .51B_o ; -1.2 < B_o \leq 0$$

(6-9)

The friction coefficient for a given boundary layer may then be evaluated as $c_f/2 = (c_f/2)_o f_o(B_o)$, where $(c_f/2)_o$ is given by Eqs. (6-4). Note that the correlation for $m = -0.20$ is based on only two boundary layers. The correlations, Eqs. (6-9) should of course not be used outside the range of experimental Reynolds numbers; these may be read off Figs. 6-1 to 6-4 .

6.2 The Outer Region

The outer region includes approximately the outer 90% of the boundary layer. It includes the logarithmic portion of the mean velocity profile as an inner asymptote.

6.2.1 Velocity Defect Profile Similarity

The analysis of Chapter 2 suggested that turbulent boundary layers subject to the boundary conditions Eqs. (2-12) and (2-13) would have a constant acceleration parameter, β , and a constant blowing parameter, B . The data tabulated in Chapter 9 show that this is indeed the case in practice for $x \geq 10$ inches, for $m = 0$, and for $x \geq 34$ inches, for $m = -0.15$ and $m = -0.20$. Therefore assumption (a), (b) and (c) of Chapter 2 which formed the basis for the analysis are verified for the present experimental range of parametric variations.

Furthermore, the boundary layers with constant β and constant B also have a constant Clauser shape factor, G (defined by Eq. (2-3)). Thus constant β and B boundary layers are equilibrium flows i.e., they have velocity defect profile similarity. Figure 6-7 shows velocity defect profiles for a blown equilibrium boundary layer. Note the near perfect similarity in the outer region of the boundary layer. This similarity is of course also indicated by the constancy of the Clauser shape factor, G .

In Fig. 6-8 G has been plotted against $(\beta + B)$ for all the runs reported (only profiles for $x \geq 34$ inches are included). Each run consists of 5 profiles along the plate. The runs for which β and B are constants are, as mentioned, equilibrium boundary layers; measured values of G are substantially the same for all profiles of the run and thus plot almost as a single (filled) symbol. The open symbols are for constant $F \neq 0$ runs. For these runs $(\beta + B)$ changes along the plate. Note that the shape factor, G , is a unique function of $(\beta + B)$ (rather than of β and B separately). The fact that $G = G(\beta + B)$ indicates that the acceleration parameter, β , and the blowing parameter, B , have identical effect on the shape of the velocity defect profile. This is true at least for equilibrium boundary layers and for flows close to equilibrium (constant F).

6.2.2 Shear Stress, Eddy Viscosity and Mixing-Length

In view of the velocity defect profile similarity demonstrated in the previous section for boundary layers with constant β and B it may be reasonable to expect that the shear stress, eddy viscosity and mixing-length profiles are also self-similar (i.e. independent of the Reynolds number) for these flows. Clauser 1956 [18] showed that the assumption of a constant eddy viscosity, $\epsilon = k\delta_1 u_\infty$ ($k \approx 0.018$), in the outer region of non-transpired equilib-

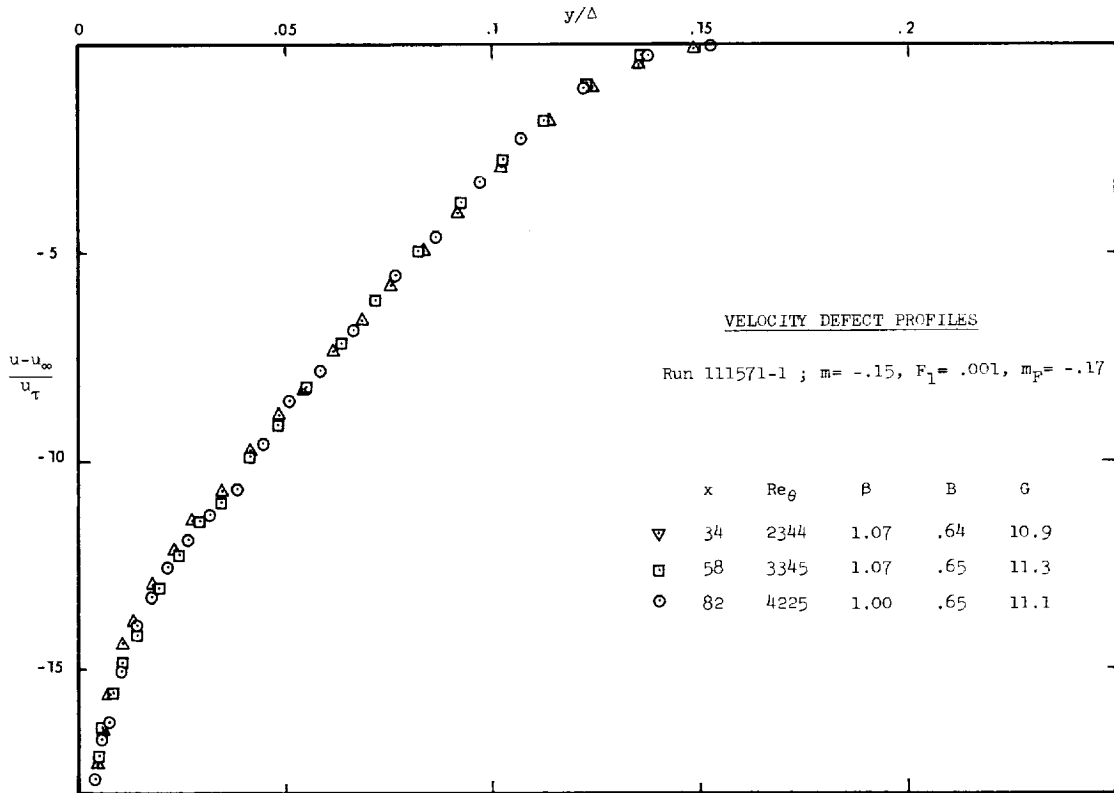


Fig. 6-7 Defect profiles for a blown equilibrium boundary layer

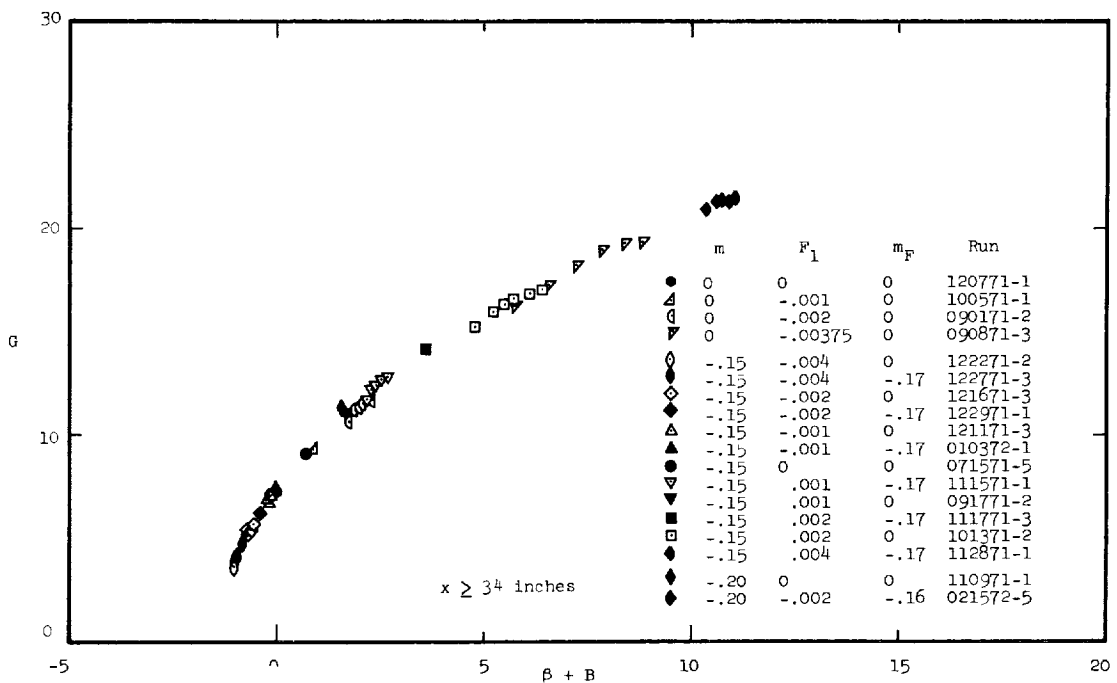


Fig. 6-8 Clauser shape factor. All runs except 102171-1 and 092271-5 are represented

rium boundary layers leads to the prediction of velocity defect profiles that compare very well with experimental profiles. In Fig. 6-9 $k = \epsilon/\delta_1 u_\infty$ is plotted against y/δ_{99} for an equilibrium boundary layer with $B = 0$. Note that the assumption of a constant k is not quite satisfactory, but that $k = \epsilon/\delta_1 u_\infty$ does show outer similarity, i.e. may be expressed as:

$$k = k(y/\Delta) \quad (6-11)$$

(Δ and δ are proportional for constant G flows (see Chapter 2)).

Velocity defect profile similarity means that $(u-u_\infty)/u_\tau = F(y/\Delta)$. Using this in Eq. (6-1) for the shear stress, and neglecting the viscous contribution one may obtain

$$\frac{\tau}{\tau_0} = k\left(\frac{y}{\Delta}\right)F'\left(\frac{y}{\Delta}\right) \quad (6-12)$$

In Fig. 6-10 experimental values of τ/τ_0 are plotted against y/δ_{99} for three equilibrium flows. It may be noted that the similarity indicated by Eq. (6-12) does indeed exist.

From the definition of the mixing length, Eq. (6-2), one may now obtain:

$$\frac{\ell}{\Delta} = \sqrt{k\left(\frac{y}{\Delta}\right)/F'\left(\frac{y}{\Delta}\right)} \quad (6-13)$$

In Fig. 6-11 experimental values of ℓ/δ_{99} is plotted against y/δ_{99} for the same boundary layer for which $\epsilon/\delta_1 u_\infty$ was displayed in Fig. 6-9. Note that the mixing length, as expected, shows the same outer region similarity as $(u-u_\infty)/u_\tau$, τ/τ_0 and $k = \epsilon/\delta_1 u_\infty$. The above conclusions concerning similarity (i.e. Reynolds number independence of $k = \epsilon/\delta_1 u_\infty$, τ/τ_0 and ℓ/δ_{99}) were based on data corresponding to a rather limited range of Reynolds numbers. There is

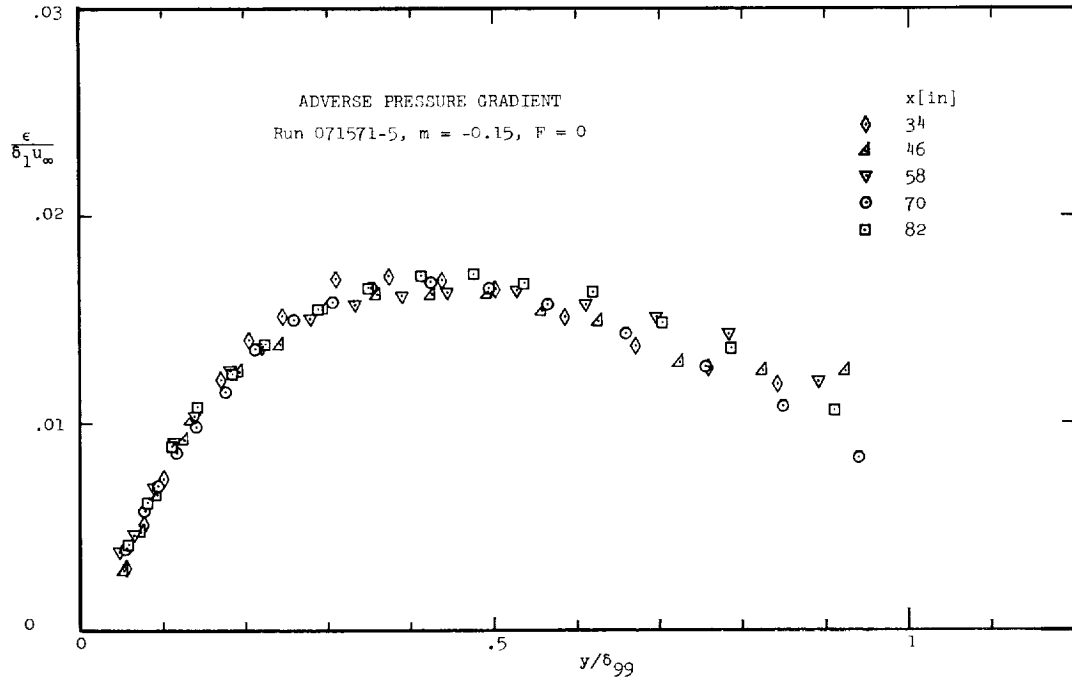


Fig. 6-9 Profiles of non-dimensional eddy viscosity in outer region. Weak adverse pressure gradient, no transpiration

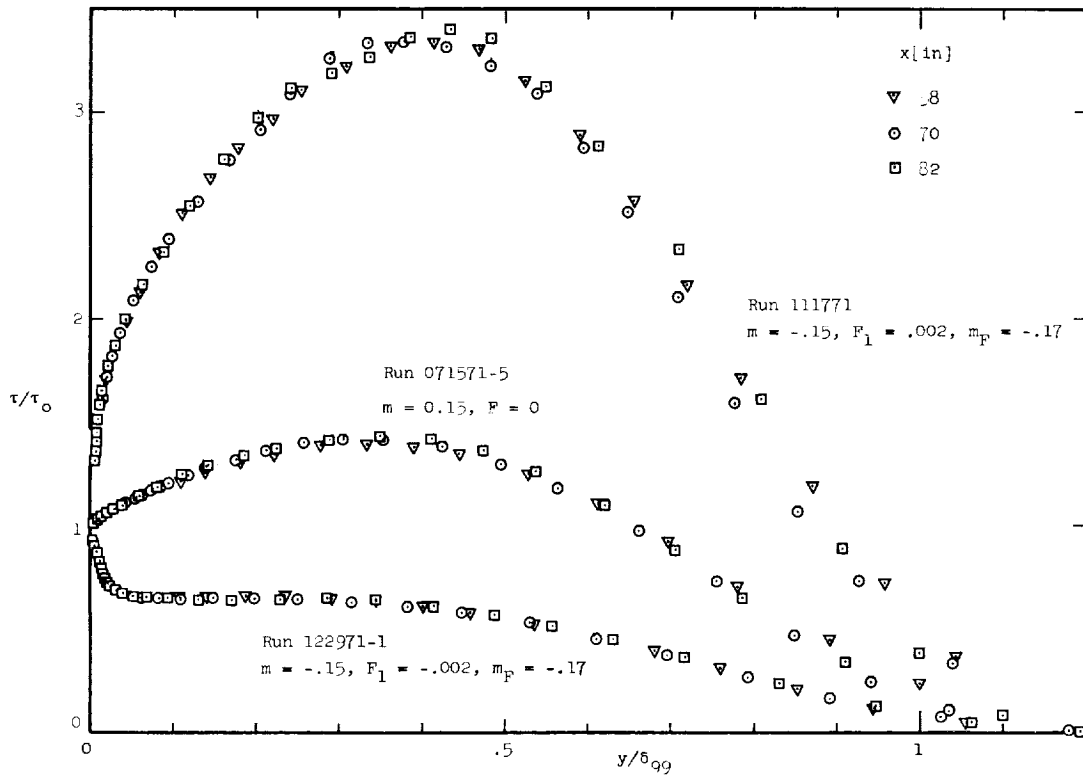


Fig. 6-10 Non-dimensional shear stress profiles for three equilibrium boundary layers. Weak adverse pressure gradient

some evidence of a slight Reynolds number effect for small Reynolds numbers. The predictions carried out in Section 7.4 indicate that the value of l/δ_{99} in the outer region decreases as $Re_{\delta_2}^{-.125}$ for $Re_{\delta_2} < 6000$. The same effect has previously been reported in connection with predictions of turbulent boundary layers in favorable pressure gradients.

In Fig. 6-12 l/δ_{99} is plotted versus y/δ_{99} for a broad range of pressure gradient and transpiration boundary conditions. All the profiles are for $x = 70$ or 82 inches. Figure 6-12 includes not only equilibrium boundary layers, but also flows with $F = \text{const.} \neq 0$; these latter boundary layers deviate slightly from equilibrium (G is not quite constant). The figure indicates a slight systematic decrease in the value of l/δ_{99} in the outer region with increasing blowing rate. However, all the profiles are for approximately the same x -position. This means that the Reynolds number, Re_{δ_2} , increases with an increasing blowing rate for a given δ_2 pressure gradient. Because of the Reynolds number effect mentioned above it is not possible to deduce a possible effect of transpiration from Fig. 6-12 alone. However, the predictions of the experimental flows carried out in Section 7.4 indicate that increasing values of the blowing fraction, F , correspond to reduced values of l/δ_{99} in the outer region.

Figure 6-12 shows very clearly that $l = ky$ becomes a common "asymptote" for the mixing length for small enough values of y/δ_{99} . The overlap region, where $l = ky$, separates the outer region from the inner region.

Figure 6-13 shows experimental profiles of $\epsilon/\delta_1 u_\infty$ versus y/δ_{99} . The plot is equivalent to Fig. 6-12 for the mixing length. It indicates the same systematic behavior for $\epsilon/\delta_1 u_\infty$ in the outer region as was observed for l/δ_{99} .

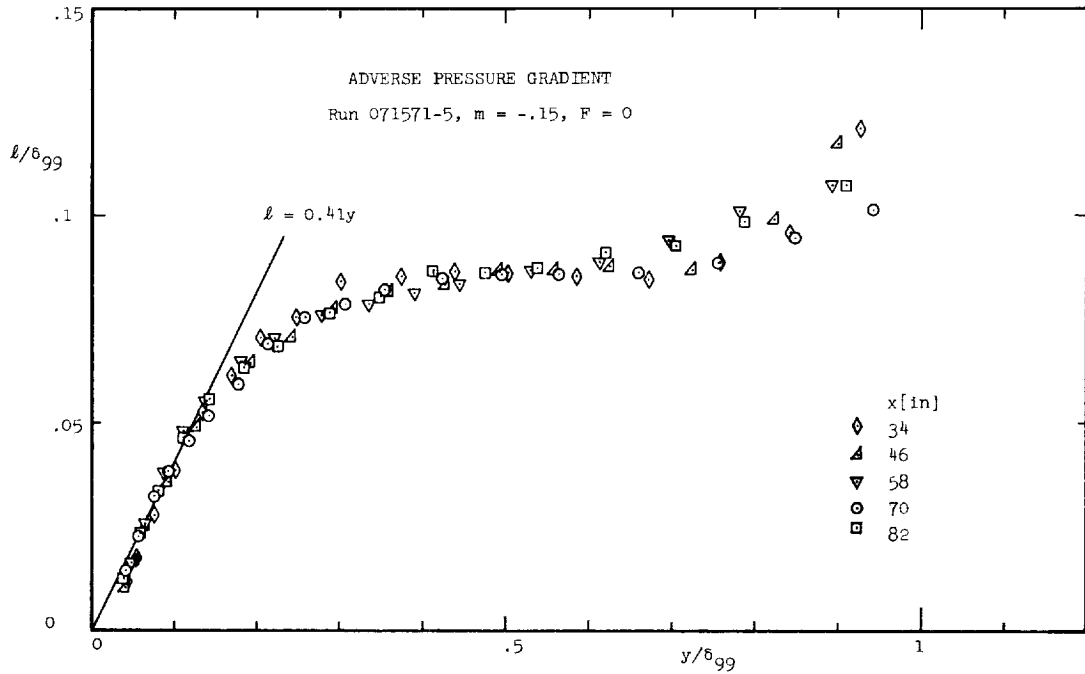


Fig. 6-11 Profiles of non-dimensional mixing-length in outer region. Weak adverse pressure gradient, no transpiration

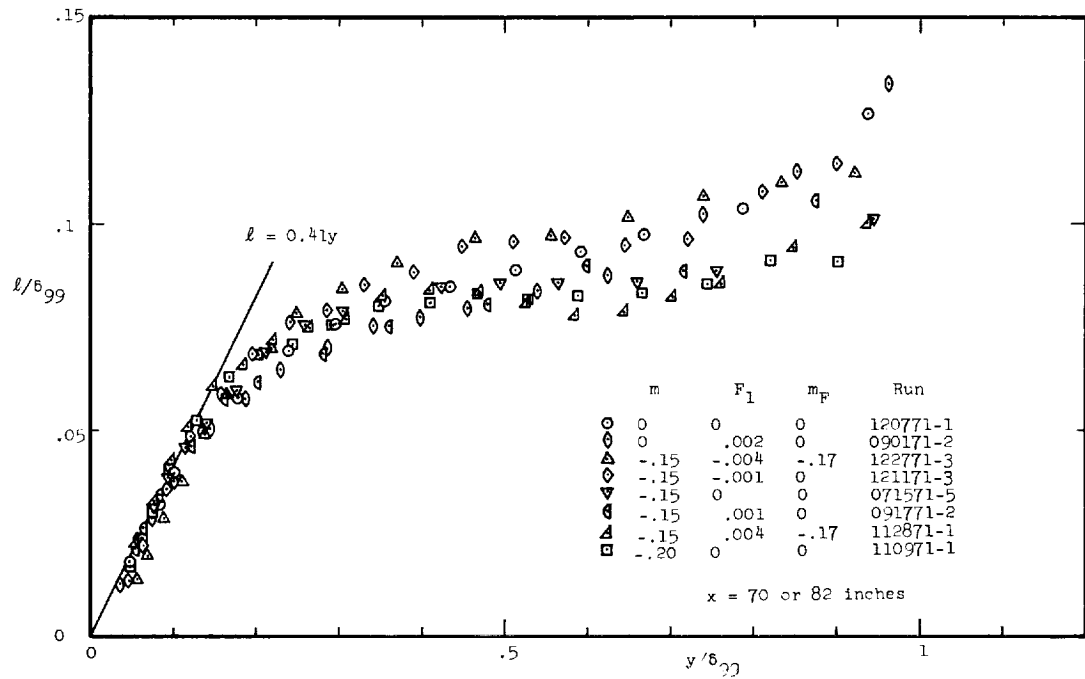


Fig. 6-12 Profiles of non-dimensional mixing-length in outer region. Comparison for selected boundary conditions

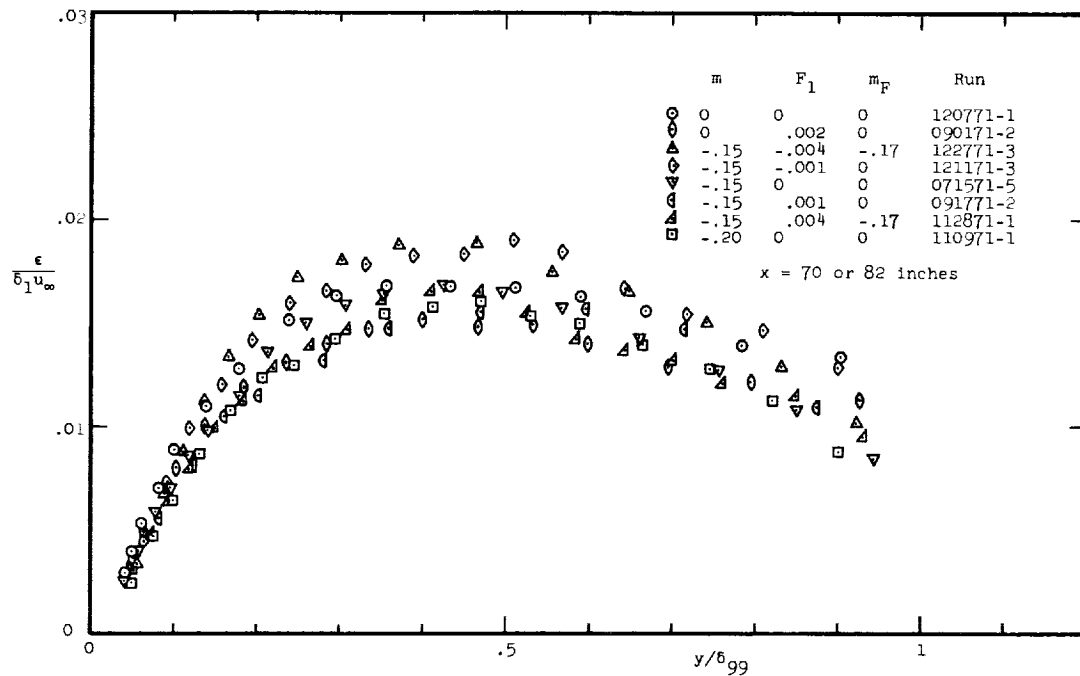


Fig. 6-13 Profiles of non-dimensional eddy viscosity in outer region. Comparison for selected boundary conditions

6.3 The Inner Region

In the inner region ("wall region") of the boundary layer, viscous effects are important and u_τ and v/u_τ are generally used as velocity and length scales. The non-dimensional mean velocity profile, for example, is described, by the "wall coordinates" $u^+ = u/u_\tau$ and $y^+ = yu_\tau/\nu$. Similarly the transpiration rate will be expressed as $v_o^+ = v_o/u_\tau$ (and not by the blowing parameter, B , which is appropriate in the outer region). The proper pressure

gradient parameter is $p^+ = \frac{\nu}{\rho u_\tau^3} \frac{dp}{dx}$.

6.3.1 Mean Velocity Profiles in Wall Coordinates

Figure 6-14 shows experimental velocity profiles in wall coordinates for the three non-transpired boundary layers (corresponding to $m = 0$, -0.15 and -0.20). Note that the three flows have pressure gradients ranging from $p^+ = 0$ to a rather severe adverse pressure gradient, $p^+ = 0.0075$, but that they all fit the law of the wall:

$$u^+ = \frac{1}{0.41} \ln y^+ + 5.0 \quad (6-14)$$

(constants from Coles [14]) reasonably well over a range of y^+ .

Figure 6-15 is a plot of experimental mean velocity profiles in wall coordinates all belonging to the same family ($m = -0.15$), but having different transpiration rates, v_o^+ , and pressure gradients, p^+ . The profiles for $v_o^+ > 0$ (blowing) lie above the law of the wall, Eq. (6-14), and those for $v_o^+ < 0$ (suction) lie below. It appears however, that all the experimental profiles have a "logarithmic portion" i.e. a region where u is proportional to $\ln y$. A "generalized law of the wall" that fits this region for all the experimental flows will be presented in Section 7.3.

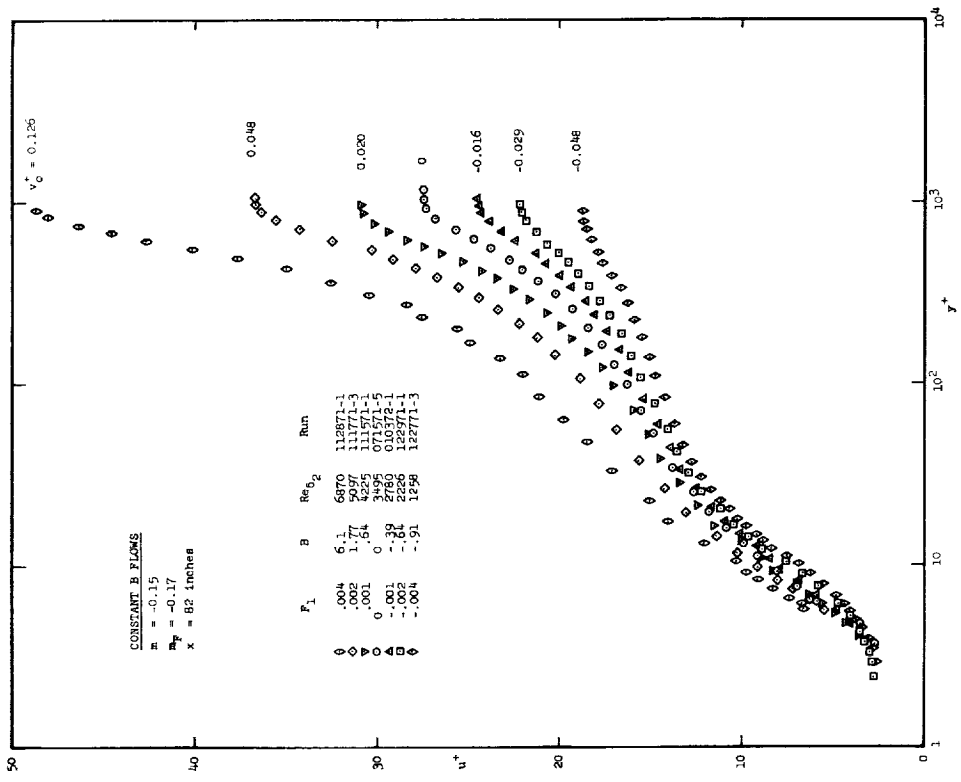


Fig. 6-15 Velocity profiles in wall coordinates for equilibrium boundary layers. Weak adverse pressure gradient

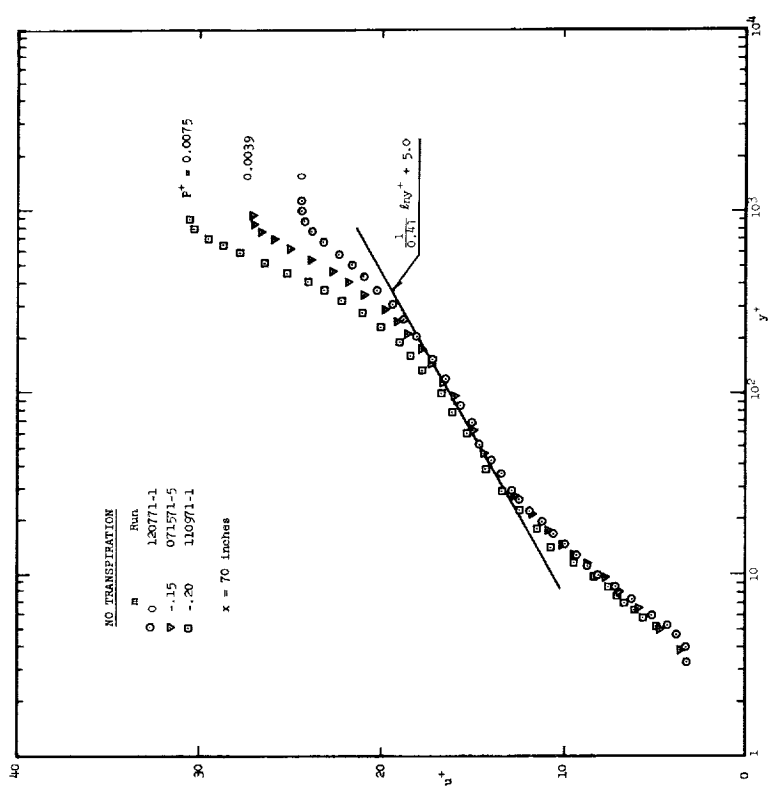


Fig. 6-14 Velocity profiles in wall coordinates for the three boundary layers without transpiration

6.3.2 Mixing-Length and Eddy Viscosity

Figure 6-16 shows experimental values of l/y plotted versus y^+ for boundary layers with different transpiration rates. Note that for large enough values of y^+ they all exhibit a range where $l/y \approx 0.41$; this is the overlap region between the inner and outer regions of the boundary layer. The thickness (in terms of y^+) of the inner region can be seen to depend greatly upon the transpiration rate, v_o^+ . It depends similarly on the pressure gradient parameter, p^+ . Large values of v_o^+ or p^+ correspond to thin sublayers.

The observed deviation from proportionality between l and y in the inner region may be accounted for by, for example, the van Driest model for the mixing length:

$$l = ky[1 - \exp(-\frac{y}{A})] \quad (6-15)$$

Note that this model assures the proper asymptotic behavior, $l = ky$, for "large" values of y . The parameter A may be considered a length scale proportional to the thickness of the inner region. The value of $A^+ = Au_\tau/\nu$ therefore must depend upon v_o^+ and p^+ i.e. $A^+ = A^+(p^+, v_o^+)$. Experimentally A^+ may be found by fitting $l/y = \kappa[1 - \exp(-y^+/A^+)]$ to the experimental values of l/y . Here, however, an indirect method that assures a correct mean velocity profile in the overlap region will be used. From the definitions of ϵ and l , Eqs. (6-1) and (6-2) together with the expression (6-15) one may obtain

$$\frac{du^+}{dy^+} = \frac{2\tau^+}{1 + \sqrt{1 + 4\tau^+ \kappa^2 y^{+2} [1 - \exp(-y^+/A^+)]^2}}, \quad (6-16)$$

where $\tau^+ = \tau/\tau_o$. Using the experimental shear stress profile this equation may be integrated (numerically) to give

u^+ as a function of y^+ with A^+ as a parameter. The experimental values of A^+ have then been chosen such that the velocity profiles thus generated match the experimental velocity profiles in the overlap region (in practice at $y^+ \approx 2.5A^+$).

In Fig. 6-17 experimental values of l/y are plotted versus $y/A = y^+/A^+$, where A^+ is determined by the above method. Note how data points for boundary layers with a wide range of sublayer thickness (as expressed by A) now plot on a single universal curve. The continuous curve in Fig. 6-17 corresponds to the behavior of the mixing-length as predicted by a van Driest model.

The successful correlation of the mixing length data obtained by plotting l/y versus y/A suggests that A may be a significant length scale of the inner region. It is therefore quite reasonable to attempt to correlate the eddy viscosity similarly by plotting $\epsilon^+ = \epsilon/\nu$ versus y/A . This has been done in Fig. 6-18; the plot shows that ϵ^+ is indeed a unique function of y/A over an extended range in the inner region.

The experimental values of A^+ have been expressed as a function of p^+ and v_o^+ by the method of least squares. The best fit was obtained by the following expression:

$$A^+ = 24 \exp \left(\sum_{i=0}^2 \sum_{j=0}^1 a_{ij} [\ln(v_o^+ + .08)]^i [\ln(p^+ + .04)]^j \right), \quad (6-20)$$

where

$$a_{ij} = \begin{bmatrix} -6.71751 & -1.50414 \\ -4.81589 & -1.24311 \\ -1.27827 & -0.388216 \end{bmatrix}$$

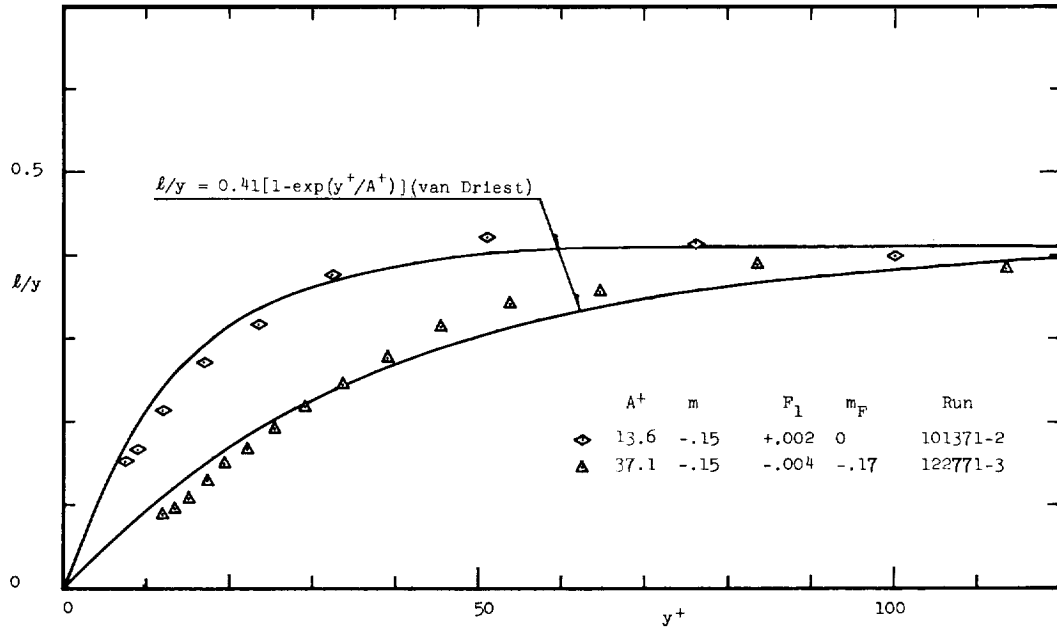


Fig. 6-16 Comparison of two profiles of the normalized mixing-length in the inner region

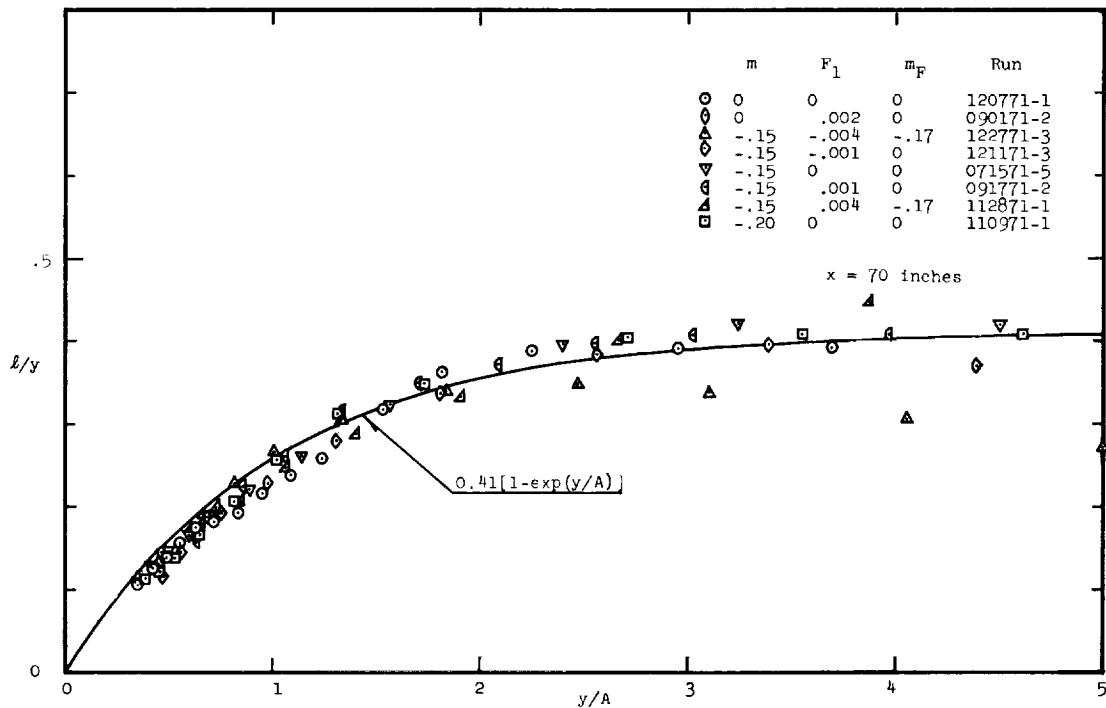


Fig. 6-17 Profiles of the normalized mixing-length versus the distance from the wall divided by van Driest's length scale

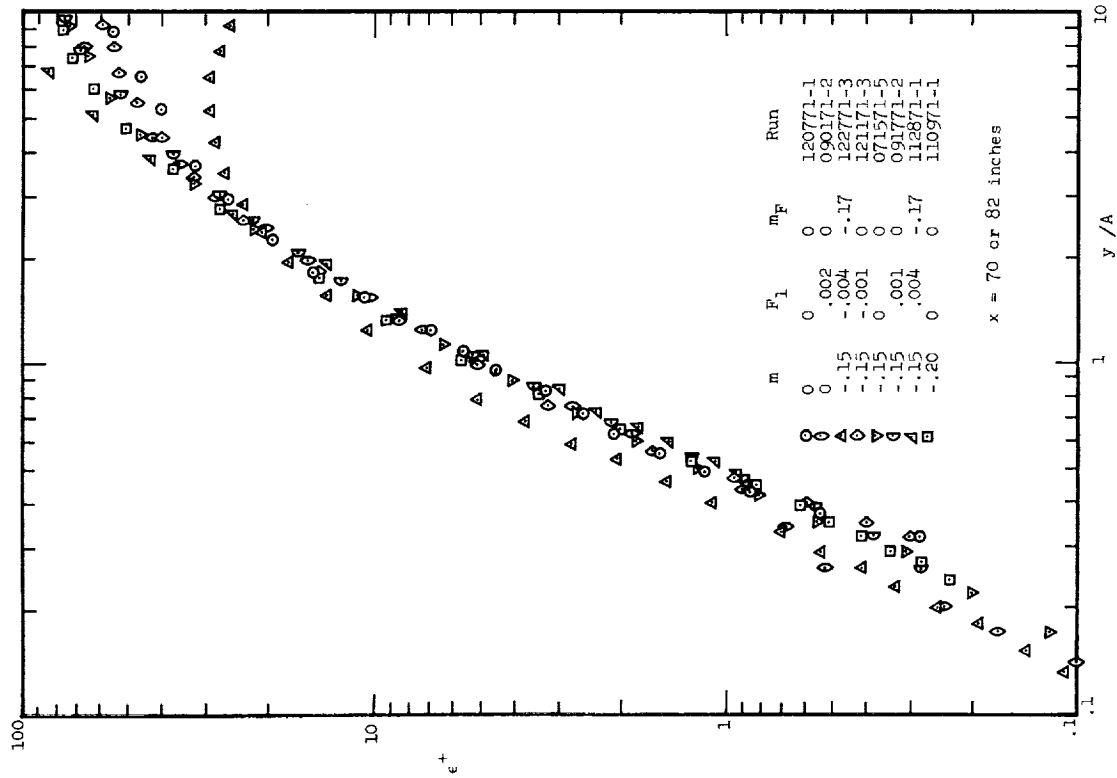


Fig. 6-18 Profiles of the non-dimensional eddy viscosity, $\epsilon^+ = \epsilon/v$

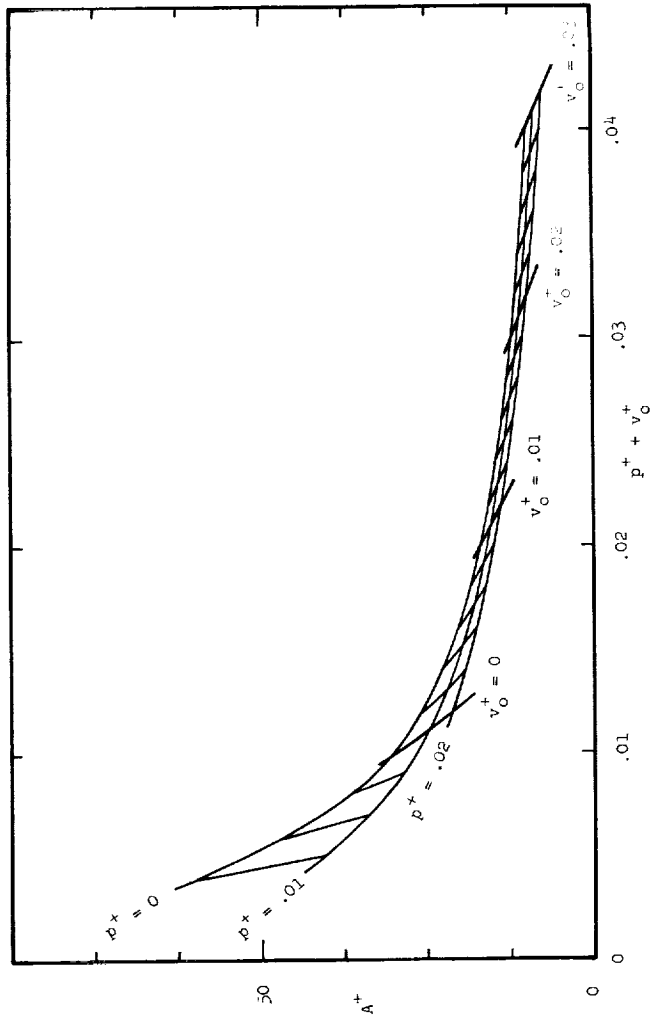


Fig. 6-19 Empirical correlation for A^+ from Eq. (6-20)

The RMS of the relative error of the fit is $\approx 6\%$. Figure 6-19 is a graphical display of the A^+ -correlation represented by Eq. (6-20).

6.4 Profiles of Turbulence Intensities

All the measured profiles of the mean square of the three components of the turbulent velocity fluctuations are presented in this section. The data are presented as profiles of the three non-dimensional intensities, $\overline{u'^2}/u_\infty^2$, $\overline{v'^2}/u_\infty^2$ and $\overline{w'^2}/u_\infty^2$, plotted versus the distance from the wall, y , in inches. All the profiles are measured at $x = 70$ inches.

Figure 6-20 is for the non-transpired, constant pressure boundary layer. Figures 6-21 to 6-32 are for the adverse pressure gradient corresponding to $m = -0.15$ and Figs. 6-33 and 6-34 are for the $m = -0.20$ pressure gradient.

The turbulence intensity profiles were measured in the hope that they may serve as reference for future theoretical work which might involve a "turbulence field closure". They are not important for the conclusions of the present investigation.

6.5 Shear Stress Profiles

Measured profiles of the Reynolds stress are plotted versus the distance from the wall for the adverse pressure gradient boundary layers. Figures 6-35 to 6-44 are for boundary layers corresponding to $m = -.15$ and Figs. 6-45 and 6-46 are for $m = -.20$ boundary layers.

Also shown in the figures is the shear stress distribution computed from the momentum equation, Eq. (5-11) and the Reynolds stress distribution computed by subtracting the viscous stress, $\tau_v = \mu \frac{du}{dy}$ from the total shear stress. The skin friction coefficients indicated in the figures

are obtained as the value of $c_f/2$ in Eq. (5-11) that will produce the measured Reynolds stress closest to the wall. See Section 4.1.2 for more details on the shear stress method.

The computed shear stress profiles shown in the figures of course correspond closely to the profiles tabulated in Chapter 9. However, because the friction coefficients used for the tabulated data in Chapter 9 is a curve fit of the measured, "raw" friction coefficients the plotted and the tabulated shear stress profiles may differ by a small constant amount, namely the difference between the raw values of $c_f/2$ (used in the figures) and the fitted values used for the tables.

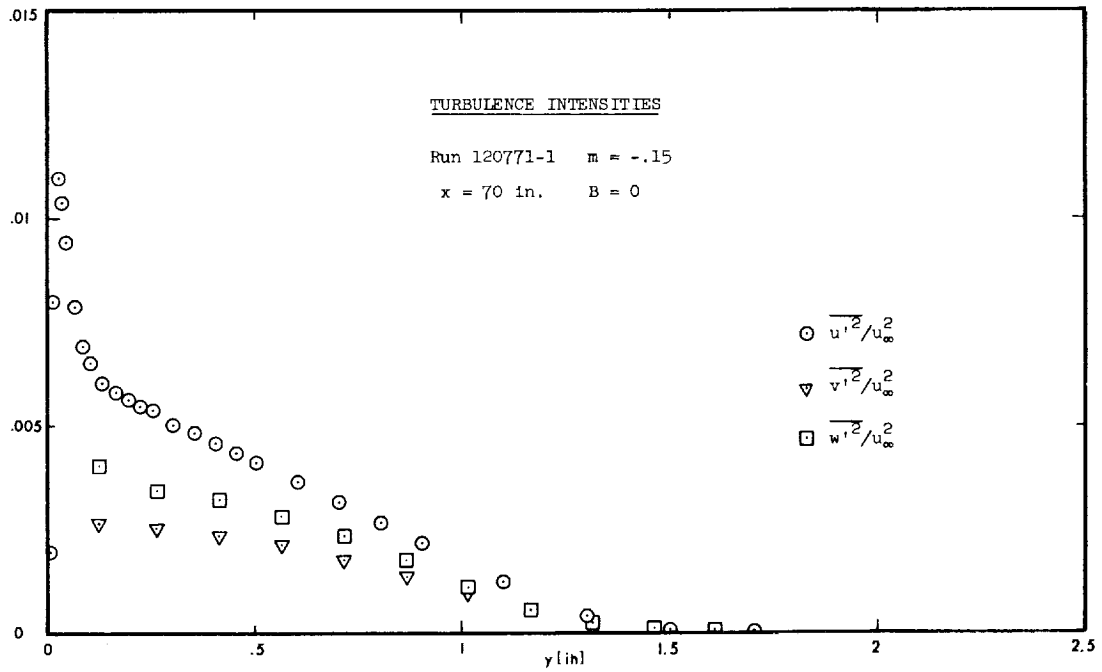


Fig. 6-20 Run 120771-1

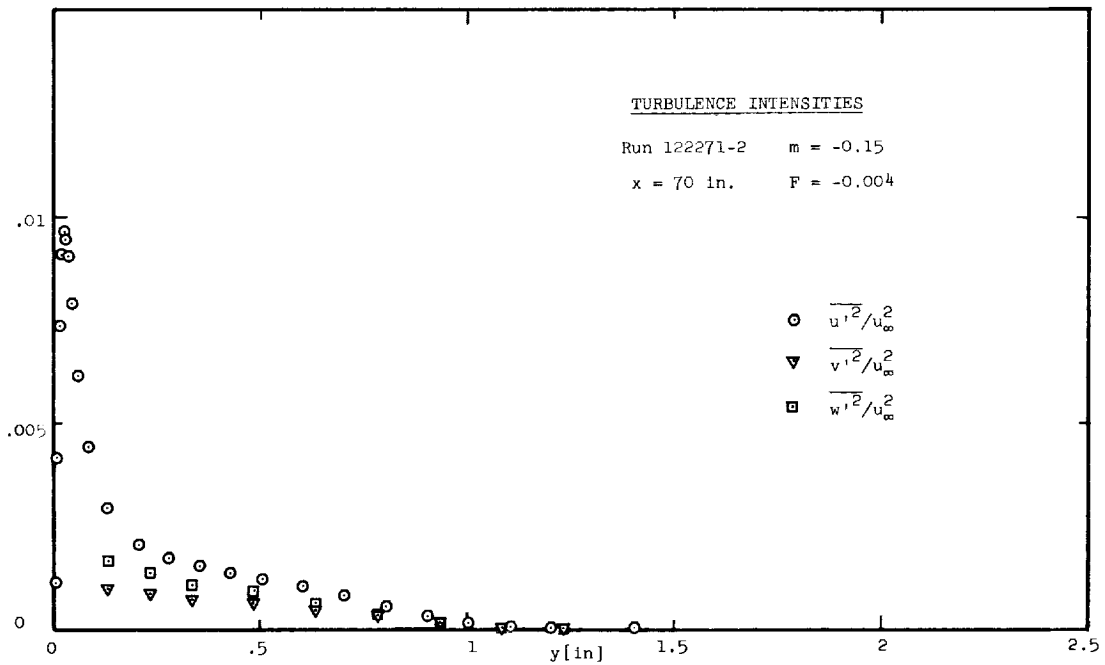


Fig. 6-21 Run 122271-2

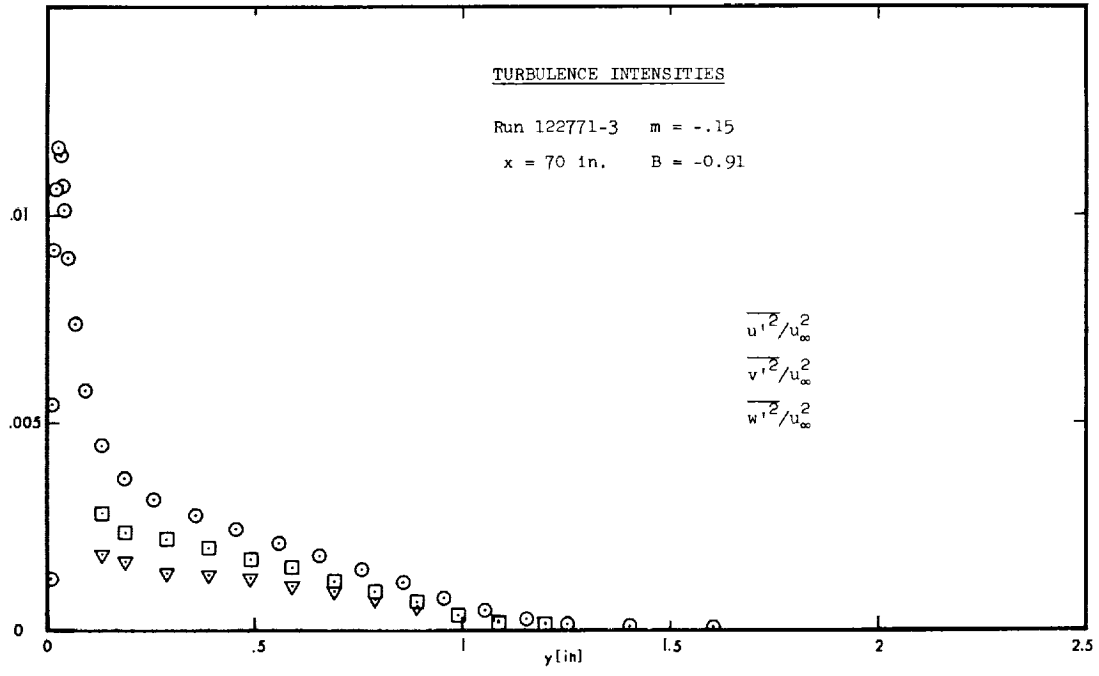


Fig. 6-22 Run 122771-3

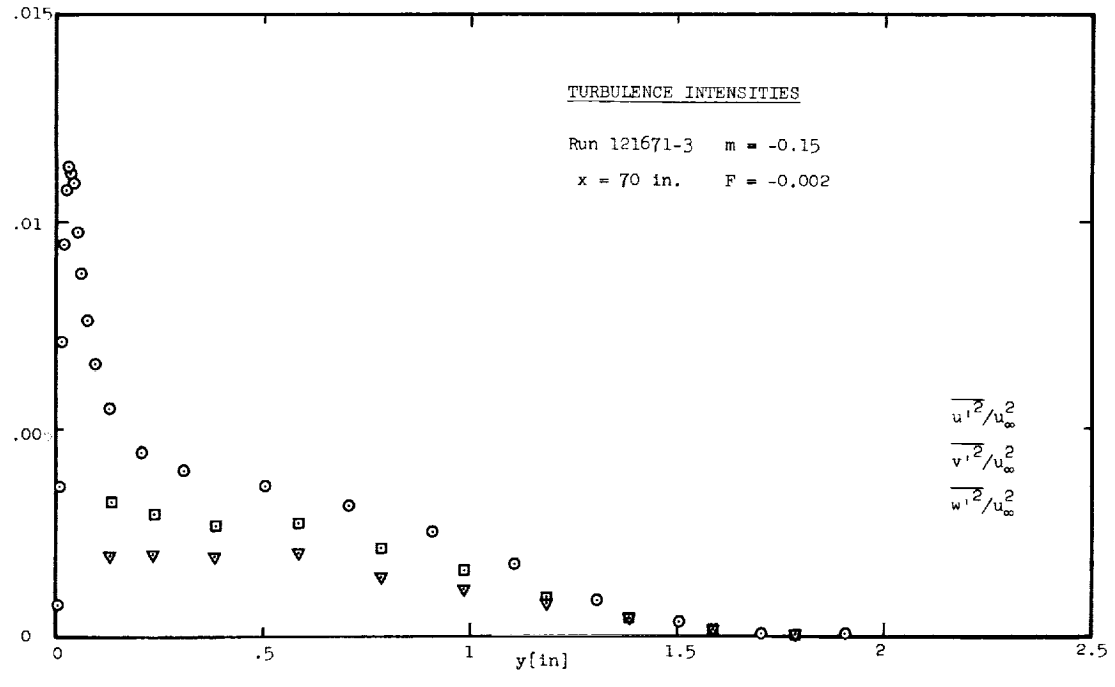


Fig. 6-23 Run 121671-3

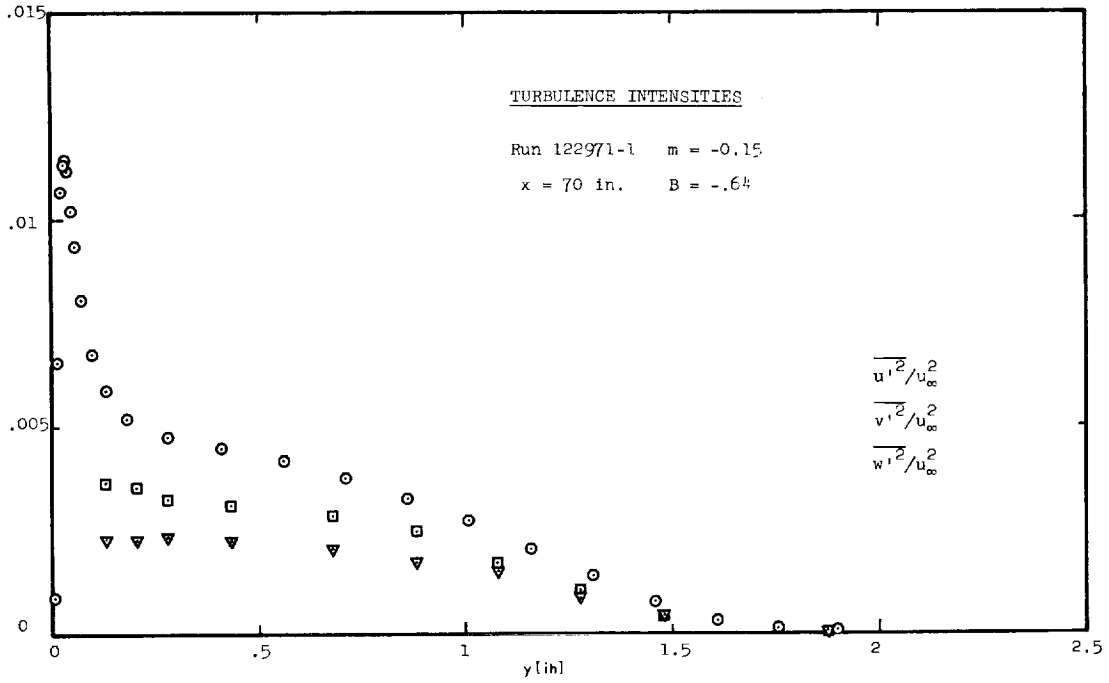


Fig. 6-24 Run 122971-1

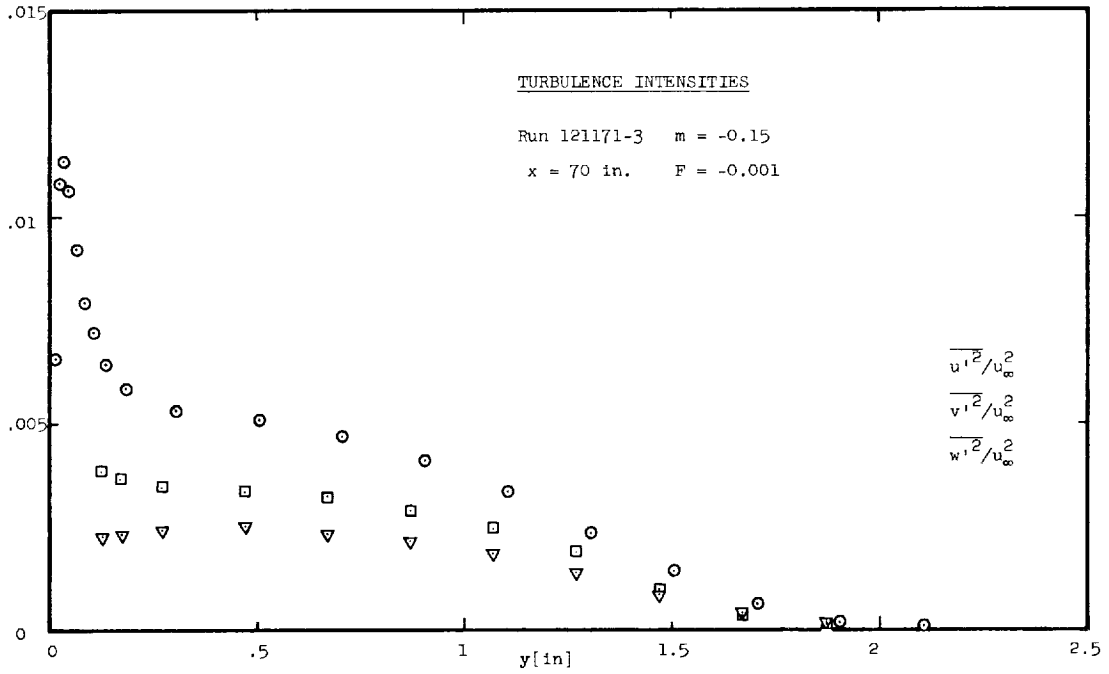


Fig. 6-25 Run 121171-3

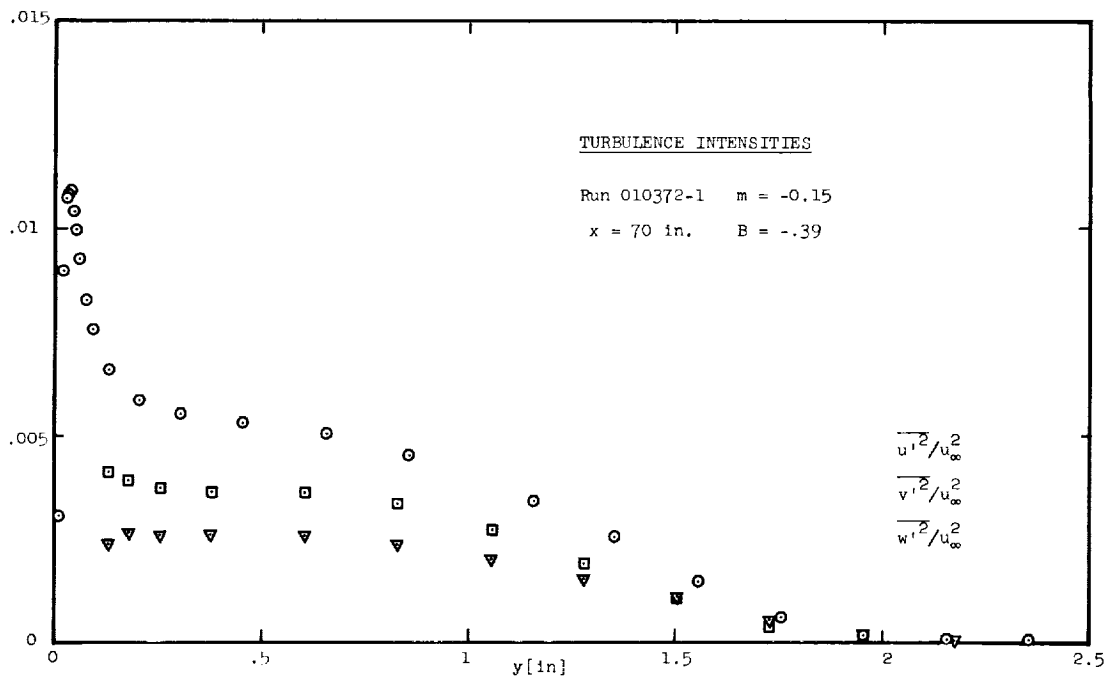


Fig. 6-26 Run 010372-1

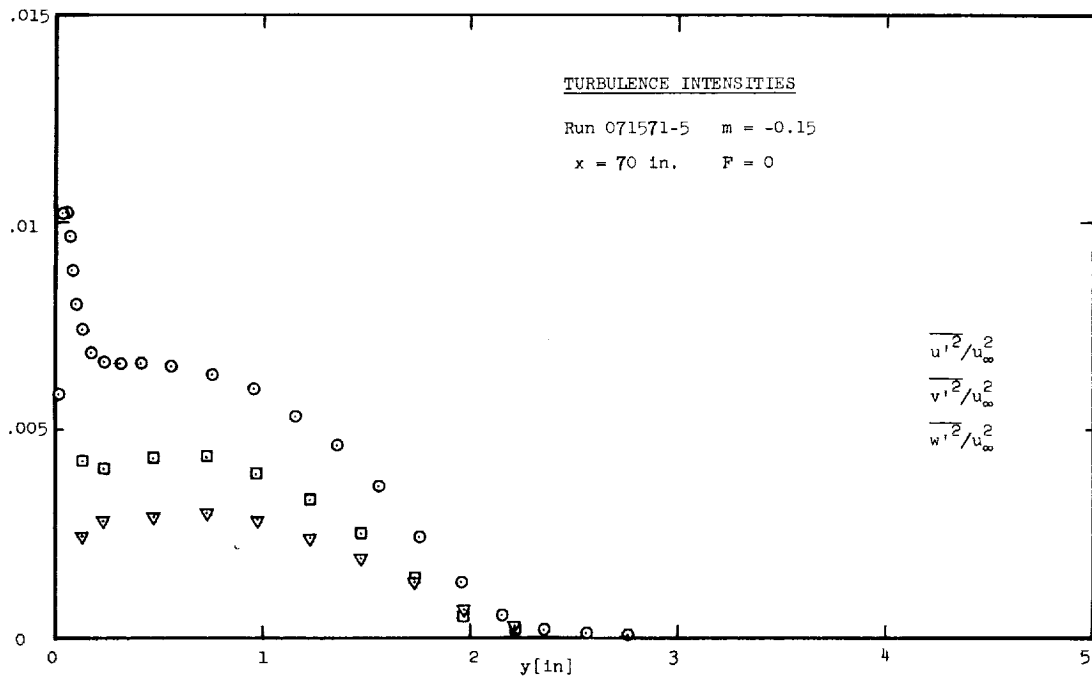


Fig. 6-27 Run 071571-5

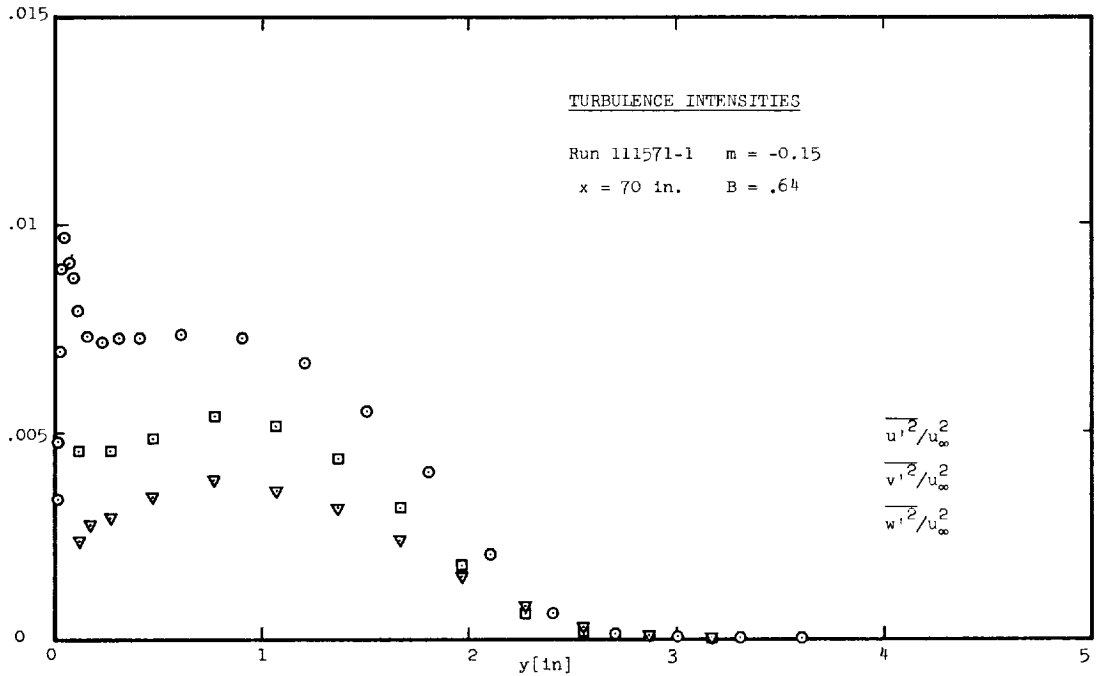


Fig. 6-28 Run 111571-1

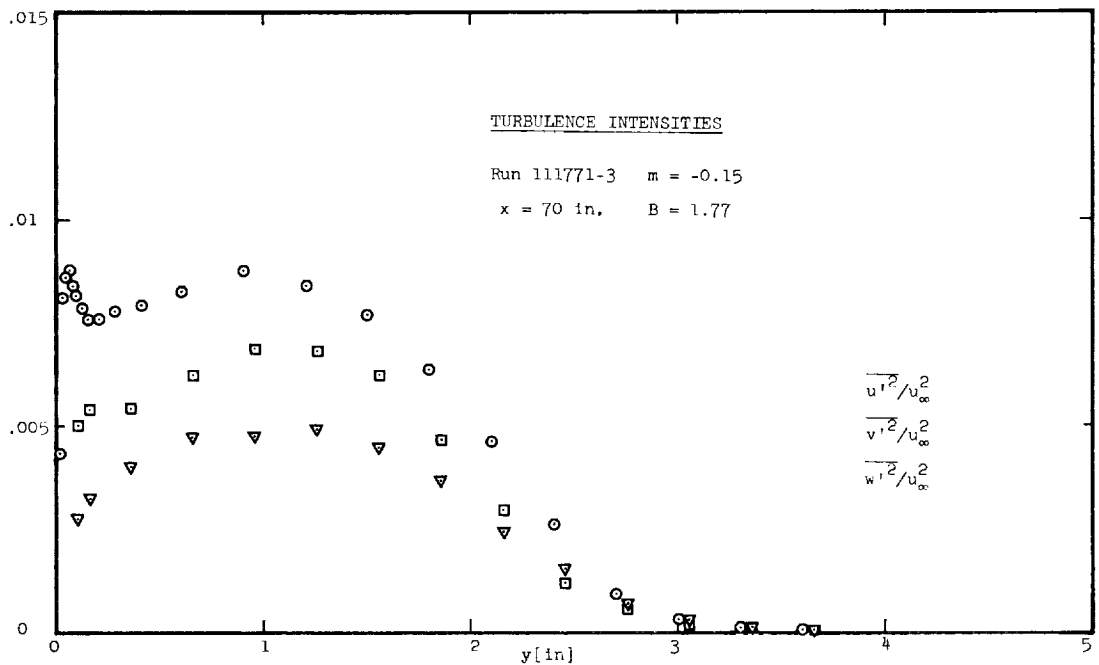


Fig. 6-29 Run 111771-3

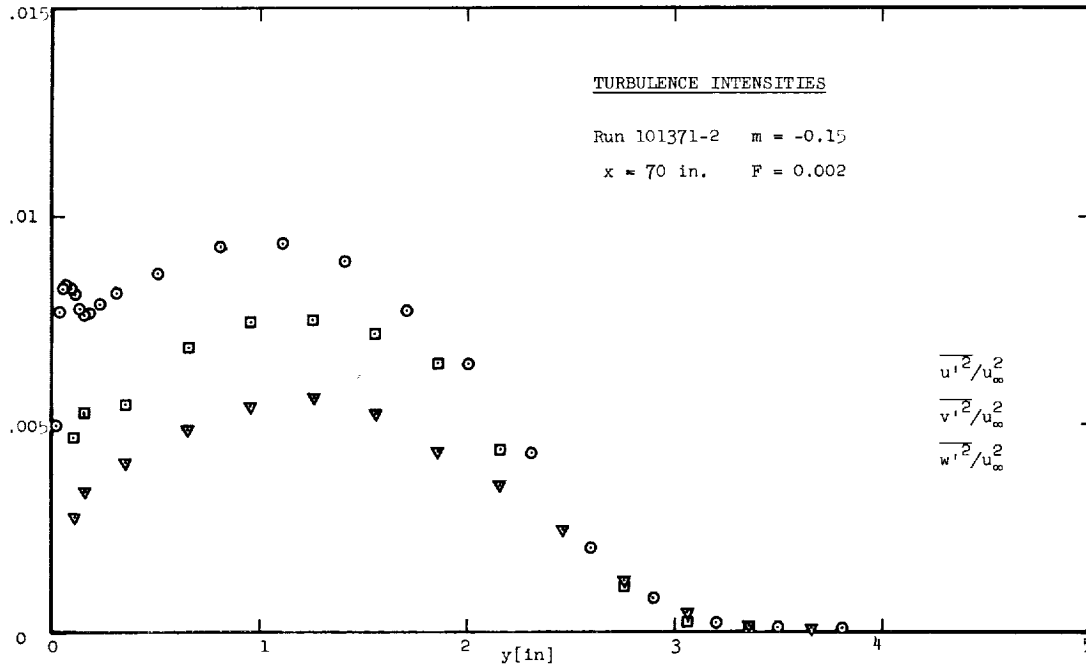


Fig. 6-30 Run 101371-2

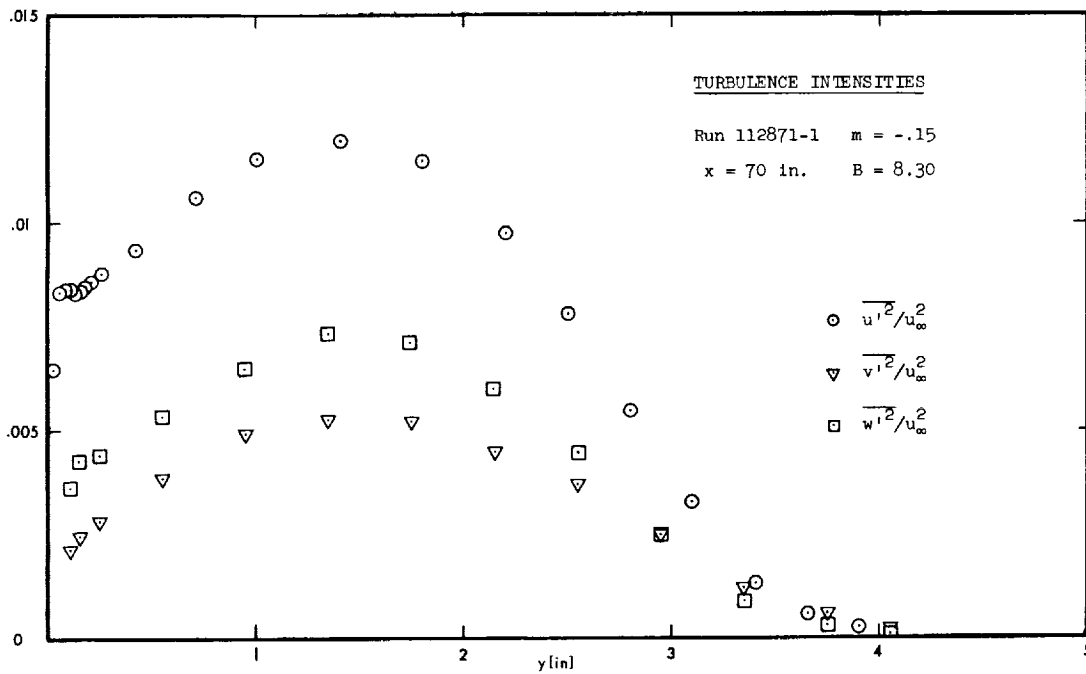


Fig. 6-31 Run 112871-1

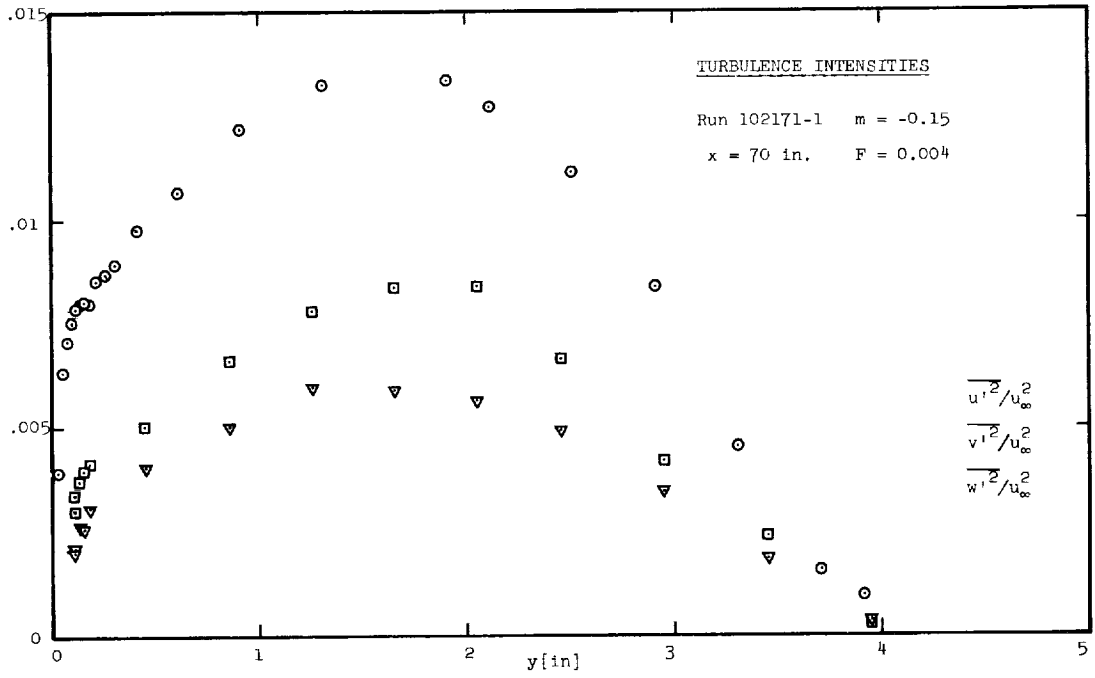


Fig. 6-32 Run 102171-1

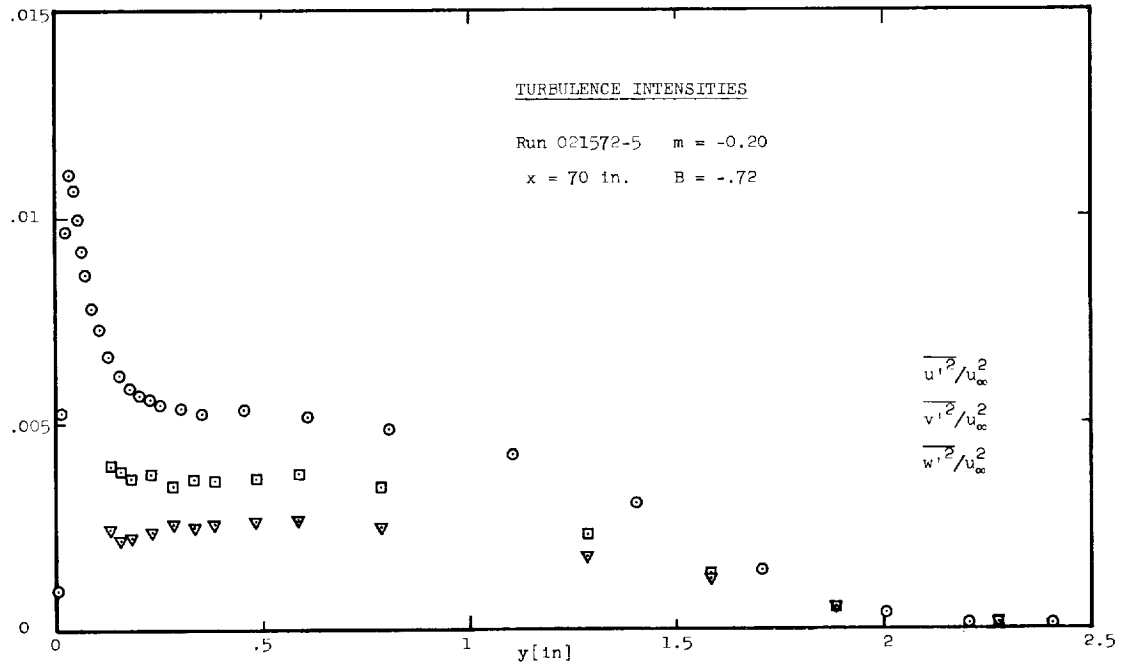


Fig. 6-33 Run 021572-5

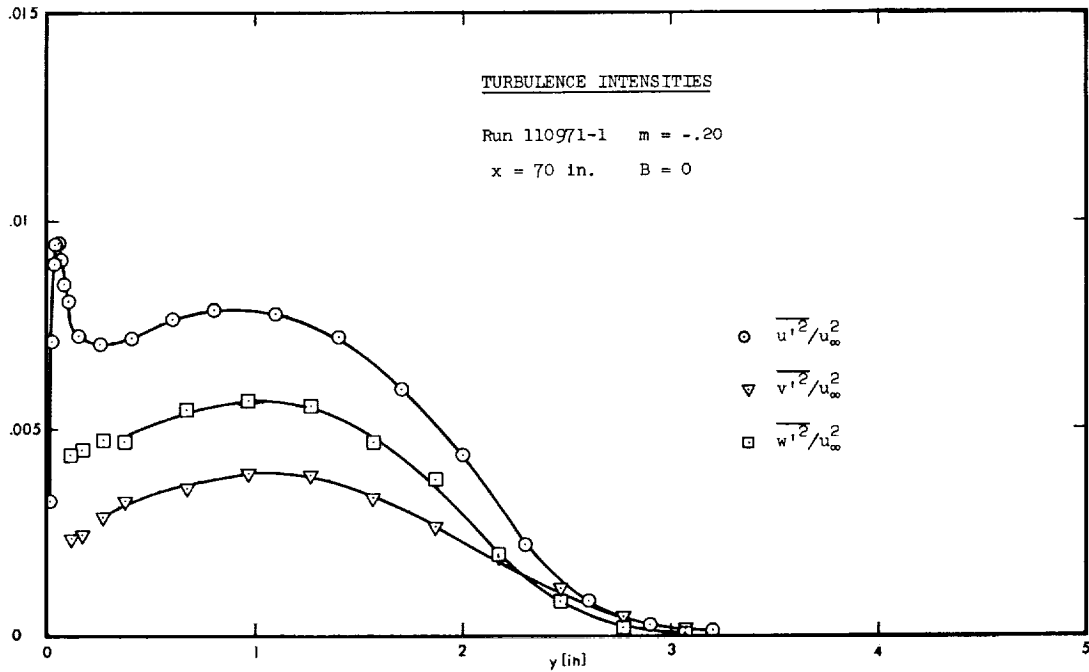


Fig. 6-34 Run 110971-1

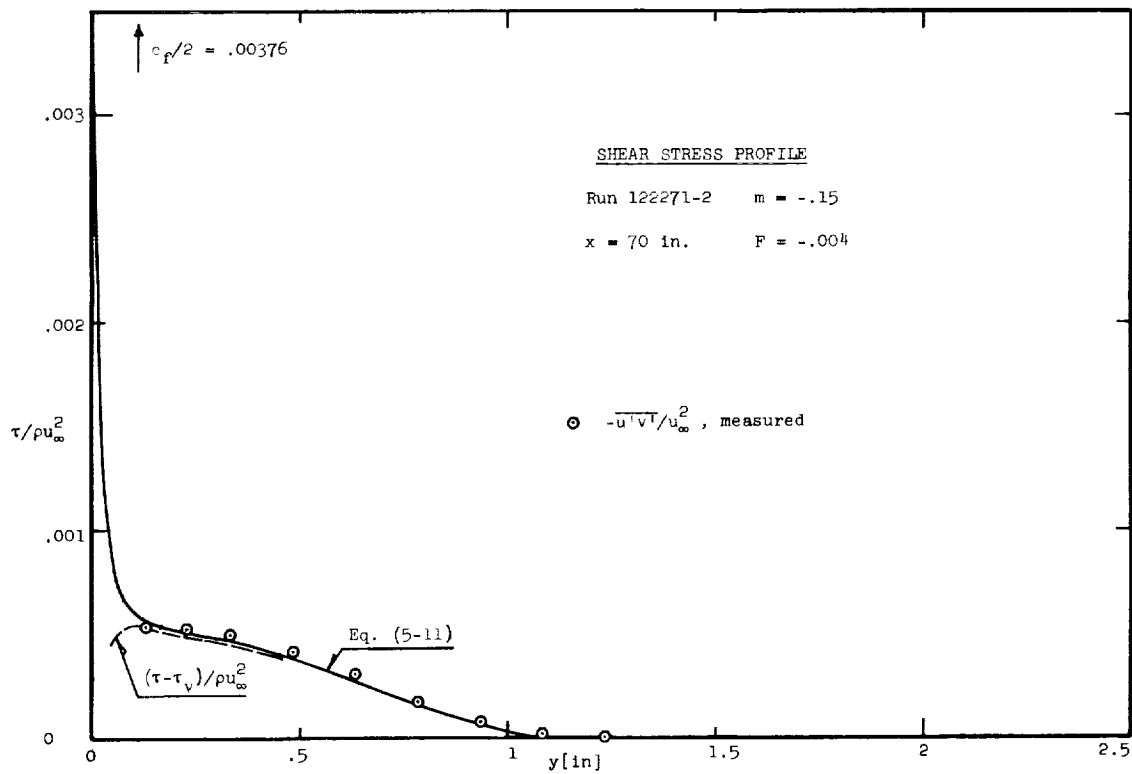


Fig. 6-35 Run 122271-2

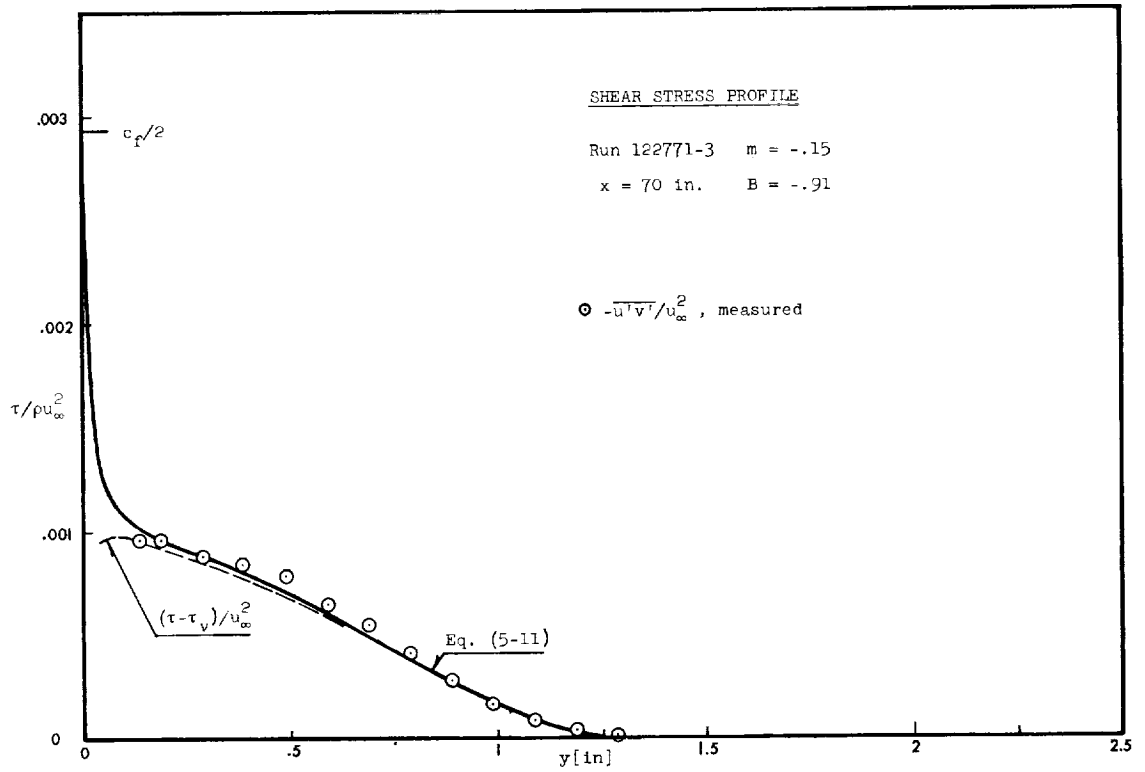


Fig. 6-36 Run 122771-3

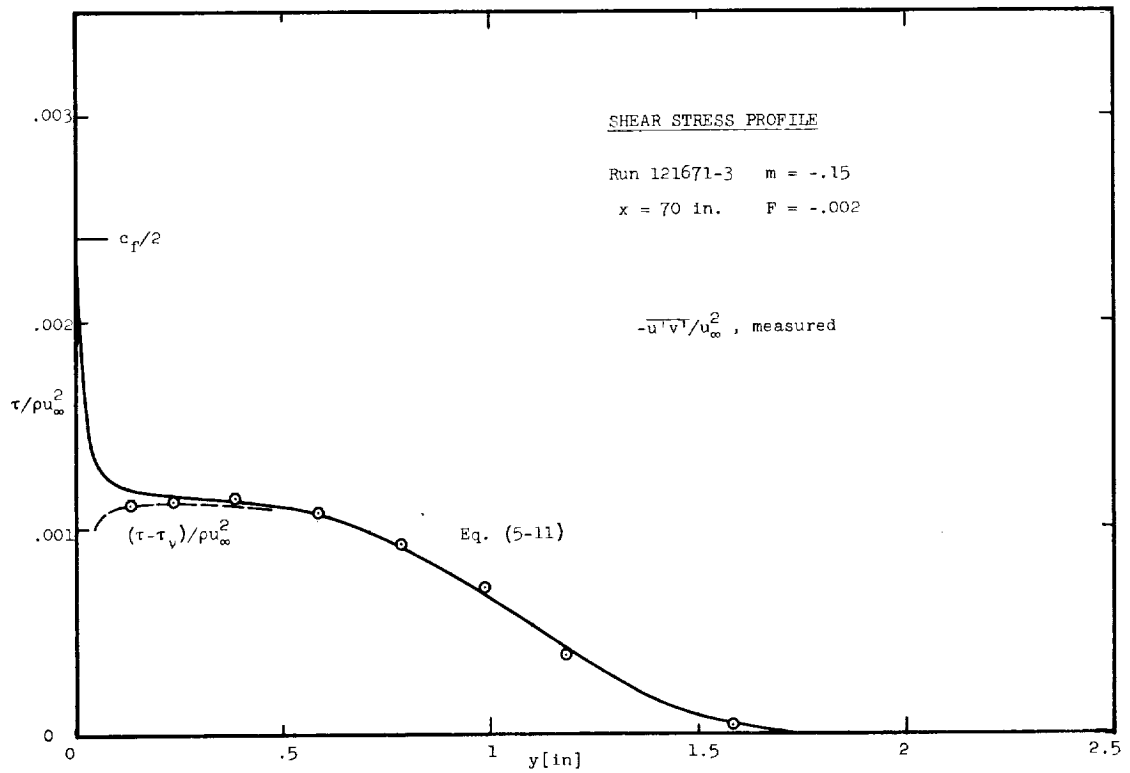


Fig. 6-37 Run 121671-3

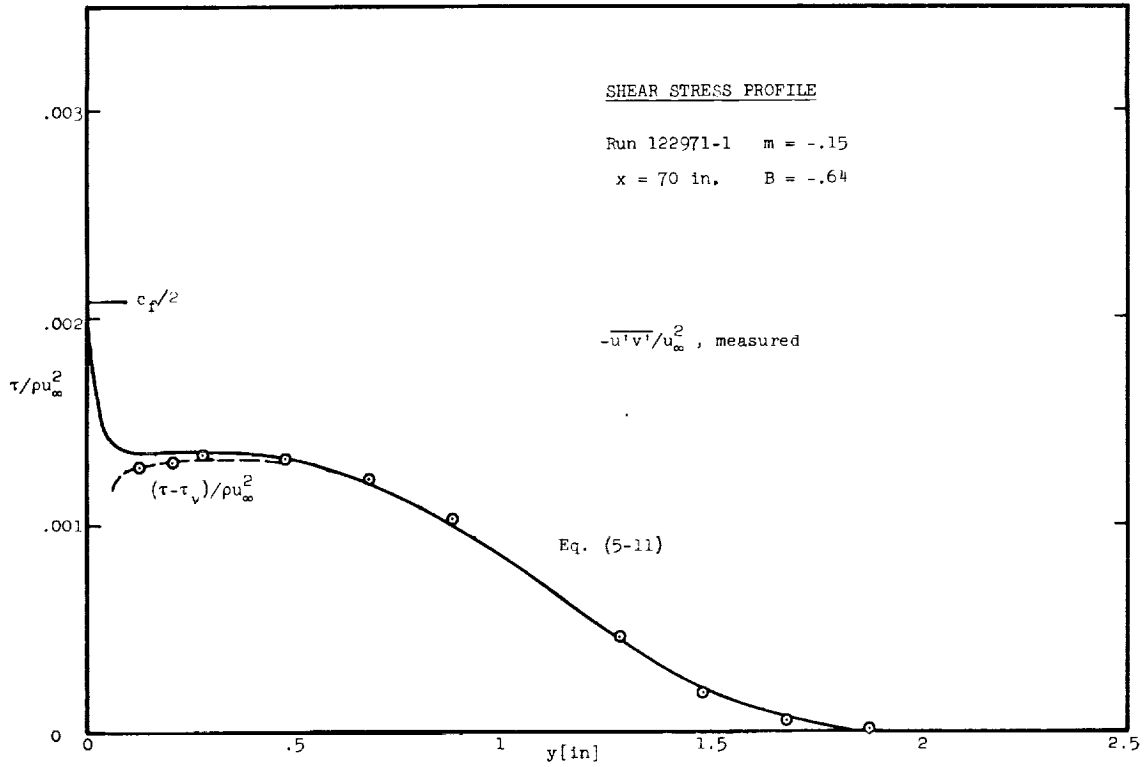


Fig. 6-38 Run 122971-1

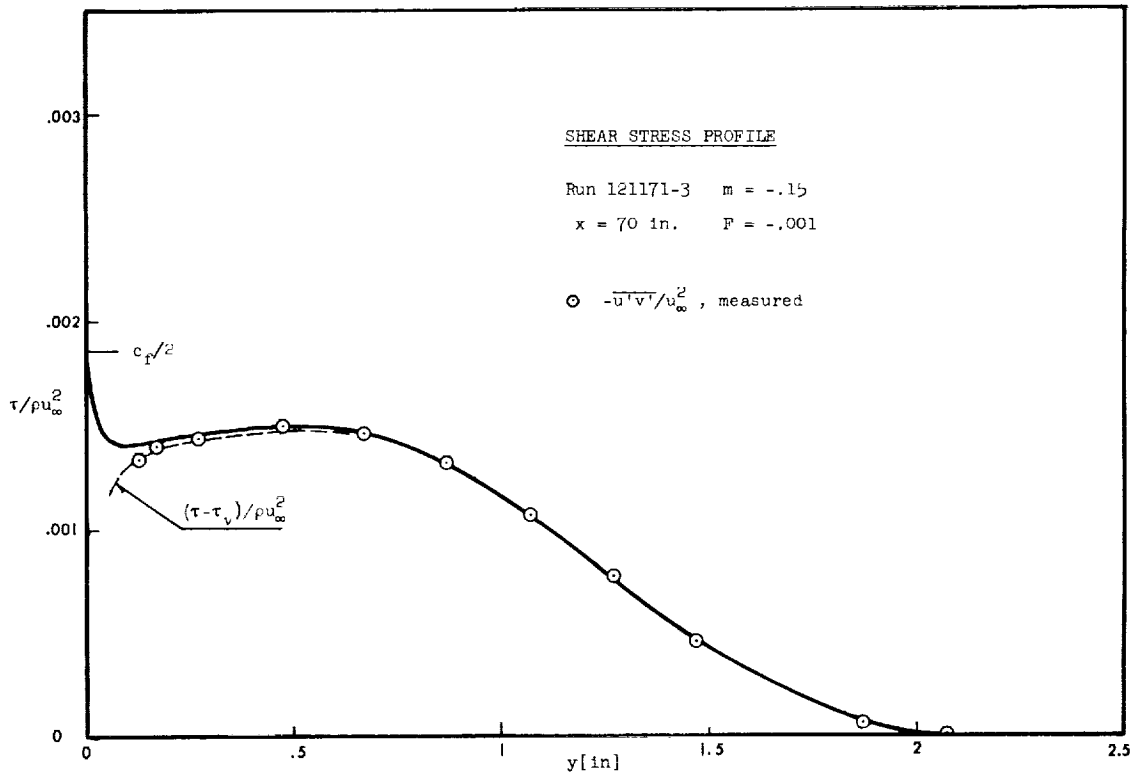


Fig. 6-39 Run 121171-3

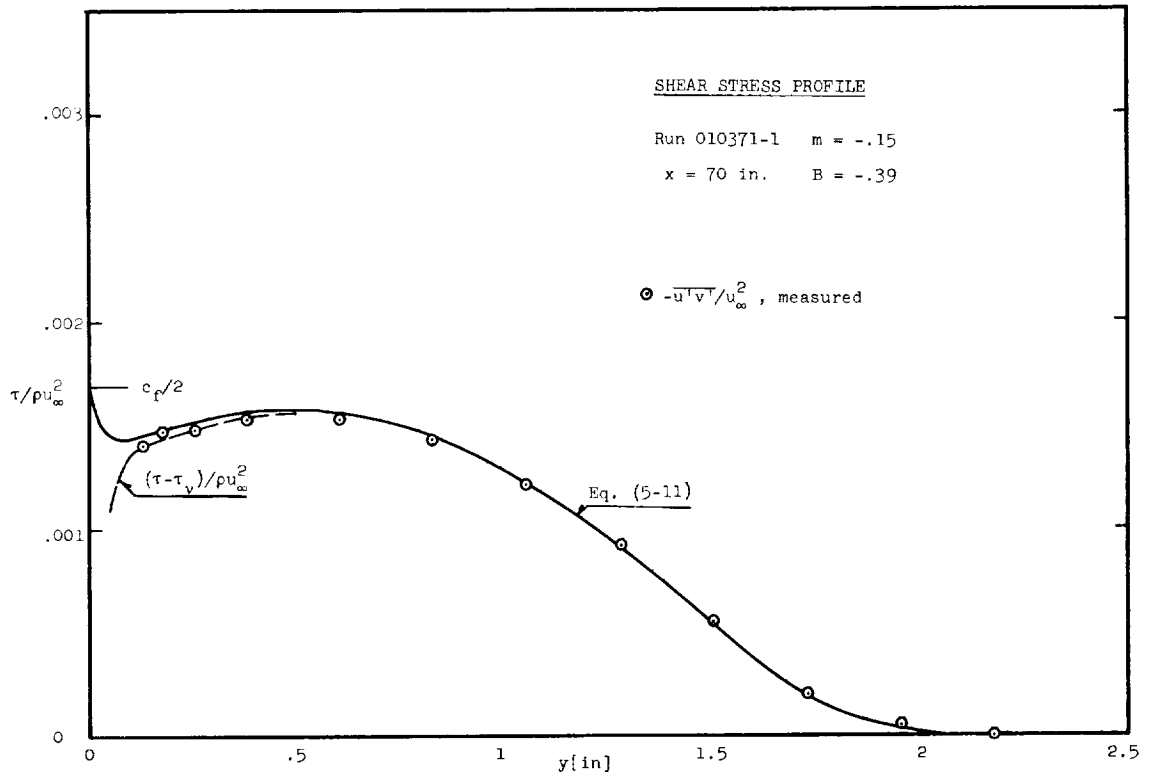


Fig. 6-40 Run 010371-1

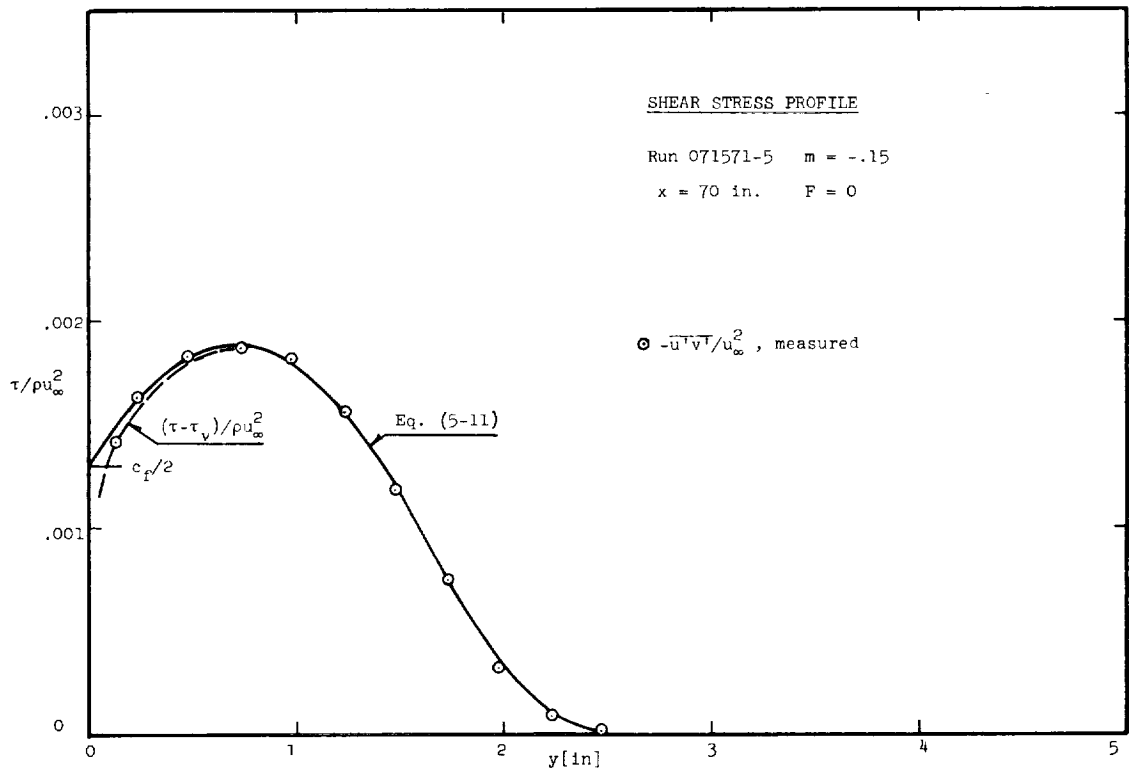


Fig. 6-41 Run 071571-5

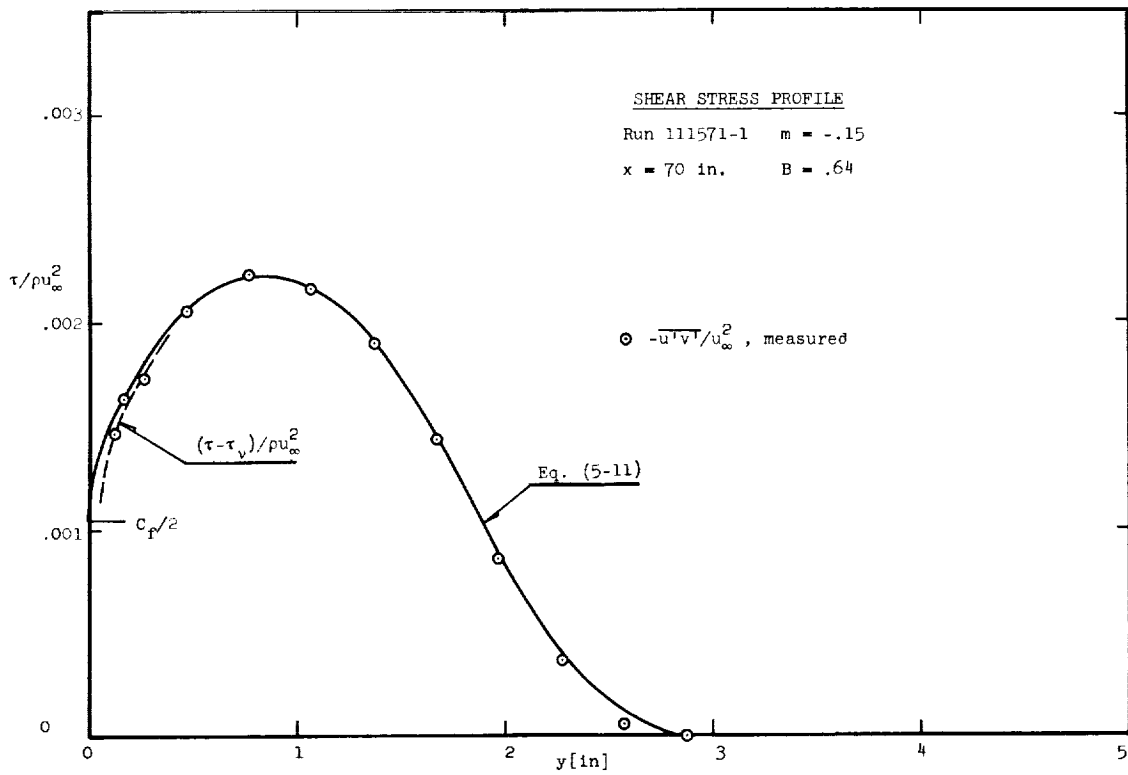


Fig. 6-42 Run 111571-1

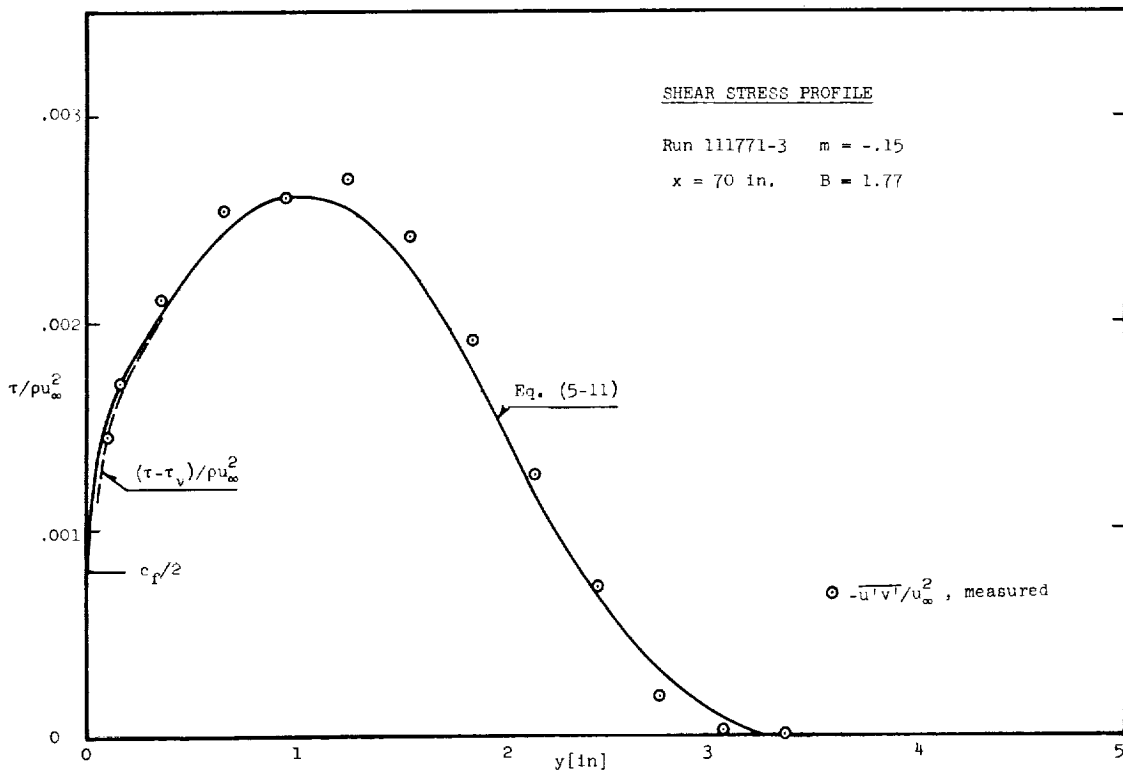


Fig. 6-43 Run 111771-3

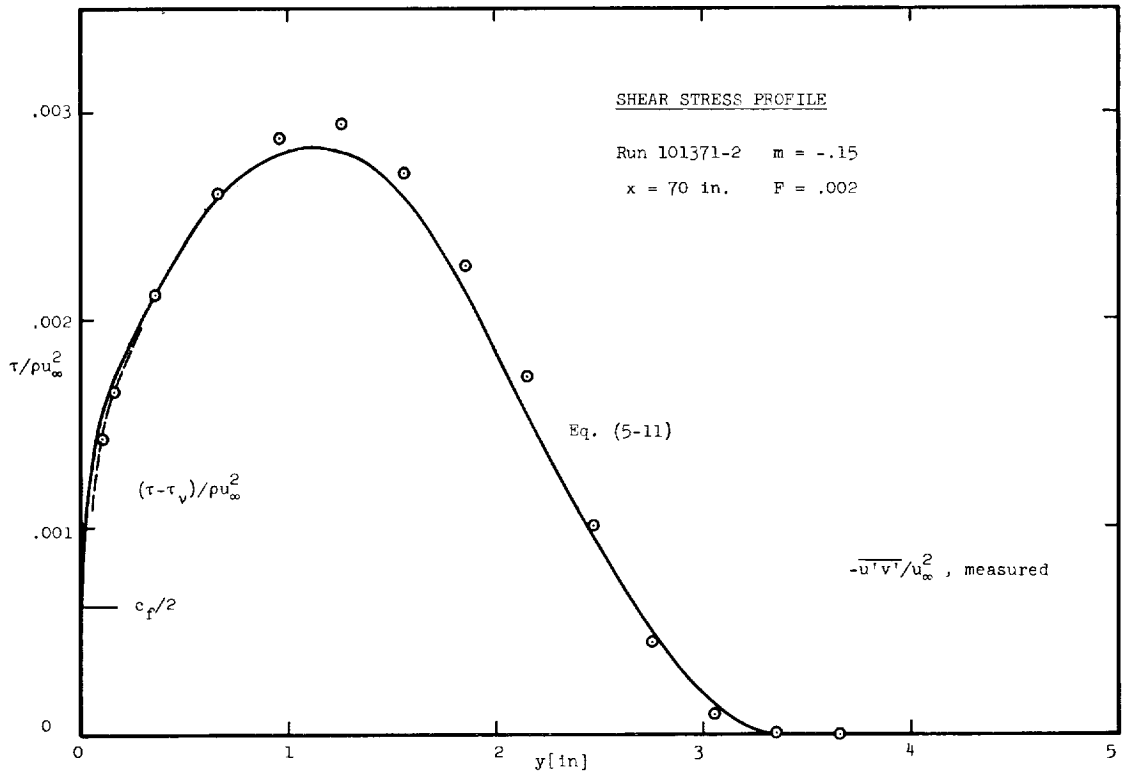


Fig. 6-44 Run 101371-2

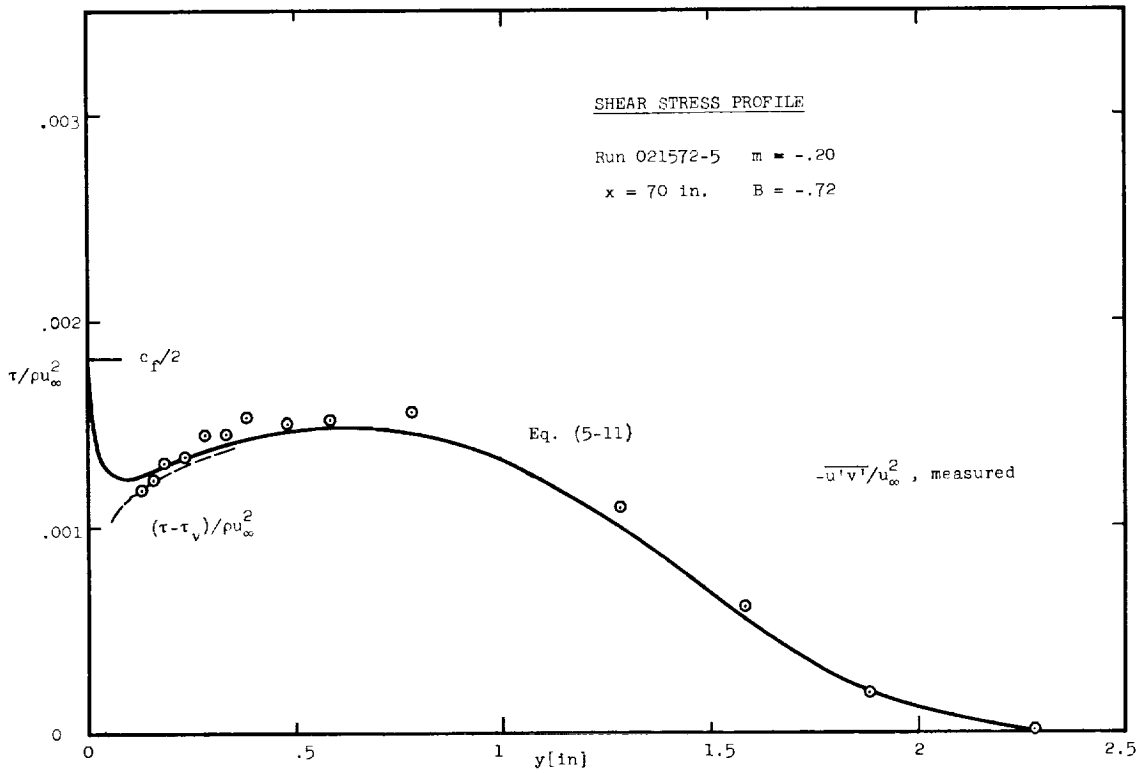


Fig. 6-45 Run 021572-5

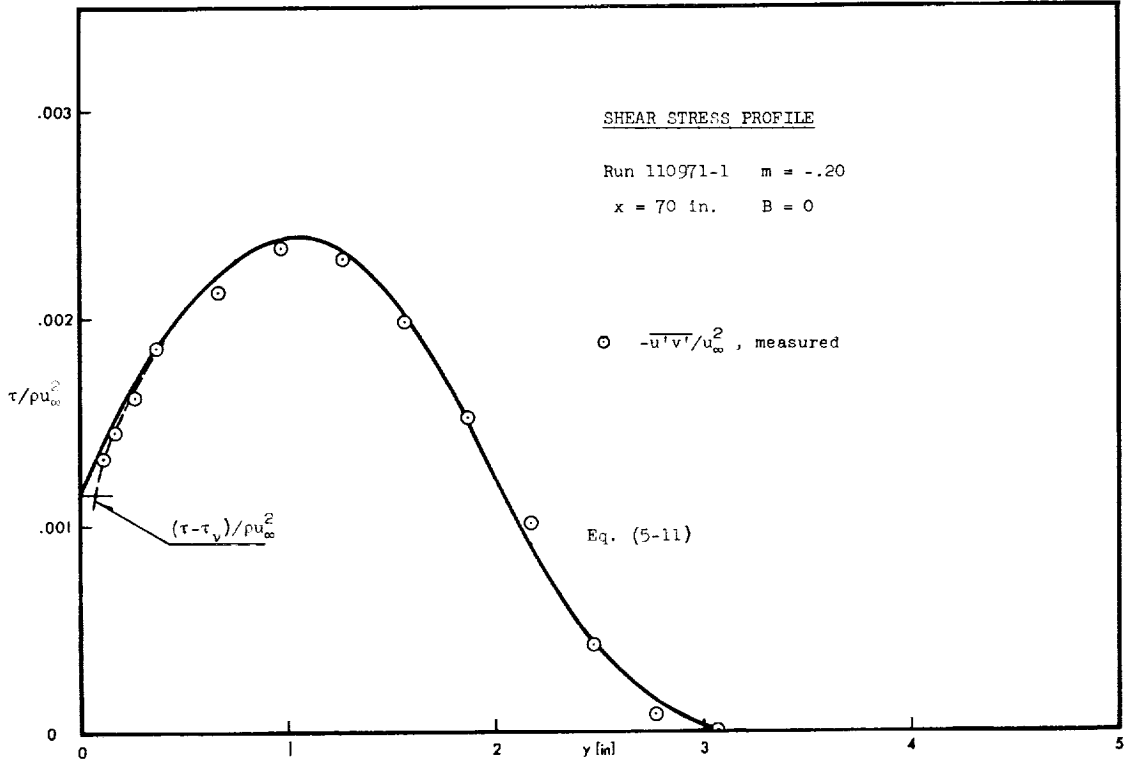


Fig. 6-46 Run 110971-1

CHAPTER 7

THEORETICAL RESULTS

7.1 Theories for A^+

As demonstrated in Chapter 6 the thickness of the wall region (expressed in the wall coordinate y^+) varies considerably with pressure gradient and transpiration rate. Adverse pressure gradients and blowing result in "thin" wall regions; favorable pressure gradients and suction have the opposite effect. In the van Driest model (Eq. (6-15)) for the mixing-length, A may be interpreted as a measure of the sublayer thickness. The measured variation of A^+ ($A^+ = Au_\tau/v$) with p^+ and v_o^+ is expressed by Eq. (6-20) which is a least squares fit of the experimental data. It would obviously be desirable to have a theory which would account for the functional dependence of A^+ upon p^+ and v_o^+ . Attempts in this direction have been reported by several authors; some of the ideas will be discussed below. One of the proposed theories, the idea of a critical "Reynolds number of turbulence" defining the thickness of the wall region is supported by the present data.

Patankar and Spalding [19] modified van Driest's mixing-length model to read:

$$l = ky \left[1 - \exp \left(- \frac{y^+}{A_o^+} \sqrt{\tau^+} \right) \right] , \quad (7-1)$$

where A_o^+ is a constant. Note that in this formulation the "effective" van Driest length scale, $A^+ = A_o^+ / \sqrt{\tau^+}$, is a function of y^+ . The behavior of the non-dimensional shear stress, τ^+ , may be expressed by the Couette-flow approximation:

$$\tau^+ = 1 + p^+ y^+ + v_o^+ u^+ \quad (7-2)$$

From this it can be seen that the factor, $\sqrt{\tau^+}$, in the modified van Driest model, Eq. (7-1), has the correct qualitative influence; it results, for example, in lower values of the effective local length scale for adverse pressure gradients and blowing (i.e. $p^+ > 0$ and $v_o^+ > 0$). However, although Eq. (7-1) appears to be adequate for flows with weak transpiration rates and pressure gradients, it is not satisfactory for larger values of p^+ and v_o^+ even if the correct value of τ^+ (rather than the Couette-approximation, Eq. (7-2)) is used.

Cebeci [20] improved the performance of the model by evaluating τ^+ in Eq. (7-1) at $y^+ = 11.8$. The result is that the van Driest length scale becomes:

$$A^+ = A_o^+ / \sqrt{\tau^+(11.8)} \quad (7-3)$$

However, in evaluating the shear stress, τ^+ , Cebeci not only used the Couette-flow approximation Eq. (7-2), but also assumed that the shear stress has no Reynolds stress contribution all the way out to $y^+ = 11.8$. The result is that the value of τ^+ used by Cebeci in Eq. (7.3) is not the actual shear stress at $y^+ = 11.8$, but rather a function of p^+ and v_o^+ that happens to account for the behavior of A^+ . This fact is further emphasized by the arbitrary value of $y^+ = 11.8$.

Launder and Jones [21] proposed that at the "edge" of the sublayer (which was taken to be at $y^+ = A^+$) a Reynolds number of turbulence,

$$Re_T = \frac{l \sqrt{-\overline{u'v'}}}{\nu} \quad (l \text{ is the mixing-length}) \quad (7-4)$$

takes on a constant, characteristic value. (Note that since by definition, $-\overline{u'v'} = \epsilon \frac{du}{dy}$ and $l = \sqrt{\epsilon / \frac{du}{dy}}$ then

$\epsilon^+ = \frac{\epsilon}{\nu} = Re_{\tau}$). This assumption seems to have some physical basis and a paper by Bradshaw [22] had indeed suggested that the Reynolds number of turbulence, Re_{τ} , remains smaller than about 12 everywhere in a turbulent boundary layer undergoing laminarization. If laminarization is interpreted as the growth of the sublayer until it penetrates to the edge of the boundary layer, then the idea of a characteristic value of Re_{τ} as defining the edge of the sublayer seems reasonable.

7.2 Sublayer Thickness and Characteristic Shear Stress

The derivative du/dy may be eliminated from the defining equations (Eqs. (6-1) and (6-2)) for the eddy viscosity, ϵ , and the mixing length, l . Introducing $\epsilon^+ = \epsilon/\nu$ and $\tau^+ = \tau/\tau_0$ the result may be expressed as

$$y^+ \sqrt{\tau^+} = \sqrt{\epsilon^+(1 + \epsilon^+)}/(\frac{l}{y}) \quad (7-5)$$

Now Figs. 6-17 and 6-18 indicate that both ϵ^+ and l/y quite adequately may be described as unique functions of $y/A = y^+/A^+$ over a range in the inner region. It is therefore to be expected that $y^+ \sqrt{\tau^+}$, the left hand side of Eq. (7-5), similarly depends upon y^+/A^+ in a range.

For the non-transpired constant pressure boundary layer $\tau^+ \approx 1$ all the way from the wall and out through the logarithmic region of the velocity profile. The right hand side of Eq. (7-5) must therefore be equal to $y^+ A_0^+/A^+$ and the equation may be written

$$\sqrt{\tau^+} \approx A_0^+/A^+ \quad (7-6)$$

The validity of this equation may be checked directly by plotting experimental profiles $\frac{A_0^+}{A^+} \sqrt{\tau^+}$ versus $y^+ A_0^+/A^+$.

This has been done in Fig. 7-1 for a wide range of boundary conditions. Examination of this graph reveals that there is a range away from the wall where Eq. (7-6) is an adequate description of the shear stress behavior. This range corresponds to the logarithmic region of the mean velocity profiles.

Figure 7-1 is highly suggestive of the idea that Eq. (7-6) might be exactly true at a certain characteristic distance, y_c , from the wall. It is thus suggested that

$$\sqrt{\tau_c^+} = A_0^+ / A^+, \quad (7-7)$$

where the "characteristic shear stress", τ_c , obtains at the "characteristic point", $y_c = \alpha A$ ($\alpha \approx 3$). It is difficult to give a precise value of the constant, α , because Eq. (7-6) is adequate for a wide range of y^+ / A^+ . (By the same token a precise value of α is not needed because $\tau \approx \tau_c$ in a range around $y = \alpha A$).

If the "characteristic velocity scale", $u_c = \sqrt{\tau_c / \rho}$, is introduced Eq. (7-7) may be written

$$\frac{Au_c}{\nu} = A_0^+ \quad (7-8)$$

Equations (7-7) and (7-8) are equivalent formulations of a relationship between the measure of the sublayer thickness, A , and the characteristic shear stress, τ_c . Equation (7-8) in particular shows that ν / u_c is a measure of the sublayer thickness entirely equivalent with and proportional to A .

The definitions of the eddy viscosity, ϵ , and the mixing length, ℓ , imply that

$$\epsilon^+ = \frac{1}{2} + \sqrt{\frac{1}{4} + \ell^{+2} \tau^+}, \quad \text{where } \ell^+ = \ell u_\tau / \nu \quad (7-9)$$

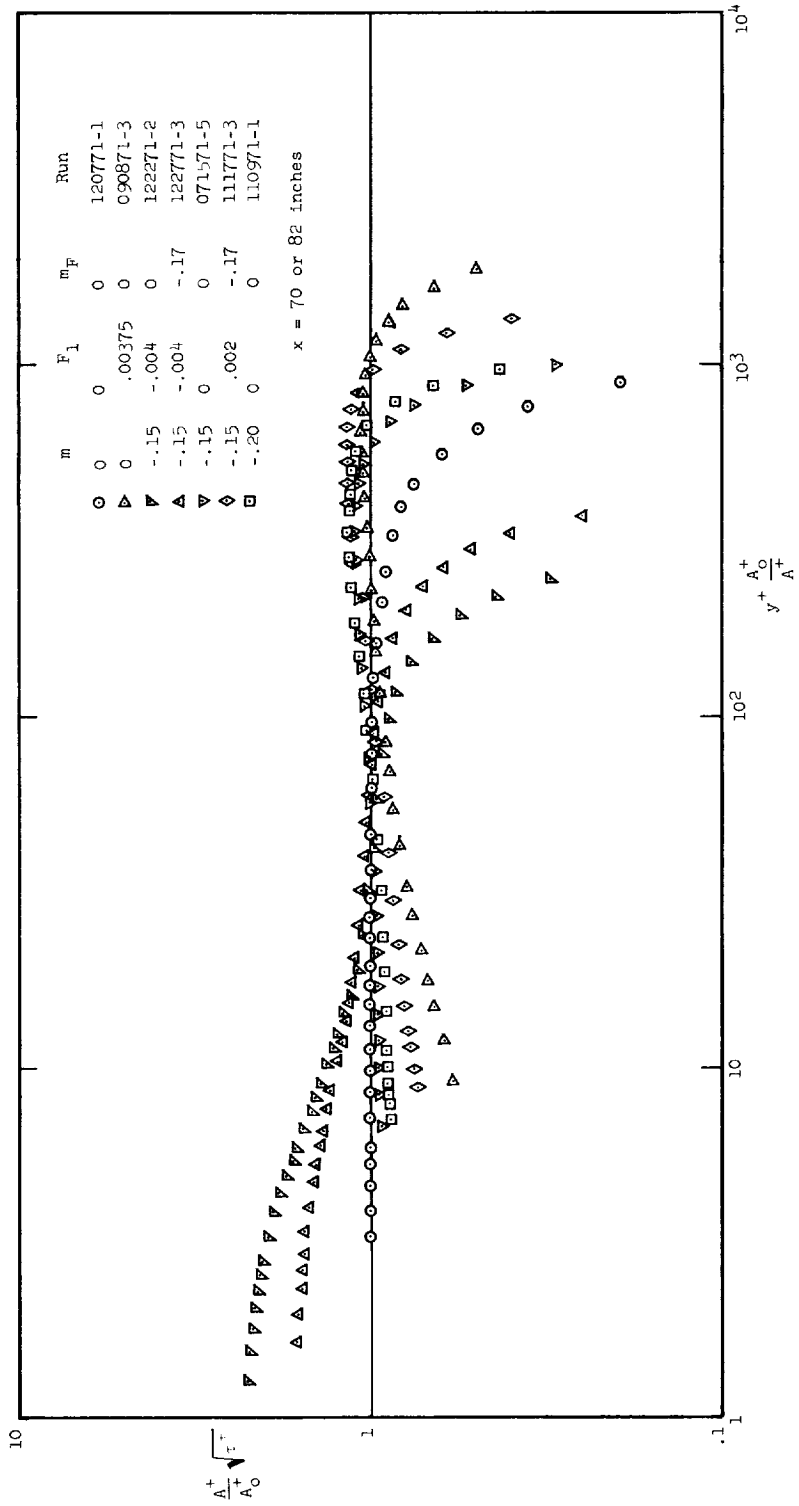


Fig. 7-1 $\frac{A^+}{A^+ + A_0} \sqrt{\tau^+}$ versus $y^+ \frac{A_0}{A^+ + A_0}$ for selected boundary conditions

The characteristic point, $y_c = 3A$, is located in the logarithmic region where, as noted, $l = 0.4ly$. The value of the Reynolds number of turbulence, $Re_T = l \sqrt{-u'v'}/\nu = \epsilon^+$, may therefore be obtained at the characteristic point by inserting $l_c^+ = 0.4ly_c^+$, $y_c^+ = 3A^+$ and the result from Eq. (7-7) into Eq. (7-9). The result is that $\epsilon_c^+ = 29$ i.e. a constant. In other words the Reynolds number of turbulence has a "characteristic" value (independent of the pressure gradient and/or transpiration rate) at the characteristic point, y_c .

A turbulent boundary layer prediction program that solves the differential boundary layer equations may use either Eq. (7-8) or the fact that $\epsilon^+(3A) = \epsilon_c^+ = 29$ to obtain A , and thereby provide "closure" in the inner region.

Predictions of some of the present experimental boundary layers with closure provided by Eq. (7-8) are presented in Section 7.4.

The measure, A , of the sublayer thickness is of course the length scale in the van Driest model

$$l = ky[1 - \exp(-\frac{y}{A})] \quad . \quad (7-10)$$

This reference to a particular mixing-length model may at first seem to limit the generality of Eqs. (7-7) and (7-8). However, experience with two alternative models has shown that this is not the case. The two mixing-length models are:

1. The two-layer model:

$$l = \begin{cases} 0 & \text{for } y \leq C \\ ky & \text{for } y > C \end{cases} \quad (7-11)$$

2. The Evans [23] model:

$$l = \begin{cases} ky^2/B & y \leq B \\ ky & y > B \end{cases} \quad (7-12)$$

For these two models C and B are measures of the sub-layer thickness equivalent to A in the van Driest model Eq. (7-10). If C_0 and B_0 represent the case of a non-transpired, constant pressure boundary layer it is found that,

$$\frac{A}{A_0} = \frac{C}{C_0} = \frac{B}{B_0} \quad (7-13)$$

In other words the ratio $A^+/A_0^+ = A/A_0$ seems to be a true measure of the relative sublayer thickness because its value is independent of any particular assumption about the mixing length behavior in the inner region. Since Eqs. (7-7) and (7-8) only involve the ratio, A^+/A_0^+ they may be thought of as universal and not dependent upon the use of the van Driest model.

7.3 Generalized Law of the Wall

In Chapter 6 it was demonstrated that the classical law of the wall

$$\frac{u}{u_\tau} = \frac{1}{k} \ln \frac{yu_\tau}{\nu} + c \quad (k = 0.41 \text{ and } c = 5.0) \quad (7-14)$$

fails for boundary layers with transpiration. It continues to hold, at least approximately, even in rather strong adverse pressure gradients whereas it rapidly becomes inapplicable for favorable pressure gradient boundary layers. (For evidence of the latter statement see for example Loyd [4]).

Several authors have proposed forms of the law of the wall applicable for constant pressure flows with transpiration. Coles [24] gives a critical survey of these laws and also proposes a new generalized law of the wall.

All the proposed laws of the wall (except Coles') rely on an integration of the Couette approximation Eq. (7-2) for the shear stress using the Prandtl assumption, $l = ky$, for the mixing length behavior in the logarithmic region. The difference between them is essentially the choice of the integration constant. However, it cannot easily be extended to boundary layers with strong adverse pressure gradients because the Couette approximation in this case becomes too inaccurate in the logarithmic region. Simpson's law of the wall, which is especially successful in fitting most available data, becomes inapplicable for very strong suction or blowing rates.

Coles' new law of the wall is based on a Millikan [25] type argument which leads to the conclusion that a logarithmic portion of the mean velocity profile must exist if both wall region similarity and outer region similarity (in the form of a defect law) exists. The difference between Coles' new law of the wall and the classical law, Eq. (7-14), is that u and y are normalized by u_0 and $y_0 = \nu u_0 / u_\tau^2$ respectively rather than on u_τ and ν / u_τ . u_0 is a shear velocity based on the average shear stress for a "laminar sublayer". This computational concept is assumed to extend from the wall to the point where the laminar velocity profile intercepts the logarithmic law of the wall.

Coles himself concludes that his new law of the wall does not fit the experimental data as well as, especially, Simpson's law of the wall. This author feels that the reason for the relative failure of Coles approach is the insistence that the normalizing scales, u_0 and y_0 , satisfy the condition, $u_0 / y_0 = u_\tau^2 / \nu$. This condition is

rooted in Coles' requirement that the normalized velocity profile (i.e. the profile in terms of u/u_0 and y/y_0) shows similarity in the entire inner region, i.e., not only in the logarithmic region, but also in the viscous sublayer. Such a requirement cannot be satisfied and is furthermore unnecessary. The reason for Coles' insistence on this point is apparently that he arrived at the law of the wall from a Millikan argument which presupposes the existence of a set of wall coordinates i.e. u/u_0 and y/y_0 in terms of which similarity exists all the way to the wall. But in order to conclude that a logarithmic region exists it is enough to assume that two distinct regions exist; the innermost of these two regions does not have to extend into the fully viscous region.

In the following a new law of the wall is proposed. The essential feature is the use of the coordinates u/u_c and yu_c/ν , where $u_c = \sqrt{\tau_c/\rho}$ is a velocity scale based on the characteristic shear stress, τ_c . It was shown in the previous section that τ_c characterizes the shear stress in the logarithmic region and furthermore is directly related to the thickness of the viscous sublayer through Eq. (7-8) which may be written:

$$\frac{u_c}{u_\tau} = \frac{A_0^+}{A^+} \quad (7-15)$$

It was found that τ_c obtains exactly at the characteristic wall distance, $y_c = 3A$, which may be said to define the thickness of the viscous sublayer. The van Driest length scale, A , in Eq. (7-15) can therefore be thought of as merely a convenient measure of the sublayer thickness for which experimental values are available.

It has been shown that both ℓ/y and ϵ/ν plot as unique functions of $y^+ A_0^+ / A^+ = yu_c/\nu$ (see Figs. 6-17

and 6-18) over an extended range in the wall region. This range includes the logarithmic region.

From the definition of the mixing-length, $\epsilon = \ell^2 du/dy$, one may obtain

$$\frac{d\left(\frac{u}{u_c}\right)}{d\left(\frac{yu_c}{v}\right)} = \frac{\epsilon/v}{\left(\frac{\ell}{y}\right)^2 \left(\frac{yu_c}{v}\right)^2} \quad (7-16)$$

The derivative on the left hand side is, in view of what was stated above, expected to be a function of yu_c/v at least in the logarithmic region.

The logarithmic part of the velocity profile will be expressed as

$$\frac{u}{u_c} = \frac{1}{0.41} \ln\left(\frac{yu_c}{v}\right) + 5.0 + h(u_\tau/u_c) \quad (7-17)$$

This expression correctly leads to a derivative,

$d\left(\frac{u}{u_c}\right)/d\left(\frac{yu_c}{v}\right)$, which is a function of yu_c/v as required

by Eq. (7-16). For a non-transpired, constant pressure boundary layer, $u_\tau = u_c$, and the function h must be such that $h = 0$ for this case. The simplest function form with this property is $h = c_1 \left(\frac{u_\tau}{u_c} - 1\right)$, where the constant, c_1 , remains to be determined. Inserting this expression for h into Eq. (7-17) and solving for c_1 one obtains

$$c_1 = \left[\frac{u}{u_\tau} - \frac{u_c}{u_\tau} \left(\frac{1}{0.41} \ln \frac{yu_c}{v} + 5.0 \right) \right] / \left(1 - \frac{u_c}{u_\tau} \right) \quad (7-18)$$

For c_1 to be a constant there must therefore exist a set of coordinates, $(u_1/u_\tau, y_1 u_c/v)$, such that

$c_1 = u_1/u_\tau = \frac{1}{0.41} \ln \frac{y_1 u_c}{v} + 5.0$. The value of the constant,

c_1 , may thus be found by plotting experimental velocity profiles as u/u_τ versus yu_c/ν . If the assumed form of the function, h , is correct, then there must be a point in these coordinates in which all the profiles intersect. Figure 7-2, in which profiles for a broad range of boundary conditions have been plotted, clearly shows that all the experimental profiles have $(u_1/u_\tau, y_1 u_c/\nu) = (14.0, 40)$ as a common point. It then follows from Eq. (7-18) that $c_1 = 14.0$ and Eq. (7-16) becomes:

$$\frac{u}{u_c} = \frac{1}{0.41} \ln\left(\frac{yu_c}{\nu}\right) + 5.0 + 14.0\left(\frac{u_\tau}{u_c} - 1\right) \quad (7-19a)$$

This new "generalized law of the wall" of course reduces to the classical law of the wall, Eq. (7-14), for $u_c = u_\tau$. Equation (7-19a) has been verified by plotting experimental

profiles of $\frac{u}{u_c} - 14\left(\frac{u_\tau}{u_c} - 1\right)$ versus yu_c/ν in Fig. 7-3.

It may be noted that the logarithmic portion of all the experimental profiles is well fitted by Eq. (7-19a), thus verifying the new law of the wall for the present data.

The new law of the wall Eq. (7-19a) may of course be expressed in the wall coordinates $u^+ = u/u_\tau$ and $y^+ = yu_\tau/\nu$ by making use of the identity, $u_c/u_\tau = \sqrt{\tau_c^+}$. The result is:

$$u^+ = \frac{\sqrt{\tau_c^+}}{0.41} \ln(y^+ \sqrt{\tau_c^+}) + 5.0 \sqrt{\tau_c^+} + 14.0(1 - \sqrt{\tau_c^+}) \quad (7-19b)$$

Since $\sqrt{\tau_c^+} = A_o^+/A^+$, Eq. (7-15), the generalized law of the wall may also be expressed as

$$u^+ = \frac{A_o^+}{A^+} \frac{1}{0.41} \ln\left(y^+ \frac{A_o^+}{A^+}\right) + 5.0 \frac{A_o^+}{A^+} + 14.0\left(1 - \frac{A_o^+}{A^+}\right) \quad (7-19c)$$

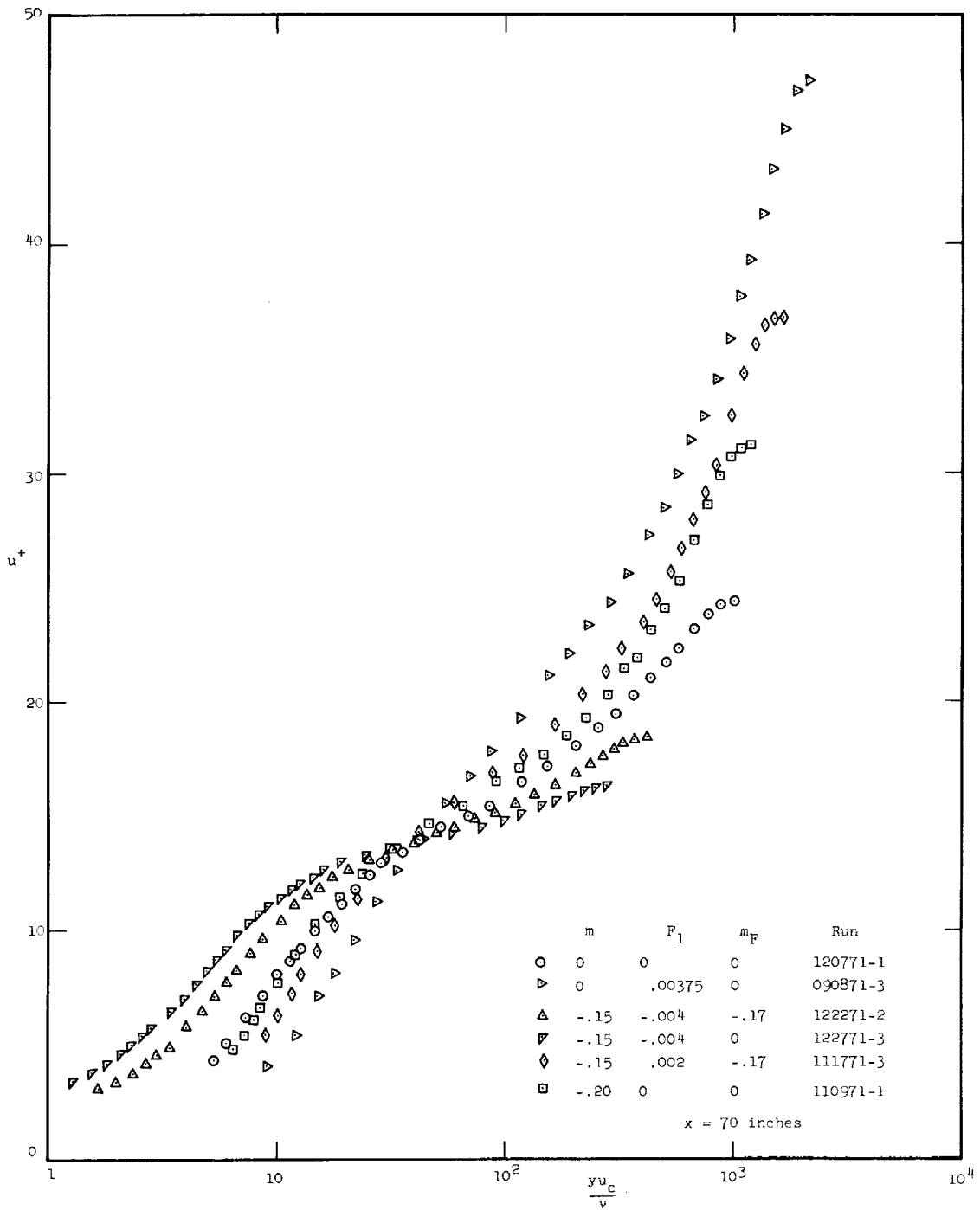


Fig. 7-2 u^+ versus $yu_c/v = y^+A_0/A^+$ for selected runs

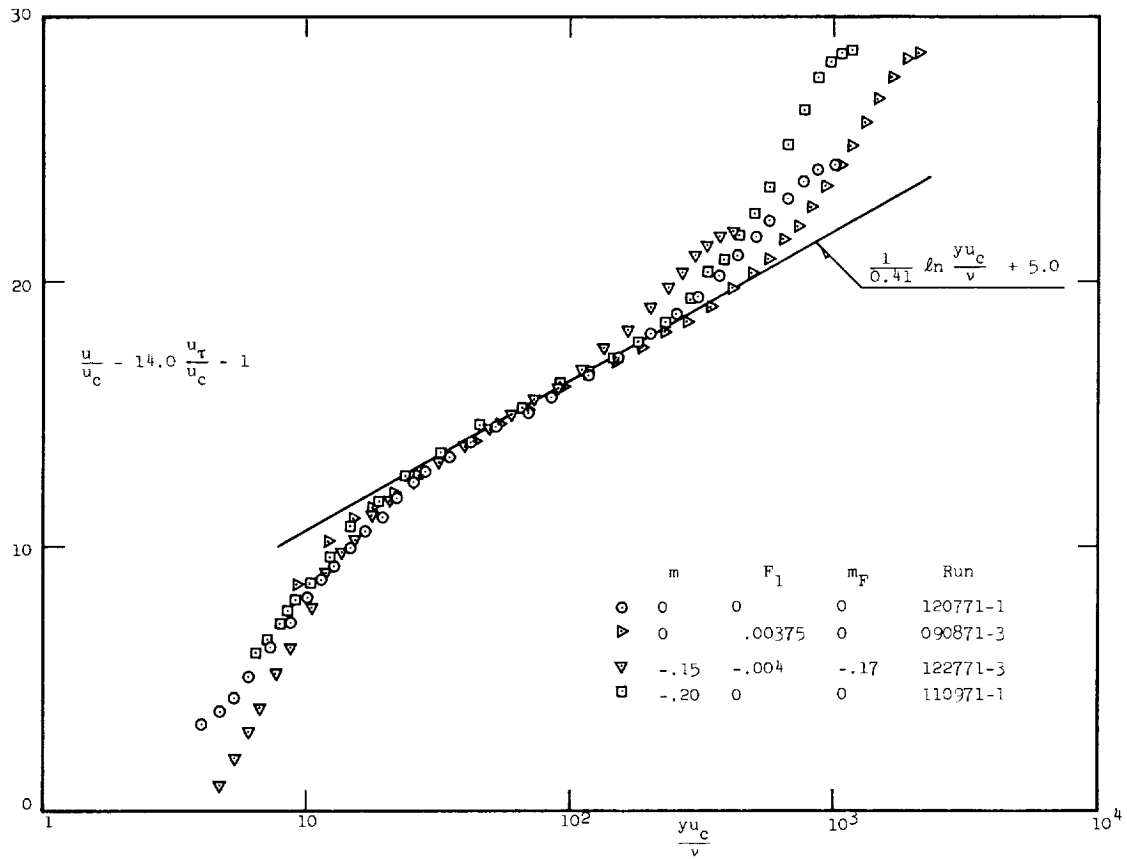


Fig. 7-3 Verification of the generalized law of the wall, Eq. (8-19)

This form of the equation makes the sublayer thickness (i.e. the van Driest length scale) appear explicitly.

Note also that the ratio A_o^+/A^+ is independent of the wall hypothesis; as demonstrated by Eq. (7-13).

In order to make the non-dimensional pressure gradient, p^+ , and the non-dimensional transpiration rate, v_o^+ , appear explicitly in the new law of the wall the characteristic shear stress, τ_c , might be expressed by the Couette approximation, Eq. (7-2). However the term, p^+y^+ , is a very poor approximation of the effect of the pressure gradient on the shear stress in the logarithmic region; only the influence of transpiration can be adequately treated by the Couette approximation. For a constant pressure boundary layer the characteristic shear stress, τ_c , may then be approximated by

$$\tau_c^+ = 1 + v_o^+ u_c^+ \quad (7-20)$$

The velocity, u_c^+ , at the characteristic point, y_c , may be obtained from Eq. (7-19b) for $y^+ \sqrt{\tau_c^+} = y_c^+ \sqrt{\tau_c^+} = 3A_o^+$. The result is

$$u_c^+ = 14 + 1.4 \sqrt{\tau_c^+} \quad (7-21)$$

Inserting this expression into Eq. (7-20) one obtains a 2nd order equation for $\sqrt{\tau_c^+}$; the solution is, with approximation,

$$\sqrt{\tau_c^+} = 1 + 7.7 v_o^+ \quad (7-22)$$

Inserting this result into Eq. (7-19b) the following approximation for the new law of the wall may be obtained:

$$u^+ = \frac{1 + 7.7 v_o^+}{0.41} \ln y^+ + 5.0 - 50 v_o^+ + 72 v_o^{+2} \quad (7-23)$$

In passing it may be noted that Eq. (7-22) for $\sqrt{\tau_c^+}$ may be used to obtain an approximate (but quite adequate for moderate transpiration rates) expression for the van Driest length scale, namely:

$$A^+ = \frac{A_o^+}{\sqrt{\tau_c^+}} = \frac{24}{1 + 7.7 v_o^+} \quad (7-24)$$

The generalized law of the wall may of course be used to obtain the friction velocity, u_τ (and thus the friction coefficient, $c_f/2 = u_\tau^2/u_\infty^2$), from experimental velocity profiles. For this purpose it is convenient to write Eq. (7-19a) in the form:

$$u = \frac{u_c}{0.41} \ln\left(\frac{yu_c}{40v}\right) + 14.0u_\tau \quad (7-25)$$

Thus if u is plotted against $\ln y$ then u_c may be obtained directly from the slope of the logarithmic region. u_τ may then be obtained, for example, as the velocity at $y = 40v/u_c$ divided by 14.0. If desired the van Driest length scale may be obtained as $A^+ = 24u_\tau/u_c$.

7.4 Predictions of Experimental Boundary Layers

Four of the experimental boundary layers representing rather extreme boundary conditions were predicted using a numerical procedure capable of solving the boundary layer Eqs. (3-1) when "closure" is provided in the form of a connection between the shear stress, τ , and the mean velocity field. The solution method is that of Patankar and Spalding [19].

The closure used in the present predictions is provided by the following model:

$$\tau = \rho(v + \epsilon) \frac{du}{dy}, \quad \text{where} \quad \epsilon = \ell^2 \frac{du}{dy} \quad (7-26)$$

The mixing-length, ℓ , is obtained from the van Driest model, Eq. (6-15) in the inner and overlap region. In the outer region ℓ is taken to be equal to $\lambda\delta_{99}$, where λ is a constant. Thus

$$\ell = \begin{cases} \kappa y \left[1 - \exp\left(-\frac{y}{A}\right) \right] & \text{for } y \leq \lambda\delta_{99}/\kappa \\ \lambda\delta_{99} & \text{for } y > \lambda\delta_{99}/\kappa \end{cases} \quad (7-27)$$

The length scale, A , in the van Driest model was obtained from Eq. (7-8) which may be written

$$A = \frac{vA_o^+}{u_c}, \text{ where } u_c = \sqrt{\tau(3A)/\rho} \quad (7-28)$$

The value of λ is very nearly a constant for all the boundary layers. It was found, however, that the following dependence of λ upon the Reynolds number, Re_{δ_2} , and the blowing fraction, F , leads to slightly improved predictions:

$$\lambda = \begin{cases} \lambda_{\infty} (6000/Re_{\delta_2})^{.125} (1 - 67.5F) & \text{for } Re_{\delta_2} < 6000 \\ \lambda_{\infty} (1 - 67.5F) & \text{for } Re_{\delta_2} > 6000 \end{cases} \quad (7-29)$$

In the above expression λ_{∞} is a constant. The dependence of λ upon Re_{δ_2} and F is rather weak, but the same dependence has been used with success (see Julien [3]) for the prediction of boundary layer with strong favorable pressure gradients; this seems to indicate that Eq. (7-29) is rather universal.

Not counting the constants in Eq. (7-29) associated with the weak Reynolds number and transpiration dependence, the present closure model contains only three empirical

constants, namely:

1. The von Kármán constant, $\kappa = 0.41$.
2. The van Driest length scale for the non-transpired constant pressure boundary layer, $A_0^+ = 24.0$.
3. The value of ℓ/δ_{99} in the outer region, $\lambda_\infty = 0.0779$.

All the predictions were started at the first experimental velocity profile (at $x = 2$ inches). The boundary conditions were specified as the measured free-stream velocity distribution and transpiration rate. The four experimental boundary layers which have been predicted are listed below.

m	F_1	m_F	Run
0	0	0	120771-1
0	.00375	0	090871-3
-.15	-.004	-.17	122271-2
-.20	0	0	110971-1

The values given for m , F_1 and m_F specify the nominal boundary conditions (see Section 2).

Figures 7-4 and 7-5 compare experimental and predicted variations of the Reynolds number, $Re\delta_2$, and the friction coefficient, $c_f/2$. The slight general overprediction of $Re\delta_2$ is possibly due to a small experimental three-dimensionality.

Figure 7-6 compares experimental and predicted values of A^+/A_0^+ . The agreement is good.

Figures 7-7 and 7-8 display for comparison experimental and predicted velocity profiles at (in wall coordinates) $x = 70$ inches. The greatest discrepancy between experiment and prediction occurs for the run (090871-3) with the highest blowing rate. The underprediction of the "strength of the wake" seems to be due to a too high value of λ rather than a faulty value of A^+ .

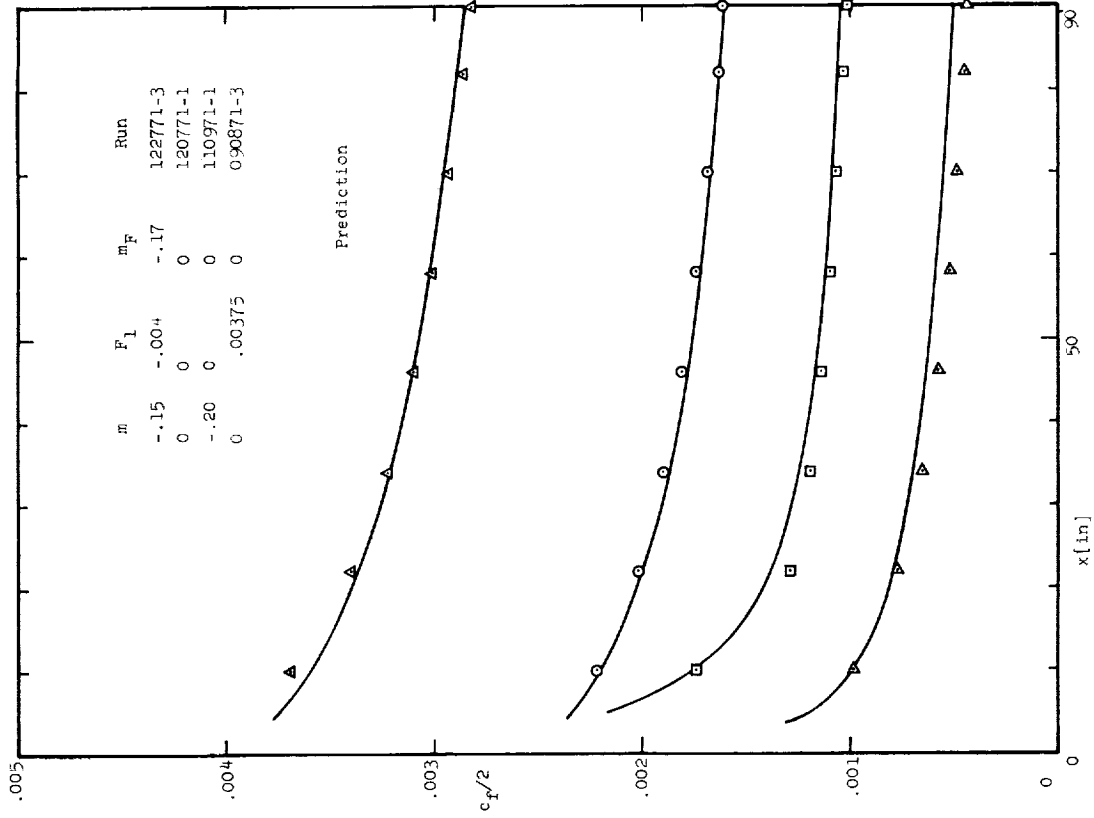


Fig. 7-5 Comparison of prediction of $c_f/2$ with experimental data

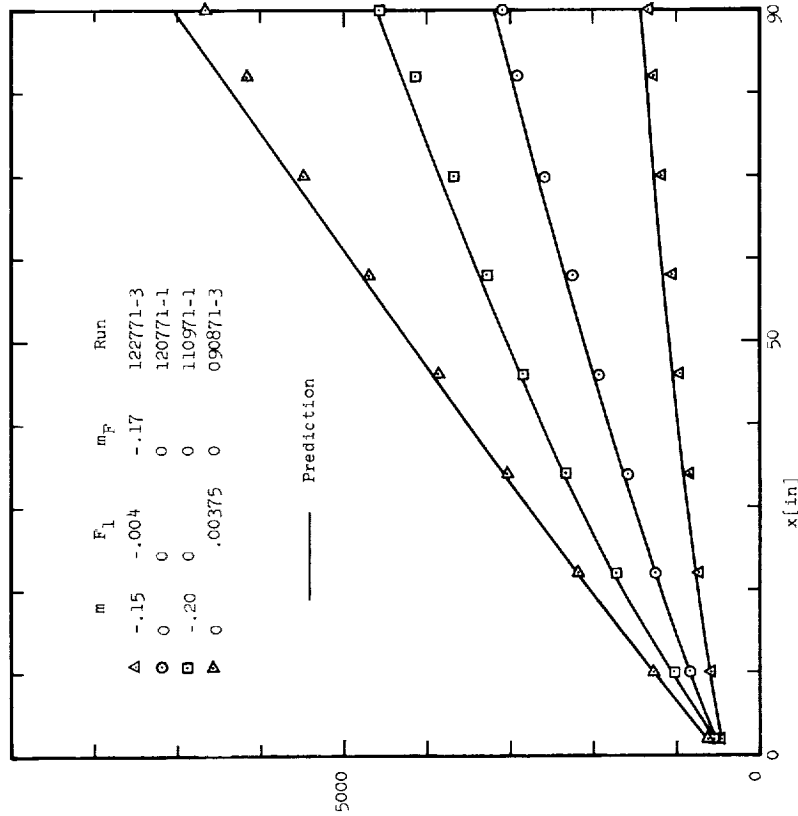


Fig. 7-4 Comparison of prediction of the Re_{62} with experimental data

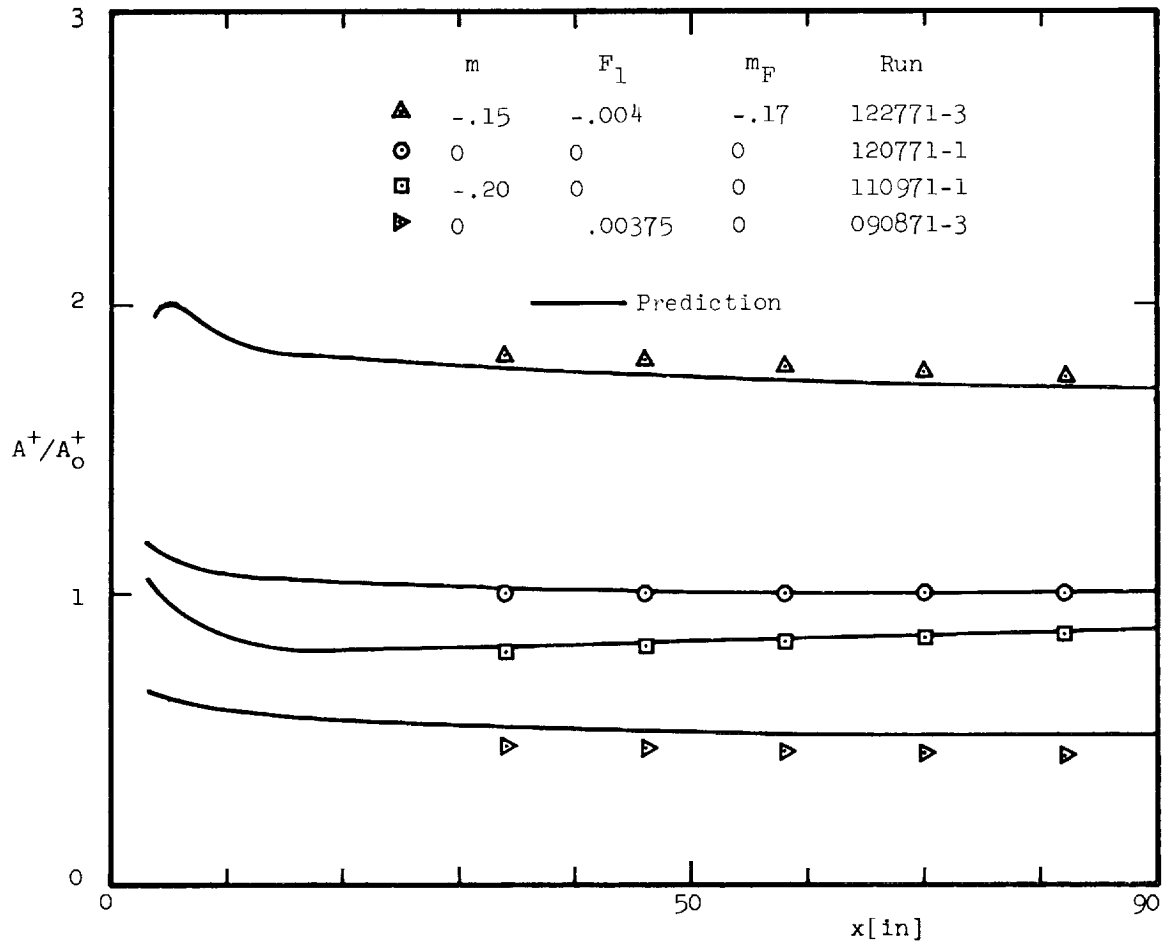


Fig. 7-6 Comparison of prediction of A^+/A_0^+ with experimental data

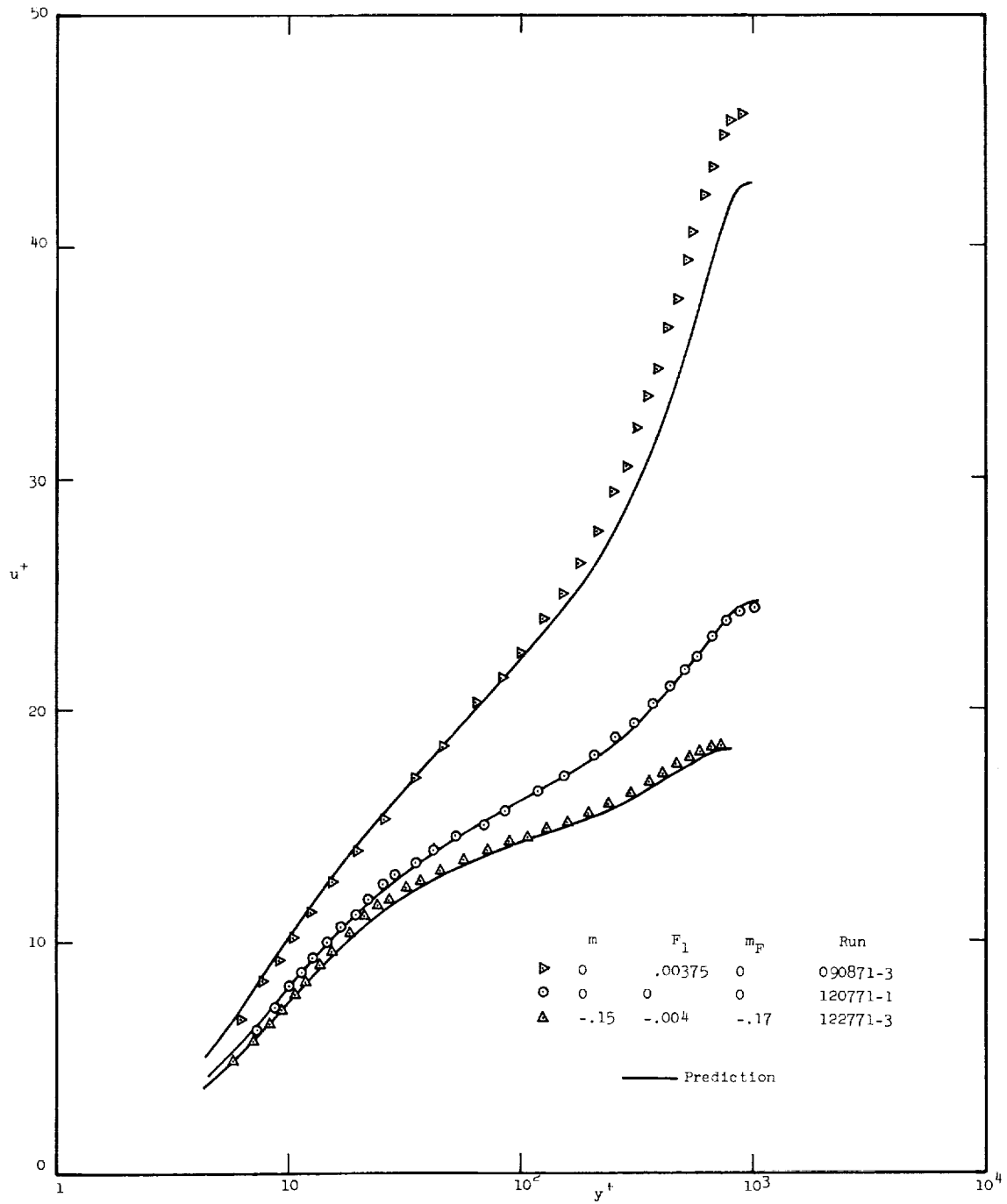


Fig. 7-7 Comparison of predicted and experimental velocity profiles

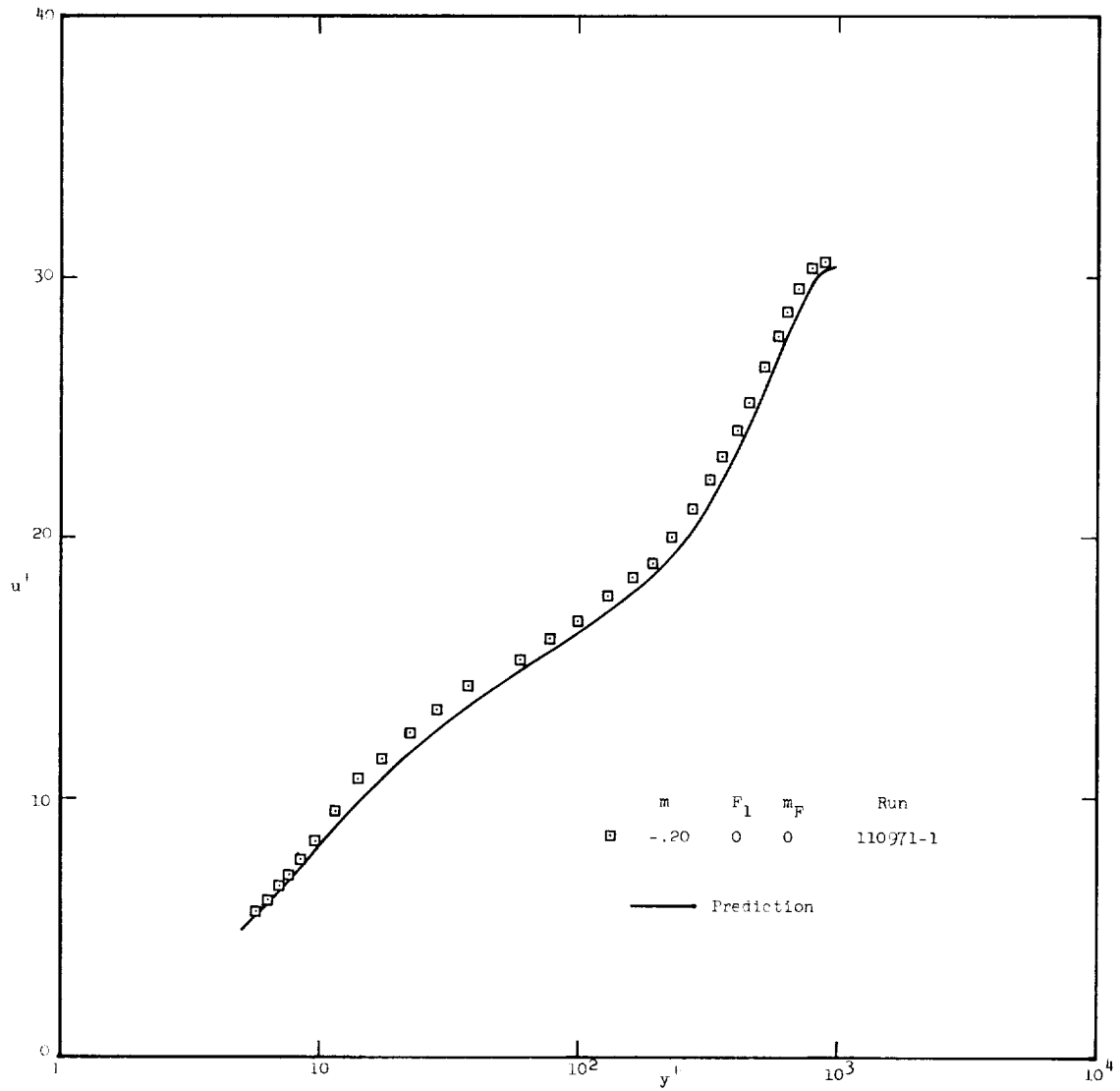


Fig. 7-8 Comparison of predicted and measured velocity profile

CHAPTER 8

SUMMARY AND CONCLUSIONS

Experimental results for turbulent incompressible boundary layers with transpiration (blowing and suction through a porous wall), and both constant pressure and adverse pressure gradients, have been presented. The three different free-stream velocity distributions may be described by an equation of the form:

$$u_{\infty} \propto u_1 x^m, \quad \text{where } m \leq 0. \quad (8-1)$$

The transpiration boundary condition may be expressed by

$$F \propto F_1 x^{m_F} \quad \text{where } F = v_o / u_{\infty} \quad \text{and} \\ F > 0 ; m_F \leq 0. \quad (8-2)$$

Table 2-2 summarizes the experimental boundary conditions. A total of 20 "runs" (i.e. sets of different boundary conditions), corresponding to a total of 179 mean velocity profiles, are presented.

All velocity profile measurements were carried out using linearized constant temperature anemometry. In addition to mean velocity profiles, Reynolds stress profiles and profiles of the three turbulence intensities were measured.

The skin friction was determined by a technique involving the measurement of the shear stress close to the wall (as the sum of the Reynolds stress and the viscous stress) and then "extrapolating" to the wall using the integrated boundary layer equations.

The analysis of the experimental results has led to the following conclusions:

1. The skin friction results for a given pressure gradient (i.e. a given m) may be correlated by an equation of the type:

$$c_f/2 = (c_f/2)_o f_o(B_o) , \text{ where } B_o = \frac{F}{(c_f/2)_o} \text{ and} \quad (8-3)$$

$$(c_f/2)_o = a \text{Re}_{\delta_2}^{-0.25} \quad (8-4)$$

The constant, a , in Eq. (8-4) for the non-transpired boundary layers depends parametrically upon m (see Eq. (6-4)). Explicit expressions for the function $f_o(B_o)$ are given in Eqs. (6-9). Although different functions are presented for each of the three pressure gradients, these functions do not differ greatly within their common ranges of applicability.

Equation (8-3) may be written in the equivalent form:

$$c_f/2 = (c_f/2)_o f(B) , \text{ where}$$

$$f(B) = f_o(B_o) \text{ and } B = \frac{F}{c_f/2} = B_o / f_o(B_o) . \quad (8-5)$$

2. Clauser-type equilibrium boundary layers (i.e. flows having a constant Clauser shape factor, G) are obtained for constant values of the Clauser pressure gradient parameter, β , and the blowing parameter, B . Furthermore it is shown that G is a function of $(\beta + B)$, indicating that constant values of β and B have identical effects upon the shape of the defect profile.
3. For all the experimental boundary layers there exists a range of y , the "logarithmic region", where the mixing-length may be expressed as

$$l = \kappa y \quad (\kappa = 0.41) \quad . \quad (8-6)$$

The von Kármán constant, κ , is therefore independent of both transpiration rate and pressure gradient.

4. The logarithmic region is characterized by a shear stress, $\tau_c = \tau(y_c)$. The "characteristic" wall distance, y_c , is related to τ_c through the equation

$$\frac{y_c u_c}{\nu} = y_{o,c}^+ \quad , \quad \text{where} \quad u_c = \sqrt{\tau_c / \rho} \quad . \quad (8-7)$$

The constant, $y_{o,c}^+ = 72$, may be interpreted as the characteristic distance (in wall coordinates) for a non-transpired constant pressure boundary layer ($u_c = u_\tau$ for this case). y_c may be identified as the thickness of the inner region. If for example the van Driest model, Eq. (7-10), is used to describe the mixing-length behavior in the inner region, then the van Driest length scale may be determined as $A = y_c/3$. The length scales for other mixing-length models are also proportional to y_c .

5. The Reynolds number of turbulence, $Re_T = l \sqrt{-u'v'}/\nu = \epsilon/\nu = \epsilon^+$, has the constant, characteristic value, $\epsilon_c^+ = 29$, at the characteristic point, $y = y_c$.
6. A new generalized law of the wall which fits the logarithmic region of all the experimental velocity profiles, may be expressed as

$$\frac{u}{u_c} = \frac{1}{0.41} \ln\left(\frac{y u_c}{\nu}\right) + 5.0 + 14.0 \left(\frac{u_\tau}{u_c} - 1\right) \quad . \quad (8-8)$$

This new law of the wall reduces to the classical law for $u_c = u_\tau$, i.e., for the case, where the shear stress in the logarithmic region is equal to the wall shear stress.

7. Successful predictions of four of the experimental boundary layers have been carried out using a numerical procedure that solves the differential boundary layer equations. The closure (mean velocity field) relies on only three empirical constants:

- a) The von Kármán constant, $\kappa = 0.41$.
- b) The constant $y_{o,c}^+ = 72$ in Eq. (8-6) .
- c) The value $\lambda_\infty = \ell/\delta_{99} = 0.0779$ used in the outer region of the boundary layer.

The van Driest model was used for the mixing-length in the inner region. (The length scale was obtained from

$$3A = \frac{v}{u_c} y_{o,c}^+) .$$

CHAPTER 9

TABULATED EXPERIMENTAL DATA

All the experimental data related to the mean velocity profiles are presented in this chapter. The run numbers together with corresponding nominal boundary conditions (see Section 2.3) are listed in the table below.

Run	m	F_1	m_F
120771-1	0	0	0
100571-1	0	.001	0
090171-2	0	.002	0
090871-3	0	.00375	0
092271-5	0	.008	0
122271-2	-.15	-.004	0
122771-3	-.15	-.004	-.17
121671-3	-.15	-.002	0
122971-1	-.15	-.002	-.17
121171-3	-.15	-.001	0
010372-1	-.15	-.001	-.17
071571-5	-.15	0	0
111571-1	-.15	.001	-.17
091771-2	-.15	.001	0
111771-3	-.15	.002	-.17
101371-2	-.15	.002	0
112871-1	-.15	.004	-.17
102171-1	-.15	.004	0
021572-5	-.20	-.004	-.16
110971-1	-.20	0	0

Table 9-1 Run numbers and nominal boundary conditions

Table 9-2 gives the measured streamwise velocity distributions for all the runs and Table 9-3 presents the measured blowing fractions.

Each of the following three sections contains a run by run summary of a few relevant parameters for each velocity profile. The profile tables following this summary contain a detailed list of boundary conditions, skin friction coefficients and integral parameters.

Note: The free-stream velocities listed in the summaries and the profile tables of the following sections are hot-wire results corresponding to the last profile points, whereas the free-stream velocity distributions listed in Table 9-2 is computed from the pressure distribution. As a consequence slight discrepancies between the two quotations of u_∞ may be found. The pressure gradient parameter, $K = \frac{v}{u_\infty^2} \frac{du_\infty}{dx}$, is computed on the basis of the velocities in Table 9-2 (see Appendix B for details).

Special Nomenclature and units:

BETA	=	β
CF2	=	$c_f/2$
D1	=	δ_1 [in]
D2	=	δ_2 [in]
D99	=	δ_{99} [in]
DC	=	Δ
NU	=	v [ft ² /s]
RD2	=	$Re\delta_2$
VO ⁺	=	v_o^+
UI	=	u_∞
U*	=	u_τ
TAU	=	$\tau/\rho u_\infty$
TAULAM	=	$\tau_v/\rho u_\infty$
X	=	x [in]
Y	=	y [in]

9.1 Constant Pressure, m = 0

RUN: 120771-1 NU= 0.159E-03

N	X	UI	K	F	RD2	CF/2	BETA	B	BETA+B	G	A ⁺
1	2.	31.21	0.139E-08	0.00000	535.	0.00249	-0.000	0.000	-0.000	7.00	
2	10.	31.13	0.123E-08	0.00000	849.	0.00222	-0.001	0.000	-0.001	6.91	
3	22.	31.14	0.924E-09	0.00000	1251.	0.00202	-0.001	0.000	-0.001	7.20	
4	34.	31.05	0.563E-09	0.00000	1588.	0.00190	-0.001	0.000	-0.001	7.07	24.0
5	46.	31.04	0.138E-09	0.00000	1926.	0.00181	-0.000	0.000	-0.000	7.20	24.0
6	58.	31.13	-0.351E-08	0.00000	2240.	0.00174	0.001	0.000	0.001	7.22	24.0
7	70.	31.04	-0.902E-09	0.00000	2574.	0.00168	0.002	0.000	0.002	7.25	24.0
8	82.	31.07	-0.152E-08	0.00000	2919.	0.00163	0.004	0.000	0.004	7.22	24.0
9	90.	31.06	-0.196E-08	0.00000	3093.	0.00161	0.005	0.000	0.005	7.17	

RUN: 100571-1 NU= 0.164E-03

N	X	UI	K	F	RD2	CF/2	BETA	B	BETA+B	G	A ⁺
1	2.	30.95	0.489E-08	0.00103	525.	0.00217	-0.002	0.475	0.473	7.80	
2	10.	30.28	0.303E-08	0.00101	802.	0.00193	-0.002	0.524	0.522	8.34	
3	22.	32.15	0.796E-09	0.00101	1623.	0.00157	-0.001	0.645	0.644	8.79	
4	34.	30.51	-0.760E-09	0.00100	1878.	0.00150	0.001	0.666	0.668	8.55	19.8
5	46.	31.28	-0.164E-08	0.00103	2404.	0.00138	0.004	0.744	0.748	9.05	19.6
6	58.	31.17	-0.186E-08	0.00102	2857.	0.00132	0.006	0.775	0.781	9.08	19.5
7	70.	31.10	-0.139E-08	0.00105	3326.	0.00125	0.006	0.842	0.848	9.34	19.3
8	82.	31.18	-0.254E-09	0.00105	3776.	0.00120	0.001	0.877	0.878	9.40	19.3
9	90.	31.02	0.879E-09	0.00104	3996.	0.00118	-0.004	0.882	0.877	9.33	

RUN: 90171-2 NU= 0.167E-03

N	X	UI	K	F	RD2	CF/2	BETA	B	BETA+B	G	A ⁺
1	2.	31.66	-0.873E-09	0.00200	566.	0.00183	0.000	1.090	1.091	8.91	
2	10.	31.57	-0.109E-08	0.00200	1034.	0.00150	0.001	1.334	1.335	9.63	
3	22.	31.57	-0.113E-08	0.00200	1661.	0.00127	0.002	1.574	1.577	10.34	
4	34.	31.62	-0.945E-09	0.00200	2259.	0.00114	0.003	1.759	1.762	10.64	16.4
5	46.	31.48	-0.508E-09	0.00200	2843.	0.00104	0.002	1.915	1.917	11.20	16.2
6	58.	31.38	0.183E-09	0.00200	3384.	0.00098	-0.001	2.045	2.044	11.40	16.0
7	70.	31.33	0.113E-08	0.00200	3918.	0.00092	-0.007	2.163	2.156	11.54	15.9
8	82.	31.34	0.232E-08	0.00199	4450.	0.00088	-0.018	2.255	2.237	11.71	15.8
9	90.	31.28	0.326E-08	0.00200	4742.	0.00086	-0.027	2.330	2.303	11.69	

RUN: 90871-3 NU= 0.166E-03

N	X	UI	K	F	RD2	CF/2	BETA	B	BETA+B	G	A ⁺
1	2.	31.62	0.105E-08	0.00375	626.	0.00133	-0.001	2.829	2.828	11.20	
2	10.	31.34	0.851E-09	0.00375	1258.	0.00098	-0.002	3.809	3.807	13.26	
3	22.	31.52	0.570E-09	0.00375	2172.	0.00077	-0.003	4.897	4.894	15.03	
4	34.	31.50	0.306E-09	0.00375	3030.	0.00065	-0.002	5.761	5.758	16.25	11.5
5	46.	31.39	0.600E-10	0.00376	3863.	0.00057	-0.001	6.554	6.554	17.62	11.2
6	58.	31.40	-0.169E-09	0.00375	4700.	0.00052	0.003	7.226	7.228	18.21	10.9
7	70.	31.31	-0.380E-09	0.00375	5494.	0.00048	0.007	7.861	7.868	18.98	10.7
8	82.	30.94	-0.575E-09	0.00375	6173.	0.00045	0.013	8.381	8.395	19.32	10.6
9	90.	30.98	-0.694E-09	0.00376	6667.	0.00043	0.018	8.802	8.820	19.38	

RUN: 92271-5 NU= 0.165E-03

N	X	UI	K	F	RD2	CF/2	BETA	B	BETA+B	G
1	2.	31.44	0.347E-08	0.00801	750.	0.00106	-0.004	7.557	7.552	13.73
2	10.	31.47	0.228E-08	0.00796	1783.	0.00031	-0.026	25.492	25.466	28.21
3	22.	31.46	0.762E-09	0.00804	3349.	0.00020	-0.026	40.032	40.005	36.45
4	34.	31.45	-0.417E-09	0.00801	4876.	0.00016	0.026	49.745	49.771	40.85
5	46.	31.51	-0.126E-08	0.00802	6340.	0.00014	0.118	57.014	57.132	43.77
6	58.	31.51	-0.178E-08	0.00798	7830.	0.00013	0.220	61.801	62.021	44.89
7	70.	31.48	-0.196E-08	0.00798	9327.	0.00012	0.305	65.634	65.939	45.98
8	82.	31.47	-0.181E-08	0.00799	10787.	0.00012	0.335	68.401	68.736	46.33

9.2 Weak Adverse Pressure Gradient, $m = -1.5$

RUN: 122271-2 NU= 0.161E-03

N	X	UI	K	F	RD2	CF/2	BETA	B	BETA+B	G	A ⁺
1	2.	29.32	-0.446E-06	-0.00399	451.	0.00397	0.073	-1.006	-0.933	4.84	
2	10.	26.81	-0.838E-06	-0.00398	557.	0.00380	0.174	-1.046	-0.873	4.75	
3	22.	24.29	-0.463E-06	-0.00399	662.	0.00383	0.111	-1.041	-0.929	4.43	
4	34.	22.95	-0.335E-06	-0.00400	712.	0.00381	0.084	-1.050	-0.966	4.13	60.4
5	46.	22.07	-0.263E-06	-0.00401	761.	0.00379	0.070	-1.059	-0.989	4.04	62.5
6	58.	21.45	-0.218E-06	-0.00399	773.	0.00377	0.059	-1.059	-1.000	3.99	63.1
7	70.	20.77	-0.187E-06	-0.00399	788.	0.00376	0.051	-1.061	-1.010	3.74	63.9
8	82.	20.38	-0.164E-06	-0.00399	814.	0.00375	0.046	-1.065	-1.018	3.81	64.6
9	90.	20.14	-0.160E-06	-0.00401	822.	0.00375	0.045	-1.068	-1.023	3.63	

RUN: 122771-3 NU= 0.161E-03

N	X	UI	K	F	RD2	CF/2	BETA	B	BETA+B	G	A ⁺
1	2.	29.29	-0.445E-06	-0.00399	465.	0.00389	0.078	-1.027	-0.948	5.05	
2	10.	26.80	-0.836E-06	-0.00360	567.	0.00369	0.184	-0.976	-0.792	4.97	
3	22.	24.29	-0.465E-06	-0.00322	720.	0.00340	0.137	-0.946	-0.809	4.86	
4	34.	22.97	-0.331E-06	-0.00300	843.	0.00322	0.118	-0.930	-0.813	4.68	43.6
5	46.	21.99	-0.257E-06	-0.00287	970.	0.00310	0.110	-0.926	-0.815	4.89	43.2
6	58.	21.30	-0.210E-06	-0.00276	1047.	0.00301	0.099	-0.916	-0.817	4.81	42.6
7	70.	20.77	-0.176E-06	-0.00268	1167.	0.00293	0.054	-0.915	-0.821	4.66	42.3
8	82.	20.35	-0.151E-06	-0.00259	1258.	0.00286	0.069	-0.907	-0.818	4.74	41.7
9	90.	20.01	-0.144E-06	-0.00256	1314.	0.00282	0.069	-0.906	-0.818	4.59	

RUN: 121671-3 NU= 0.158E-03

N	X	UI	K	F	RD2	CF/2	BETA	B	BETA+B	G	A ⁺
1	2.	29.30	-0.441E-06	-0.00199	510.	0.00323	0.104	-0.617	-0.512	5.86	
2	10.	26.95	-0.826E-06	-0.00198	741.	0.00282	0.322	-0.703	-0.381	6.13	
3	22.	24.59	-0.457E-06	-0.00199	1070.	0.00264	0.270	-0.755	-0.485	6.09	
4	34.	23.21	-0.325E-06	-0.00200	1285.	0.00256	0.230	-0.780	-0.550	5.74	34.0
5	46.	22.11	-0.253E-06	-0.00199	1482.	0.00250	0.210	-0.795	-0.585	5.74	34.8
6	58.	21.55	-0.210E-06	-0.00199	1642.	0.00246	0.192	-0.808	-0.616	5.48	35.3
7	70.	20.95	-0.182E-06	-0.00197	1797.	0.00242	0.184	-0.814	-0.630	5.40	35.5
8	82.	20.50	-0.166E-06	-0.00199	1956.	0.00240	0.184	-0.830	-0.646	5.40	36.0
9	90.	20.21	-0.166E-06	-0.00199	2065.	0.00238	0.194	-0.837	-0.643	5.27	

RUN: 122971-1 NU= 0.159E-03

N	X	UI	K	F	RD2	CF/2	BETA	B	BETA+B	G	A ⁺
1	2.	29.20	-0.440E-06	-0.00199	504.	0.00320	0.104	-0.623	-0.519	5.88	
2	10.	26.91	-0.826E-06	-0.00178	752.	0.00275	0.335	-0.647	-0.312	6.20	
3	22.	24.38	-0.460E-06	-0.00159	1089.	0.00244	0.298	-0.650	-0.352	6.34	
4	34.	23.00	-0.328E-06	-0.00149	1353.	0.00231	0.275	-0.645	-0.371	6.25	30.2
5	46.	21.97	-0.257E-06	-0.00142	1592.	0.00221	0.263	-0.642	-0.379	6.32	30.3
6	58.	21.27	-0.211E-06	-0.00138	1801.	0.00215	0.248	-0.643	-0.396	6.15	30.5
7	70.	20.68	-0.179E-06	-0.00132	2010.	0.00208	0.242	-0.635	-0.394	6.23	30.4
8	82.	20.26	-0.155E-06	-0.00129	2226.	0.00203	0.237	-0.636	-0.400	6.24	30.5
9	90.	19.91	-0.149E-06	-0.00128	2316.	0.00201	0.237	-0.637	-0.400	6.16	

RUN: 121171-3 NU= 0.160E-03

N	X	UI	K	F	RD2	CF/2	BETA	B	BETA+B	G	A ⁺
1	2.	29.35	-0.445E-06	-0.00099	514.	0.00294	0.120	-0.336	-0.217	6.47	
2	10.	26.89	-0.832E-06	-0.00099	826.	0.00244	0.425	-0.406	0.018	6.80	
3	22.	24.35	-0.461E-06	-0.00098	1253.	0.00212	0.407	-0.463	-0.056	7.14	
4	34.	22.94	-0.326E-06	-0.00098	1560.	0.00203	0.369	-0.484	-0.115	7.09	26.9
5	46.	21.98	-0.254E-06	-0.00099	1871.	0.00196	0.353	-0.505	-0.153	7.05	27.5
6	58.	21.29	-0.210E-06	-0.00098	2093.	0.00191	0.330	-0.512	-0.183	6.93	27.8
7	70.	20.73	-0.181E-06	-0.00098	2332.	0.00187	0.321	-0.523	-0.202	6.90	28.1
8	82.	20.28	-0.165E-06	-0.00098	2573.	0.00184	0.325	-0.533	-0.208	6.75	28.3
9	90.	19.96	-0.165E-06	-0.00098	2774.	0.00181	0.354	-0.541	-0.187	6.72	

RUN: 10372-1 NU= 0.161E-03

N	X	UI	K	F	RD2	CF/2	BETA	B	BETA+B	G	A ⁺
1	2.	29.27	-0.433E-06	-0.00103	515.	0.00293	0.116	-0.341	-0.225	6.35	
2	10.	26.94	-0.821E-06	-0.00090	841.	0.00238	0.438	-0.378	0.060	6.93	
3	22.	24.43	-0.455E-06	-0.00079	1271.	0.00204	0.427	-0.388	0.039	7.44	
4	34.	23.06	-0.325E-06	-0.00074	1624.	0.00191	0.408	-0.388	0.020	7.38	25.5
5	46.	22.12	-0.256E-06	-0.00071	1973.	0.00182	0.409	-0.390	0.019	7.52	25.8
6	58.	21.50	-0.212E-06	-0.00069	2262.	0.00176	0.396	-0.392	0.004	7.43	26.0
7	70.	20.94	-0.180E-06	-0.00067	2545.	0.00171	0.388	-0.392	-0.004	7.46	26.1
8	82.	20.50	-0.156E-06	-0.00065	2780.	0.00167	0.373	-0.389	-0.017	7.41	26.2
9	90.	20.16	-0.148E-06	-0.00064	2946.	0.00164	0.379	-0.389	-0.010	7.43	

RUN: 71571-5 NU= 0.166E-03

N	X	UI	K	F	RD2	CF/2	BETA	B	BETA+B	G	A*
1	2.	29.69	-0.460E-06	0.00000	532.	0.00271	0.141	0.000	0.141	6.89	
2	10.	26.93	-0.867E-06	0.00000	971.	0.00198	0.674	0.000	0.674	8.29	
3	22.	24.57	-0.485E-06	0.00000	1528.	0.00269	0.686	0.000	0.686	8.77	
4	34.	23.26	-0.348E-06	0.00000	1986.	0.00153	0.696	0.000	0.696	8.96	21.4
5	46.	22.27	-0.274E-06	0.00000	2434.	0.00145	0.708	0.000	0.708	9.23	21.7
6	58.	21.36	-0.228E-06	0.00000	2781.	0.00140	0.685	0.000	0.685	9.10	22.0
7	70.	20.74	-0.196E-06	0.00000	3177.	0.00136	0.693	0.000	0.693	9.19	22.2
8	82.	20.35	-0.174E-06	0.00000	3495.	0.00133	0.685	0.000	0.685	9.08	22.3
9	90.	20.05	-0.170E-06	0.00000	3681.	0.00131	0.712	0.000	0.712	9.09	

RUN: 111571-1 NU= 0.161E-03

N	X	UI	K	F	RD2	CF/2	BETA	B	BETA+B	G	A*
1	2.	29.39	-0.444E-06	0.00099	563.	0.00249	0.160	0.397	0.557	7.48	
2	10.	26.52	-0.843E-06	0.00092	1100.	0.00176	0.865	0.523	1.387	9.31	
3	22.	24.26	-0.469E-06	0.00081	1785.	0.00144	0.548	0.563	1.110	10.19	
4	34.	22.90	-0.336E-06	0.00076	2344.	0.00118	1.066	0.643	1.709	10.91	17.8
5	46.	21.98	-0.265E-06	0.00072	2910.	0.00112	1.103	0.643	1.746	11.22	18.2
6	58.	21.19	-0.218E-06	0.00070	3345.	0.00108	1.072	0.648	1.720	11.25	18.5
7	70.	20.61	-0.184E-06	0.00067	3788.	0.00105	1.046	0.638	1.684	11.26	18.8
8	82.	20.23	-0.156E-06	0.00065	4225.	0.00102	1.002	0.636	1.637	11.14	19.0
9	90.	20.09	-0.145E-06	0.00064	4506.	0.00101	1.000	0.635	1.642	11.17	

RUN: 91771-2 NU= 0.166E-03

N	X	UI	K	F	RD2	CF/2	BETA	B	BETA+B	G	A*
1	2.	29.49	-0.467E-06	0.00099	555.	0.00249	0.167	0.398	0.564	7.52	
2	10.	26.89	-0.872E-06	0.00099	1090.	0.00173	0.908	0.572	1.480	9.50	
3	22.	24.30	-0.490E-06	0.00100	1785.	0.00138	1.055	0.725	1.780	10.75	
4	34.	22.87	-0.352E-06	0.00100	2395.	0.00109	1.271	0.917	2.189	11.86	16.7
5	46.	21.80	-0.276E-06	0.00099	2959.	0.00102	1.313	0.971	2.284	12.21	16.9
6	58.	21.41	-0.227E-06	0.00099	3548.	0.00096	1.364	1.032	2.396	12.41	17.0
7	70.	21.13	-0.193E-06	0.00099	4095.	0.00091	1.411	1.114	2.525	12.69	17.0
8	82.	20.36	-0.169E-06	0.00100	4544.	0.00088	1.403	1.139	2.542	12.71	17.2
9	90.	20.16	-0.164E-06	0.00099	4911.	0.00086	1.502	1.154	2.656	12.80	

RUN: 111771-3 NU= 0.160E-03

N	X	UI	K	F	RD2	CF/2	BETA	B	BETA+B	G	A*
1	2.	29.26	-0.452E-06	0.00200	587.	0.00230	0.187	0.871	1.059	8.00	
2	10.	26.59	-0.847E-06	0.00181	1219.	0.00150	1.165	1.207	2.372	10.56	
3	22.	24.11	-0.472E-06	0.00161	2062.	0.00108	1.542	1.491	3.032	12.64	
4	34.	22.78	-0.336E-06	0.00152	2758.	0.00087	1.806	1.751	3.557	13.88	14.5
5	46.	21.79	-0.263E-06	0.00145	3412.	0.00082	1.853	1.768	3.621	14.30	14.8
6	58.	20.96	-0.218E-06	0.00139	3973.	0.00079	1.820	1.757	3.576	14.17	15.2
7	70.	20.46	-0.188E-06	0.00135	4544.	0.00076	1.839	1.769	3.607	14.16	15.4
8	82.	20.00	-0.169E-06	0.00131	5097.	0.00074	1.897	1.765	3.662	14.25	15.5
9	90.	19.73	-0.168E-06	0.00129	5471.	0.00073	2.053	1.771	3.825	14.28	

RUN: 101371-2 NU= 0.164E-03

N	X	UI	K	F	RD2	CF/2	BETA	B	BETA+B	G	A*
1	2.	29.77	-0.454E-06	0.00200	591.	0.00228	0.189	0.877	1.067	7.94	
2	10.	27.05	-0.855E-06	0.00201	1213.	0.00152	1.164	1.322	2.486	10.60	
3	22.	24.64	-0.477E-06	0.00201	2081.	0.00103	1.675	1.951	3.626	13.23	
4	34.	23.31	-0.342E-06	0.00202	2855.	0.00078	2.185	2.603	4.788	15.23	12.9
5	46.	22.36	-0.268E-06	0.00202	3585.	0.00071	2.361	2.860	5.220	15.95	12.9
6	58.	21.53	-0.222E-06	0.00202	4222.	0.00066	2.448	3.064	5.512	16.33	12.9
7	70.	20.97	-0.189E-06	0.00200	4877.	0.00062	2.524	3.205	5.729	16.60	12.9
8	82.	20.62	-0.165E-06	0.00202	5576.	0.00058	2.657	3.457	6.114	16.85	12.8
9	90.	20.43	-0.159E-06	0.00201	6015.	0.00057	2.840	3.543	6.383	17.06	

RUN: 112871-1 NU= 0.163E-03

N	X	UI	K	F	RD2	CF/2	BETA	B	BETA+B	G	A*
1	2.	29.49	-0.445E-06	0.00399	641.	0.00194	0.248	2.057	2.305	9.25	
2	10.	26.66	-0.844E-06	0.00360	1431.	0.00071	3.148	5.070	8.218	17.25	
3	22.	24.18	-0.469E-06	0.00322	2549.	0.00056	4.077	5.745	9.822	20.14	
4	34.	22.85	-0.336E-06	0.00300	3546.	0.00051	4.435	5.882	10.317	20.95	9.2
5	46.	21.77	-0.265E-06	0.00286	4425.	0.00048	4.596	5.972	10.568	21.35	9.5
6	58.	21.04	-0.220E-06	0.00275	5258.	0.00046	4.668	6.020	10.687	21.40	9.8
7	70.	20.55	-0.187E-06	0.00266	6046.	0.00044	4.663	6.039	10.702	21.42	10.0
8	82.	20.13	-0.162E-06	0.00260	6870.	0.00042	4.684	6.152	10.836	21.29	10.2
9	90.	19.81	-0.155E-06	0.00256	7331.	0.00042	4.867	6.161	11.028	21.50	

RUN: 102171-1 NU= 0.162E-03

N	X	UI	K	F	RD2	CF/2	BETA	B	BETA+B	G	A*
1	2.	29.71	-0.455E-06	0.00399	639.	0.00194	0.251	2.052	2.303	9.17	
2	10.	27.02	-0.850E-06	0.00402	1472.	0.00073	3.179	5.507	8.685	17.06	
3	22.	24.57	-0.470E-06	0.00402	2757.	0.00042	6.117	9.502	15.620	24.27	
4	34.	23.18	-0.331E-06	0.00400	3891.	0.00035	7.333	11.296	18.628	26.78	6.0
5	46.	22.13	-0.255E-06	0.00402	4986.	0.00031	8.252	12.985	21.237	28.55	5.9
6	58.	21.46	-0.209E-06	0.00401	6040.	0.00028	8.947	14.218	23.165	29.76	5.8
7	70.	20.97	-0.179E-06	0.00399	7146.	0.00026	9.625	15.250	24.875	30.42	5.7
8	82.	20.48	-0.160E-06	0.00400	8207.	0.00025	10.301	16.287	26.588	30.69	5.7
9	90.	20.27	-0.160E-06	0.00399	8785.	0.00024	11.319	16.686	28.005	31.08	

9.3 Strong Adverse Pressure Gradient, $m = -.20$

RUN: 110971-1 NU= 0.161E-03

N	X	UI	K	F	RD2	CF/2	BETA	B	BETA+B	G	A*
1	2.	29.13	-0.699E-06	0.00000	541.	0.00269	0.219	0.000	0.219	6.93	
2	10.	25.70	-0.127E-05	0.00000	1024.	0.00174	1.201	0.000	1.201	9.05	
3	22.	22.31	-0.702E-06	0.00000	1727.	0.00129	1.559	0.000	1.559	11.05	
4	34.	20.53	-0.504E-06	0.00000	2331.	0.00119	1.626	0.000	1.626	11.43	19.1
5	46.	19.39	-0.396E-06	0.00000	2845.	0.00114	1.630	0.000	1.630	11.62	19.8
6	58.	18.55	-0.328E-06	0.00000	3269.	0.00110	1.577	0.000	1.577	11.48	20.2
7	70.	17.97	-0.282E-06	0.00000	3673.	0.00107	1.547	0.000	1.547	11.39	20.5
8	82.	17.42	-0.249E-06	0.00000	4139.	0.00103	1.575	0.000	1.575	11.43	20.7
9	90.	17.10	-0.242E-06	0.00000	4578.	0.00101	1.750	0.000	1.750	11.72	

RUN: 21572-5 NU= 0.160E-03

N	X	UI	K	F	RD2	CF/2	BETA	B	BETA+B	G	A*
1	2.	29.42	-0.685E-06	-0.00201	519.	0.00276	0.194	-0.728	-0.535	6.37	
2	10.	26.05	-0.125E-05	-0.00177	801.	0.00246	0.611	-0.720	-0.109	6.72	
3	22.	22.55	-0.690E-06	-0.00159	1250.	0.00221	0.590	-0.719	-0.129	7.20	
4	34.	20.69	-0.499E-06	-0.00151	1608.	0.00208	0.571	-0.726	-0.155	7.12	28.8
5	46.	19.49	-0.396E-06	-0.00143	1911.	0.00198	0.565	-0.722	-0.158	7.25	29.2
6	58.	18.73	-0.330E-06	-0.00138	2121.	0.00193	0.524	-0.715	-0.191	7.01	29.5
7	70.	18.10	-0.283E-06	-0.00132	2381.	0.00186	0.518	-0.710	-0.192	6.96	29.5
8	82.	17.53	-0.246E-06	-0.00130	2619.	0.00182	0.505	-0.714	-0.210	7.00	29.8
9	90.	17.02	-0.236E-06	-0.00129	2860.	0.00179	0.542	-0.721	-0.178	7.20	

RUN: 120771-1 X= 2. Z= 0. U1 = 31.21 D1 = C.C504 BETA=-0.000 PC2 = 535. CF/2= 0.00249 D2 = 0.0328 B = 0.000 H = 1.538 F = 0.00000 OC = 1.0089 P+ = -0.00000 G = 7.002 K = 0.139E-08 D99 = 0.2871 W+ = 0.0000

Table with 11 columns: Y, U, Y/DC, U/UI, (U-UI)/U*, Y+, U+, TAL, TAU, U+U, TAU,LAH. Rows contain numerical data for various parameters.

RUN: 120771-1 X=10. Z= 0. U1 = 31.13 D1 = 0.0772 BETA=-0.001 RD2 = 849. CF/2= 0.00222 D2 = 0.0521 B = 0.000 H = 1.484 F = 0.00000 OC = 1.6383 P+ = -0.0000 G = 6.913 K = 0.123E-08 D99 = 0.4225 W+ = 0.0000

Table with 11 columns: Y, U, Y/DC, U/UI, (U-UI)/U*, Y+, U+, TAL, TAU, U+U, TAU,LAH. Rows contain numerical data for various parameters.

RUN: 120771-1 X=22. Z= 0. U1 = 31.14 D1 = C.1135 BETA=-C.001 RD2 = 1251. CF/2= 0.00202 D2 = 0.0758 B = 0.000 H = 1.476 F = 0.00000 OC = 2.9260 P+ = -0.00000 G = 7.201 K = 0.924E-09 D99 = 0.6242 W+ = 0.0000

Table with 11 columns: Y, U, Y/DC, U/UI, (U-UI)/U*, Y+, U+, TAL, TAU, U+U, TAU,LAH. Rows contain numerical data for various parameters.

RUN: 120771-1 X=34. Z= 0. U1 = 31.05 D1 = 0.1412 BETA=-C.001 RD2 = 1588. CF/2= 0.00190 D2 = 0.0577 B = C.000 H = 1.444 F = 0.00000 OC = 3.2389 P+ = -0.00000 G = 7.069 K = 0.563E-09 D99 = 0.7854 W+ = 0.0000

Table with 11 columns: Y, U, Y/DC, U/UI, (U-UI)/U*, Y+, U+, TAL, TAU, U+U, TAU,LAH. Rows contain numerical data for various parameters.

RUN: 120771-1 X=66. Z= 0.

UI = 31.04 DI = 0.1709 BETA=0.000 RD2 = 1926.
CF/Z= 0.00181 D2 = 0.1185 B = 0.000 H = 1.442
F = 0.00000 CC = 4.0149 P = -0.0000 G = 7.199
K = 0.138E-09 D99 = 0.9590 V0+ = 0.0000

Table with columns: Y, U, Y/DC, U/UI, (U-UI)/U*, Y+, U+, TAU, TAU/LAM. Rows include data points for various Y values from 0.005 to 1.424.

RUN: 120771-1 X=58. Z= 0.

UI = 31.13 DI = 0.1968 BETA= 0.001 RD2 = 2240.
CF/Z= 0.00174 D2 = 0.1375 B = 0.000 H = 1.432
F = 0.00000 CC = 4.7124 P = -0.0000 G = 7.219
K = -0.351E-09 D99 = 1.1045 V0+ = 0.0000

Table with columns: Y, U, Y/DC, U/UI, (U-UI)/U*, Y+, U+, TAU, TAU/LAM. Rows include data points for various Y values from 0.005 to 1.706.

RUN: 120771-1 X=70. Z= 0.

UI = 31.04 DI = 0.2295 BETA= 0.002 RD2 = 2574.
CF/Z= 0.00168 D2 = 0.1584 B = 0.000 H = 1.424
F = 0.00000 CC = 5.4933 P = 0.0000 G = 7.249
K = -0.902E-09 D99 = 1.2755 V0+ = 0.0000

Table with columns: Y, U, Y/DC, U/UI, (U-UI)/U*, Y+, U+, TAU, TAU/LAM. Rows include data points for various Y values from 0.005 to 1.878.

RUN: 120771-1 X=82. Z= 0.

UI = 31.07 DI = 0.2533 BETA= 0.004 RD2 = 2919.
CF/Z= 0.00163 D2 = 0.1794 B = 0.000 H = 1.412
F = 0.00000 CC = 6.2686 P = 0.0000 G = 7.218
K = -0.152E-08 D99 = 1.4880 V0+ = 0.0000

Table with columns: Y, U, Y/DC, U/UI, (U-UI)/U*, Y+, U+, TAU, TAU/LAM. Rows include data points for various Y values from 0.005 to 2.096.

RUN: 120771-1 X=90. Z=0.

U1 = 31.06 D1 = 0.2670 BETA = 0.005 RDZ = 3093.
CF/Z = 0.00161 D2 = 0.1902 B = 0.0000 H = 1.404
F = 0.00000 DC = 6.6566 P+ = 0.0000 G = 7.169
K = -0.196E-08 D99 = 1.5810 V0+ = 0.00000

Table with columns Y, U, Y/DC, U/U1, (U-U1)/U1, Y+, U+, TAL, TAULAH. Contains multiple rows of numerical data.

RUN: 100571-1 X=2. Z=0.

U1 = 30.95 D1 = 0.0524 BETA = -0.002 RDZ = 525.
CF/Z = 0.00217 D2 = 0.0334 B = 0.475 H = 1.570
F = 0.00103 DC = 1.1252 P+ = -0.0000 G = 7.799
K = 0.489E-08 D99 = 0.2946 V0+ = 0.00221

Table with columns Y, U, Y/DC, U/U1, (U-U1)/U1, Y+, U+, TAL, TAULAH. Contains multiple rows of numerical data.

RUN: 100571-1 X=10. Z=0.

U1 = 30.28 D1 = 0.0822 BETA = -0.002 RDZ = 802.
CF/Z = 0.00193 D2 = 0.0521 B = 0.524 H = 1.577
F = 0.00101 DC = 1.8720 P+ = -0.00000 G = 8.339
K = 0.303E-08 D99 = 0.3951 V0+ = 0.0230

Table with columns Y, U, Y/DC, U/U1, (U-U1)/U1, Y+, U+, TAL, TAULAH. Contains multiple rows of numerical data.

RUN: 100571-1 X=22. Z=0.

U1 = 32.15 D1 = 0.1523 BETA = -0.001 RDZ = 1623.
CF/Z = 0.00157 D2 = 0.0493 B = 0.645 H = 1.533
F = 0.00101 DC = 3.8493 P+ = -0.0000 G = 8.791
K = 0.796E-09 D99 = 0.7549 V0+ = 0.0255

Table with columns Y, U, Y/DC, U/U1, (U-U1)/U1, Y+, U+, TAL, TAULAH. Contains multiple rows of numerical data.

RUN: 100571-1 X=34. Z= 0.

UI = 30.51 D1 = 0.1811 BETA= 0.001 F02 = 1.078.
CF/Z= 0.00150 D2 = 0.1211 B = 0.466 H = 1.495
F = 0.00100 DC = 6.8750 P+ = 0.0000 G = 8.551
K = -0.760E-05 D99 = 0.9212 V0+ = 0.0258

Table with columns Y, U, Y/DC, U/II, (U-UI)/U*, Y+, U+, TAU, TAUAM. Contains multiple rows of numerical data.

RUN: 100571-1 X=58. Z= 0.

UI = 31.17 D1 = 0.2688 BETA= 0.006 F02 = 2.857.
CF/Z= 0.00132 D2 = 0.1803 B = 0.775 H = 1.491
F = 0.00102 DC = 7.4113 P+ = 0.0000 G = 9.075
K = -0.186E-08 D99 = 1.3490 V0+ = 0.0281

Table with columns Y, U, Y/DC, U/II, (U-UI)/U*, Y+, U+, TAU, TAUAM. Contains multiple rows of numerical data.

RUN: 100571-1 X=46. Z= 0.

UI = 31.28 D1 = 0.2275 BETA= 0.004 F02 = 2.404.
CF/Z= 0.00138 D2 = 0.1512 B = 0.744 H = 1.508
F = 0.00103 DC = 6.1264 P+ = 0.0000 G = 9.049
K = -0.164E-08 D99 = 1.1291 V0+ = 0.0277

Table with columns Y, U, Y/DC, U/II, (U-UI)/U*, Y+, U+, TAU, TAUAM. Contains multiple rows of numerical data.

RUN: 100571-1 X=70. Z= 0.

UI = 31.10 D1 = 0.3135 BETA= 0.006 F02 = 3.326.
CF/Z= 0.00125 D2 = 0.2104 B = 0.842 H = 1.492
F = 0.00105 DC = 8.8911 P+ = 0.0000 G = 9.336
K = -0.139E-08 D99 = 1.5565 V0+ = 0.0297

Table with columns Y, U, Y/DC, U/II, (U-UI)/U*, Y+, U+, TAU, TAUAM. Contains multiple rows of numerical data.

RUN: 100571-1 X=82. Z= 0.

UI = 31.18 O1 = 0.1531 BETA= 0.001 RDZ = 3.776.
CF/2= 0.00120 O2 = 0.2383 B = 0.877 H = 1.482
F = 0.00105 DC = 13.2032 P = 0.0000 G = 9.397
K = -0.254F-09 D99 = 1.8018 V0+ = 0.0303

Table with columns: Y, U, Y/DC, U/UI, (U-UI)/U*, Y+, U+, TAU, TAU*AM. Rows include data points for various Y and U values, such as 0.005, 0.012, 0.014, etc.

RUN: 90171-2 X= 2. Z= 0.

UI = 31.66 O1 = 0.0579 BETA= 0.000 RDZ = 566.
CF/2= 0.00183 O2 = 0.0398 B = 1.090 H = 1.618
F = 0.00200 DC = 1.3528 P = 0.0000 G = 8.914
K = -0.873E-09 D99 = 0.3028 V0+ = 0.0467

Table with columns: Y, U, Y/DC, U/UI, (U-UI)/U*, Y+, U+, TAU*AM. Rows include data points for various Y and U values, such as 0.004, 0.005, 0.006, etc.

RUN: 100571-1 X=90. Z= 0.

UI = 31.02 O1 = 0.3730 BETA=-0.004 RDZ = 3.996.
CF/2= 0.00118 O2 = 0.2535 B = 0.852 H = 1.442
F = 0.00106 DC = -13.8605 P = -0.0070 G = 9.330
K = -0.879E-C9 D99 = 1.8770 V0+ = 0.0303

Table with columns: Y, U, Y/DC, U/UI, (U-UI)/U*, Y+, U+, TAU, TAU*AM. Rows include data points for various Y and U values, such as 0.007, 0.008, 0.009, etc.

RUN: 90171-2 X=10. Z= 0.

UI = 31.57 O1 = 0.1047 BETA= 0.001 RDZ = 1034.
CF/2= 0.00150 O2 = 0.0657 B = 1.334 H = 1.595
F = 0.00200 DC = 2.7040 P = 0.0000 G = 9.631
K = -0.109E-08 D99 = 0.4839 V0+ = 0.0517

Table with columns: Y, U, Y/DC, U/UI, (U-UI)/U*, Y+, U+, TAU, TAU*AM. Rows include data points for various Y and U values, such as 0.005, 0.006, 0.007, etc.

RUN: 90171-2 X=22. Z= 0.

UI = 31.57 D1 = 0.1670 BETA= 0.002 RDZ = 1661.
CF/2= 0.00127 D2 = 0.1055 B = 1.574 H = 1.584
F = 0.00200 DC = 4.6865 P+ = 0.0000 G = 10.343
K = -0.113E-08 D99 = 0.7460 V0+ = 0.0561

Table with 12 columns: Y, U, Y/DC, U/UI, (U-UI)/U*, Y+, U+, TAU, TAU/LAM. Contains multiple rows of numerical data.

RUN: 90171-2 X=34. Z= 0.

UI = 31.62 D1 = 0.2233 BETA= 0.003 RDZ = 2259.
CF/2= 0.00114 D2 = 0.1432 B = 1.759 H = 1.560
F = 0.00200 DC = 6.6207 P+ = 0.0000 G = -10.640
K = -0.945E-09 D99 = 1.0030 V0+ = 0.0593

Table with 12 columns: Y, U, Y/DC, U/UI, (U-UI)/U*, Y+, U+, TAU, TAU/LAM. Contains multiple rows of numerical data.

RUN: 90171-2 X=46. Z= 0.

UI = 31.48 D1 = 0.2837 BETA= 0.002 RDZ = 2843.
CF/2= 0.00104 D2 = 0.1810 B = 1.915 H = 1.567
F = 0.00200 DC = 8.7785 P+ = 0.0000 G = 11.200
K = -0.508E-09 D99 = 1.2818 V0+ = 0.0619

Table with 12 columns: Y, U, Y/DC, U/UI, (U-UI)/U*, Y+, U+, TAU, TAU/LAM. Contains multiple rows of numerical data.

RUN: 90171-2 X=58. Z= 0.

UI = 31.38 D1 = 0.3359 BETA= -0.001 RDZ = 3384.
CF/2= 0.00098 D2 = 0.2161 B = 2.045 H = 1.554
F = 0.00200 DC = 10.7416 P+ = -0.0000 G = -11.405
K = 0.183E-09 D99 = 1.5208 V0+ = 0.0640

Table with 12 columns: Y, U, Y/DC, U/UI, (U-UI)/U*, Y+, U+, TAU, TAU/LAM. Contains multiple rows of numerical data.

RUN: 90171-2 X=70. Z= 0.

UI = 31.33 D1 = 0.3860 BETA=-0.007 RDZ = 3918.
CF/2= 0.00092 O2 = 0.2506 B = 2.163 H = 1.540
F = 0.00200 DC = 12.6946 P+ = -0.0000 G = -11.537
K = 0.113E-08 D99 = 1.7713 V0+ = 0.0658

Table with columns: Y, U, Y/DC, U/UI, (U-UI)/U0, Y+, U+, TAU, TAU/LAM. Rows include data points for various Y values from 0.005 to 2.608.

RUN: 90171-2 X=82. Z= 0.

UI = 31.34 D1 = 0.4364 BETA=-0.018 RDZ = 4450.
CF/2= 0.00088 O2 = 0.2846 B = 2.255 H = 1.534
F = 0.00199 DC = 14.6925 P+ = -0.0001 G = -11.712
K = 0.232E-08 D99 = 2.0255 V0+ = 0.0670

Table with columns: Y, U, Y/DC, U/UI, (U-UI)/U0, Y+, U+, TAU, TAU/LAM. Rows include data points for various Y values from 0.005 to 2.704.

RUN: 90171-2 X=90. Z= 0.

UI = 31.28 D1 = 0.4619 BETA=-0.027 RDZ = 4742.
CF/2= 0.00086 O2 = 0.3038 B = 2.330 H = 1.521
F = 0.00200 DC = 15.7674 P+ = -0.0001 G = -11.687
K = 0.326E-08 D99 = 2.1644 V0+ = 0.0683

Table with columns: Y, U, Y/DC, U/UI, (U-UI)/U0, Y+, U+, TAU, TAU/LAM. Rows include data points for various Y values from 0.007 to 2.916.

RUN: 90071-3 X= 2. Z= 0.

UI = 31.62 D1 = 0.0666 BETA=-0.001 RDZ = 626.
CF/2= 0.00133 O2 = 0.0394 B = 2.829 H = 1.689
F = 0.00375 DC = 1.8285 P+ = -0.0000 G = -11.201
K = 0.105E-08 D99 = 0.3159 V0+ = 0.1030

Table with columns: Y, U, Y/DC, U/UI, (U-UI)/U0, Y+, U+, TAU, TAU/LAM. Rows include data points for various Y values from 0.004 to 0.355.

RUN: 90871-3 X=10. Z= 0.

UI = 31.34 D1 = 0.1369 BETA=-0.002 RD2 = 1298.
CF/Z= 0.00098 D2 = 0.0799 B = 3.809 H = 1.713
F = 0.00375 DC = 6.3628 P+ = -0.0000 G = -13.244
K = 0.851E-09 D99 = 0.5362 V0+ = 0.1195

Table with columns: Y, U, Y/DC, U/UI, (U-UI)/U*, Y+, U+, TAU, TAU/LAM. Contains multiple rows of numerical data.

RUN: 90871-3 X=22. Z= 0.

UI = 31.52 D1 = 0.2348 BETA=-0.003 RD2 = 2172.
CF/Z= 0.00077 D2 = 0.1377 B = 4.897 H = 1.712
F = 0.00375 DC = 8.4864 P+ = -0.0000 G = -15.025
K = 0.570E-09 D99 = 0.8914 V0+ = 0.1355

Table with columns: Y, U, Y/DC, U/UI, (U-UI)/U*, Y+, U+, TAU, TAU/LAM. Contains multiple rows of numerical data.

RUN: 90871-3 X=34. Z= 0.

UI = 31.50 D1 = 0.3271 BETA=-0.002 RD2 = 3030.
CF/Z= 0.00065 D2 = 0.1915 B = 5.761 H = 1.708
F = 0.00375 DC = 12.8194 P+ = -0.0000 G = -16.246
K = 0.306E-09 D99 = 1.2300 V0+ = 0.1470

Table with columns: Y, U, Y/DC, U/UI, (U-UI)/U*, Y+, U+, TAU, TAU/LAM. Contains multiple rows of numerical data.

RUN: 90871-3 X=46. Z= 0.

UI = 31.39 D1 = 0.423P BETA=-0.001 RD2 = 3863.
CF/Z= 0.00057 D2 = 0.2450 B = 6.554 H = 1.730
F = 0.00376 DC = 17.6945 P+ = -0.0000 G = -17.616
K = 0.600E-10 D99 = 1.5807 V0+ = 0.1570

Table with columns: Y, U, Y/DC, U/UI, (U-UI)/U*, Y+, U+, TAU, TAU/LAM. Contains multiple rows of numerical data.

RUN: 90871-3 X=58. Z= 0.

UI = 31.40 D1 = 0.5091 BETA= 0.003 RD2 = 4700.
CF/Z= 0.00052 D2 = 0.2980 B = 7.226 H = 1.709
F = 0.00375 DC = 22.3489 P+ = 0.0000 G = -18.207
K = -0.169E-09 D99 = 1.9347 VC+ = 0.1646

Table with 10 columns: Y, U, Y/DC, U/UI, (U-U1)/U*, Y+, U+, TAU, TAU/LAM. Contains multiple rows of numerical data.

RUN: 90871-3 X=70. Z= 0.

UI = 31.31 D1 = 0.5969 BETA= 0.007 RD2 = 5494.
CF/Z= 0.00048 D2 = 0.3494 B = 7.861 H = 1.708
F = 0.00375 DC = 22.347 P+ = 0.0000 G = -18.982
K = -0.380E-C9 D99 = 2.2310 VC+ = 0.1717

Table with 10 columns: Y, U, Y/DC, U/UI, (U-U1)/U*, Y+, U+, TAU, TAU/LAM. Contains multiple rows of numerical data.

RUN: 90871-3 X=82. Z= 0.

UI = 30.94 D1 = 0.4716 BETA= 0.013 RD2 = 6173.
CF/Z= 0.00045 D2 = 0.3972 B = 8.381 H = 1.491
F = 0.00375 DC = 31.7522 P+ = 0.0001 G = -19.318
K = -0.575E-09 D99 = 2.5111 VC+ = 0.1773

Table with 10 columns: Y, U, Y/DC, U/UI, (U-U1)/U*, Y+, U+, TAU, TAU/LAM. Contains multiple rows of numerical data.

RUN: 90871-3 X=90. Z= 0.

UI = 30.98 D1 = 0.7147 BETA= 0.018 RD2 = 6667.
CF/Z= 0.00043 D2 = 0.4285 B = 8.402 H = 1.668
F = 0.00376 DC = 34.5813 P+ = 0.0001 G = -19.379
K = -0.694E-09 D99 = 2.7922 VC+ = 0.1819

Table with 10 columns: Y, U, Y/DC, U/UI, (U-U1)/U*, Y+, U+, TAU, TAU/LAM. Contains multiple rows of numerical data.

RUN: 92271-5 X=2. Z=0.
UI = 31.44 D1 = 0.0856 BETA=-0.004
CF/Z = 0.00106 O2 = 0.0473 B = 7.557
F = 0.00801 DC = 2.6280 P+ = 0.0001
K = 0.347E-08 D99 = 0.3556 VU+ = 0.2460

R02 = 750.
H = 1.808
G = 13.728

RUN: 92271-5 X=10. Z=0.
UI = 31.47 D1 = 0.2261 BETA=-0.026
CF/Z = 0.00031 O2 = 0.1124 B = 25.492
F = 0.00796 DC = 12.6839 P+ = 0.00004
K = 0.228E-08 D99 = 0.6839 VU+ = 0.4505

R02 = 1783.
H = 1.964
G = 28.211

Table with columns Y, U, Y/DC, U/UI, (U-UI)/U*, Y+, U+, TAULAP. Contains data for 100 iterations.

Table with columns Y, U, Y/DC, U/UI, (U-UI)/U*, Y+, U+, TAULAP. Contains data for 100 iterations.

RUN: 92271-5 X=22. Z=0.
UI = 31.46 D1 = 0.4368 BETA=-0.026
CF/Z = 0.00020 O2 = 0.2112 B = 40.032
F = 0.00804 DC = 30.8216 P+ = 0.00003
K = 0.762E-09 D99 = 1.2546 VU+ = 0.5873

R02 = 3349.
H = 2.068
G = 36.446

RUN: 92271-5 X=34. Z=0.
UI = 31.45 D1 = 0.6386 BETA=0.026
CF/Z = 0.00016 O2 = 0.3076 B = 49.745
F = 0.00801 DC = 50.3253 P+ = 0.0002
K = -0.417E-09 D99 = 1.8358 VU+ = 0.6312

R02 = 4876.
H = 2.076
G = 40.845

Table with columns Y, U, Y/DC, U/UI, (U-UI)/U*, Y+, U+, TAULAP. Contains data for 100 iterations.

Table with columns Y, U, Y/DC, U/UI, (U-UI)/U*, Y+, U+, TAULAP. Contains data for 100 iterations.

RUN: 92271-5 X=46. Z=0.

UI = 31.51 01 = 0.8303 BETA= 0.118
CF/2= 0.00014 D2 = 0.3993 B = 57.014
F = 0.00802 DC = 70.0101 P = 0.0008
K = -0.126E-08 D99 = 2.3793 VD* = 0.6762

RD2 = 6340.
H = 2.080
G = +3.770

Table with columns: Y, U, Y/DC, U/UI, (U-UI)/U*, Y+, U+, TAU/LAM. Rows include data points for various Y and U values, such as 0.028, 0.035, 0.044, etc.

RUN: 92271-5 X=58. Z=0.

UI = 31.51 01 = 1.0066 BETA= 0.220
CF/2= 0.00013 D2 = 0.4931 B = 61.801
F = 0.00798 DC = 89.5819 P = 0.0012
K = -0.178E-08 D99 = 2.9569 VD* = 0.7023

RD2 = 7830.
H = 2.041
G = +44.891

Table with columns: Y, U, Y/DC, U/UI, (U-UI)/U*, Y+, U+, TAU/LAM. Rows include data points for various Y and U values, such as 0.031, 0.041, 0.051, etc.

RUN: 92271-5 X=70. Z=0.

UI = 31.48 01 = 1.1924 BETA= 0.305
CF/2= 0.00012 D2 = 0.5879 B = 65.634
F = 0.00798 DC = 108.1 P = 0.0015
K = -0.196E-08 D99 = 3.4972 VD* = 0.7237

RD2 = 9327.
H = 2.028
G = +5.977

Table with columns: Y, U, Y/DC, U/UI, (U-UI)/U*, Y+, U+, TAU/LAM. Rows include data points for various Y and U values, such as 0.034, 0.044, 0.054, etc.

RUN: 92271-5 X=82. Z=0.

UI = 31.47 01 = 1.3625 BETA= 0.335
CF/2= 0.00012 D2 = 0.6802 B = 66.401
F = 0.00799 DC = 126.1 P = 0.0014
K = -0.181E-08 D99 = 4.1139 VD* = 0.7393

RD2 = 11747.
H = 2.003
G = +6.334

Table with columns: Y, U, Y/DC, U/UI, (U-UI)/U*, Y+, U+, TAU/LAM. Rows include data points for various Y and U values, such as 0.037, 0.047, 0.057, etc.

RUN: 122271-2 X=2. Z= C.

UI = 20.32 O1 = 0.0428 BETA = 0.073 RD2 = 451.
CF/2 = 0.0397 O2 = 0.0297 B = -1.006 H = 1.438
F = -0.00399 OC = 0.0790 P+ = 0.002 G = 4.839
K = -0.446E-06 O99 = 0.2833 V0+ = -0.063

RUN: 122271-2 X=10. Z= 0.

UI = 26.81 O1 = 0.0568 BETA = 0.174 RD2 = 557.
CF/2 = 0.00380 O2 = 0.0402 B = -1.046 H = 1.414
F = -0.00398 OC = 0.0916 P+ = 0.004 G = 4.746
K = -0.838E-06 O99 = 0.3956 V0+ = -0.065

Table with columns: Y, U, Y/DC, U/U1, (U-U1)/U*, Y+, U+, TAU, TAU/LAM. Contains 100 rows of numerical data.

Table with columns: Y, U, Y/DC, U/U1, (U-U1)/U*, Y+, U+, TAU, TAU/LAM. Contains 100 rows of numerical data.

RUN: 122271-2 X=22. Z= 0.

UI = 24.29 O1 = 0.0777 BETA = 0.111 RD2 = 667.
CF/2 = 0.0393 O2 = 0.0528 B = -1.041 H = 1.375
F = -0.00399 OC = 0.1174 P+ = 0.002 G = 4.431
K = -0.446E-06 O99 = 0.5466 V0+ = -0.064

RUN: 122271-2 X=34. Z= 0.

UI = 22.95 O1 = 0.0806 BETA = 0.054 RD2 = 712.
CF/2 = 0.00381 O2 = 0.0601 B = -1.050 H = 1.342
F = -0.00400 OC = 0.1306 P+ = 0.001 G = 4.133
K = -0.335E-06 O99 = 0.6494 V0+ = -0.065

Table with columns: Y, U, Y/DC, U/U1, (U-U1)/U*, Y+, U+, TAU, TAU/LAM. Contains 100 rows of numerical data.

Table with columns: Y, U, Y/DC, U/U1, (U-U1)/U*, Y+, U+, TAU, TAU/LAM. Contains 100 rows of numerical data.

RUN: 122271-2 X=46. Z=0.

UI = 22.07 D1 = 0.0888 BETA= 0.070 RD2 = 761.
CF/Z = 0.00379 D2 = 0.0667 B = -1.059 H = 1.331
F = -0.00401 DC = 1.4433 P+ = 0.001 G = 4.042
K = -0.261E-06 D99 = 0.7610 V0+ = -0.065

Table with columns: Y, U, Y/DC, U/U1, (U-U1)/U*, Y+, U+, TAU, TAU/LAM. Contains multiple rows of numerical data.

RUN: 122271-2 X=70. Z=0.

UI = 20.77 D1 = 0.0953 BETA= 0.051 RD2 = 780.
CF/Z = 0.00376 D2 = 0.0734 B = -1.061 H = 1.298
F = -0.00399 DC = 1.5536 P+ = 0.001 G = 3.739
K = -0.147E-06 D99 = 0.9165 V0+ = -0.065

Table with columns: Y, U, Y/DC, U/U1, (U-U1)/U*, Y+, U+, TAU, TAU/LAM. Contains multiple rows of numerical data.

RUN: 122271-2 X=58. Z=0.

UI = 21.45 D1 = 0.0923 BETA= 0.059 RD2 = 773.
CF/Z = 0.00377 D2 = 0.0697 B = -1.059 H = 1.325
F = -0.00399 DC = 1.5037 P+ = 0.001 G = 3.991
K = -0.218E-06 D99 = 0.8322 V0+ = -0.065

Table with columns: Y, U, Y/DC, U/U1, (U-U1)/U*, Y+, U+, TAU, TAU/LAM. Contains multiple rows of numerical data.

RUN: 122271-2 X=82. Z=0.

UI = 20.38 D1 = 0.1007 BETA= 0.046 RD2 = 814.
CF/Z = 0.00375 D2 = 0.0772 B = -1.065 H = 1.304
F = -0.00399 DC = 1.6497 P+ = 0.001 G = 3.410
K = -0.194E-06 D99 = 0.9870 V0+ = -0.065

Table with columns: Y, U, Y/DC, U/U1, (U-U1)/U*, Y+, U+, TAU, TAU/LAM. Contains multiple rows of numerical data.

RUN: 122771-2 X=90. Z= 0.

UI = 20.14 D1 = 0.1016 BETA= 0.045 RDZ = 822.
CF/2= 0.00375 D2 = 0.0790 B = -1.068 H = 1.286
F = -0.00401 D3 = 1.5874 P+ = 0.0011 G = 3.629
K = -0.160E-06 D99 = 1.0294 V0+ = -0.065

Table with columns: Y, U, Y/DC, U/UT, (U-UI)/U*, Y+, U+, TAUAM. Rows contain numerical data for various points.

RUN: 122771-3 X= 2. Z= 0.

UI = 29.29 D1 = 0.0451 BETA= 0.078 RDZ = 469.
CF/2= 0.00385 D2 = 0.0305 B = -1.027 H = 1.466
F = -0.00359 D3 = 0.1213 P+ = 0.0018 G = 5.055
K = -0.445E-C6 D99 = 0.2880 V0+ = -0.0640

Table with columns: Y, U, Y/DC, U/UT, (U-UI)/U*, Y+, U+, TAUAM. Rows contain numerical data for various points.

RUN: 122771-3 X=10. Z= 0.

UI = 26.80 D1 = 0.0555 BETA= 0.184 RDZ = 507.
CF/2= 0.00369 D2 = 0.0576 B = -0.576 H = 1.432
F = -0.00360 D3 = 0.5625 P+ = 0.0037 G = 4.906
K = -0.836E-C6 D99 = 0.1977 V0+ = -0.0593

Table with columns: Y, U, Y/DC, U/UT, (U-UI)/U*, Y+, U+, TAUAM. Rows contain numerical data for various points.

RUN: 122771-3 X=22. Z= 0.

UI = 24.20 D1 = 0.0704 BETA= 0.137 RDZ = 700.
CF/2= 0.00340 D2 = 0.0571 B = -0.544 H = 1.396
F = -0.00322 D3 = 1.3676 P+ = 0.0023 G = 4.864
K = -0.465E-C6 D99 = 0.5472 V0+ = -0.0552

Table with columns: Y, U, Y/DC, U/UT, (U-UI)/U*, Y+, U+, TAUAM. Rows contain numerical data for various points.

RUN: 122771-3 X=34. Z=0.

UI = 22.97 O1 = C.0044 BETA = 0.118 RDZ = 843.
CF/2 = 0.00322 C2 = 0.0708 B = -0.930 H = 1.362
F = -0.00300 DC = 1.658F P = 0.0018 G = 4.683
K = -0.331E-06 OC = 0.6896 V0 = -0.0528

Table with 12 columns: Y, U, Y/DC, U/UT, (U-UT)/U*, Y+, U+, TAU, TAU*AM. Rows of numerical data.

RUN: 122771-3 X=58. Z=0.

UI = 21.30 O1 = 0.1298 BETA = 0.099 RDZ = 1647.
CF/2 = 0.00301 C2 = 0.0548 B = -0.916 H = 1.358
F = -0.00276 DC = 2.3462 P = 0.0013 G = 4.605
K = -0.210E-06 OC = 0.9474 V0 = -0.0503

Table with 12 columns: Y, U, Y/DC, L/LI, (U-LI)/U*, Y+, U+, TAU, TAU*AM. Rows of numerical data.

RUN: 122771-3 X=46. Z=0.

UI = 21.99 O1 = 0.1168 BETA = 0.110 RDZ = 570.
CF/2 = 0.00310 C2 = 0.0851 B = -0.926 H = 1.374
F = -0.00267 DC = 2.0586 P = 0.0015 G = 4.887
K = -0.257E-06 OC = 0.8314 V0 = -0.0515

Table with 12 columns: Y, U, Y/DC, U/UT, (U-UT)/U*, Y+, U+, TAU, TAU*AM. Rows of numerical data.

RUN: 122771-3 X=70. Z=0.

UI = 20.77 O1 = 0.1449 BETA = 0.094 RDZ = 1167.
CF/2 = 0.00293 C2 = 0.1084 B = -0.915 H = 1.337
F = -0.00308 DC = 2.2452 P = 0.0011 G = 4.655
K = -0.176E-06 OC = 1.0951 V0 = -0.0495

Table with 12 columns: Y, U, Y/DC, L/LI, (U-LI)/U*, Y+, U+, TAU, TAU*AM. Rows of numerical data.

RUN: 122771-3 X=E2. Z=0.

UI = 20.35 O1 = 0.1597 BETA = 0.089 RD2 = 1.58.
CF/2 = 0.00286 O2 = 0.1193 B = -0.907 H = 1.339
F = -0.00259 O3 = 2.5887 P = 0.0010 G = 4.739
K = -0.151E-06 O9 = 1.2074 VO = -0.0465

Table with columns: Y, U, Y/DC, U/UI, (U-UI)/U*, Y+, U+, TAU, TAU/LAM. Rows contain numerical data for various Y values from 0.005 to 1.596.

RUN: 122771-3 X=E0. Z=C.

UI = 20.01 O1 = 0.1674 BETA = 0.089 RD2 = 1.314.
CF/2 = 0.00282 O2 = 0.1264 B = -0.906 H = 1.323
F = -0.00296 O3 = 3.1507 DC = 1.1507 P = 0.0010 G = 4.589
K = -0.144E-06 O9 = 1.2588 VO = -0.0482

Table with columns: Y, U, Y/DC, U/UI, (U-UI)/U*, Y+, U+, TAU, TAU/LAM. Rows contain numerical data for various Y values from 0.007 to 1.913.

RUN: 121671-3 X=2. Z=0.

UI = 29.30 O1 = 0.0495 BETA = 0.104 RD2 = 510.
CF/2 = 0.00321 O2 = 0.0330 B = 1.4498 H = 1.4498
F = -0.00190 O3 = 0.8706 P = 0.002 G = 5.855
K = -0.461E-06 O9 = 0.2973 VO = -0.035

Table with columns: Y, U, Y/DC, U/UI, (U-UI)/U*, Y+, U+, TAU, TAU/LAM. Rows contain numerical data for various Y values from 0.004 to 0.950.

RUN: 121671-3 X=10. Z=0.

UI = 26.95 O1 = 0.0774 BETA = 0.122 RD2 = 741.
CF/2 = 0.00282 O2 = 0.0522 B = -0.703 H = 1.482
F = -0.00198 O3 = 1.4571 DC = 1.4571 P = 0.006 G = 6.129
K = -0.826E-06 O9 = 0.4537 VO = -0.037

Table with columns: Y, U, Y/DC, U/UI, (U-UI)/U*, Y+, U+, TAU, TAU/LAM. Rows contain numerical data for various Y values from 0.005 to 0.724.

RUN: 121671-3 X=22. Z= 0.

UI = 24.98 D1 = 0.1203 BETA = 0.270 RDZ = 1070.
CF/2 = 0.00264 D2 = 0.0826 B = -0.755 H = 1.455
F = -0.00199 DC = 2.3428 P+ = 0.003 G = 6.095
K = -0.457E-06 D99 = 0.6765 V0+ = -0.039

Table with 12 columns: Y, U, Y/DC, U/UI, (U-UI)/U*, Y+, U+, TAU, TAU/LAM. Contains multiple rows of numerical data.

RUN: 121671-3 X=34. Z= 0.

UI = 23.21 D1 = 0.1482 BETA = 0.230 RDZ = 1285.
CF/2 = 0.00256 D2 = 0.1051 B = -0.780 H = 1.410
F = -0.00200 DC = 2.9267 P+ = 0.003 G = 5.743
K = -0.325E-06 D99 = 0.8755 V0+ = -0.039

Table with 12 columns: Y, U, Y/DC, U/UI, (U-UI)/U*, Y+, U+, TAU, TAU/LAM. Contains multiple rows of numerical data.

RUN: 121671-3 X=46. Z= 0.

UI = 22.11 D1 = 0.1785 BETA = 0.210 RDZ = 1482.
CF/2 = 0.00250 D2 = 0.1272 B = -0.795 H = 1.403
F = -0.00199 DC = 3.5676 P+ = 0.002 G = 5.740
K = -0.072E-06 D99 = 1.0702 V0+ = -0.040

Table with 12 columns: Y, U, Y/DC, U/UI, (U-UI)/U*, Y+, U+, TAU, TAU/LAM. Contains multiple rows of numerical data.

RUN: 121671-3 X=58. Z= 0.

UI = 21.55 D1 = 0.1987 BETA = 0.192 RDZ = 1642.
CF/2 = 0.00246 D2 = 0.1444 B = -0.808 H = 1.374
F = -0.00199 DC = 4.0931 P+ = 0.002 G = 5.482
K = -0.210E-06 D99 = 1.2496 V0+ = -0.040

Table with 12 columns: Y, U, Y/DC, U/UI, (U-UI)/U*, Y+, U+, TAU, TAU/LAM. Contains multiple rows of numerical data.

RUN: 121671-3 X=70. Z=0.

UI = 20.95 OI = 0.2217 BETA = 0.184 RDZ = 1797.
CF/2 = 0.00242 O2 = 0.1629 B = -0.814 H = 1.3627
F = -0.00197 O2 = 4.5067 P = 0.0002 G = 3.4017
K = -0.182E-06 DC = 1.4422 VQ = -0.040

Table with columns Y, U, Y/OC, U/UI, (U-UI)/U*, Y+, U+, TAU, TAULAM. Contains multiple rows of numerical data.

RUN: 121671-3 X=90. Z=0.

UI = 20.21 OI = 0.2409 BETA = 0.194 RDZ = 2065.
CF/2 = 0.00238 O2 = 0.1939 B = -0.837 H = 0.346
F = -0.00199 O2 = 5.3506 P = 0.0001 G = 5.2629
K = -0.166E-06 DC = 1.7362 VQ = -0.041

Table with columns Y, U, Y/OC, U/UI, (U-UI)/U*, Y+, U+, TAU, TAULAM. Contains multiple rows of numerical data.

RUN: 121671-3 X=82. Z=0.

UI = 20.50 OI = 0.2461 BETA = 0.184 RDZ = 1956.
CF/2 = 0.00240 O2 = 0.1811 B = -0.830 H = 1.355
F = -0.00199 O2 = 4.5067 P = 0.0002 G = 3.4017
K = -0.166E-06 DC = 1.6662 VQ = -0.041

Table with columns Y, U, Y/OC, U/UI, (U-UI)/U*, Y+, U+, TAU, TAULAM. Contains multiple rows of numerical data.

RUN: 122971-1 X=2. Z=0.

UI = 28.20 OI = 0.0493 BETA = 0.174 RDZ = 506.
CF/2 = 0.00320 O2 = 0.0329 B = -0.623 H = 1.498
F = -0.00199 O2 = 5.3506 P = 0.0001 G = 5.888
K = -0.444E-06 DC = 0.2998 VQ = -0.035

Table with columns Y, U, Y/OC, U/UI, (U-UI)/U*, Y+, U+, TAU, TAULAM. Contains multiple rows of numerical data.

RUN: 122971-1 K=10. Z=0.

UI = 26.91 D1 = 0.0796 BETA= 0.335 RDZ = 752.
CF/2= 0.00275 O2 = 0.0833 H = -0.647 H = 1.482
F = -0.00178 D3 = 1.4062 P+ = 0.006 G = 6.233
K = -0.826E-06 OC = 0.4469 V+ = -0.034

Table with columns: Y, U, Y/DC, U/UI, (U-U1)/U*, Y+, U+, TAU, TAU/LAM. Rows contain numerical data for various parameters.

RUN: 122971-1 K=22. Z=0.

UI = 24.38 D1 = 0.1241 BETA= 0.298 RDZ = 1689.
CF/2= 0.00244 O2 = 0.0852 H = -0.65C H = 1.456
F = -0.00159 DC = 2.5037 P+ = 0.004 G = 6.335
K = -0.460E-06 D9 = 0.6831 V+ = -0.032

Table with columns: Y, U, Y/DC, U/UI, (U-U1)/U*, Y+, U+, TAU, TAU/LAM. Rows contain numerical data for various parameters.

RUN: 122971-1 K=34. Z=0.

UI = 23.00 D1 = 0.1603 BETA= 0.275 RDZ = 1353.
CF/2= 0.00231 O2 = 0.1122 H = -0.645 H = 1.423
F = -0.00149 DC = 3.3373 P+ = 0.003 G = 6.251
K = -0.328E-06 OC = 0.8938 V+ = -0.031

Table with columns: Y, U, Y/DC, U/UI, (U-U1)/U*, Y+, U+, TAU, TAU/LAM. Rows contain numerical data for various parameters.

RUN: 122971-1 K=46. Z=0.

UI = 21.97 D1 = 0.1967 BETA= 0.263 RDZ = 1592.
CF/2= 0.00221 O2 = 0.1382 H = -0.642 H = 1.423
F = -0.00142 DC = 4.1827 P+ = 0.002 G = 6.325
K = -0.257E-06 D9 = 1.1196 V+ = -0.030

Table with columns: Y, U, Y/DC, U/UI, (U-U1)/U*, Y+, U+, TAU, TAU/LAM. Rows contain numerical data for various parameters.

RUN: I22971-1 X=58. Z= 0.

UI = 21.27 OI = 0.2257 BETA= 0.248 R02 = 1801.
CF/2= 0.00215 O2 = 0.1614 B = -0.643 H = 1.398
F = -0.00138 DC = 6.8719 P+ = 0.002 G = 6.146
K = -0.211E-06 D99 = 1.3394 V0+ = -0.030

Table with 12 columns: Y, U, Y/DC, U/UI, (U-UI)/U*, Y+, U+, TAU, TAULAM. Contains multiple rows of numerical data.

RUN: I22971-1 X=70. Z= 0.

UI = 20.68 OI = 0.2588 BETA= 0.242 R02 = 2013.
CF/2= 0.00208 O2 = 0.1853 B = -0.635 H = 1.398
F = -0.00132 DC = 5.6776 P+ = 0.002 G = 6.220
K = -0.179E-06 D99 = 1.5199 V0+ = -0.029

Table with 12 columns: Y, U, Y/DC, U/UI, (U-UI)/U*, Y+, U+, TAU, TAULAM. Contains multiple rows of numerical data.

RUN: I22971-1 X=82. Z= 0.

UI = 20.26 OI = 0.2913 BETA= 0.237 R02 = 2220.
CF/2= 0.00203 O2 = 0.2095 B = -0.636 H = 1.393
F = -0.00129 DC = 6.4767 P+ = 0.002 G = 6.237
K = -0.155E-06 D99 = 1.7392 V0+ = -0.029

Table with 12 columns: Y, U, Y/DC, U/UI, (U-UI)/U*, Y+, U+, TAU, TAULAM. Contains multiple rows of numerical data.

RUN: I22971-1 X=90. Z= 0.

UI = 19.91 OI = 0.3065 BETA= 0.237 R02 = 2316.
CF/2= 0.00201 O2 = 0.2218 B = -0.637 H = 1.386
F = -0.00128 DC = 6.8599 P+ = 0.002 G = 6.164
K = -0.149E-06 D99 = 1.8692 V0+ = -0.029

Table with 12 columns: Y, U, Y/DC, U/UI, (U-UI)/U*, Y+, U+, TAU, TAULAM. Contains multiple rows of numerical data.

RUN: 121171-3 X=2. Z=0.

UI = 29.35 D1 = 0.0518 BETA = 0.127 ROZ = 0.14
CF/Z = 0.00294 D2 = 0.0337 B = -0.336 H = 1.547
F = -0.00199 DC = 0.9555 P = 0.073 G = 0.463
K = -0.445E-06 D9 = 0.2991 V = -0.118

Table with columns: Y, U, Y/DC, U/UI, (U-UI)/U, Y+, U+, TAU, TAUAN. Rows include data points like 0.004, 5.02, 0.0045, 1.171, -15.28, 3.6, 3.15, etc.

RUN: 121171-3 X=10. Z=0.

UI = 26.89 D1 = 0.0888 BETA = 0.425 ROZ = 0.26
CF/Z = 0.00244 D2 = 0.0390 B = -0.406 H = 1.503
F = -0.00099 DC = 1.7994 P = 0.037 G = 0.793
K = -0.832E-06 D9 = 1.4732 V = -0.321

Table with columns: Y, U, Y/DC, U/UI, (U-UI)/U, Y+, U+, TAU, TAUAN. Rows include data points like 0.005, 5.23, 0.0028, 0.194, -16.32, 3.5, 3.94, etc.

RUN: 121171-3 X=22. Z=0.

UI = 24.35 D1 = 0.1473 BETA = 0.497 ROZ = 1.53
CF/Z = 0.00212 D2 = 0.0989 B = -0.463 H = 1.487
F = -0.00198 DC = 3.2512 P = 0.005 G = 7.143
K = -0.461E-06 D9 = 0.7584 V = -0.721

Table with columns: Y, U, Y/DC, U/UI, (U-UI)/U, Y+, U+, TAU, TAUAN. Rows include data points like 0.005, 3.83, 0.0016, 0.157, -18.32, 2.9, 3.42, etc.

RUN: 121171-3 X=34. Z=0.

UI = 22.94 D1 = 0.1918 BETA = 0.369 ROZ = 1.55
CF/Z = 0.00203 D2 = 0.1306 B = -0.484 H = 1.469
F = -0.00098 DC = 4.2612 P = 0.004 G = 7.022
K = -0.326E-06 D9 = 1.9607 V = -0.922

Table with columns: Y, U, Y/DC, U/UI, (U-UI)/U, Y+, U+, TAU, TAUAN. Rows include data points like 0.006, 3.22, 0.0013, 0.140, -19.10, 3.0, 3.14, etc.

RUN: 121171-3 X=46. Z= 1.

UI = 21.98 D1 = 7.2376 BETA= 0.353 RDZ = 1871.
CF/Z= 0.00196 D2 = 0.1635 B = -0.505 H = 1.454
F = -0.11199 DC = 5.3687 P = 0.0093 G = 7.052
K = -0.254E-06 D99 = 1.2337 V0+ = -0.022

Table with columns: Y, U, Y/DC, U/UI, (U-UI)/U*, Y+, U+, TAU, TAULAN. Contains multiple rows of numerical data.

RUN: 121171-3 X=58. Z= 0.

UI = 21.29 D1 = 0.2710 BETA= 0.330 RDZ = 2093.
CF/Z= 1.00191 D2 = 0.1888 B = -0.512 H = 1.455
F = -1.00098 DC = 4.1973 P = 0.0093 G = 6.933
K = -0.210E-06 D99 = 1.4683 V0+ = -0.022

Table with columns: Y, U, Y/DC, U/UI, (U-UI)/U*, Y+, U+, TAU, TAULAN. Contains multiple rows of numerical data.

RUN: 121171-3 X=76. Z= 1.

UI = 21.73 D1 = 7.3079 BETA= 0.321 RDZ = 2332.
CF/Z= 1.00187 D2 = 0.2160 B = -0.523 H = 1.425
F = -0.00098 DC = 7.1155 P = 0.0092 G = 6.855
K = -0.181E-06 D99 = 1.6713 V0+ = -0.023

Table with columns: Y, U, Y/DC, U/UI, (U-UI)/U*, Y+, U+, TAU, TAULAN. Contains multiple rows of numerical data.

RUN: 121171-3 X=82. Z= 0.

UI = 21.28 D1 = 7.3429 BETA= 0.325 RDZ = 2573.
CF/Z= 1.00184 D2 = 0.2436 B = -0.533 H = 1.407
F = -0.00098 DC = 7.9988 P = 0.0092 G = 6.752
K = -0.165E-06 D99 = 1.9825 V0+ = -0.023

Table with columns: Y, U, Y/DC, U/UI, (U-UI)/U*, Y+, U+, TAU, TAULAN. Contains multiple rows of numerical data.

RUN: 121171-3 X=9.0 Z= 0

UI = 19.96 D1 = 0.3738 BETA = 0.354
CF/Z = 0.00181 D2 = 0.2669 B = -0.561
F = -0.00098 DC = 8.7820 P+ = 0.002
K = -0.165E-06 D99 = 2.1015 V0+ = -0.023

RD2 = 2.774
H = 1.400
G = 6.719

Table with columns: Y, U, Y/DC, U/UI, (U-UI)/U, Y+, U+, TAU, TAU/LAM. Rows include data points for various Y and U values, such as 3.007, 2.80, 0.0008, 0.140, -20.20, 3.0, 3.29, etc.

RUN: 10372-1 X= 2. Z= 0

UI = 29.27 D1 = 0.0517 BETA = 0.116
CF/Z = 0.00293 D2 = 0.0347 B = -0.341
F = -0.00100 DC = 0.9661 P+ = 0.003
K = -0.433E-06 D99 = 0.2985 V0+ = -0.018

RD2 = 515.
H = 1.524
G = 6.353

Table with columns: Y, U, Y/DC, U/UI, (U-UI)/U, Y+, U+, TAU, TAU/LAM. Rows include data points for various Y and U values, such as 0.004, 5.77, 0.0045, 0.197, -14.83, 3.5, 3.44, etc.

RUN: 10372-1 X=10. Z= 0

UI = 26.94 D1 = 0.0999 BETA = 0.438
CF/Z = 0.00238 D2 = 0.0602 B = -0.378
F = -0.00090 DC = 1.8639 P+ = 0.007
K = -0.821E-06 D99 = 0.4682 V0+ = -0.018

RD2 = 841.
H = 1.511
G = 6.927

Table with columns: Y, U, Y/DC, U/UI, (U-UI)/U, Y+, U+, TAU, TAU/LAM. Rows include data points for various Y and U values, such as 3.905, 5.20, 0.0207, 0.193, -16.93, 3.4, 3.96, etc.

RUN: 10372-1 X=22. Z= 0

UI = 24.43 D1 = 0.1517 BETA = 0.427
CF/Z = 0.00204 D2 = 0.1003 B = -0.388
F = -0.00079 DC = 3.3477 P+ = 0.003
K = -0.455E-06 D99 = 0.7647 V0+ = -0.018

RD2 = 1271.
H = 1.505
G = 7.439

Table with columns: Y, U, Y/DC, U/UI, (U-UI)/U, Y+, U+, TAU, TAU/LAM. Rows include data points for various Y and U values, such as 3.095, 3.52, 0.0735, 0.144, -18.56, 3.9, 3.19, etc.

RUN: 10372-1 X=34. Z= 0.

UI = 23.04 D1 = 0.2005 9ETA= 0.408 RDZ = 1.624
CF/Z= 0.00191 D2 = 0.1359 8 = -0.388 H = 1.475
F = -0.00074 D3 = 4.5002 P+ = 0.004 G = 7.377
K = -0.325E-06 09 = 1.0112 V0+ = -0.017

Table with columns: Y, U, Y/DC, U/UT, (U-U1)/L*, Y+, U+, TAU, TAU/LAM. Rows contain numerical data for various parameters.

RUN: 10372-1 X=46. Z= 0.

UI = 22.12 D1 = 0.2574 9ETA= 1.409 RDZ = 1.973
CF/Z= 0.00187 D2 = 0.1771 8 = -0.390 H = 1.472
F = -0.00171 D3 = 5.9612 P+ = 0.003 G = 7.519
K = -0.256E-06 09 = 1.2802 V0+ = -0.017

Table with columns: Y, U, Y/DC, U/UT, (U-U1)/L*, Y+, U+, TAU, TAU/LAM. Rows contain numerical data for various parameters.

RUN: 10372-1 X=58. Z= 0.

UI = 21.50 D1 = 0.2948 9ETA= 0.396 RDZ = 2.262
CF/Z= 0.00176 D2 = 0.2030 8 = -0.392 H = 1.452
F = -0.00049 D3 = 7.0291 P+ = 0.003 G = 7.425
K = -0.212E-06 09 = 1.5242 V0+ = -0.016

Table with columns: Y, U, Y/DC, U/UT, (U-U1)/L*, Y+, U+, TAU, TAU/LAM. Rows contain numerical data for various parameters.

RUN: 10372-1 X=70. Z= 0.

UI = 20.94 D1 = 0.3397 9ETA= 0.388 RDZ = 2.545
CF/Z= 0.00171 D2 = 0.2344 8 = -0.392 H = 1.446
F = -0.00067 D3 = 9.2066 P+ = 0.003 G = 7.464
K = -0.181E-06 09 = 1.7847 V0+ = -0.016

Table with columns: Y, U, Y/DC, U/UT, (U-U1)/L*, Y+, U+, TAU, TAU/LAM. Rows contain numerical data for various parameters.

RUN: 71571-5 X=22. Z= 0.

UI = 24.57 D1 = 0.1936 BETA= 0.686 RCZ = 1528.
CF/Z= 0.00169 D2 = 0.1238 B = 0.0000 F = 1.563
F = 0.00000 DC = 4.7088 P+ = 0.0870 G = 8.766
K = -0.485E-06 D99 = 0.8628 V0+ = 0.0000

Table with columns Y, U, Y/DC, U/UI, (U-U1)/U*, Y+, U+, TAU, TAULAM. Contains multiple rows of numerical data.

RUN: 71571-5 X=34. Z= D.

UI = 23.26 D1 = 0.2616 BETA= 0.696 RBZ = 1986.
CF/Z= 0.00153 D2 = 0.1700 B = 0.0000 F = 1.533
F = 0.00000 DC = 6.6824 P+ = 0.0058 G = 8.960
K = -0.348E-06 D99 = 1.1752 V0+ = 0.0000

Table with columns Y, U, Y/DC, U/UI, (U-U1)/U*, Y+, U+, TAU, TAULAM. Contains multiple rows of numerical data.

RUN: 71571-5 X=46. Z= B.

UI = 22.27 D1 = 0.3356 BETA= 0.708 RBZ = 2434.
CF/Z= 0.00145 D2 = 0.2116 B = 0.0000 F = 1.542
F = 0.00000 DC = 8.8058 P+ = 0.0050 G = 9.225
K = -0.274E-06 D99 = 1.5029 V0+ = 0.0000

Table with columns Y, U, Y/DC, U/UI, (U-U1)/U*, Y+, U+, TAU, TAULAM. Contains multiple rows of numerical data.

RUN: 71571-5 X=58. Z= C.

UI = 21.36 D1 = 0.3934 BETA= 0.685 RBZ = 2781.
CF/Z= 0.00140 D2 = 0.2592 B = 0.0000 F = 1.518
F = 0.00000 DC = 10.4960 P+ = 0.0043 G = 9.101
K = -0.228E-06 D99 = 1.7870 V0+ = 0.0000

Table with columns Y, U, Y/DC, U/UI, (U-U1)/U*, Y+, U+, TAU, TAULAM. Contains multiple rows of numerical data.

RUN: 71571-5 X=70. Z= 0.

UI = 20.74 D1 = 8.4410 BETA= 0.693 RD2 = 3177.
CF/2= 0.00134 D2 = 0.3049 B = 0.000 H = 1.512
F = 0.00000 DC = 12.5079 P+ = 0.0039 G = 9.191
K = -0.196E-06 D99 = 2.1211 V0+ = 0.0000

Table with columns: Y, U, Y/DC, U/UI, (U-U1)/U*, Y+, U+, TAU, TAULAM. Rows include data points for Y values from 0.010 to 2.450.

RUN: 71571-5 X=82. Z= 0.

UI = 20.35 D1 = 0.5168 BETA= 0.685 RD2 = 3495.
CF/2= 0.00133 D2 = 0.3419 B = 0.000 H = 1.494
F = 0.00000 DC = 14.0251 P+ = 0.0036 G = 9.080
K = -0.174E-06 D99 = 2.4043 V0+ = 0.0000

Table with columns: Y, U, Y/DC, U/UI, (U-U1)/U*, Y+, U+, TAU, TAULAM. Rows include data points for Y values from 0.010 to 3.193.

RUN: 71571-5 X=90. Z= 0.

UI = 20.05 D1 = 0.5449 BETA= 0.712 RD2 = 3681.
CF/2= 0.00131 D2 = 0.3656 B = 0.000 H = 1.491
F = 0.00000 DC = 15.0589 P+ = 0.0036 G = 9.094
K = -0.170E-06 D99 = 2.5701 V0+ = 0.0000

Table with columns: Y, U, Y/DC, U/UI, (U-U1)/U*, Y+, U+, TAULAM. Rows include data points for Y values from 0.009 to 3.807.

RUN: 111571-1 X= 2. Z= 0.

UI = 29.39 D1 = 0.0592 BETA= 0.160 RD2 = 563.
CF/2= 0.00249 D2 = 0.0371 B = 0.357 H = 1.586
F = 0.00099 DC = 1.1647 P+ = 0.0036 G = 7.476
K = -0.444E-06 D99 = 0.3127 V0+ = 0.0198

Table with columns: Y, U, Y/DC, U/UI, (U-U1)/U*, Y+, U+, TAULAM. Rows include data points for Y values from 0.004 to 0.410.

RUN: 111571-1 X=10. Z=0.

UI = 26.52 D1 = 0.1317 BETA = 0.855 PD2 = 1100.
CF/Z = 0.00176 D2 = 0.0803 B = 0.523 H = 1.441
F = 0.00092 DC = 3.1392 P = 0.0114 G = 0.310
K = -0.843E-06 D99 = 0.5445 V0+ = 0.0219

Table with columns Y, U, Y/DC, U/U1, (U-U1)/U0, Y4, J4, TAU, TAU1AW. Rows include data points for various Y values from 0.005 to 0.748.

RUN: 111571-1 X=22. Z=0.

UI = 24.26 D1 = 0.2321 BETA = 0.548 PD2 = 1795.
CF/Z = 0.00144 D2 = 0.1424 B = 0.563 H = 1.430
F = 0.00081 DC = 6.1156 P = 0.0795 G = 0.16187
K = -0.469E-06 D99 = 0.5279 V0+ = 0.0213

Table with columns Y, U, Y/DC, U/U1, (U-U1)/U0, Y4, J4, TAU, TAU1AW. Rows include data points for various Y values from 0.005 to 1.233.

RUN: 111571-1 X=34. Z=0.

UI = 22.90 D1 = 0.3168 BETA = 1.056 PD2 = 2744.
CF/Z = 0.00118 D2 = 0.1980 B = 0.647 H = 1.570
F = 0.00076 DC = 9.2159 P = 0.0783 G = 0.0713
K = -0.336E-06 D99 = 1.3082 V0+ = 0.0221

Table with columns Y, U, Y/DC, U/U1, (U-U1)/U0, Y4, J4, TAU, TAU1AW. Rows include data points for various Y values from 0.007 to 1.646.

RUN: 111571-1 X=46. Z=0.

UI = 21.98 D1 = 0.4160 BETA = 1.109 PD2 = 2610.
CF/Z = 0.00112 D2 = 0.2961 B = 0.668 H = 1.623
F = 0.00072 DC = 12.2929 P = 0.0771 G = 0.0715
K = -0.265E-06 D99 = 1.6937 V0+ = 0.0215

Table with columns Y, U, Y/DC, U/U1, (U-U1)/U0, Y4, J4, TAU, TAU1AW. Rows include data points for various Y values from 0.010 to 2.102.

RUN: 111571-1 X=58. Z= 0.

UI = 21.19 D1 = 0.4846 BETA = 1.072 F02 = 3345.
CF/F2 = 0.00108 D2 = 0.3054 B = 0.6448 H = 1.567
F = 0.00070 DC = 14.7476 P+ = 0.0261 G = 11.254
K = -0.218E-06 D99 = 1.9937 VC+ = 0.0213

Table with columns: Y, U, Y/DC, U/U, (U-UI)/U*, Y+, U+, TAU, TAU/LAM. Rows include data points for various Y values from 0.016 to 3.601.

RUN: 111571-1 X=70. Z= 0.

UI = 20.61 D1 = 0.5600 BETA = 1.046 F02 = 3789.
CF/F2 = 0.00105 D2 = 0.3556 B = 0.6338 H = 1.575
F = 0.00067 DC = 17.2852 P+ = 0.0254 G = 11.245
K = -0.184E-06 D99 = 2.3843 VC+ = 0.0207

Table with columns: Y, U, Y/DC, U/U, (U-UI)/U*, Y+, U+, TAU, TAU/LAM. Rows include data points for various Y values from 0.012 to 3.107.

RUN: 111571-1 X=82. Z= 0.

UI = 20.23 D1 = 0.6275 BETA = 1.052 F02 = 4275.
CF/F2 = 0.00102 D2 = 0.4040 B = 0.6338 H = 1.553
F = 0.00065 DC = 19.6277 P+ = 0.0242 G = 11.141
K = -0.156E-06 D99 = 2.6869 VC+ = 0.0203

Table with columns: Y, U, Y/DC, U/U, (U-UI)/U*, Y+, U+, TAU, TAU/LAM. Rows include data points for various Y values from 0.015 to 3.601.

RUN: 111571-1 X=90. Z= 0.

UI = 20.00 D1 = 0.6719 BETA = 1.036 F02 = 4506.
CF/F2 = 0.00101 D2 = 0.4339 B = 0.6338 H = 1.554
F = 0.00064 DC = 21.1867 P+ = 0.0245 G = 11.145
K = -0.145E-06 D99 = 2.9187 VC+ = 0.0202

Table with columns: Y, U, Y/DC, U/U, (U-UI)/U*, Y+, U+, TAU, TAU/LAM. Rows include data points for various Y values from 0.014 to 3.601.

RUN: 91771-2 X=2, Z=0

UI = 29.49 D1 = 0.7601 BETA= 0.167 RDZ = 555.
CF/2= 3.00249 D2 = 0.0376 B = 7.398 H = 1.661
F = 0.70090 DC = 1.2053 P+ = 0.004 G = 7.523
K = -0.467E-06 D99 = 0.3197 V0+ = 0.020

Table with columns: Y, U, Y/DC, U/UI, (U-U1)/U*, Y+, U+, TAU, TAU*AM. Contains multiple rows of numerical data.

RUN: 91771-2 X=10, Z=0

UI = 26.89 D1 = 0.1337 BETA= 1.968 RDZ = 1090.
CF/2= 0.00173 D2 = 0.0809 B = 3.572 H = 1.653
F = 0.00099 DC = 3.2151 P+ = 0.012 G = 9.501
K = -0.872E-06 D99 = 0.5533 V0+ = 0.024

Table with columns: Y, U, Y/DC, U/UI, (U-U1)/U*, Y+, U+, TAU, TAU*AM. Contains multiple rows of numerical data.

RUN: 91771-2 X=22, Z=0

UI = 24.30 D1 = 0.2442 BETA= 1.055 RDZ = 1765.
CF/2= 0.00118 D2 = 0.1467 B = 7.725 H = 1.663
F = 0.00100 DC = 4.5737 P+ = 0.012 G = 10.750
K = -0.497E-06 D99 = 0.9489 V0+ = 0.027

Table with columns: Y, U, Y/DC, U/UI, (U-U1)/U*, Y+, U+, TAU, TAU*AM. Contains multiple rows of numerical data.

RUN: 91771-2 X=34, Z=0

UI = 22.87 D1 = 0.3477 BETA= 1.271 RDZ = 2395.
CF/2= 0.00109 D2 = 0.0929 B = 7.917 H = 1.544
F = 0.00100 DC = 10.4155 P+ = 0.010 G = 11.865
K = -0.352E-06 D99 = 1.3671 V0+ = 0.037

Table with columns: Y, U, Y/DC, U/UI, (U-U1)/U*, Y+, U+, TAU, TAU*AM. Contains multiple rows of numerical data.

RUN: 91771-2 X=46. Z=0.

UI = 21.80 D1 = 0.4441 BETA = 1.313 PDZ = 2959.
CF/2 = 0.00102 D2 = 0.2709 B = 0.971 H = 1.539
F = 0.00099 DC = 13.9093 P+ = 0.008 G = 12.213
K = -0.276E-06 D99 = 1.7662 V0+ = 0.031

Table with 12 columns: Y, U, Y/DC, U/UI, (U-UI)/U*, Y+, U+, TAU, TAULAM. Contains multiple rows of numerical data.

RUN: 91771-2 X=58. Z=0.

UI = 21.41 D1 = 0.5373 BETA = 1.364 RDZ = 3588.
CF/2 = 0.00096 D2 = 0.3307 B = 1.032 H = 1.623
F = 0.00099 DC = 17.3472 P+ = 0.008 G = 12.412
K = -0.227E-06 D99 = 2.1751 V0+ = 0.032

Table with 12 columns: Y, U, Y/DC, U/UI, (U-UI)/U*, Y+, U+, TAU, TAULAM. Contains multiple rows of numerical data.

RUN: 91771-2 X=70. Z=0.

UI = 21.13 D1 = 0.6262 BETA = 1.411 PDZ = 4095.
CF/2 = 0.00091 D2 = 0.3819 B = 1.114 H = 1.613
F = 0.00101 DC = 20.7965 P+ = 0.007 G = 12.691
K = -0.193E-06 D99 = 2.5267 V0+ = 0.034

Table with 12 columns: Y, U, Y/DC, U/UI, (U-UI)/U*, Y+, U+, TAU, TAULAM. Contains multiple rows of numerical data.

RUN: 91771-2 X=87. Z=0.

UI = 20.36 D1 = 0.7146 BETA = 1.403 RDZ = 4544.
CF/2 = 0.00088 D2 = 0.4456 B = 1.139 H = 1.604
F = 0.00100 DC = 24.7201 P+ = 0.006 G = 12.709
K = -0.169E-06 D99 = 2.9028 V0+ = 0.034

Table with 12 columns: Y, U, Y/DC, U/UI, (U-UI)/U*, Y+, U+, TAU, TAULAM. Contains multiple rows of numerical data.

PUN: 91771-2 X=90. Z= 0.

UI = 20.16 D1 = 0.7783 BETA= 1.502 RDZ = 4911.
CF/Z= 0.00086 D2 = 0.4864 B = 1.154 H = 1.630
F = 0.00099 DC = 26.5704 P = 0.097 G = -12.803
K = -0.164E-06 D99 = 3.1636 V0 = 0.034

Table with columns Y, U, Y/DC, U/UI, (U-UI)/U*, Y+, U+, TAU, TAU/LAM. Contains multiple rows of numerical data.

PUN: 111771-3 X= 2. Z= 0.

UI = 20.26 D1 = 0.0023 BETA= 0.187 RDZ = 587.
CF/Z= 0.00230 D2 = 0.0384 B = 0.871 H = 1.621
F = 0.00200 DC = 1.2998 P = 0.094 G = 7.997
K = -0.452E-06 D99 = 0.3194 V0 = 0.047

Table with columns Y, U, Y/DC, U/UI, (U-UI)/U*, Y+, U+, TAU, TAU/LAM. Contains multiple rows of numerical data.

PUN: 111771-3 X=10. Z= 0.

UI = 24.59 D1 = 0.1486 BETA= 1.165 RDZ = 1219.
CF/Z= 0.00150 D2 = 0.0978 B = 1.207 H = 1.697
F = 0.00181 DC = 3.8531 P = 0.035 G = -10.583
K = -0.847E-06 D99 = 0.5788 V0 = 0.047

Table with columns Y, U, Y/DC, U/UI, (U-UI)/U*, Y+, U+, TAU, TAU/LAM. Contains multiple rows of numerical data.

PUN: 111771-3 X=22. Z= 0.

UI = 24.11 D1 = 0.2901 BETA= 1.547 RDZ = 2042.
CF/Z= 0.00109 D2 = 0.1638 B = 1.491 H = -1.710
F = 0.00161 DC = 8.5238 P = -0.013 G = -12.638
K = -0.472E-06 D99 = 1.0319 V0 = 0.049

Table with columns Y, U, Y/DC, U/UI, (U-UI)/U*, Y+, U+, TAU, TAU/LAM. Contains multiple rows of numerical data.

RUN: 111771-3 X=34. Z=0.

UI = 22.78 D1 = 0.3921 BETA= 1.808 RD2 = 2754.
FF/Z= 0.00087 D2 = 0.2318 H = 1.491
F = 0.00152 DC = 13.3107 P+ = 0.013 G = 13.475
K = -0.336E-06 D9 = 1.4647 V0+ = 0.052

Table with 12 columns: Y, U, Y/DC, U/U1, (U-U1)/U*, Y+, U+, TAU, TAULAM. Rows include data points for various Y values from 0.012 to 1.985.

RUN: 111771-3 X=46. Z=0.

UI = 21.73 D1 = 0.5078 BETA= 1.853 RD2 = 3412.
FF/Z= 0.00082 D2 = 0.2959 H = 1.768
F = 0.00145 DC = 17.7313 P+ = 0.011 G = 14.297
K = -0.263E-06 D9 = 1.8774 V0+ = 0.051

Table with 12 columns: Y, U, Y/DC, U/U1, (U-U1)/U*, Y+, U+, TAU, TAULAM. Rows include data points for various Y values from 0.014 to 2.502.

RUN: 111771-3 X=58. Z=0.

UI = 20.96 D1 = 0.6034 BETA= 1.820 RD2 = 3973.
FF/Z= 0.00079 D2 = 0.3629 H = 1.757
F = 0.00139 DC = 21.4484 P+ = 0.010 G = 14.165
K = -0.218E-06 D9 = 2.3054 V0+ = 0.049

Table with 12 columns: Y, U, Y/DC, U/U1, (U-U1)/U*, Y+, U+, TAU, TAULAM. Rows include data points for various Y values from 0.017 to 3.010.

RUN: 111771-3 X=70. Z=0.

UI = 20.46 D1 = 0.6927 BETA= 1.839 RD2 = 4544.
FF/Z= 0.00076 D2 = 0.4253 H = 1.768
F = 0.00135 DC = 25.2076 P+ = 0.009 G = 14.162
K = -0.198E-06 D9 = 2.7056 V0+ = 0.049

Table with 12 columns: Y, U, Y/DC, U/U1, (U-U1)/U*, Y+, U+, TAU, TAULAM. Rows include data points for various Y values from 0.020 to 3.607.

RUN: 111771-3 X=82. Z= 0.

UI = 20.00 D1 = 0.7977 BETA= 1.897 RD2 = 5097.
CF/Z= 0.30074 D2 = 0.4881 B = 1.765 H = 1.634
F = 0.00131 DC = 29.2779 P+ = 0.008 G = 14.246
K = -0.169E-06 D99 = 3.0886 VO+ = 0.048

Table with columns: Y, U, Y/DC, U/UI, (U-U1)/U*, Y+, U+, TAU, TAU*AM. Contains multiple rows of numerical data.

RUN: 111771-3 X=90. Z= 0.

UI = 19.73 D1 = 0.8660 BETA= 2.053 RD2 = 5471.
CF/Z= 0.05073 D2 = 0.5308 B = 1.771 H = 1.627
F = 0.00120 DC = 32.0137 P+ = 0.009 G = 14.285
K = -0.168E-06 D99 = 3.3884 VO+ = 0.048

Table with columns: Y, U, Y/DC, U/UI, (U-U1)/U*, Y+, U+, TAU, TAU*AM. Contains multiple rows of numerical data.

RUN: 101371-2 X= 2. Z= 0.

UI = 29.77 D1 = 0.0629 BETA= 0.189 RD2 = 591.
CF/Z= 0.00228 D2 = 0.0391 B = 0.877 H = 1.611
F = 0.00200 DC = 1.3178 P+ = 0.0042 G = 7.940
K = -0.454E-06 D99 = 0.3210 VO+ = 0.0419

Table with columns: Y, U, Y/DC, U/UI, (U-U1)/U*, Y+, U+, TAU, TAU*AM. Contains multiple rows of numerical data.

RUN: 101371-2 X=10. Z= 0.

UI = 27.05 D1 = 0.1506 BETA= 1.164 RD2 = 1213.
CF/Z= 0.00152 D2 = 0.0883 B = 1.322 H = 1.705
F = 0.00201 DC = 3.8620 P+ = 0.0144 G = -10.604
K = -0.855E-06 D99 = 0.5772 VO+ = 0.0516

Table with columns: Y, U, Y/DC, U/UI, (U-U1)/U*, Y+, U+, TAU, TAU*AM. Contains multiple rows of numerical data.

RUN: 101371-2 X=22. Z= 0.

UI = 24.64 D1 = 0.2890 BETA= 1.675 RD2 = 2081.
CF/Z= 0.00103 D2 = 0.1663 B = 1.951 H = 1.738
F = 0.00201 DC = 9.0051 P+ = 0.0144 G = 13.232
K = -0.477E-06 D99 = 1.0379 V0+ = 0.0626

Table with 12 columns: Y, U, Y/DC, U/UI, (U-UI)/U*, Y+, U+, TAU, TAU/LAM. Contains multiple rows of numerical data.

RUN: 101371-2 X=34. Z= 0.

UI = 23.31 D1 = 0.4189 BETA= 2.185 RD2 = 2855.
CF/Z= 0.00078 D2 = 0.2412 B = 2.603 H = 1.737
F = 0.00202 DC = 15.0382 P+ = 0.0158 G = 15.227
K = -0.342E-06 D99 = 1.5027 V0+ = 0.0725

Table with 12 columns: Y, U, Y/DC, U/UI, (U-UI)/U*, Y+, U+, TAU, TAU/LAM. Contains multiple rows of numerical data.

RUN: 101371-2 X=46. Z= 0.

UI = 22.36 D1 = 0.5480 BETA= 2.361 RD2 = 3585.
CF/Z= 0.00071 D2 = 0.3157 B = 2.860 H = 1.736
F = 0.00202 DC = 20.6197 P+ = 0.0143 G = 15.949
K = -0.268E-06 D99 = 1.9414 V0+ = 0.0760

Table with 12 columns: Y, U, Y/DC, U/UI, (U-UI)/U*, Y+, U+, TAU, TAU/LAM. Contains multiple rows of numerical data.

RUN: 101371-2 X=58. Z= 0.

UI = 21.53 D1 = 0.6647 BETA= 2.448 RD2 = 4222.
CF/Z= 0.00066 D2 = 0.3860 B = 3.064 H = 1.722
F = 0.00202 DC = 25.8853 P+ = 0.0131 G = 16.329
K = -0.222E-06 D99 = 2.3763 V0+ = 0.0787

Table with 12 columns: Y, U, Y/DC, U/UI, (U-UI)/U*, Y+, U+, TAU, TAU/LAM. Contains multiple rows of numerical data.

RUN: 101371-2 X=70. Z= 0.

UI = 20.97 D1 = 0.7826 BETA= 2.524 RD2 = 4877.
CF/Z= 0.00062 D2 = 0.4580 B = 3.205 H = 1.709
F = 0.00200 DC = 31.3285 P+ = 0.011 G = -16.604
K = -0.189E-06 D99 = 2.8244 V0+ = 0.0801

Table with 10 columns: Y, U, Y/DC, U/UI, (U-UI)/U*, Y+, U+, TAU, TAU/LAM. Contains multiple rows of numerical data.

RUN: 101371-2 X=82. Z= 0.

UI = 20.62 D1 = 0.8987 BETA= 2.657 RD2 = 3576.
CF/Z= 0.00058 D2 = 0.5325 B = 3.457 H = 1.688
F = 0.00202 DC = 37.1748 P+ = 0.0117 G = 16.855
K = -0.165E-06 D99 = 3.2985 V0+ = 0.0836

Table with 10 columns: Y, U, Y/DC, U/UI, (U-UI)/U*, Y+, U+, TAU, TAU/LAM. Contains multiple rows of numerical data.

RUN: 101371-2 X=90. Z= 0.

UI = 20.43 D1 = 0.5767 BETA= 2.840 RD2 = 6015.
CF/Z= 0.00057 D2 = 0.5798 B = 3.563 H = 1.684
F = 0.00201 DC = 41.0050 P+ = 0.0118 G = 17.059
K = -0.159E-06 D99 = 3.6141 V0+ = 0.0844

Table with 10 columns: Y, U, Y/DC, U/UI, (U-UI)/U*, Y+, U+, TAU, TAU/LAM. Contains multiple rows of numerical data.

RUN: 112P71-1 X= 2. Z= 0.

UI = 29.49 D1 = 0.0711 BETA= 0.248 RD2 = 641.
CF/Z= 0.00194 D2 = 0.0425 B = 2.057 H = 1.687
F = 0.00399 DC = 1.6282 P+ = 0.0052 G = 9.247
K = -0.445E-06 D99 = 0.3362 V0+ = 0.0906

Table with 10 columns: Y, U, Y/DC, U/UI, (U-UI)/U*, Y+, U+, TAU, TAU/LAM. Contains multiple rows of numerical data.

RUN: 112871-1 X=58. Z= 0.

UI = 21.94 D1 = 0.9009 BETA= 4.668 RDZ = 5258.
CF/2= 0.00046 D2 = 0.4887 B = 6.020 H = 1.863
F = 0.00275 DC = +42.1483 PA = 0.0225 G = +21.404
K = -0.220E-06 D99 = 2.9299 VG+ = 0.1287

Table with 10 columns: Y, U, Y/DC, U/UI, (U-U1)/U*, Y+, U+, TAU, TAU/LAM. Rows include data points for Y values from 0.028 to 3.708.

RUN: 112871-1 X=70. Z= 0.

UI = 20.55 D1 = 1.0454 BETA= 4.663 RDZ = 6046.
CF/2= 0.00044 D2 = 0.5754 B = 6.039 H = 1.817
F = 0.00266 DC = +49.8095 PA = 0.0202 G = -21.423
K = -0.187E-06 D99 = 3.4270 VG+ = 0.1267

Table with 10 columns: Y, U, Y/DC, U/UI, (U-U1)/U*, Y+, U+, TAU, TAU/LAM. Rows include data points for Y values from 0.028 to 4.308.

RUN: 112871-1 X=82. Z= 0.

UI = 20.13 D1 = 1.1871 BETA= 4.694 RDZ = 6870.
CF/2= 0.00042 D2 = -0.6674 B = 6.152 H = 1.779
F = 0.00260 DC = +57.7434 PA = 0.0186 G = +21.295
K = -0.162E-06 D99 = 3.9999 VG+ = 0.1265

Table with 10 columns: Y, U, Y/DC, U/UI, (U-U1)/U*, Y+, U+, TAU, TAU/LAM. Rows include data points for Y values from 0.027 to 4.302.

RUN: 112871-1 X=90. Z= 0.

UI = 19.81 D1 = 1.2877 BETA= 4.867 RDZ = 7311.
CF/2= 0.00042 D2 = 0.7234 B = 6.161 H = 1.780
F = 0.00256 DC = +63.1724 PA = 0.0183 G = +21.497
K = -0.155E-06 D99 = 4.2811 VG+ = 0.1256

Table with 10 columns: Y, U, Y/DC, U/UI, (U-U1)/U*, Y+, U+, TAU, TAU/LAM. Rows include data points for Y values from 0.030 to 4.415.

RUN: 102171-1 X= Z. Z= 0.

UI = 29.71 D1 = 0.C702 BETA= 0.251 RD2 = 639.
CF/2= 0.00194 D2 = 0.0418 B = 2.052 H = 1.679
F = 0.0038 DC = 1.9925 P+ = 0.0093 G = 0.169
K = -0.455E-06 D99 = 0.3301 V0+ = 0.0905

Table with 12 columns: Y, U, Y/DC, U/UT, (U-UI)/U*, Y+, U+, TAU, TAILAM. Contains multiple rows of numerical data.

RUN: 102171-1 X=10. Z= 0.

UI = 27.02 D1 = 0.1964 BETA= 3.179 RD2 = 1472.
CF/2= 0.00073 D2 = 0.1059 B = 5.507 H = 1.85
F = 0.00402 DC = 7.2700 P+ = 0.0431 G = 17.040
K = -0.850E-06 D99 = 0.6491 V0+ = 0.1488

Table with 12 columns: Y, U, Y/DC, U/UT, (U-UI)/U*, Y+, U+, TAU, TAILAM. Contains multiple rows of numerical data.

RUN: 102171-1 X=22. Z= 0.

UI = 24.57 D1 = 0.4357 BETA= 6.117 RD2 = 2757.
CF/2= 0.00042 D2 = 0.2182 B = 9.502 H = 1.997
F = 0.00402 DC = 21.1852 P+ = 0.0540 G = -24.273
K = -0.470E-06 D99 = 1.2763 V0+ = 0.1954

Table with 12 columns: Y, U, Y/DC, U/UT, (U-UI)/U*, Y+, U+, TAU, TAILAM. Contains multiple rows of numerical data.

RUN: 102171-1 X=34. Z= 0.

UI = 23.18 D1 = 0.6578 BETA= 7.333 RD2 = 3891.
CF/2= 0.00035 D2 = 0.3263 B = 11.296 H = 2.016
F = 0.00400 DC = 34.9565 P+ = 0.0497 G = 26.783
K = -0.331E-06 D99 = 1.9199 V0+ = 0.2126

Table with 12 columns: Y, U, Y/DC, U/UT, (U-UI)/U*, Y+, U+, TAU, TAILAM. Contains multiple rows of numerical data.

RUN: 102171-1 X=46. Z= 0.

UI = 22.13 D1 = 0.8801 BETA= 8.252 RD2 = 4986.
CF/Z= 0.00031 D2 = 0.4380 B = 12.985 H = 2.009
F = 0.00402 DC = 50.0180 P+ = 0.0468 G = 28.551
K = -0.235E-06 D99 = 2.3698 V0+ = 0.2285

Table with 10 columns: Y, U, Y/DC, U/U1, (U-U1)/U*, Y+, U+, TAU, TAULAM. Contains multiple rows of numerical data.

RUN: 102171-1 X=58. Z= 0.

UI = 21.46 D1 = 1.0938 BETA= 8.947 RD2 = 6040.
CF/Z= 0.00028 D2 = 0.5472 B = 14.218 H = 1.999
F = 0.00401 DC = 65.1328 P+ = 0.0441 G = 29.756
K = -0.209E-06 D99 = 3.2329 V0+ = 0.2388

Table with 10 columns: Y, U, Y/DC, U/U1, (U-U1)/U*, Y+, U+, TAU, TAULAM. Contains multiple rows of numerical data.

RUN: 102171-1 X=70. Z= 0.

UI = 20.97 D1 = 1.3042 BETA= 9.425 PD2 = 7146.
CF/Z= 0.00026 D2 = 0.6625 B = 15.250 H = 1.969
F = 0.00399 DC = 80.6323 P+ = 0.0423 G = 30.420
K = -0.179E-06 D99 = 3.9518 V0+ = 0.2467

Table with 10 columns: Y, U, Y/DC, U/U1, (U-U1)/U*, Y+, U+, TAU, TAULAM. Contains multiple rows of numerical data.

RUN: 102171-1 X=82. Z= 0.

UI = 23.48 D1 = 1.5008 BETA= 10.301 RD2 = 8207.
CF/Z= 0.00025 D2 = 0.7789 B = 16.287 H = 1.927
F = 0.00400 DC = 95.7636 P+ = 0.0416 G = 30.692
K = -0.160E-06 D99 = 4.7414 V0+ = 0.2552

Table with 10 columns: Y, U, Y/DC, U/U1, (U-U1)/U*, Y+, U+, TAU, TAULAM. Contains multiple rows of numerical data.

RUN: 102171-1 X=90. Z= 0.

UI = 20.27 D1 = 1.6225 BETA=11.319 RDZ = 8785.
CF/Z= 0.00024 D2 = 0.8427 B = 16.486 H = 1.925
F = 0.00399 DC = 104.9 P+ = 0.0433 G = 31.083
K = -0.160E-06 D99 = 4.8166 V0+ = 0.2580

Y	U	V/DC	U/UI	(U-UI)/U*	Y+	U+	TAULAM
0.055	3.47	0.0005	0.171	-53.58	8.8	11.09	0.000160
0.065	3.66	0.0006	0.180	-53.00	10.4	11.67	0.000154
0.085	4.54	0.0008	0.224	-50.17	13.7	14.50	0.000142
0.115	4.74	0.0011	0.234	-49.56	18.5	15.11	0.000074
0.215	5.86	0.0020	0.289	-45.95	34.6	18.71	0.000041
0.415	7.18	0.0040	0.354	-41.76	66.9	22.91	0.000027
0.615	7.78	0.0059	0.384	-39.85	99.1	24.82	0.000020
0.815	8.82	0.0078	0.435	-36.51	131.4	28.16	0.000018
1.115	9.98	0.0106	0.493	-32.81	179.7	31.86	0.000017
1.415	10.39	0.0135	0.513	-31.51	228.1	33.16	0.000016
1.815	11.80	0.0173	0.587	-26.72	292.6	37.94	0.000015
2.215	13.19	0.0211	0.651	-22.59	357.0	42.07	0.000015
2.615	14.35	0.0249	0.708	-18.88	421.5	45.79	0.000015
3.015	15.65	0.0287	0.772	-14.73	486.0	49.94	0.000014
3.415	16.90	0.0325	0.834	-10.73	550.5	53.94	0.000013
3.915	18.20	0.0373	0.898	-6.58	631.1	58.09	0.000012
4.915	20.27	0.0468	1.000	0.00	792.3	64.67	0.000000

RUN: 110971-1 X= 2. Z= 0.

UI = 29.13 D1 = 0.0561 BETA= 0.219 RD2 = 541.
CF/2= 0.00269 D2 = 0.0359 B = 0.000 K = 1.562
F = 0.00000 DC = 1.0802 P+ = 0.00050 G = 6.933
K = -0.699E-06 D99 = 0.3064 V0+ = 0.0000

Table with columns Y, U, Y/DC, U/UI, (U-UI)/U*, Y+, U+, TAU, TAULAM. Contains multiple rows of numerical data.

RUN: 110971-1 X=10. Z= 0.

UI = 25.70 D1 = 0.1237 BETA= 1.201 RD2 = 1024.
CF/2= 0.00174 D2 = 0.0770 B = 0.000 H = 1.607
F = 0.00000 DC = 2.9662 P+ = 0.0175 G = 9.052
K = -0.127E-05 D99 = 0.5366 V0+ = 0.0000

Table with columns Y, U, Y/DC, U/UI, (U-UI)/U*, Y+, U+, TAU, TAULAM. Contains multiple rows of numerical data.

RUN: 110971-1 X=22. Z= 0.

UI = 22.31 D1 = 0.2478 BETA= 1.559 RD2 = 1727.
CF/2= 0.00129 D2 = 0.1496 B = 0.000 h = 1.657
F = 0.00000 DC = 8.9052 P+ = 0.0152 G = 11.046
K = -0.702E-06 D99 = 0.9542 V0+ = 0.0000

Table with columns Y, U, Y/DC, U/UI, (U-UI)/U*, Y+, U+, TAU, TAULAM. Contains multiple rows of numerical data.

RUN: 110971-1 X=34. Z= 0.

UI = 20.53 D1 = 0.3628 BETA= 1.626 RD2 = 2331.
CF/2= 0.00119 D2 = 0.2195 B = 0.000 H = 1.653
F = 0.00000 DC = 10.4980 P+ = 0.0122 G = 11.427
K = -0.504E-06 D99 = 1.3935 V0+ = 0.0000

Table with columns Y, U, Y/DC, U/UI, (U-UI)/U*, Y+, U+, TAU, TAULAM. Contains multiple rows of numerical data.

RUN: 21572-5 X=34. Z= 0.

UI = 20.69 D1 = 0.2211 BETA= 0.571 RD2 = 1608.
CF/2= 0.00208 D2 = 0.1493 B = -0.726 H = 1.481
F = -0.00151 DC = 4.8479 P+ = 0.0053 G = 7.118
K = -0.499E-06 D99 = 1.1037 V0+ = -0.0331

Table with 12 columns: Y, U, Y/DC, U/UI, (U-U1)/U*, Y+, U+, TAU, TAU/LAM. Contains multiple rows of numerical data.

RUN: 21572-5 X=46. Z= 0.

UI = 19.49 D1 = 0.2782 BETA= 0.565 RD2 = 1911.
CF/2= 0.00198 D2 = 0.1884 B = -0.722 H = 1.477
F = -0.00143 DC = 6.2517 P+ = 0.0045 G = 7.255
K = -0.396E-06 D99 = 1.3716 V0+ = -0.0321

Table with 12 columns: Y, U, Y/DC, U/UI, (U-U1)/U*, Y+, U+, TAU, TAU/LAM. Contains multiple rows of numerical data.

RUN: 21572-5 X=58. Z= 0.

UI = 18.73 D1 = 0.3143 BETA= 0.524 RD2 = 2121.
CF/2= 0.00193 D2 = 0.2175 B = -0.715 H = 1.445
F = -0.00138 DC = 7.1540 P+ = 0.0039 G = 7.011
K = -0.330E-06 D99 = 1.6292 V0+ = -0.0314

Table with 12 columns: Y, U, Y/DC, U/UI, (U-U1)/U*, Y+, U+, TAU, TAU/LAM. Contains multiple rows of numerical data.

RUN: 21572-5 X=70. Z= 0.

UI = 18.10 D1 = 0.3613 BETA= 0.518 RD2 = 2381.
CF/2= 0.00186 D2 = 0.2528 B = -0.710 H = 1.429
F = -0.00132 DC = 8.3767 P+ = 0.0035 G = 6.962
K = -0.283E-06 D99 = 1.9116 V0+ = -0.0306

Table with 12 columns: Y, U, Y/DC, U/UI, (U-U1)/U*, Y+, U+, TAU, TAU/LAM. Contains multiple rows of numerical data.

RUN: 21572-5 X=82. Z= 0.

UI = 17.53 D1 = 0.4091 BETA= 0.505 RDZ = 2619.
CF/2= 0.00182 D2 = 0.2869 B = -0.714 H = 1.426
F = -0.00130 DC = 9.5894 P+ = 0.0032 G = 7.001
K = -0.246E-06 D99 = 2.1881 V0+ = -0.0305

Y	U	Y/DC	U/UI	(U-UI)/U*	Y+	U+	TAU	TAULAN
0.008	2.61	0.0008	0.149	-19.45	3.1	3.49	0.00164	0.001686
0.009	2.79	0.0009	0.159	-19.71	3.5	3.73	0.00163	0.001627
0.011	3.19	0.0011	0.182	-19.17	4.3	4.27	0.00161	0.001509
0.013	3.70	0.0014	0.211	-18.50	5.1	4.94	0.00157	0.001369
0.016	4.23	0.0017	0.242	-17.78	6.2	5.66	0.00154	0.001307
0.019	4.97	0.0020	0.284	-16.79	7.4	6.65	0.00149	0.001187
0.024	5.89	0.0025	0.336	-15.56	9.3	7.88	0.00143	0.000974
0.029	6.68	0.0030	0.381	-14.51	11.3	8.93	0.00138	0.000806
0.039	7.73	0.0041	0.441	-13.10	15.2	10.34	0.00132	0.000530
0.049	8.50	0.0051	0.485	-12.07	19.1	11.37	0.00128	0.000376
0.064	9.18	0.0067	0.523	-11.17	24.9	12.27	0.00125	0.000240
0.079	9.65	0.0082	0.550	-10.55	30.8	12.89	0.00123	0.000169
0.099	10.10	0.0103	0.576	-9.93	38.5	13.51	0.00121	0.000116
0.149	10.63	0.0155	0.606	-9.23	58.0	14.21	0.00122	0.000065
0.199	11.02	0.0208	0.628	-8.71	77.5	14.73	0.00123	0.000047
0.299	11.77	0.0312	0.671	-7.70	116.4	15.74	0.00125	0.000034
0.399	12.00	0.0416	0.684	-7.40	155.4	16.04	0.00127	0.000030
0.549	12.68	0.0573	0.723	-6.49	213.8	16.95	0.00129	0.000026
0.699	13.28	0.0729	0.758	-5.68	272.2	17.76	0.00128	0.000024
0.899	13.99	0.0937	0.798	-4.74	350.0	18.70	0.00124	0.000023
1.099	14.72	0.1146	0.839	-3.76	427.9	19.68	0.00117	0.000020
1.399	15.63	0.1459	0.891	-2.55	544.7	20.89	0.00095	0.000017
1.699	16.52	0.1772	0.942	-1.35	661.5	22.09	0.00063	0.000013
1.999	17.16	0.2085	0.979	-0.50	778.3	22.94	0.00031	0.000009
2.299	17.47	0.2397	0.997	-0.08	895.1	23.36	0.00008	0.000006
2.499	17.55	0.2606	1.001	0.02	973.0	23.46	0.00000	0.000005
2.599	17.53	0.2710	1.000	0.00	1011.9	23.44	0.00000	0.000000

RUN: 21572-5 X=90. Z= 0.

UI = 17.02 D1 = 0.4641 BETA= 0.542 RDZ = 2860.
CF/2= 0.00179 D2 = 0.3228 B = -0.721 H = 1.438
F = -0.00129 DC = 10.9695 P+ = 0.0031 G = 7.198
K = -0.236E-06 D99 = 2.3911 V0+ = -0.0305

Y	U	Y/DC	U/UI	(U-UI)/U*	Y+	U+	TAULAN
0.010	2.70	0.0009	0.159	-19.89	3.7	3.75	0.001565
0.011	2.92	0.0010	0.171	-19.59	4.0	4.05	0.001518
0.013	3.32	0.0012	0.195	-19.02	4.8	4.62	0.001423
0.015	3.69	0.0013	0.217	-18.51	5.5	5.13	0.001313
0.018	4.35	0.0016	0.256	-17.60	6.7	6.04	0.001209
0.023	5.13	0.0021	0.302	-16.51	8.5	7.13	0.001002
0.028	5.97	0.0025	0.351	-15.35	10.4	8.29	0.000814
0.038	7.17	0.0034	0.421	-13.68	14.2	9.96	0.000548
0.048	7.64	0.0044	0.449	-13.03	17.9	10.60	0.000397
0.063	8.40	0.0057	0.493	-11.98	23.5	11.66	0.000257
0.083	9.06	0.0075	0.532	-11.05	31.0	12.59	0.000164
0.113	9.65	0.0103	0.567	-10.24	42.3	13.40	0.000108
0.163	10.17	0.0148	0.597	-9.52	61.0	14.12	0.000063
0.213	10.46	0.0194	0.614	-9.11	79.8	14.52	0.000046
0.313	11.08	0.0285	0.651	-8.25	117.3	15.38	0.000034
0.463	11.56	0.0422	0.679	-7.59	173.5	16.04	0.000029
0.613	12.20	0.0559	0.717	-6.70	229.7	16.94	0.000026
0.813	12.93	0.0741	0.760	-5.68	304.7	17.95	0.000023
1.013	13.61	0.0923	0.800	-4.74	379.7	18.90	0.000022
1.313	14.50	0.1197	0.852	-3.50	492.2	20.14	0.000019
1.613	15.24	0.1470	0.895	-2.47	604.6	21.16	0.000016
1.813	15.89	0.1653	0.933	-1.58	679.6	22.06	0.000013
2.113	16.50	0.1926	0.969	-0.73	792.1	22.90	0.000009
2.413	16.88	0.2200	0.992	-0.20	904.5	23.44	0.000006
2.713	17.01	0.2473	0.999	-0.02	1017.0	23.62	0.000004
3.013	17.02	0.2747	1.000	0.00	1129.5	23.64	0.000000

REFERENCES

1. Moffat, R. J. and Kays, W. M., "The Turbulent Boundary Layer on a Porous Plate: Experimental Heat Transfer with Uniform Blowing and Suction," Report No. HMT-1, Thermosciences Division, Dept. of Mech. Engrg., Stanford Univ., (1967).
2. Simpson, R. L., Kays, W. M. and Moffat, R. J., "The Turbulent Boundary Layer on a Porous Plate: An Experimental Study of the Fluid Dynamics with Injection and Suction," Report No. HMT-2, Thermosciences Division, Dept. of Mech. Engrg., Stanford Univ., (1967).
3. Julien, H. L., Kays, W. M. and Moffat, R. J., "The Turbulent Boundary Layer on a Porous Plate: Experimental Study of the Effects of a Favorable Pressure Gradient," Report No. HMT-4, Thermosciences Division, Dept. of Mech. Engrg., Stanford Univ., (1969).
4. Loyd, R. J., Moffat, R. J. and Kays, W. M., "The Turbulent Boundary Layer on a Porous Plate: An Experimental Study of the Fluid Dynamics with Strong Favorable Pressure Gradients and Blowing," Report No. HMT-13, Thermosciences Division, Dept. of Mech. Engrg., Stanford Univ., (1970).
5. Kays, W. M., "Heat Transfer to the Transpired Turbulent Boundary Layer," Report No. HMT-14, Thermosciences Division, Dept. of Mech. Engrg., Stanford Univ., (1971).
6. Squire, L. C., "The Constant Property Turbulent Boundary Layer with Injection; A Reanalysis of Some Experimental Results," Int. Jn. Heat and Mass Transfer, Vol. 13, pp. 939-942, (1970).
7. McLean, J. D., "The Transpired Turbulent Boundary Layer in an Adverse Pressure Gradient," PhD Thesis, Department of Aerospace and Mechanical Sciences, Princeton Univ., (1970).
8. Stevenson, T. N., "A Law of the Wall for Turbulent Boundary Layers with Suction or Injection," The College of Aeronautics, Cranfield, Aero Report No. 166, (1963).
9. Clauser, F. H., "Turbulent Boundary Layers in Adverse Pressure Gradients, J. of Aero Sci., 21, 91, (1954).
10. Bradshaw, P., "The Turbulence Structure of Equilibrium Boundary Layers," J. Fluid Mech., Vol. 29, Part 4, pp. 625-645, (1967).

11. Young, A. D. and Maas, J. N., "The Behavior of a Pitot Tube in a Transverse Total Pressure Gradient," A.R.C. R & M No. 1770, (1936).
12. Jorgensen, F. E., "Directional Sensitivity of Wire and Hot-film Probes," DISA Information No. 11, (1971).
13. MacMillan, F. A., "Experiments on Pitot Tubes in Shear Flow," A.R.C. R & M No. 3028, (1956).
14. Coles, D. E., "The Young Persons's Guide to the Data, Proceedings, Computation of Turbulent Boundary Layers," 1968 AFOSR-IFP Stanford Conference, Vol. II, pp. 1-45.
15. Bradshaw, P., "The Effect of Wind-Tunnel Screens on Nominally Two-Dimensional Boundary Layers," J. Fluid Mech., Vol. 22, Part 4, pp. 679-687, (1965).
16. Coles, D. E., "The Turbulent Boundary Layer in a Compressible Fluid," The Rand Corporation, Report R-403-PR, (1962).
17. Keenan, J. H., Keyes, F. G., Hill, P. G., Moore, J. G., Steam Tables, John Wiley and Sons, New York, 1969.
18. Clauser, F. H., "The Turbulent Boundary Layer," Advances in Applied Mechanics, Vol. IV, pp. 1-51, Academic Press, New York, (1956).
19. Spalding, D. B., and Patankar, S. V., Heat and Mass Transfer in Boundary Layers, Morgan-Granpian: London (1967).
20. Cebeci, T., "The Behavior of Turbulent Flow Near a Porous Wall with Pressure Gradient," McDonnell Douglas, Report No. DAC 70014, (1969).
21. Launder, B. E. and Jones, W. P., "A Note on Bradshaw's Hypothesis for Laminarization," ASME-AIChE Conference, 69-HT-12, (1969).
22. Bradshaw, P., "A Note on Reverse Transition," J. Fluid Mech., Vol. 35, Part 2, pp. 387-390, (1969).
23. Evans, H. L., Lea, J. F., and Swayne, D. A., "The Couette-Flow Model in Turbulent Boundary Layers," Research Report No. 16, Dept. of Mech. Engrg., Univ. of Waterloo, Ontario, (1970).
24. Coles, D. E., "Survey of Data for Turbulent Boundary Layers with Mass Transfer," AGARD-CP-93, (1972).

25. Millikan, C. B., "A Critical Discussion of Turbulent Flows in Channels and Circular Tubes," Proc. 5th International Congress of Applied Mechanics, Cambridge, Mass., (1938).
26. Laufer, J., "The Structure of Fully Developed Pipe Flow," NACA Report 1174, (1957).
27. McQuaid, J., "Incompressible Turbulent Boundary Layers with Distributed Injection," PhD Thesis, Cambridge Univ., (1966).

APPENDIX A

MEASUREMENT OF TURBULENCE INTENSITIES AND REYNOLDS STRESS

The directional sensitivity of the hot-wire makes it possible to use it for measurement of individual components of the velocity vector. In what follows it will be shown how a slant hot-wire may be used for measurement of the statistical mean values of the three components of the turbulent fluctuations and the Reynolds stress $-\overline{u'v'}$. (The Reynolds stresses $-\overline{v'w'}$ and $-\overline{u'w'}$ can also be measured, but from reasons of symmetry they are known to be zero for the two-dimensional flows considered in this report. The postulate of zero value of $-\overline{v'w'}$ and $-\overline{u'w'}$ will be used to eliminate first order errors due to a lateral misalignment of the probe with the flow).

1. Directional Sensitivity of the Hot-Wire

As shown in Ref. [12] the response of the hot-wire may be approximated by

$$u_1^2 = u_2^2 + k_1^2 v_2^2 + k_2^2 w_2^2 \quad , \quad (A-1)$$

where u_2 , v_2 and w_2 are the velocity components in the coordinate system of the wire: v_2 is the velocity component parallel to the wire, w_2 is perpendicular to the wire and the wire supports and u_2 is perpendicular to the wire and lies in the plane of the wire supports. u_1 , the 'indicated velocity' is defined by Eq. (A-1); it may be thought of, for example, as the velocity one would deduce by using a calibration curve that was obtained for $v_2 = w_2 = 0$. k_1 and k_2 are constants which to some extent depend upon the hot-wire probe design. (The hot-wire used in the present experiments is a DISA which has a wire diameter of 5μ , length-to-diameter ratio of 200, and gold-plated wire ends to reduce prong

interference with the flow over the central sensitive part of the wire. For this probe design Ref. [12] indicates that $k_1 = .2$ and $k_2 = 1.02$).

2. Probe Position and Velocity Decomposition

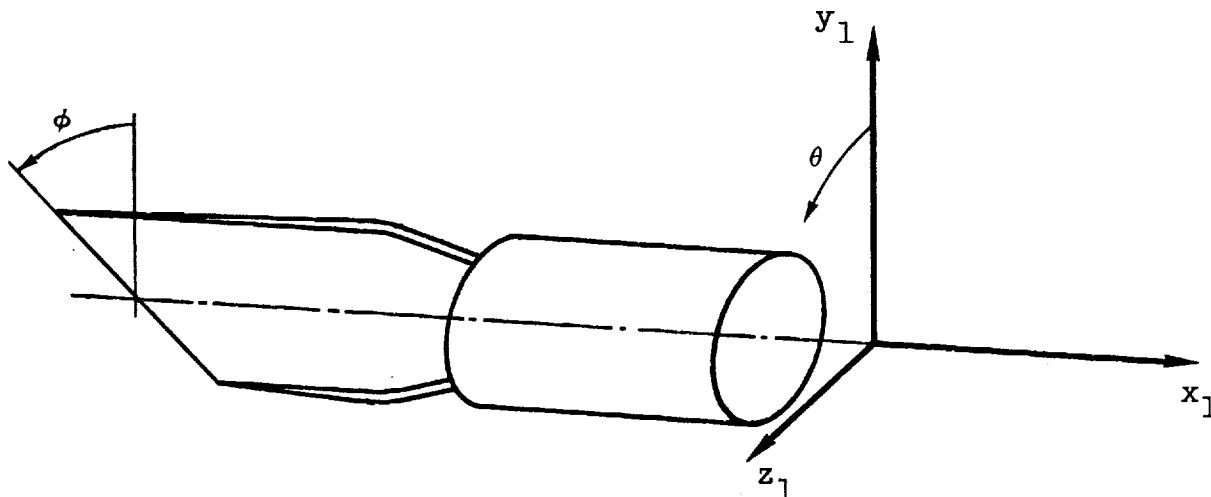


Fig. A-1 Geometry and position of hot-wire probe (schematic). Probe shown for $\theta = 0$.

The hot-wire forms an angle, ϕ , with a plane perpendicular to the probe axis (see Fig. (A-1)). For a slant hot-wire, $\phi \neq 0$.

In describing the position of the hot-wire probe in the flow we shall start from a 'mean flow' coordinate system (x_1, y_1, z_1) in which the mean velocity vector has the components $(\bar{u}_1, 0, 0)$. This coordinate system is in general not completely coincident with the laboratory coordinate system (x, y, z) in which the mean velocity vector is $(\bar{u}, \bar{v}, \bar{w})$. However, for the two-dimensional boundary layer flows considered in this report, one has that $\bar{w} = 0$ and $\bar{v} \ll \bar{u}$ (boundary layer approximation). In fact, for all flows considered it

is true that $v < .02u$, anywhere. The measured values of the correlations $\overline{u'^2}$, $\overline{v'^2}$, $\overline{w'^2}$ and $-\overline{u'v'}$ will strictly speaking be expressed in the (x_1, y_1, z_1) coordinate system, but a transformation into the laboratory plane of reference (x, y, z) would only result in a negligible correction. The hot-wire probe axis will be assumed to be aligned with the mean velocity vector, i.e. the probe axis is in the direction of x_1 .

The angle of rotation around the probe axis is ϕ . (See Fig. (A-1)). The relationship between the velocity components (u_1, v_1, w_1) in the 'mean flow' reference system (x_1, y_1, z_1) and the components (u_2, v_2, w_2) in the wire reference system is then

$$\begin{Bmatrix} u_2 \\ v_2 \\ w_2 \end{Bmatrix} = \begin{bmatrix} \cos\phi & \sin\phi\cos\theta & \sin\phi\sin\theta \\ -\sin\phi & \cos\phi\cos\theta & \cos\phi\sin\theta \\ 0 & -\sin\theta & \cos\theta \end{bmatrix} \begin{Bmatrix} u_1 \\ v_1 \\ w_1 \end{Bmatrix} \quad (\text{A-2})$$

Inserting this result in Eq. (A-1) gives

$$u_i^2 = Au_1^2 + Bv_1^2 + Cw_1^2 + Du_1v_1 + Ev_1w_1 + Fu_1w_1, \text{ where}$$

$$A = \cos^2\phi + k_1^2\sin^2\phi$$

$$B = (\sin^2\phi + k_1^2\cos^2\phi)\cos^2\theta + k_2^2\sin^2\theta$$

$$C = (\sin^2\phi + k_1^2\cos^2\phi)\sin^2\theta + k_2^2\cos^2\theta$$

$$D = (1-k_1^2)\sin 2\phi\cos\theta$$

$$E = (\sin^2\phi + k_1^2\cos^2\theta - k_2^2)\sin 2\theta$$

$$F = (1-k_1^2)\sin 2\phi\sin\theta.$$

3. The Hot-Wire Response to Turbulence

The velocity components in the 'mean flow' frame of reference may be expressed as

$$\begin{aligned} u_1 &= \bar{u} + u' \\ v_1 &= v' \\ w_1 &= w' \end{aligned} \tag{A-4}$$

where the primed velocities represent the turbulent fluctuations (assumed to have zero statistical mean values). Note that from now on we shall make no distinction between \bar{u} and \bar{u}_1 ; also u' , v' and w' in Eqs. (A-4) should really be u'_1 , v'_1 and w'_1 because they are expressed in the 'mean flow' frame of reference. Introducing the decomposition Eq. (A-4) into Eq. (A-3) results in

$$u_1^2 = A\bar{u}^2 + 2A\bar{u}u' + D\bar{u}v' + F\bar{u}w' + O(2), \tag{A-5}$$

where $O(2)$ represents terms of the order of the turbulent fluctuations squared.

Taking the square root of this expression and introducing the fluctuation of the indicated velocity, u'_1 , leads to

$$u'_1 = \sqrt{A}u' + \frac{D}{2\sqrt{A}}v' + \frac{F}{2\sqrt{A}}w' + O(2). \tag{A-6}$$

Squaring this equation and taking the time average one obtains:

$$\overline{u_1'^2} = A\overline{u'^2} + \frac{D^2}{4A}\overline{v'^2} + \frac{F^2}{4A}\overline{w'^2} + D\overline{u'v'} + \frac{DF}{2A}\overline{v'w'} + F\overline{u'w'} + O(3), \tag{A-7}$$

where $O(3)$ represents terms of the order of the triple correlations of the turbulent fluctuations. (See Section 6 for the explicit expression for $O(3)$). Equation (A-7) re-

lates the mean square of the indicated velocity fluctuations to the correlations of the turbulent velocity fluctuations.

4. Measurement of Turbulent Velocity Correlations

Note that the coefficients in Eq. (A-1) depend upon ϕ , the slant of the hot-wire and θ , the angle of rotation of the hot-wire probe. By performing measurements of $\overline{u_i'^2}$ for six suitable combinations of ϕ and θ the resulting six equations (7) may be solved for the six unknown correlations, $\overline{u'^2}$, $\overline{v'^2}$, $\overline{w'^2}$, $\overline{u'v'}$, $\overline{v'w'}$ and $\overline{u'w'}$. In practice, however, $\overline{v'w'}$ and $\overline{u'w'}$ will not be treated as unknowns, but put equal to zero from reasons of symmetry. This a priori knowledge of $\overline{v'w'}$ and $\overline{u'w'}$ permits elimination of an error that would occur if the probe axis of rotation accidentally were slightly misaligned with the x-y plane of the flow (see Section 5 for details).

Two hot-wire probes with different geometries were used:

- 1) A horizontal, $\phi = \frac{\pi}{2}$ wire (hot-wire along z-axis) was used for the measurement of $\overline{u'^2}$. For $\phi = \frac{\pi}{2}$ Eq. (A-7) becomes

$$\overline{u_i'^2} = \overline{u'^2} + 0(3) \quad (A-8)$$

The horizontal hot-wire thus measures $\overline{u_i'^2}$ directly.

- 2) A rotatable hot-wire probe that permitted measurement at six different $\theta = \theta_m$ (i.e. $\theta_m = (m-1)\frac{\pi}{6}$; $m = 1, 2, \dots, 6$) was used for the measurement of $\overline{v'^2}$, $\overline{w'^2}$ and $\overline{u'v'}$. Using six measurements rather than the minimum required three, gives a degree of redundancy that is exploited to reduce the statis-

tical uncertainty. Furthermore, by averaging the 'symmetric' measurements, the error due to a slight misalignment of the probe axis with the x-y plane of the flow is practically eliminated (see Section 5).

The unknowns $\overline{v'^2}$, $\overline{w'^2}$ and $\overline{u'v'}$ are computed as follows:

Equation (A-7) is written for the angles $\theta = \theta_m$, $m = 1, 2, \dots, 6$. Then, putting $\overline{u'w'} = \overline{u'w'} = 0$ and adding Eq. 1 to Eq. 2 and Eq. 4 to Eq. 2 gives

$$\left[\begin{array}{cc} D_m^2 & F_m^2 \\ 4A & 4A \end{array} D_m \right] \begin{Bmatrix} \overline{v'^2} \\ \overline{w'^2} \\ \overline{u'v'} \end{Bmatrix} = \begin{Bmatrix} \overline{u'_{i1}^2} \\ (\overline{u'_{i2}^2} + \overline{u'_{i6}^2})/2 \\ (\overline{u'_{i3}^2} + \overline{u'_{i5}^2})/2 \\ \overline{u'_{i4}^2} \end{Bmatrix} - A \begin{Bmatrix} \overline{u'^2} \\ \overline{u'^2} \\ \overline{u'^2} \\ \overline{u'^2} \end{Bmatrix} \quad ; m=1, 2, \dots, 4. \quad (A-9)$$

In these equations $\overline{u'^2}$ is considered a known quantity (since it has been measured by the horizontal hot-wire).

Note that $\overline{u'v'}$ may be computed in two different ways from this set of equations, namely as

$$\overline{u'v'}_{(2)} = (\overline{u'_{i1}^2} - \overline{u'_{i4}^2})/2D_1 \quad \text{or} \quad (A-10)$$

$$\overline{u'v'}_{(4)} = (\overline{u'_{i2}^2} + \overline{u'_{i6}^2} - \overline{u'_{i3}^2} - \overline{u'_{i5}^2})/4D_2. \quad (A-11)$$

It was found that in general the difference between $\overline{u'v'}_{(2)}$ and $\overline{u'v'}_{(4)}$ is very small (less than 1%) and of random sign; but for the flows with the highest blowing rates

the difference becomes of somewhat greater magnitude ($\approx 10\%$ for Run 112871-1).

Furthermore, for these flows it was found consistently that $\overline{u'v'}(4) > \overline{u'v'}(2)$ for the measurements close to the wall. The reason for this is probably the neglect of the $O(3)$ terms in Eq. (A-7). Section 6 will discuss this point in detail.

Since no reason was found for preferring either $\overline{u'v'}(2)$ or $\overline{u'v'}(4)$ the average of the two was used i.e.,

$$\overline{u'v'}(6) = (\overline{u'_{i1}{}^2} + \overline{u'_{i2}{}^2} + \overline{u'_{i6}{}^2} - \overline{u'_{i3}{}^2} - \overline{u'_{i5}{}^2} - \overline{u'_{i4}{}^2})/4D_1 .$$

Inserting the known values of $\overline{u'^2}$ and $\overline{u'v'}$ into the $m = 1$ and $m = 2$ equations of the system (A-9) one obtains:

$$\begin{bmatrix} D_1^2 & F_1^2 \\ D_2^2 & F_2^2 \end{bmatrix} \begin{Bmatrix} \overline{v'^2} \\ \overline{w'^2} \end{Bmatrix} / 4A = \begin{Bmatrix} \overline{u'_{i1}{}^2} \\ \overline{u'_{i2}{}^2} \end{Bmatrix} - \overline{u'^2} \begin{Bmatrix} A \\ A \end{Bmatrix} - \overline{u'v'} \begin{Bmatrix} D_1 \\ D_2 \end{Bmatrix} , \quad (A-13)$$

from which $\overline{v'^2}$ and $\overline{w'^2}$ may be computed.

5. Error Due to Misalignment of Probe

In this section it will be assumed that the axis of the probe is not perfectly aligned with the mean flow vector. Thus we shall assume that the probe axis is turned a small angle, β , around the y_1 -axis and γ around the z_1 -axis (see Fig. (A-2)). Here, as previously defined (x_1, y_1, z_1) is the 'mean flow' frame of reference. It will be shown that the measured values of $\overline{v'^2}$, $\overline{w'^2}$ and $\overline{u'v'}$ are independent of β . (This is because of the averaging of 'symmetric' measurements made possible by the postulate of

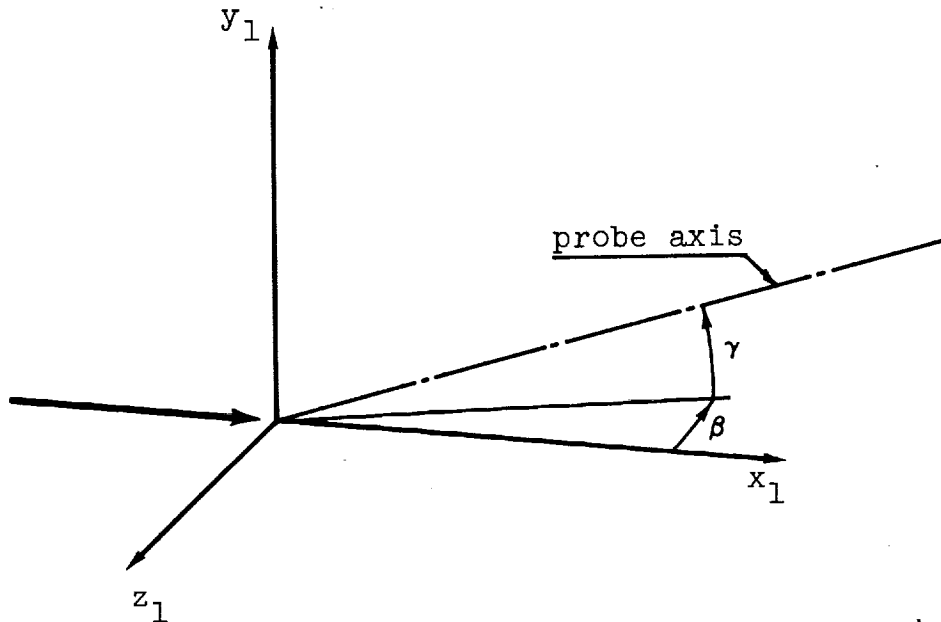


Fig. A-2 Misalignment of probe axis - (x_1, y_1, z_1) is the 'mean flow' coordinate system

$\overline{v'w} = \overline{u'w} = 0$). It will also be shown that the error in the measured value of $\overline{u'v'}$ is $\approx \gamma(\overline{u'^2} - \overline{v'^2})$. The effect of γ on $\overline{v'^2}$ and $\overline{w'^2}$ has not been worked out.

Because of the assumed misalignment the velocity vector (u_1, v_1, w_1) in Eq. (A-2) should be replaced by

$$u' + \gamma v' + \beta w'$$

$$v' - \gamma u'$$

$$w' - \beta u'$$

(to a first order approximation). The coefficients in Eq. (A-3) must as a consequence be modified to

$$\begin{aligned}
A' &= A - \gamma D - \beta F \\
B' &= B + \gamma D \\
C' &= C + \beta F \\
D' &= D + 2\gamma(A-B) - \beta F \\
E' &= E + \beta D + \gamma F \\
F' &= F + 2\beta(A-C) - \gamma E
\end{aligned} \tag{A-14}$$

With these new coefficients the equations (A 9) which form the basis for the computation of $\overline{u'^2}$, $\overline{v'^2}$ and $\overline{w'^2}$ become (terms of 2nd order in β and γ have been neglected).

$$\begin{aligned}
& \left([c] + 2\gamma \left[\frac{D_n}{A}(A-B_n) + \frac{D_n^3}{4A^2} \left(\frac{D_2 F_2^2}{A^2} - \frac{2E_2 F_2}{A} \right) (A-B_n) \right] \right) \left\{ \begin{array}{l} \overline{u'^2} + \Delta \overline{v'^2} \\ \overline{w'^2} + \Delta \overline{w'^2} \\ \overline{u'v'} + \Delta \overline{u'v'} \end{array} \right\} \\
&= \left\{ \begin{array}{l} \overline{u'_{i1}^2} \\ (\overline{u'_{i2}^2} + \overline{u'_{i6}^2})/2 \\ (\overline{u'_{i3}^2} + \overline{u'_{i5}^2})/2 \\ \overline{u'_{i4}^2} \end{array} \right\} - (A - \gamma [D_n]) \left\{ \begin{array}{l} \overline{u'^2} \\ \overline{u'^2} \\ \overline{u'^2} \\ \overline{u'^2} \end{array} \right\} ; n = 1, 2, \dots, 4
\end{aligned} \tag{A-15}$$

Here $[c]$ is the coefficient matrix from Eqs. (A-9). $\overline{\Delta v'^2}$, $\overline{\Delta w'^2}$ and $\overline{\Delta u'v'}$ represent the changes in the measured correlations due to the correction for misalignment. Note that the angle β (the rotation around y_1) does not appear in this system of equations. Thus the measured correlations are independent of β to a first order approximation.

We shall now evaluate $\overline{\Delta u'v'}$ by manipulating Eqs. (A-15) in a manner analogous to the treatment of Eqs. (A-7). Thus we obtain

$$\overline{\Delta u'v'}_{(2)} \doteq \gamma \left[\overline{u'^2} - \left(\frac{1 - k_1^2}{1 + k_1^2} \right)^2 \overline{v'^2} \right] \quad \text{and}$$

$$\overline{\Delta u'v'}_{(4)} \doteq \gamma \left\{ \overline{u'^2} - \left[\frac{3}{4} + \left(\frac{1 - k_1^2}{1 + k_1^2} \right)^2 \frac{1}{4} - \frac{3k_2^2}{2(1 + k_1^2)} \right] \overline{v'^2} \right\} \quad (\text{A-17})$$

To a sufficient degree of accuracy for the error estimate, we have $k_1^2 = 0$ and $k_2^2 = 1$, therefore

$$\overline{\Delta u'v'}_{(2)} \doteq \gamma [\overline{u'^2} - \overline{v'^2}] \quad (\text{A-16a})$$

$$\overline{\Delta u'v'}_{(4)} \doteq \gamma [\overline{u'^2} - \frac{1}{3} \overline{v'^2}] \quad (\text{A-17a})$$

For $\gamma = .5^0$ (probably the greatest error of alignment in the present experiments) and $\overline{u'^2}/u_\infty^2 = .008$, $\overline{v'^2}/u_\infty^2 = .003$ (typical values close to the wall) we have

$$\overline{\Delta u'v'}/u_\infty^2 \approx .00006$$

This may be considered to be the greatest error in the measured Reynolds stress, due to misalignment of the probe.

6. Error on $\overline{u'v'}$ Due to the Neglect of the Triple Correlations

The third order term, $O(3)$, in Eq. (A-7) contains the non-zero triple correlations ($\overline{u'v'w'} = \overline{u'^2w'} = \overline{v'^2w'} = 0$ for symmetry reasons):

$$\begin{aligned}
o(3) = \frac{1}{\bar{u}} & \left[\overline{u'v'^2}_B + \overline{u'w'^2}_C + \overline{u'^2v'}_D + \overline{v'^3} \left(\frac{BD}{2A} - \frac{D^3}{8A^2} \right) \right. \\
& \left. + \overline{v'w'^2} \left(\frac{DC}{2A} - \frac{DF^2}{8A^2} + \frac{EF}{2A} \right) \right] \quad (A-18)
\end{aligned}$$

If the $O(3)$ - terms are retained Eqs. (A-11) and (A-12), which are used for the evaluation of $\overline{u'v'}$, would be corrected by

$$\Delta\overline{u'v'}_{(2)} = - [O_1(3) - O_4(3)]/2D_1 \quad \text{and} \quad (A-19)$$

$$\Delta\overline{u'v'}_{(4)} = - [O_2(3) + O_6(3) - O_3(3) - O_5(3)]/4D_2 \quad (A-20)$$

where $O_n(3)$ means the third order terms from Eq. (A-18) evaluated at $\theta = \theta_n$. Note that in general the error introduced by ignoring the triple correlations is not the same for $\overline{u'v'}_{(2)}$ and $\overline{u'v'}_{(4)}$.

As an example let us choose $\phi = \frac{\pi}{4}$ and $k_1^2 = .04$ (values corresponding to the probe used for the measurement of $\overline{u'v'}$). We then obtain

$$\Delta\overline{u'v'}_{(2)} = (\overline{u'^2v'} + .044 \overline{v'^3} + .996 \overline{v'w'^2})/\bar{u} \quad (A-19a)$$

$$\Delta\overline{u'v'}_{(4)} = (\overline{u'^2v'} + .758 \overline{v'^3} + .258 \overline{v'w'^2})/\bar{u} \quad (A-20a)$$

Since the triple correlations were not measured in the present experiments, we can only arrive at a very crude estimate of their importance.

Laufer [26] reports triple correlations for pipe flow. To get a very rough estimate of the upper limit of the error

we shall take the largest value of the largest of the three correlations as measured by Laufer. Thus

$$\frac{\overline{u'^2 v'}}{\bar{u}} < (0.1) \frac{\overline{u'^2} \sqrt{\overline{v'^2}}}{\bar{u}}$$

so that the error becomes

$$\Delta \overline{u'v'}/u_\infty^2 < (0.1) \frac{\overline{u'^2}}{u_\infty^2} \frac{\sqrt{\overline{v'^2}}}{u_\infty} \frac{u_\infty}{\bar{u}} \quad (\text{A-21})$$

As a first example let us consider a flow with zero pressure gradient and no transpiration (Run 120771-1). For $x = 70$ inches the measured friction coefficient is $c_f/2 = 0.00180$. $c_f/2$ has been evaluated on the basis of a Reynolds stress measurement at $y = 0.125$ inches for which we obtain

$$\Delta \overline{u'v'}/u_\infty^2 < 0.00005$$

The relative error on the friction coefficient due to the neglect of the triple correlations is therefore $< 3\%$.

Examination of a few more cases shows that the error unfortunately tends to increase with decreasing friction coefficient. It is therefore appropriate as our next example to consider the run with the lowest $c_f/2$ for which the measured Reynolds stress has been used for determination of skin friction. This is Run 101371-2 ($m = -0.15$, $F_1 = 0.002$, $m_F = 0$). For $x = 70$ inches we have $c_f/2 = .00053$. The Reynolds stress measurement at $y = 0.120$ inches is used to determine the wall shear. The error is:

$$\Delta \overline{u'v'}/u_\infty^2 < 0.00011$$

Thus under the most unfavorable circumstances and assumptions, the relative error on $c_f/2$ due to the neglected 3rd order correlation is $< 20\%$.

APPENDIX B

Description of the Computer Program "SLOT"

The basic feature of the computer program, SLOT, is an analytical modeling of the potential flow in the test section. The program serves three purposes:

- a. SLOT predicts slot-width distribution and rotameter settings required for a given set of free-stream velocity and transpiration boundary conditions. This makes the program an invaluable tool in setting up a new run. It accepts as input the measured dynamic pressure distribution and rotameter settings; from this it computes a measured velocity distribution and a measured distribution of the blowing fraction. These are then compared with the desired boundary conditions and necessary changes in slot widths and rotameter settings are computed.
- b. The program performs an analytical fit of the measured free-stream velocities. The velocity gradient is computed as the derivative of this fit.
- c. SLOT served as an aid in the initial design of the slots, in particular of their spacing.

1. Principles of the Program

The predictive capability of SLOT is based on the following model of the physical situation:

The "real" flow is approximated by two-dimensional potential flow between infinitely long walls separated by a distance of $h = 6$ inches (the height of the test section). The effect of the slots is modeled by 23 line sinks in the upper wall.

The assumption of two-dimensional flow completely disregards the boundary layers on the bottom and side walls of the test-section. (The boundary layer on the top wall never develops because of the effect of the slots). Note, however, that the displacement thickness of the bottom wall boundary layer is never more than ≈ 1.5 inches thick i.e. only a fraction of the height of the test section. Moreover, the function of the program is primarily to predict a correction to the slot-widths; a correction for the presence of the boundary layers would therefore amount to a correction on a correction.

The nominal free-stream velocity distribution is given by Eq. (2-12) as

$$u = u_1 \left(\frac{x - x_0}{x_1 - x_0} \right)^m \quad (B-1)$$

This "ideal" distribution can obviously not be maintained upstream of the first slot (at $x = x_0$): A transitional length is required to permit establishment of the velocity distribution described by Eq. (B-1). It turns out that even maintaining the ideal velocity distribution only downstream from the first slot would require that the first slot be opened more than the slot design permits. It is therefore necessary to define a "modified" velocity distribution which can be approached in practice and which is identical to the "ideal" distribution a short distance downstream of the first slot. This "modified" distribution will be defined shortly.

The potential flow problem is solved by superposition of the contributions to the velocity field from each of the line sinks on a constant velocity. The sink strength distribution is obtained by requiring that the x-derivative of the potential flow velocity at $y = 1$ inch equals the derivative of the "modified" velocity distribution at the x-position of the 23 slots.

The derivative of the modified velocity distribution will be taken to be

$$\frac{du}{dx} = \frac{mu_1}{x_1-x_0} \left[\left(\frac{x-x_0}{x_1-x_0} \right)^{m-1} - \frac{1}{2} \exp\left(6 \frac{x_1-x}{x_1-x_0}\right) \right] . \quad (B-2)$$

Note that the modification of the derivative of the "ideal" velocity distribution, Eq. (B-1), is represented by the term containing the exponential. By integrating the derivative expressed by Eq. (B-2) one obtains the "modified" velocity distribution:

$$u = u_1 \left[\left(\frac{x-x_0}{x_1-x_0} \right)^m + \frac{1}{12^m} \exp\left(6 \frac{x_1-x}{x_1-x_0}\right) \right] \quad (B-3)$$

The effect of the modification of the "ideal" velocity distribution is negligible a few inches downstream of the first slot.

Because it is required to have available a very realistic theoretical velocity distribution also upstream of the first slot it has been necessary to introduce the "practical" velocity distribution. It is defined as the distribution computed from the potential flow solution described above, and can presumably be approached very closely in practice. The "practical" velocity distribution therefore serves as a natural yardstick for the measured velocity distribution. The analytical expression for the "practical" velocity distribution is:

$$u = C + \frac{1}{2h} \sum_{i=1}^{23} Q_i \frac{\cosh \frac{\pi}{2h}(x-\xi_1) \sinh \frac{\pi}{2h}(x-\xi_1)}{\cosh^2 \frac{\pi}{2h}(x-\xi_1) - \cos^2 \frac{\pi}{2h}(h-y)}; \quad y = 1 \text{ inch} \quad (B-4)$$

In this equation Q_i and ξ_i represent the sink strengths and positions respectively. h is the height of the test-section and C is a constant which is determined such that the velocity distribution from Eq. (B-4) matches the "modified" velocity distribution, Eq. (B-3), at $x = x_1$. The sink strengths, Q_i , are determined such that the x-derivative of u is equal to the derivative of the "modified" velocity distribution, Eq. (B-2), for $x = \xi_i$; $i = 1, 2 \dots 23$.

2. Fit of the Measured Velocity

The "practical" velocity distribution Eq. (B-4) is subtracted from the 47 measured velocities. The resulting difference is then least square fitted by a fourth order polynomial. The sum of this fit and the practical velocity distribution represents a fit of the measured velocities. The x-derivative of this fit is obtained analytically.

3. Correction of Slot-Widths

The polynomial fit of the difference between the measured velocities and the "practical" velocity distribution represents the error, $\Delta u(x)$, in the measured velocity distribution. Elimination of this error is attempted by computing the change in sink strengths, ΔQ_i , that will produce a change in the velocity distribution equal to $-\Delta u(x)$. The 23 ΔQ_i then correspond to the change in slot widths, $\Delta t_{u,i}$, required to make the measured velocity distribution equal to the "practical" distribution, Eq. (B-3). $\Delta t_{u,i}$ is computed as

$$\Delta t_{u,i} = \frac{\Delta Q_i}{u_{\text{slot},i}}, \text{ where } u_{\text{slot},i} = \sqrt{\frac{2P_i}{K\rho}}. \quad (\text{B-5})$$

The equation for the air velocity in the slot, $u_{\text{slot},i}$, is based on the static pressure above ambient, p_i , at the location of the slot. K is an empirical loss coefficient (= 1.8).

An error, ΔF , in the blowing fraction is corrected by readjusting the rotameter settings according to the calibration curve. This adjustment of the transpiration flow rate will require a correction in the slot widths to avoid an effect on the velocity distribution in the test-section. This correction, $\Delta t_{F,i}$, is simply obtained by associating each porous plate with the two slots located just upstream and downstream of that plate. Therefore

$$\Delta t_{F,i} = \frac{\Delta F_{i-1} u_{i-1} + \Delta F_i u_i}{2u_{\text{slot},i}} L, \quad (\text{B-6})$$

where ΔF_i corresponds to the porous plate located between slots numbers i and $i + 1$; u_i represents the free-stream velocity at the center of that plate and L is the plate width.

4. Potential Flow Field in Test Section

The "practical" velocity distributions for $y = 0$ and $y = 3$ inches are almost identical: there are no visible non-uniformities in the free-stream velocity due to the slots where the experimental boundary layer is formed on the floor of the test-section.

